CANADIAN THESES ON MICROFICHE

I.S.B.N.

THESES CANADIENNES SUR MICROFICHE

National Library of Canada
Collections Development Branch

Canadian Theses on
Microfiche Service

Ottawa, Canada
K1A 0N4

Bibliothèque nationale du Canada
Direction du développement des collections

Service des thèses canadiennes
sur microfiche

NOTICE

The quality of this microfiche is heavily dependent upon the quality of the original thesis submitted for microfilming. Every effort has been made to ensure the highest quality of reproduction possible.

If pages are missing, contact the university which granted the degree.

Some pages may have indistinct print especially if the original pages were typed with a poor typewriter ribbon or if the university sent us a poor photocopy.

Previously copyrighted materials (journal articles, published tests, etc.) are not filmed.

Reproduction in full or in part of this film is governed by the Canadian Copyright Act, R.S.C. 1970, c. C-30. Please read the authorization forms which accompany this thesis.

THIS DISSERTATION
HAS BEEN MICROFILMED
EXACTLY AS RECEIVED

AVIS

La qualité de cette microfiche dépend grandement de la qualité de la thèse soumise au microfilmage. Nous avons tout fait pour assurer une qualité supérieure de reproduction.

S'il manque des pages, veuillez communiquer avec l'université qui a conféré le grade.

La qualité d'impression de certaines pages peut laisser à désirer, surtout si les pages originales ont été dactylographiées à l'aide d'un ruban usé ou si l'université nous a fait parvenir une photocopie de mauvaise qualité.

Les documents qui font déjà l'objet d'un droit d'auteur (articles de revue, examens publiés, etc.) ne sont pas microfilmés.

La reproduction, même partielle, de ce microfilm est soumise à la Loi canadienne sur le droit d'auteur, SRC 1970, c. C-30. Veuillez prendre connaissance des formules d'autorisation qui accompagnent cette thèse.

LA THÈSE A ÉTÉ
MICROFILMÉE TELLE QUE
NOUS L'AVONS REÇUE

NL-339 (r. 82/08)

Canada

0-315-05993-1

National Library of Canada
Canadian Theses Division
Ottawa, Canada
K1A 0N4

Bibliothèque nationale du Canada
Division des thèses canadiennes

53914

PERMISSION TO MICROFILM — AUTORISATION DE MICROFILMER

- Please print or type — Écrire en lettres moulées ou dactylographier

Full Name of Author — Nom complet de l'auteur: Bernard Frederick Francis

Date of Birth — Date de naissance: 23 June 1955

Country of Birth — Lieu de naissance: Canada

Permanent Address — Résidence fixe:
Apt- 1615
1423 Mississauga Valley Blvd.
Mississauga, Ontario
L5A 4A5

Title of Thesis — Titre de la thèse: Raman Spectra of Ice II and Ice IX at 35 K and Atmospheric Pressure

University — Université: University of Alberta

Degree for which thesis was presented — Grade pour lequel cette thèse fut présentée: Ph.D.

Year this degree conferred — Année d'obtention de ce grade: 1981

Name of Supervisor — Nom du directeur de thèse: Dr. John E. Bertie

Permission is hereby granted to the NATIONAL LIBRARY OF CANADA to microfilm this thesis and to lend or sell copies of the film.

The author reserves other publication rights, and neither the thesis nor extensive extracts from it may be printed or otherwise reproduced without the author's written permission.

L'autorisation est, par la présente, accordée à la BIBLIOTHÈQUE NATIONALE DU CANADA de microfilmer cette thèse et de prêter ou de vendre des exemplaires du film.

L'auteur se réserve les autres droits de publication; ni la thèse ni de longs extraits de celle-ci ne doivent être imprimés ou autrement reproduits sans l'autorisation écrite de l'auteur.

Date: 22 July 1981

Signature: Bernard Francis

NL-91 (4/77)

THE UNIVERSITY OF ALBERTA

RAMAN SPECTRA OF ICE II AND ICE IX
AT 35 K AND ATMOSPHERIC PRESSURE

BY

© BERNARD FREDERICK FRANCIS

A THESIS
SUBMITTED TO THE FACULTY OF GRADUATE STUDIES AND RESEARCH
IN PARTIAL FULFILMENT OF THE REQUIREMENTS FOR THE DEGREE
OF
DOCTOR OF PHILOSOPHY

DEPARTMENT OF CHEMISTRY
EDMONTON, ALBERTA
FALL, 1981

THE UNIVERSITY OF ALBERTA

RELEASE FORM

NAME OF AUTHOR Bernard Frederick Francis

TITLE OF THESIS Raman Spectra of Ice II and Ice IX at 35 K and Atmospheric Pressure

DEGREE FOR WHICH THESIS WAS PRESENTED Ph. D.

YEAR THIS DEGREE GRANTED 1981

Permission is hereby granted to THE UNIVERSITY OF ALBERTA LIBRARY to reproduce single copies of this thesis and to lend to or sell such copies for private, scholarly or scientific research purposes only.

The author reserves other publication rights, and neither the thesis nor extensive extracts from it may be printed or otherwise reproduced without the author's written permission.

(Signed) Bernard F. Francis

PERMANENT ADDRESS:

25 Keats Drive, Westmount,
Sydney, Nova Scotia B1R 1H5

DATED 17 July 1981

THE UNIVERSITY OF ALBERTA

FACULTY OF GRADUATE STUDIES AND RESEARCH

The undersigned certify that they have read, and recommend to the Faculty of Graduate Studies and Research for acceptance, a thesis entitled

'RAMAN SPECTRA OF ICE II AND ICE IX
AT 35 K AND ATMOSPHERIC PRESSURE'

submitted by BERNARD FREDERICK FRANCIS in partial fulfilment of the requirements for the degree of Doctor of Philosophy.

John E. Bertie
Supervisor

Dallas Rabenstein

Fraser W. Birss

Jurgen Frank

E Whalley
External Examiner

Date: 17 July 1981

To my parents

ABSTRACT

The laser-excited Raman spectra of the O-H and O-D stretching and the lattice vibrations of the ordered ices II and IX at 35 K are reported. The temperature dependence to 100 K of the frequencies of the well-defined Raman features, and polarized spectra of near-single crystals of H_2O and D_2O ice II are also reported. The laser excitation makes the spectra vastly superior to the mercury arc-excited Raman spectra reported in 1964 by Taylor and Whalley. Many weak peaks and shoulders were observed in addition to the stronger peaks that they reported.

The normal coordinate calculations used by Bertie and Bates in 1977 in their interpretation of the infrared spectra of the O-D stretching vibrations of D_2O ices II and IX provided a credible interpretation of the Raman spectra. This interpretation was further corroborated by the polarized Raman spectra of ice II and by Raman intensity calculations under the bond polarizability approximation. These observed features are therefore believed to be well understood. The peaks due to the O-D stretching vibrations are superimposed on a broad feature that is much more intense in the infrared transmission spectra than in the Raman spectrum. It has been argued that the previous interpretation of the intense breadth in the transmission spectrum is not correct and LO-TO splitting has been offered as a more likely explanation.

The frequencies of the translational vibrations of ices II and IX were calculated under the rigid molecule approxima-

tion with simple force fields based on the O••O stretching and O••O••O angle deformation coordinates of the lattice, and the absorption and scattering intensities of the normal modes were calculated under the bond moment and bond polarizability approximations. The observed and calculated spectra were sufficiently similar that it was possible to assign in detail nearly all of the features of the observed absorption and scattering spectra of the translational vibrations of ices II and IX.

Exploratory work was carried out on the more difficult calculation of both translational and rotational lattice vibrations from the same force field. Several parametrized potential functions were used to describe the restoring forces of the lattice, but none of these could reproduce both the observed isotope ratios and the observed ranges of frequencies of both the translational and rotational vibrations. The potential function that was suggested by Clementi et al in 1976 for the potential energy of interaction of a water dimer was used to express the restoring forces as interatomic interactions between nearest-neighbour water molecules of ice II, but the energy of the lattice could not be minimized with the programs used, and therefore imaginary frequencies were calculated. Further work is needed before a suitable force field for the calculation of the translational and rotational vibrations together is found.

ACKNOWLEDGEMENTS

It is with deepest gratitude that I acknowledge the important contribution of Dr. John E. Bertie to the work and writing of this thesis. The scientific excellence and conscience that guides his work has left a deep impression on me that hopefully will continue to influence me throughout my career. It is indeed an honour and a privilege to have worked with him. I would especially like to express my appreciation of his endless patience and constant encouragement during the course of this work.

I would like to thank the present and former members of Dr. Bertie's research group for their help along the way, the staff of the Electronics, Glass-Blowing, and Machine Shops for their excellent and prompt service, Spectral Services for their help and equipment whenever needed, the members of the secretarial staff who helped in the preparation of this thesis, and various members of the academic staff who were always willing to provide consultation.

Finally, I would like to thank my parents, relatives, and friends, who provided constant support and encouragement. This thesis would not have been possible without them.

TABLE OF CONTENTS

Page

Abstract v

Acknowledgements vii

List of Tables xi

List of Figures xiv

Chapter One. Introduction 1

- 1.1 General 1
- 1.2 The Ice Phases 1
- 1.3 The Crystal Structures of the Ices 7
- 1.4 Vibrations in Molecular Crystals 18
- 1.5 The Vibrational Spectra of the Ices 40
- 1.6 Objectives of this Work 73

Chapter Two. Experimental Techniques 76

- 2.1 Introduction 76
- 2.2 Preparation of Ice II and Ice IX 76
- 2.3 Characterization of the Ices 83
- 2.4 The Raman Cryostat 84
- 2.5 Sample-Handling Procedures 91
- 2.6 Raman Instrumentation 95
- 2.7 Calibration of the Raman Spectrometer 97

Chapter Three. Experimental Results 103

- 3.1 Introduction 103
- 3.2 Characterization of the Samples 103
- 3.3 Determination of the Sample Temperature 106

3.4 The Intensity Response of the Instrument 111

3.5 The Raman Spectra of Ice II and Ice IX 114

Chapter Four. Discussion of the Raman Spectra of the O-H and O-D Stretching Vibrations of Ice II and Ice IX 145

4.1 Introduction 145

4.2 Assignment of the Raman Spectra of the O-H and O-D Stretching Vibrations of Ice II and Ice IX 146

4.3 Calculation of the Raman Spectra of the O-D Stretching Vibrations of Ice II and Ice IX 155

4.4 Refinement of the Force Fields for D_2O Ices II and IX 168

4.5 Discussion of the Effects of Disorder, LO-TO Splitting and Fermi Resonance on the Spectra of Ice II and Ice IX 170

Chapter Five. Discussion of the Raman Spectra of the Lattice Vibrations of Ice II and Ice IX 180

5.1 Introduction 180

5.2 Discussion of the Low-Frequency Raman Spectra of Ices II and IX 181

5.3 Normal Coordinate Calculations of Lattice Vibrations 184

5.4 General Discussion of the Calculations of the Lattice Vibrations of Ices II and IX 199

5.5 Discussion of the Calculations of the Translational Vibrations of Ice II and Ice IX 205

5.5.1 Ice II 205

5.5.2 Ice IX 215

5.5.3 LO-TO Splitting of the Translational Vibrations of Ice II and IX 222

5.6 Calculations of the Translational and Rotational Vibrations of Ice II and IX using Parametrized Potential Functions 225

5.7 Calculation of the Lattice Vibrations of Ice II using Clementi's Interatomic Interaction Potential Function for Water Molecules 237

5.8 Conclusions 241

References 243

Appendix I 255

Appendix II 259

Appendix III 260

Appendix IV 270

Appendix V 271

Appendix VI 279

Appendix VII 283

LIST OF TABLES

Table Page

1.1 Structural data for ices Ih, II and IX 13

1.2 Representations of the degrees of freedom of of a water molecule in the gas phase 31

1.3 Correlation table and vibrational representations of ice II 33

1.4 Correlation table and vibrational representations of ice IX 34

1.5 The vibrations of a water molecule in the gas phase 42

1.6 HDO frequencies and bandwidths in ice Ih 47

1.7 Features of the O-H and O-D stretching bands of ice Ih 53

3.1 Results of the calibration of the germanium resistance thermometer 109

3.2 Features of the Raman scattering by ice II at 35 K 119

3.3 Temperature dependence of the frequencies and half-widths of the well-defined features in the Raman spectra of ice II 120

3.4 Features of the Raman scattering by ice IX at 35 K 136

3.5 Temperature dependence of the frequencies and half-widths of the well-defined features in the Raman spectra of ice IX 138

3.6 Relative intensities of the Raman scattering due to the O-H or O-D stretching vibrations, the translational vibrations and the rotational vibrations of ices II and IX 143

4.1 The calculated frequencies, infrared and Raman relative intensities, and assignments, of the $\underline{k}=0$, O-D stretching vibrations of ice II at 10 K. 148

List of Tables, continued

Table Page

4.2 The calculated frequencies, infrared and Raman relative intensities, and assignments of the k=0, O-D stretching vibrations of ice IX at 10 K. 152

4.3 Assignments of the features due to the O-D stretching vibrations in the infrared and Raman spectra of D_2O ice IX at 10 K. 166

4.4 Assignments of the features due to the O-D stretching vibrations in the infrared and Raman spectra of D_2O ice II at 10 K. 167

4.5 Calculated LO-TO splittings of the infrared-active O-D stretching vibrations of D_2O ices II and IX. 174

5.1 Summary of observed Raman and infrared frequencies of the rotational vibrations of D_2O ice II. 184

5.2 Summary of observed Raman and infrared frequencies of the translational vibrations of D_2O ice II. 185

5.3 Summary of observed Raman and infrared frequencies of the rotational vibrations of D_2O ice IX. 187

5.4 Summary of observed Raman and infrared frequencies of the translational vibrations of D_2O ice IX. 188

5.5 Comparison of calculated frequencies of the lattice vibrations of benzene at 269 K. 197

5.6 Summary of normal coordinate calculations of lattice vibrations of ices II and IX. 200

5.7 Calculated frequencies of ice II, with A^{ox}, A^D and A^M and with translational problem coordinates. 206

5.8 Calculated frequencies and isotope ratios for ice II, with A^{ox} and A^D and with translational and rotational problem coordinates. 208

List of Tables, continued

Table Page

5.9 Calculated frequencies and infrared and Raman intensities of the translational vibrations of D_2O ice II, with A^{ox} and two force fields. 210

5.10 Assignment of the infrared and Raman spectra due to translational vibrations in D_2O ice II at 10 K. 214

5.11 Calculated frequencies and isotope ratios of the translational vibrations of ice IX, under the true structure and point mass models 217

5.12 Calculated frequencies and infrared and Raman intensities of the translational vibrations of D_2O ice IX. 218

5.13 Assignment of the infrared and Raman spectra due to translational vibrations in D_2O ice II at 10 K. 221

5.14 Calculated LO-TO splittings of the infrared-active translational vibrations of D_2O ices II and IX. 223

5.15 Calculated frequencies of the translational and rotational vibrations of the true structure model of ice II, with coordinate set A^{ox}(H··O-H). 226

5.16 Calculated frequencies of the translational and rotational vibrations of the true structure model of ice II, with coordinate set A^{ox}(O··O-H). 229

5.17 Calculated frequencies of the translational and rotational vibrations of the true structure model of ice II, with coordinate set A^{ox}(H-H'). 232

5.18 Calculated frequencies of the translational and rotational vibrations of the linear structure model of ice IX, with coordinate set A^{ox}(O-H··O,H-H'). 235

5.19 Calculated frequencies of the lattice vibrations of the true structure model of ice II with the Clementi pair potential. 240

LIST OF FIGURES

Figure Page

1.1 Phase diagram of ice 3

1.2 The structures of ices Ih and Ic 11

1.3 The unit cell of ice II 16

1.4 The unit cell of ice IX 17

1.5 Dispersion curves of a covalent crystal with the diamond structure 23

1.6 Calculated dispersion curves for ice Ih 27

1.7 Survey infrared and Raman spectra of H_2O ice Ih at 100 K 44

1.8 ν_{OH}(HDO) and ν_{OD}(HDO) of ices Ih, II, IX and V at 100 K 45

1.9 Raman and infrared spectra of the O-H and O-D stretching vibrations of H_2O and D_2O ice Ih at 100 K 52

1.10 Raman spectra of the O-H and O-D stretching vibrations of ices VIII, Ih, II, IX, V and VI at 100 K 59

1.11 Infrared spectra of the O-H and O-D stretching vibrations of ices Ih, II, IV, V and VI 61

1.12 Infrared and Raman spectra of the translational vibrations of H_2O ices Ih, Ic, V, VI, II and IX 67

2.1 The pressure apparatus 78

2.2 The Teflon pieces used to shape the sample during preparation 82

2.3 The Raman cryostat 85

2.4 The sample holder-rotator and the junction ring 87

2.5 The Raman optical cells 89

2.6 Methods for frequency calibration of the Raman spectrometer 99

3.1 Temperature correction curve for the Raman samples 110

List of Figures, continued

Figure		Page
3.2	The intensity response of the Raman spectrometer	112
3.3	Raman spectra of the O-H and O-D stretching vibrations of H_2O and D_2O ice II	116
3.4	Raman spectra of the rotational vibrations of H_2O and D_2O ice II	117
3.5	Raman spectra of the translational vibrations of H_2O and D_2O ice II	118
3.6	Temperature dependence of the frequencies of the well-defined Raman features due to the O-H and O-D stretching vibrations of ice II	121
3.7	Temperature dependence of the frequencies of the well-defined Raman features due to the rotational vibrations of ice II	123
3.8	Temperature dependence of the frequencies of the well-defined Raman features due to the translational vibrations of ice II	124
3.9	Polarized Raman spectra of the O-D stretching vibrations of D_2O ice II	126
3.10	Polarized Raman spectra of the rotational vibrations of D_2O ice II	127
3.11	Polarized Raman spectra of the translational vibrations of D_2O ice II	128
3.12	Polarized Raman spectra of the O-H stretching vibrations of H_2O ice II	130
3.13	Polarized Raman spectra of the rotational vibrations of H_2O ice II	131
3.14	Raman spectra of the O-H and O-D stretching vibrations of H_2O and D_2O ice IX	133
3.15	Raman spectra of the rotational vibrations of H_2O and D_2O ice IX	134
3.16	Raman spectra of the translational vibrations of H_2O and D_2O ice IX	135

List of Figures, continued

Figure Page

3.17 Temperature dependence of the frequencies of the well-defined Raman features due to the O-H and O-D stretching vibrations of ice IX 139

3.18 Temperature dependence of the frequencies of the well-defined Raman features due to the rotational vibrations of ice IX 140

3.19 Temperature dependence of the frequencies of the well-defined Raman features due to the translational vibrations of ice IX 141

4.1 Observed and calculated infrared spectra of the O-D stretching vibrations of ice II 149

4.2 Observed and calculated infrared spectra of the O-D stretching vibrations of ice IX 153

4.3 Calculated relative Raman intensities of D_2O ice II as a function of RP 160

4.4 Calculated relative Raman intensities of D_2O ice IX as a function of RP 161

4.5 Observed and calculated Raman spectra of the O-D stretching vibrations of D_2O ice II 163

4.6 Observed and calculated Raman spectra of the O-D stretching vibrations of D_2O ice IX 164

5.1 Observed and calculated infrared and Raman spectra of the translational vibrations of D_2O ice II 213

5.2 Observed and calculated infrared and Raman spectra of the translational vibrations of D_2O ice IX 220

CHAPTER ONE

INTRODUCTION

1.1 General

A reinvestigation of the Raman spectra of the H_2O and D_2O forms of two ordered ice phases, ice II and ice IX, is reported in this thesis, and a detailed interpretation is proposed. The Raman scattering by the O-H and O-D stretching vibrations is explained by an extension of the interpretation of their infrared absorption, which was reported in previous work from this laboratory.[1,2] Various lattice dynamical calculations were attempted to explain the spectra of the rotational and translational lattice vibrations, and the results are reported here.

An overview of the structural and spectral studies of the ice phases is presented in this chapter, and more detail can be found in reviews.[3-8] The phase diagram and an introduction to the ice phases are presented in Section 1.2. The structures of the ices, with emphasis on those ices of particular interest in this work, are described in Section 1.3. Some aspects of intramolecular and lattice vibrations in crystals are discussed in Section 1.4 before the accepted interpretations of the vibrational spectra of the ices are described in Section 1.5. Finally, the objectives of the present work are given in Section 1.6.

1.2 The Ice Phases

The phase diagram of ice, complete to 1980,[3,8,9] is shown in Figure 1.1. The region labelled Ih is the region of stability of ice Ih, and includes, at low temperatures, the regions of existence of ice Ic and amorphous ice. Ices Ih and Ic are called low-pressure ices and ice Ih is often simply called ice. The phases labelled II to IX can be formed only under high pressure and are called the high-pressure ices.

The only phase found naturally on earth is ice Ih, where the h refers to its hexagonal structure. Amorphous ice and, possibly, ice Ic probably occur in outer space but have not yet been positively identified. Ice Ic, the c denoting its cubic structure, was first made by condensing water vapor onto a cold plate.[10] X-ray and electron diffraction patterns have shown that ice Ih is formed if the cold plate is above ~180 K, that ice Ic is formed if the plate is between ~140 and 180 K, and that amorphous ice is formed at condensation temperatures below ~140 K.[3] Ice Ic slowly transforms at ~170 K to ice Ih, the exact temperature depending on the thermal history of the sample,[11] but the reverse transformation has never been observed. Ice Ic is also formed when the high pressure ices revert to a low pressure form below ~180 K.[11,12] Although it has not yet been proved that ice Ic is not the stable phase between 140 and 180 K, it is generally believed that ice Ic simply nucleates more readily than does ice Ih and then persists metastably below 180 K because the transformation to ice Ih is extremely slow.[3]

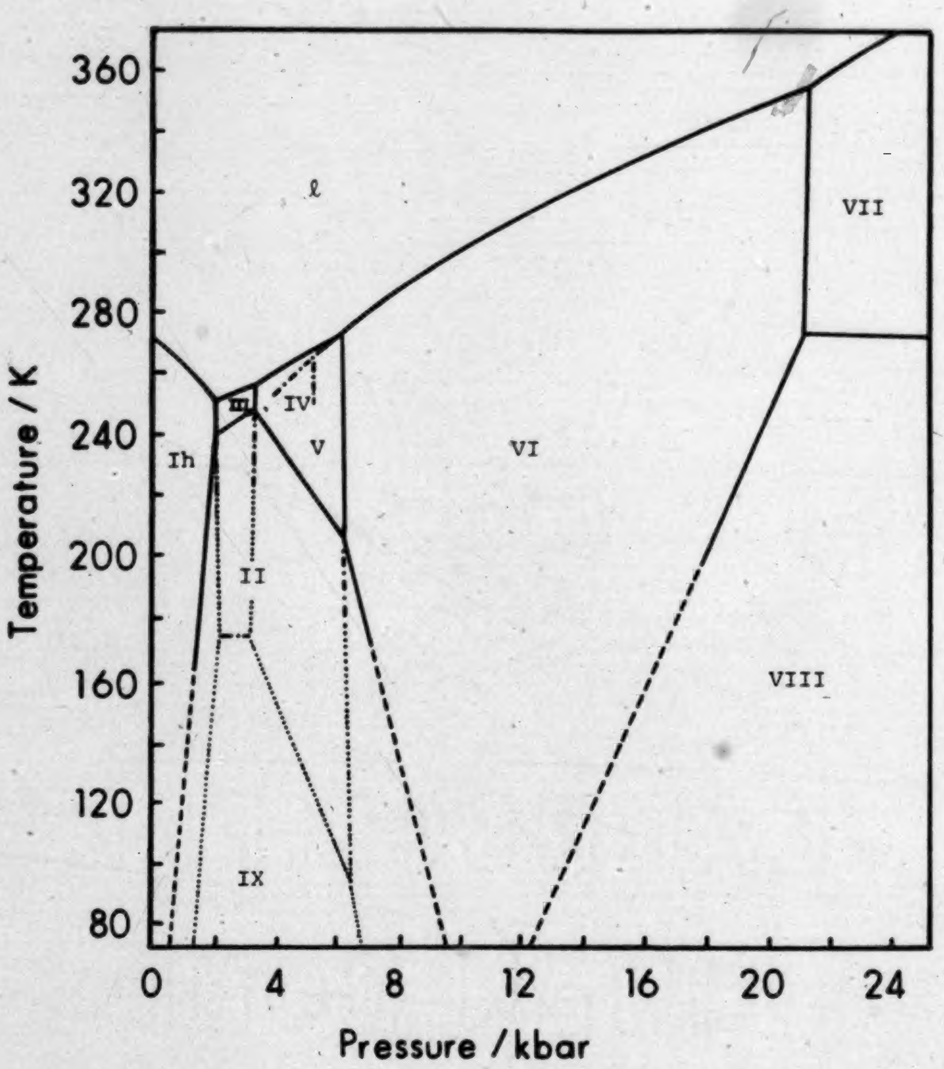

Figure 1.1 Phase diagram of ice.[3,8,9] ——— measured stable lines; -·-·- measured metastable lines; ----- extrapolated lines; ····· extrapolated or estimated metastable lines.

In 1903 Tammann[12] reported his measurements of the isothermal volume change of H_2O with pressures up to 3500 bars, at temperatures above 160 K. He reported the existence of two new ice phases, ice II and ice III, which were denser than liquid water,[13] and a third phase, ice IV, which was less dense than liquid water.[14] Tammann found[15] that ice II and ice III are metastable at ~80 to 150 K and atmospheric pressure. This method of recovering high-pressure phases of ice at atmospheric pressure is called the quenching technique.

In 1912 Bridgman[16] reported his detailed work on the phase diagram of H_2O ice to pressures of 20 kbar. He confirmed the existence of ice II and ice III and observed two new forms, ice V and ice VI, at pressures higher than those reached by Tammann. He was, however, unable to prepare the ice IV that Tammann[14] observed above 0.5 kbar and below 268 K. Bridgman's careful measurements enabled him to correct and extend Tammann's equilibrium lines in the phase diagram and to report the missing II-III equilibrium line. Above 160 K ice II existed only in its region of stability, but each of the other ices could exist metastably in the regions of stability of its neighbours, especially at pressures and temperatures well removed from the triple points.

In 1935 Bridgman[17] reported the phase diagram of 99.9% D_2O to 12 kbar between 213 and 368 K. He observed all of the phases known for H_2O ice and a new phase of ice was found to exist in the region of stability of ice V, being totally metastable with respect to ice V. Since the H_2O phase that Tammann had named ice IV[14] was still unconfirmed, it was replaced in the numbering scheme by this new, metastable phase, the H_2O form of which had never been prepared. Otherwise the phase diagrams for D_2O and H_2O were very similar though not identical. The triple points for the D_2O equilibria occurred 2 to 3.5 K higher in temperature and 0.3 to 0.6% higher in pressure than the corresponding points for H_2O, with the difference decreasing as the pressure was increased.

In 1937 Bridgman[18] extended the phase diagram of H_2O to 44 kbar, discovering ice VII. The melting curve of ice VII was extended to 170 kbar by Pistorius et al[19,20] with no indication of new phases at very high pressures.

The remaining ice phases were discovered by methods other than pressure-volume-temperature measurements. Dielectric studies by Whalley et al[21,22] have shown that ice VII and ice III undergo disorder-to-order transitions on cooling, to yield ice VIII at 0°C[21] and ice IX at ~-100 C[22] respectively.

Evans[23] and Engelhardt and Whalley[24] have used nucleating compounds to promote the formation of H_2O ice IV, but Nishibata[25] was able to prepare H_2O ice IV several times from ice VI without their use. Reports of its structure[26] and infrared spectrum[27] have eliminated any doubt of the existence of ice IV. Thus, ten crystalline ice phases are agreed to exist. The existence of three other phases of ice has recently been suggested by experiment[6,28,29] but the evidence is still inconclusive. There also exists one amorphous phase[30] and a second with greater density has been reported once.[31]

The phase diagram provides information about the order or disorder of the ice phases through the entropy changes at the transitions.[32] The entropy change is calculated from the phase diagram and the volume change at the transition via the Clausius equation,

$$\frac{dT}{dp} = \frac{\Delta V}{\Delta S} \quad . \tag{1.1}$$

The volume change is negative for all transitions which proceed from low to high pressure, and is close to zero for all transitions whose temperature is independent of pressure. Thus the entropy change for a transition that occurs with increasing pressure is negative if dT/dp is positive, and vice versa, is nearly zero if dT/dp is very large, and is very large if dT/dp is very small. Significant entropy changes are usually attributed to changes in zero point entropy, since changes in vibrational entropy are usually small. Ice Ih is disordered[33] and the above arguments indicate that ices III, IV, V, VI and VII are disordered to a similar extent, while ices II, VIII and IX are much more ordered. These indications are supported by X-ray diffraction,[26] neutron diffraction,[6,29,34-39] dielectric relaxation,[21,22,40] and infrared measurements,[2,41-49] and ice II and ice VIII are believed to be fully ordered while ice

IX is very nearly ordered.

Before leaving the phase diagram it is desirable to indicate the criteria that Whalley[8] used to extrapolate several of the stable and metastable lines. The Ih - II line, the Ih - III metastable line, the III - V metastable line, the II - VI line, the V - VI metastable line, and the VI - VIII line are linear extrapolations of the measurements. The Ih - IX metastable line, the IX - V metastable line, and the IX - VI metastable line have not been measured but their slopes at the triple points are fixed by the cyclic conditions on the changes in state functions about the triple points.

It is of particular interest to the work in this thesis that ice IX has no region of stability (Figure 1.1). It exists in the region of stability of ice II and sometimes transforms irreversibly to ice II.[22] The unmeasured equilibrium lines defining the ice IX region of the phase diagram indicate that ice IX can transform reversibly only to the ices Ih, III, V and VI. Ice IX clearly exists only because it does not transform readily to ice II. The only transformation to ice IX that has ever been observed is the III → IX, disorder → order, transition. It follows that the only known method to prepare ice IX is through ice III, for example through the sequence Ih → III → IX.

1.3 The Crystal Structures of the Ices

The fundamental difference between the ice phases is, of course, the crystal structure, that is, the location of both the oxygen atoms and the hydrogen or deuterium atoms in the crystal lattice. The structure of a phase must be known if its vibrational spectra are to be fully interpreted. Therefore the structures of the ice phases are discussed in this section. A more complete and detailed treatment can be found in reviews.[3-8]

The crystalline ices are classified as either ordered or disordered, meaning orientationally ordered or orientationally disordered. In the ordered phases, each water molecule in a unit cell generates corresponding molecules in other unit cells through translational symmetry operations, and the orientations of all corresponding, or translationally equivalent, molecules are identical. Thus the crystallographic unit cell, which is determined by diffraction studies, of ordered crystals is the same as the unit cell that is repeated exactly throughout the crystal. In the disordered ices, molecules are still related to corresponding molecules through translational operations, but several orientations occur with equal (for totally disordered crystals) or preferred (for partially ordered crystals) probability within each set of translationally-equivalent molecules. The crystallographic unit cell of a disordered crystal is the weighted average of the unit cells that actually form the crystal. The crystallographic space group reflects this averaging over the crystal that necessarily occurs in structural determinations.

The third type of 'ice' is amorphous ice or amorphous solid water,[44] for which there are no translationally equivalent molecules and therefore no unit cell. Obviously the structure of amorphous ice is not known in as much detail as those of the crystalline ices, and it will not be discussed further here.

Orientational disorder occurs in those phases for which several orientations of a water molecule have the same, or nearly the same, energy. In each of the ices, each water molecule is hydrogen bonded to four surrounding molecules. The central water molecule is the donor molecule in two of the hydrogen bonds and the acceptor in the other two hydrogen bonds in which it is involved. The four molecules are arranged nearly tetrahedrally about the central molecule in all of the ice phases, although the exact angles vary from one phase to another. There are, then, six possible orientations for each molecule. The diffraction symmetry indicates that all six orientations of a molecule in ice Ic have the same energy, provided that the orientations of the neighbouring molecules adjust cooperatively. Thus ice Ic is disordered at 80 K[45] and is expected to be disordered at all temperatures. In ice II one orientation for each translationally-equivalent set apparently has a much lower energy than all other orientations, because ice II is ordered at all temperatures.[34,40,46] Ices V and VI are disordered at high temperatures[40] but show some ordering at 100 K,[6,29] suggesting that there is only a small energy difference between orientations in ices V and VI which becomes significant with decreasing temperature.

Ice Ih is composed of planes of six-membered puckered rings that have the 'chair' configuration in the planes perpendicular to the crystallographic c-axis and the 'boat' configuration in the planes parallel to the c-axis[47] (Figure 1.2a). The oxygen atoms form the wurtzite structure in ice Ih, and thus there are long, open, hexagonal channels parallel to the c-axis and narrower channels normal to the c-axis. The structure of ice Ic is similar except that all six-membered rings have the 'chair' configuration (Figure 1.2b) and so the oxygen atoms form the diamond structure. Thus ice Ic has narrow channels in several directions and a very open structure. In spite of the different structures, ice Ic has the same density as ice Ih[47-48] and each water molecule in both ices is tetrahedrally surrounded by four hydrogen-bonded nearest neighbours and twelve second-nearest neighbours, the O···O distances, 2.755 ± 0.008 and 4.50 ± 0.01 Å between 120 and 220 K,[33] being the same for both phases. The oxygen atoms are arranged with nearly C_{3v} symmetry in ice Ih and nearly T_d symmetry in ice Ic. Therefore the diffraction site symmetry is C_{3v} for molecules in ice Ih and T_d in ice Ic. The nearest neighbour distances are required under diffraction symmetry to be equal in ice Ic, but there is no symmetry requirement in ice Ih that the O···O distances parallel to the c-axis are the same as those in planes perpendicular to the c-axis. In fact, since the ratio $c/a = 1.6280 \pm 0.0002$ for ice Ih between 13 and 193 K[49] does not equal 1.6330,

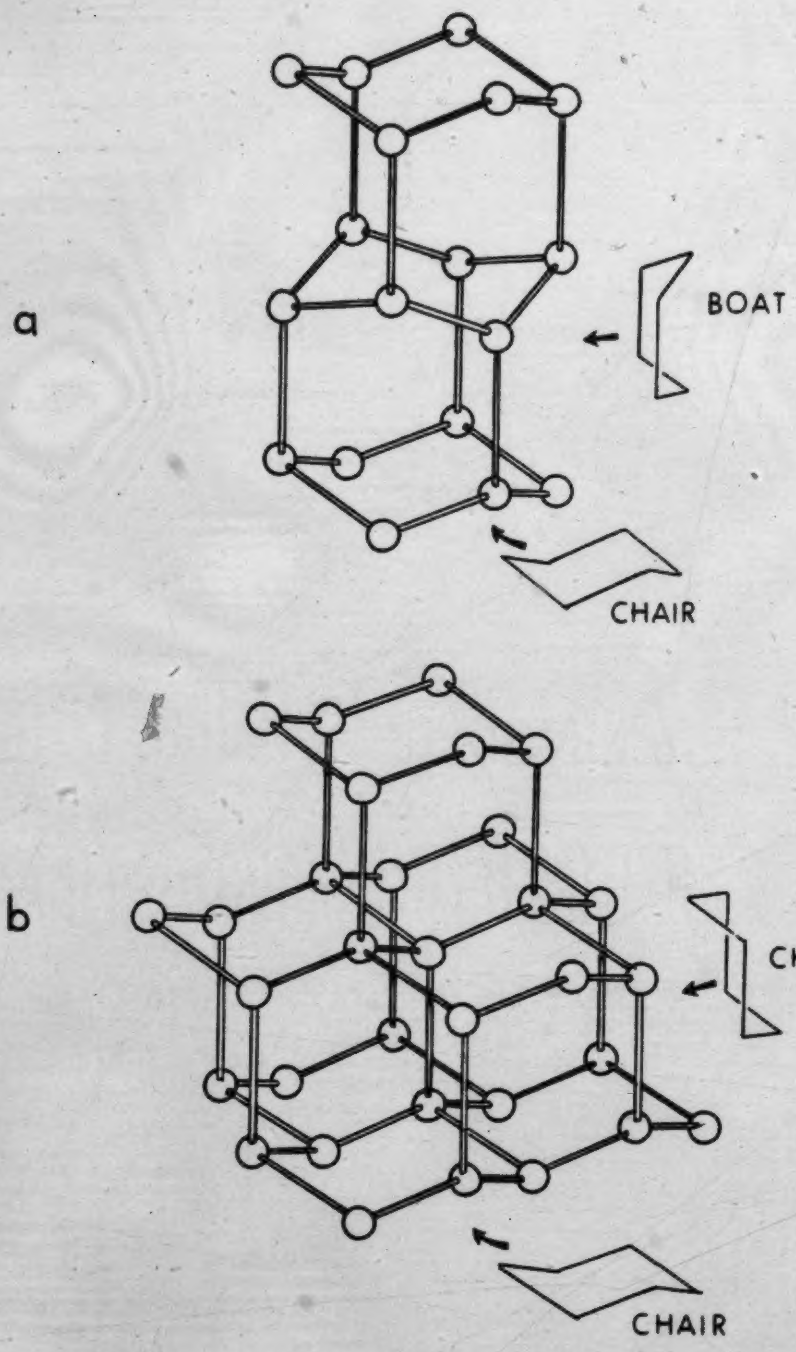
a
BOAT
CHAIR
b
CHAIR
CHAIR

Figure 1.2 a) The structure of ice Ih. b) The structure of ice Ic. Only the oxygen positions are shown.

the ratio required for tetrahedral coordination, then either the O•••O distances parallel to the c-axis are shorter than those inclined to it or the O•••O•••O angles in planes parallel to the c-axis are smaller than those in planes perpendicular to c.[5] However, the deviation is very small for either of these cases, so the nearest-neighbour geometry is essentially the same for ices Ih and Ic.

Ice Ih and ice Ic are orientationally disordered at all temperatures, so the hydrogen atom positions always average in structural determinations to fall exactly on the bonded O•••O line with half of a hydrogen atom situated 1.01 Å from each oxygen atom.[33] The H-O-H angle is thus given as 109.5°, the tetrahedral angle. The second moments of the proton magnetic resonance spectra of ices Ih, Ic, II and IX are consistent with an average H-O-H angle of 104 ± 1° in each ice.[50] The D-O-D angles in ices II and IX have since been measured by neutron diffraction,[34,39] and the average D-O-D angles of 105.4° in ice II and 105.35° in ice IX are in reasonable agreement with the pmr result. The H-O-H angle in ices Ih and Ic is therefore likely close to the gas-phase value of 104.5°.[51] The H-O-H angles can be compared in Table 1.1, where some structural parameters of ices Ih, II and IX are given.

The high-pressure phases are denser than ice I, even though the hydrogen-bonded O•••O distances are greater than in ice I. The density increase results from decreases in the non-bonded intermolecular distances, which are accom-

Table 1.1

Structural data[a] for ices Ih, II and IX

	ice Ih[b]	ice II[c]	ice IX[d]
crystal system	hexagonal	rhombohedral	tetragonal
space group	$P6_3/mmc(D_{6h}^4)$	$R\bar{3}(C_{3i}^2)$	$P4_12_12(D_4^4)$
density ($g{\cdot}cm^{-3}$) (1 bar, 110 K)	0.931	1.18[b]	1.16[b]
cell parameters (1 bar, 110 K)	$a_1=a_2=4.499$ Å $c=7.324$ Å	$a_1=a_2=a_3=7.78$ Å $\alpha=113.1°$	$a=b=6.73$ Å $c=6.83$ Å
no. of molecules per unit cell	4	12	12
site symmetries	C_{3v}	C_1, C_1	C_1, C_2
nearest-neighbour O•••O (O-D) distances	2.755(1.008)	I: 2.803(0.956) 2.768(0.975) II: 2.781(0.937) 2.844(1.014)	1: 2.750(0.977) 2.763(0.972) 2: 2.797[e](0.979)
non-bonded O•••O distances	4.50	3.340, 3.416, 3.513, 3.596,•••	3.451, 3.645, 3.726, 3.939,•••
D-O-D angles	104.5°(?)	I: 103.2° II: 107.6°	1: 106.0° 2: 104.7°
O•••O•••O donor angles	109.5°	I: 87.9° II: 99.6°	1: 99.17°[e] 2: 100.84°
other O•••O•••O angles	109.5°	I: 83.8°, 115.1°, 116.0°, 126.2°, 130.4° II: 81.0°, 108.9°, 118.7°, 121.9°, 127.7°	1: 91.85°, 96.85°, 99.18°, 112.67°, 143.68° 2: 90.94°, 106.08°, 106.08°, 128.07°, 128.07°

---

[a] distances in Å.

[b] Reference 4. O•••O and O-D distances from Reference 33. Non-bonded O•••O distances calculated from data of Reference 33.

[c] Reference 34. I and II refer to molecule type.

[d] Reference 39. 1 and 2 refer to molecule type. Non-bonded O•••O distances calculated from atomic positions in Reference 39.

[e] recalculated from data in Reference 39.

plished in several ways.[5] In the phases that exist at pressures between 2 and 6 kbar (Figure 1.1), the large empty channels in the ice Ih structure (Figure 1.2a) become occupied and the nearest neighbour coordination is distorted from tetrahedral[26,29,34,35,38,39,46,52] to increase the packing efficiency. The molecular packing efficiency is further increased in the very high pressure phases, ices VI, VII and VIII, in which two open sublattices interpenetrate but do not interbond.[4,6,37,53,54] For example, each of the interpenetrating sublattices in ice VII are the same as the ice Ic lattice. The molecular orientations are totally disordered in ice VII, but an ordered version of the same structure is found in ice VIII, where the molecular dipoles in each sublattice are aligned and opposed in direction to the dipoles on the other sublattice.

The interesting structures of the disordered ices IV,[26] V[35,36,55] and VI[6,53] are much more complicated and are not of immediate concern to this thesis and will not be discussed. The structure of ice III[36] is the orientationally disordered form of the ice IX structure,[38,39,52] so most of the remarks about the ice IX structure also apply to ice III, if the symmetry is understood to mean the diffraction symmetry. The structures of the ordered ices II and IX are described in the remainder of this section.

Ice II crystallizes in the space group $R\bar{3}$ (C_{3i}^{2}) with two occupied sets of general (C_1) positions, i.e. two occupied sites of symmetry C_1 and multiplicity six, for a total of twelve molecules in the primitive unit cell.[34,46] The structure as viewed along the S_6 ($\bar{3}$) axis is illustrated in Figure 1.3. The hydrogen atoms are fully ordered in the positions shown. There are, thus, four different O-H•••O hydrogen bonds in the structure, with six of each type per unit cell. The water molecules on each six-fold site form a six-membered puckered ring that sits on the origin of the rhombohedral cell for the type I molecules or on the center of the cell for the type II molecules. Both types of rings lie in planes perpendicular to the S_6 axis, which is along the rhombohedral cell diagonal. The six-membered rings suggest the structure of ice Ih, but they are flattened more in ice II[46] and the bonding between rings is quite different, so the relation between the ice Ih and ice II structures is not obvious.

Ice IX crystallizes in the tetragonal space group $P4_12_12$ (D_4^4) with eight molecules (type 1) on one set of general positions, i.e. one eight-fold site of symmetry C_1, and four molecules (type 2) on one four-fold site of symmetry C_2, for a total of twelve molecules in the primitive unit cell.[38,39,52] Figure 1.4 shows the structure as viewed along the unique axis, the crystallographic c-axis. The six-membered rings of ice Ih and ice II have been replaced by five-, seven- and eight-membered rings in ice IX, but these rings are not a very distinctive part of the ice IX structure. The structure is characterized by spiral chains of water molecules (type 1) around the 4_1 screw axes that

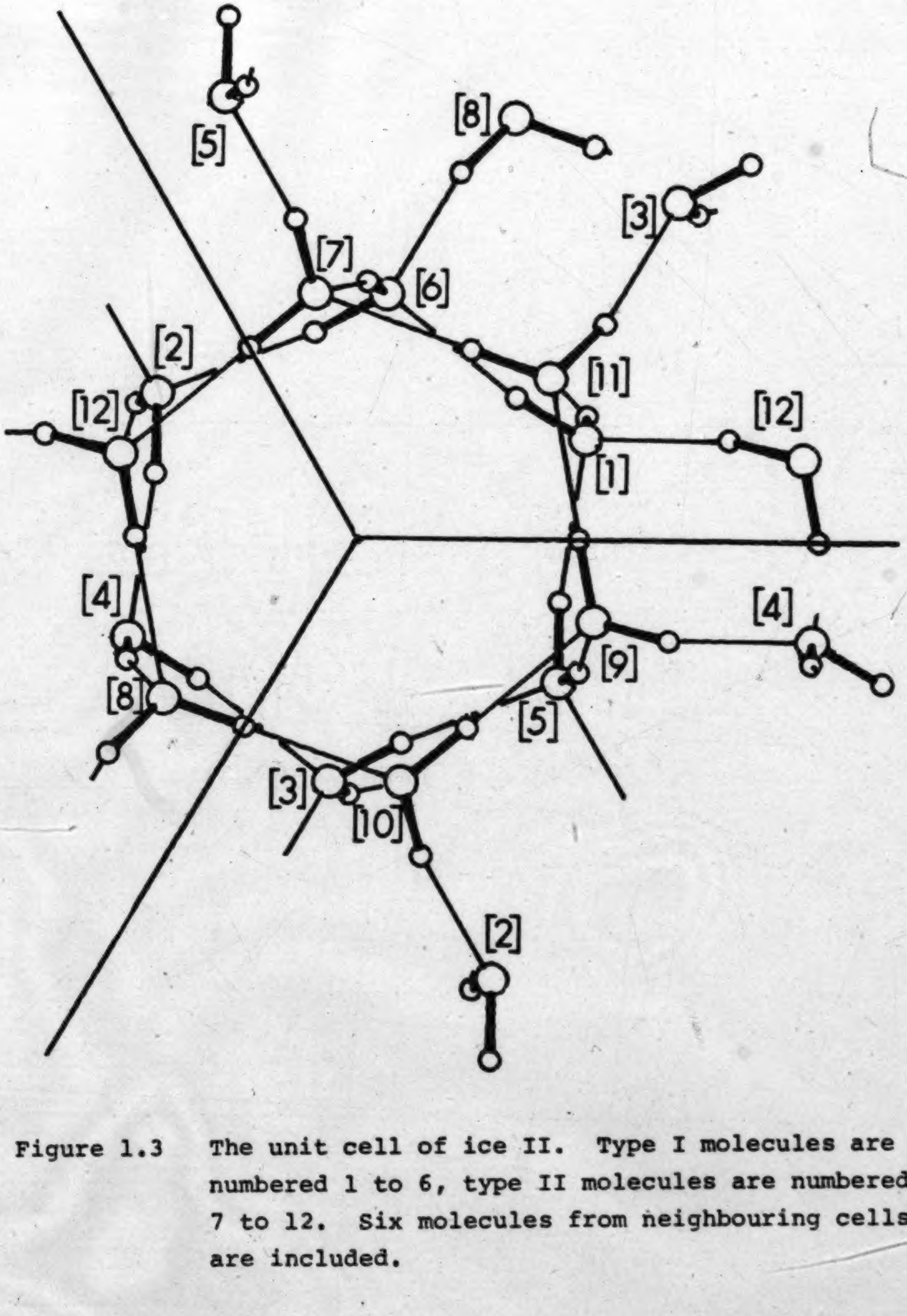
[5]
[8]
[3]
[7]
[6]
[2]
[11]
[12]
[12]
[1]
[4]
[4]
[9]
[8]
[5]
[3]
[10]
[2]

Figure 1.3 The unit cell of ice II. Type I molecules are numbered 1 to 6, type II molecules are numbered 7 to 12. Six molecules from neighbouring cells are included.

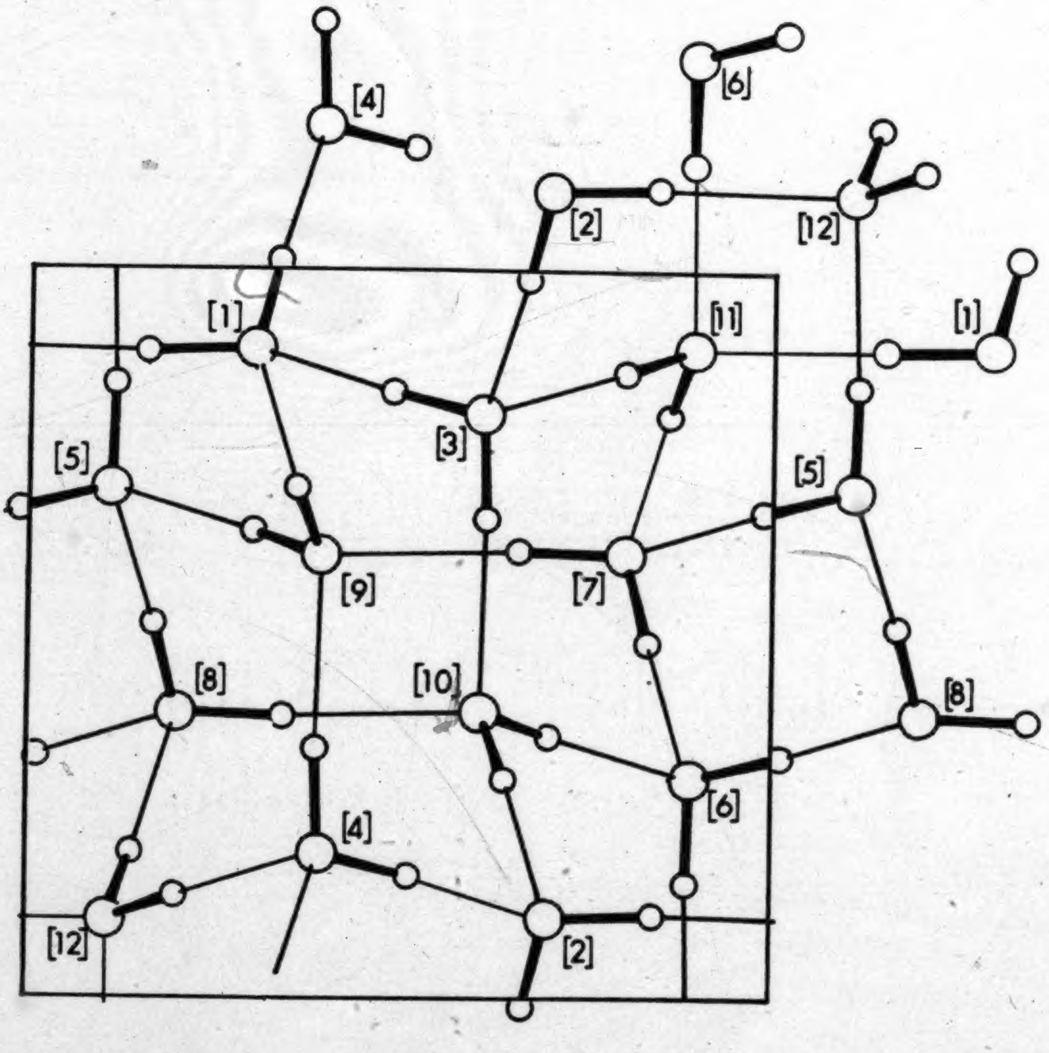
[4]
[6]
[2]
[12]
[1]
[11]
[1]
[3]
[5]
[5]
[9]
[7]
[8]
[10]
[8]
[6]
[4]
[12]
[2]

Figure 1.4 The unit cell of ice IX. Type 1 molecules are numbered 1 to 8, type 2 molecules are numbered 9 to 12. Seven molecules from neighbouring cells are included.

bisect the a and b cell edges. The spirals are linked together by the type 2 molecules. In their refinement of the structure of ice IX, LaPlaca, Hamilton, Kamb and Prakash[38] found evidence for about 4% disorder in some positions of the deuterium atoms. This disorder is real, but it is small enough to be undetectable by most experimental methods. Therefore ice IX is normally considered an ordered ice with the hydrogen atoms arranged as shown. There are three different O-H•••O bonds in the structure, and eight of each type in the unit cell.

As shown in Table 1.1, the nearest-neighbour O•••O distances are larger in both ice II and ice IX than in ice Ih but some non-hydrogen-bonded distances are substantially shorter than the shortest in ice Ih, which explains the increase in density. Although the O•••O•••O donor angles are distorted by 10° to 20° from the tetrahedral angle, the coordination about each molecule is still quasi-tetrahedral. The D-O-D angles do not equal the O•••O•••O donor angles, so the hydrogen bonds are bent.

1.4 Vibrations in Molecular Crystals

The vibrations of molecular crystals are classified as either intramolecular or intermolecular vibrations. The intramolecular vibrations are vibrations of the gas phase molecules that have been perturbed by intermolecular forces. The static and dynamic intermolecular potentials shift the frequencies and couple molecular motions so that the frequency of the crystal vibration may be considerably higher or lower than the frequency of the analogous vibration in the gas phase molecule. Single peaks in the spectrum of the gas often appear as multiplets in the spectrum of the crystal because of site splitting, Davydov splitting and longitudinal optic-transverse optic splitting. The intermolecular vibrations, which are also called lattice vibrations, are derived from the zero-frequency rotations and translations of the gas phase molecules, which are transformed by the intermolecular potential into vibrations with non-zero frequency. These effects are considered in this section, and the consequences of orientational disorder are discussed.

There are three symmetry groups that are important in discussions of the vibrations of a molecular crystal: the point group of the free molecule, the site group, and the unit-cell group. The point group of the free molecule[56-59] is the well-known group formed by the symmetry elements that leave the gas phase molecule invariant. The site group[57,59] is the group formed by those symmetry elements that leave the site in the crystal invariant. The unit-cell group, or the factor group,[57,59] is isomorphous with the crystal class, i.e. the point group of symmetry operations that describes the symmetry of a unit cell.[59] The crystal class can be found by dropping the superscript on the Schoenflies symbol that accompanies the Hermann-Maugin symbol in the standard space group notation for a crystal, e.g. in $P4_12_12$ (D_4^4) the crystal class is D_4.

The symmetry of a molecule in a crystal is the site symmetry and is described by the site group. The site group is determined by the intra- and intermolecular forces and is either the point group of the free molecule or one of its subgroups. In the latter case, the degeneracy of a vibration of the gas phase molecule may be reduced in the crystal, causing site splitting. The intermolecular forces also cause the frequency of a molecular vibration in the crystal to differ from that in the gas phase, and this is called the site shift. An example of a site shift occurs in the ices, in which the O-H stretching frequencies are much lower than in gaseous water because of the O-H···O bonds.[60-62] The site shift can also cause a form of site splitting, which may be called multiple site splitting, because a non-degenerate vibration of a gaseous molecule can have two or more different frequencies in the crystal if two or more sites are occupied. Site splitting, multiple site splitting and site shifts are all caused by the static intermolecular potential, i.e. by the presence and not the motion of other molecules, and are called static field effects.[57]

In a primitive unit cell[57,59] containing m molecules on one site, each site group intramolecular vibration is m-fold degenerate under the static intermolecular potential. However, an intramolecular vibration is also affected by the dynamic intermolecular potential, i.e. by the motion of other molecules and in particular by the relative phase of the same vibration in other molecules. Therefore the m-fold degeneracy is removed when the m vibrations couple to form m unit-cell-group vibrations, usually called the unit-cell-group, or factor-group, components. The splitting of a site-group vibration into unit-cell-group components is known as Davydov splitting or correlation splitting, and the effect of site splitting and Davydov splitting together is known as unit-cell-group or factor-group splitting.[57,59]

The frequency difference between the unit-cell-group components is determined by the magnitude of the dynamic intermolecular forces, i.e. by the magnitude of the intermolecular coupling. When the coupling is sufficiently large, the unit-cell-group components can be resolved. When the intermolecular coupling is small, the unit-cell-group components may not be resolved and the vibrations of each molecule are essentially unaffected by those of its neighbours. In the latter case it is common and useful to assign the spectrum to site-group vibrations.

The intermolecular vibrations of a crystal arise from the rotational and translational degrees of freedom of the molecules. Thus, for a crystal with m non-linear molecules in the primitive unit cell there are 3m rotational and 3m translational lattice vibrations, and the frequency is necessarily zero only for the three translational lattice vibrations that correspond to translations of the entire unit cell. The non-zero frequencies of intermolecular vibrations are solely due to intermolecular forces, so they are highly coupled vibrations and are only usefully described as unit-cell-group vibrations.

So far the discussion has focussed on the vibrations of a single molecule in the solid (static field effects) and on the effect of coupling of the vibrations of the molecules in one unit cell (unit-cell-group splitting). The final consideration is the coupling of vibrations in different unit cells. The actual crystal vibrations extend throughout the crystal and are spatially periodic with wavelength λ because of the periodicity of the potential energy. A crystal vibrational state is characterized by its vibrational frequency, $\nu(\underline{k})$ or ν, and by its spatial periodicity, which is specified by its wavevector $\underline{k}$, where $|\underline{k}| = 1/\lambda$ and the direction of $\underline{k}$ is the direction of propagation of the vibration-wave. The plots of $\nu(\underline{k})$ versus $\underline{k}$ are called the dispersion curves. The dispersion curves in two directions for a covalent crystal with the diamond structure and two atoms in the unit cell are shown in Figure 1.5. These are also the dispersion curves for the translational lattice vibrations of any molecular crystal with the diamond structure, e.g. ice Ic with the water molecules treated as point masses. The origin of the wavevector axis is called the Brillouin zone center, and it represents those vibrations that have the same phase in all unit cells of the crystal. The positions of maximum unique wavevector, $\underline{k} = (2a)^{-1}$, where a is the cell length in the direction of propagation, define the Brillouin zone boundary and represent those vibrations that are 180° out of phase in neighbouring cells

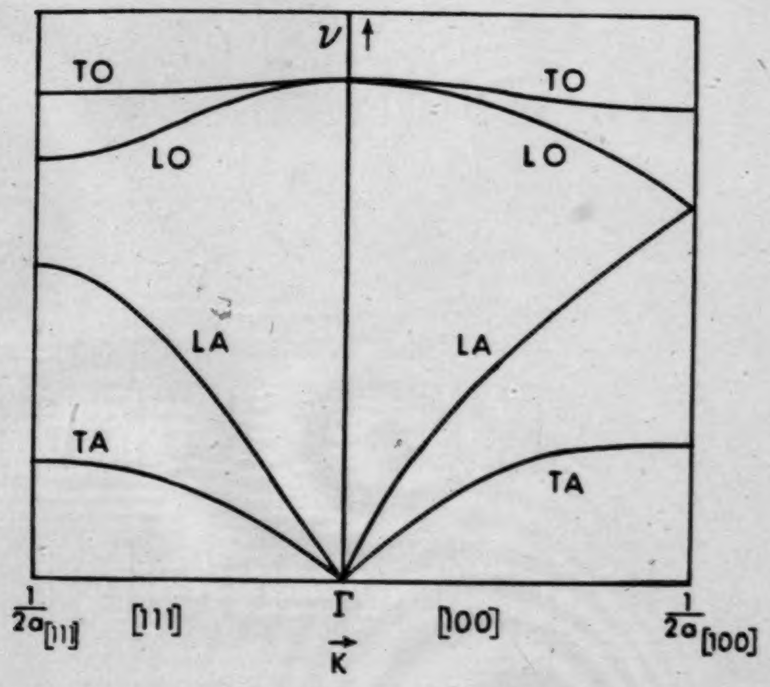

Figure 1.5 The dispersion curves in the [100] and [111] directions for a covalent crystal with the diamond structure. Redrawn from Reference 63.

along the direction of propagation.

Each vibration of a single unit cell gives rise to a separate branch in the dispersion curve diagram. Each branch contains N discrete points, where N is the number of unit cells along the direction of propagation, but, since N is very large, each branch is essentially continuous. There are 3m branches of translational vibrations for a covalent crystal with m atoms in the unit cell, as shown in Figure 1.5 for diamond with two atoms in the primitive unit cell. The three branches for which the frequency is zero at $\underline{k} = 0$ are called acoustic branches while the others are optic branches. The longitudinal acoustic (LA) and longitudinal optic (LO) branches in Figure 1.5 correspond to vibrations with atom displacements along the propagation direction. The vibrations in the transverse acoustic (TA) and transverse optic (TO) branches in Figure 1.5 are doubly degenerate and correspond to vibrations with atom displacements perpendicular to the propagation direction.

The dispersion curves for a molecular crystal are similar to those for a covalent crystal (Figure 1.5) but include optic branches due to the rotational vibrations and the intramolecular vibrations. If there are m N-atomic molecules per primitive unit cell there are m(3N - 6) branches [m(3N - 5) for linear molecules] of dispersion curves due to intramolecular vibrations and 3m branches [2m for linear molecules] due to rotational vibrations, in addition to the 3m - 3 optic and 3 acoustic branches due to translational vibrations. The crystal vibrations at the Brillouin zone center are the same as the vibrations of one primitive unit cell, which were discussed earlier. Thus, at the zone center the frequencies of the intramolecular vibrations are perturbed from those of the isolated molecules by site shifts, and are split into unit-cell-group components by site splitting, multiple site splitting and Davydov splitting within each range, with the frequency separations between the resultant unit-cell-group components depending on the intermolecular coupling. Away from the zone center, the intermolecular forces determine the amount of dispersion, i.e. the wavevector dependence of the frequency, of each branch. As examples, the dispersion curves of ices Ic, Ih, II and IX are discussed in the following paragraphs.

For ice Ic the water molecules have been represented[63] by point masses so that the dispersion curves of the translational vibrations are approximated by Figure 1.5. The dispersion curves of the translational vibrations of an ordered model of ice Ic in which the hydrogen atoms were not neglected have also been calculated and were found to be similar to those in Figure 1.5, but the vibrations in the transverse branches were no longer degenerate.[64] In both the point-mass and the ordered-molecule models the dispersion curves of the translational vibrations of ice Ic span the 0 to ~325 cm^{-1} frequency range. No information exists about the higher frequency branches of ice Ic but, for an ordered model of ice Ic, they must consist of six optic branches of rotational vibrations, probably in the 400 to 1000 cm^{-1} range, two optic branches around 1600 cm^{-1} due to the bending vibration ν_2 of the water molecules, and four optic branches around 3200 cm^{-1} of the symmetric and antisymmetric O-H stretching vibrations ν_1 and ν_3.

Ice Ih has four molecules in the primitive unit cell. Therefore its dispersion curves are more complicated than those for ice Ic, with twice the number of branches in the same spectral ranges. The inelastic neutron scattering by the vibrations of the dispersion curves of ice Ih has been measured[65,66] and the dispersion curves of the translational vibrations have been calculated[65-71] using various force fields with reasonable agreement between workers, particularly below 240 cm^{-1}. The curves calculated by Wong, Klug and Whalley[67] are shown in Figure 1.6. Bosi et al[68] have calculated the dispersion curves of the rotational vibrations of an ordered model of ice Ih and reported low dispersion in this region. Nothing is known about the dispersion curves of the intramolecular vibrations of ice Ih.

The dispersion curves for ice II or ice IX, each with twelve molecules in the primitive unit cell, have 108 branches, with 3 acoustic and 33 optic branches below 325 cm^{-1} of translational vibrations, 36 optic branches between 400 and 1000 cm^{-1} of rotational vibrations, 12 optic branches around 1600 cm^{-1} of bending vibrations, and 24 optic branches around 3200 cm^{-1} of O-H stretching vibrations. It follows that the dispersion curve diagrams for ice II and

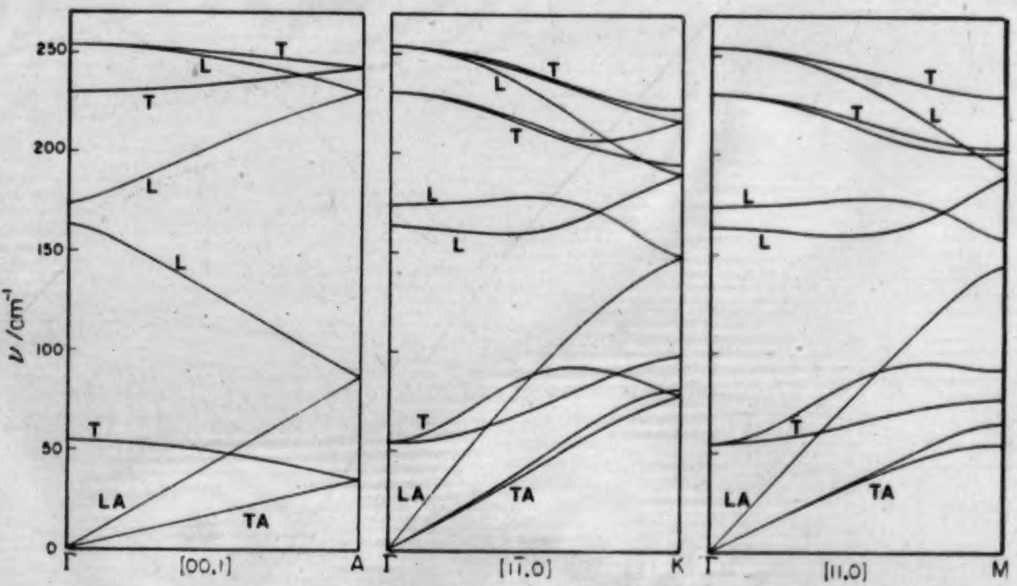

Figure 1.6 Calculated dispersion curves in high symmetry directions for ice Ih. Modified from Reference 67. Transverse optic and longitudinal optic branches are labelled T and L; transverse acoustic and longitudinal acoustic branches are labelled TA and LA.

ice IX are complex, but the curves have neither been measured nor calculated. However it is not necessary to know the dispersion curves of an ordered crystal to interpret its optical spectra, and this is now shown.

The vibrations that are observed in the optical spectra of a crystal are those that obey the selection rules for infrared or Raman activity. The first selection rule requires that there be energy conservation, so that the energy gain by the crystal equals the energy loss of the photon. The second selection rule requires that there be conservation of momentum, so that the gain in crystal momentum $h\underline{k}_p$[72] equals the loss of photon momentum. In ordered crystals this can occur in absorption only if the wavevector of the excited crystal vibration equals the wavevector of the incident photon; in Raman scattering the wavevector of the incident photon must equal the vector sum of the wavevectors of the scattered photon and the excited crystal vibration. Thus, in either absorption or scattering only one vibration per branch can satisfy the momentum selection rule, so the number of translational, rotational and intramolecular vibrations of an ordered crystal that are potentially observable equals the number of branches of dispersion curves. Furthermore, the wavevectors of infrared and visible light dictate that the wavevectors of vibrations excited by absorption must be less than $\sim 10^4$ cm^{-1}, while the wavevectors of vibrations excited in Raman scattering must be less than $\sim 10^5$ cm^{-1}. In both cases the wavevector of the active vibrations is small compared to the wavevectors of $\sim 10^8$ cm^{-1} for vibrations at the zone boundary. The approximation usually used is that the optically-active vibrations of an ordered crystal must have zero wavevector.

In orientationally-disordered crystals, on the other hand, there is no momentum selection rule, so all of the vibrations are optically active. The infrared or Raman spectrum is then $I(\nu) \cdot g(\nu)$, where $I(\nu)$ is the infrared or Raman intensity function for a vibration with frequency ν and $g(\nu)$ is the density of states function, which describes the number of vibrational states with frequency ν. The density of states is, therefore, extremely important in interpreting the spectra of disordered crystals. These points are discussed later in this section.

For ordered crystals the wavevector selection rule is a necessary but not sufficient condition for optical activity. The zero-wavevector approximation means that the forms of the vibrations are subject to the symmetry of the unit-cell group, just as the vibrations of molecules in the gas phase are subject to the symmetry of the molecular point group. The infrared-active vibrations must have a non-zero dipole moment change $(\partial\underline{\mu}/\partial Q)$, or in quantum mechanical language a non-zero transition moment, so they must have the same symmetry under the unit-cell group as a component of the dipole moment $\underline{\mu}$. The Raman-active vibrations must have a non-zero polarizability derivative $(\partial\underset{\sim}{\alpha}/\partial Q)$, so they must have the same symmetry under the unit-cell group as a component of the polarizability $\underset{\sim}{\alpha}$. The infrared- and Raman-active vibrations of a crystal are readily determined through the correlation method[59,73] by which the representations formed by the vibrations, rotations and translations under the point group of an isolated molecule are correlated to the representations of the intramolecular and intermolecular vibrations under the unit-cell group of the crystal, through the site group. In the following paragraphs this method is applied to ice II and ice IX.

In the first step of the correlation method, the representation of the degrees of freedom of the isolated molecule are determined. These are given in Table 1.2 for a water molecule. The three vibrational, three rotational and three translational degrees of freedom form the representations $2A_1 + B_1$, $A_2 + B_1 + B_2$ and $A_1 + B_1 + B_2$ respectively under the point group C_{2v}. The two O-H stretching displacements form a totally symmetric (A_1) vibration and an antisymmetric (B_1) vibration under the point group, and these are labelled ν_1 and ν_3 respectively.[74] The bending vibration, which is also totally symmetric, is labelled ν_2.[74]

The representations under the point group are then correlated to the representations under the site group and the unit-cell group. The unit-cell group of ice II is isomorphous with the point group $C_{3i} \equiv S_6$. The twelve molecules in the unit cell occupy two sets of general positions, so the site group is C_1 for each type, I and II, of water molecule. The correlation table[56,57,59] for ice II is

Table 1.2

Representations of the degrees of freedom of a water molecule in the gas phase

normal modes of vibration [a]	intermolecular degrees of freedom [a]	representation under C_{2v}
ν_1, ν_2	T_z	A_1
	R_z	A_2
ν_3	T_x, R_y	B_1
	T_y, R_x	B_2

---

[a] The normal modes of vibration of the water molecule are:

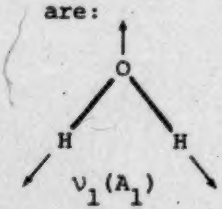

$\nu_1(A_1)$

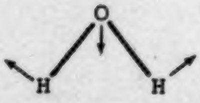

$\nu_2(A_1)$

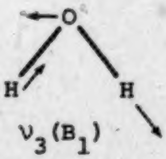

$\nu_3(B_1)$

axis convention:

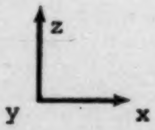

shown in Table 1.3. Each degree of freedom of the isolated molecule yields the regular representation $\Gamma = A_g + E_g + A_u + E_u$ under the unit-cell group. The combined contributions from type I and type II molecules to the vibrational representations are given in Table 1.3, where Γ_{OH} is the total representation formed by the O-H stretching vibrations, Γ_{ν_2} is the representation formed by the intramolecular bending vibrations, and Γ_R and Γ_T are the representations formed by the rotational and translational optic vibrations. $\Gamma_{acoustic}$ is the representation formed by the acoustic translational vibrations, which have zero frequency at zero wavevector and thus are not observed. The infrared-active vibrations have A_u or E_u symmetry under the unit-cell group, while the Raman-active vibrations have A_g or E_g symmetry. The number of vibrations that are infrared or Raman active are given in Table 1.3 for each type of vibration. No vibrations are active in both the infrared and Raman because the unit-cell group is centrosymmetric.

The unit-cell group of ice IX is isomorphous to the point group D_4. Eight molecules (type 1) occupy one set of general positions and four molecules (type 2) occupy one C_2 site, so the site group is C_1 for type 1 molecules and C_2 for type 2 molecules. From the correlation table [56,57,59] for ice IX in Table 1.4, each degree of freedom of type 1 molecules yields the regular representation $\Gamma = A_1 + A_2 + B_1 + B_2 + 2E$, while the degrees of freedom of type 2 molecules with symmetry A_1 or A_2 under C_{2v} (i.e. ν_1, ν_2, T_z and R_z) yield

Table 1.3

Correlation table and vibrational representations of ice II

Correlation table for each type of water molecule in ice II

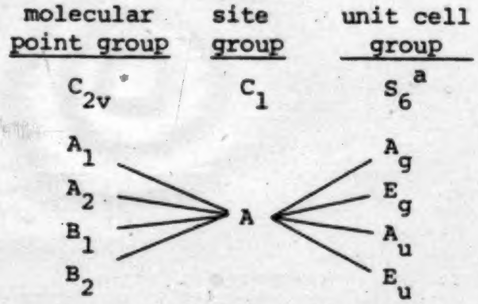
molecular point group
site group
unit cell group
C_{2v}
C_1
$S_6{}^a$
A_1
A_2
B_1
B_2
A
A_g
E_g
A_u
E_u

Vibrational representations of ice II

	no. of active vibrations		
	infrared active[a]	Raman active[a]	ir and Raman active
$\Gamma_{OH} = 4A_g + 4E_g + 4A_u + 4E_u$	8	8	0
$\Gamma_{\nu_2} = 2A_g + 2E_g + 2A_u + 2E_u$	4	4	0
$\Gamma_R = 6A_g + 6E_g + 6A_u + 6E_u$	12	12	0
$\Gamma_T = 6A_g + 6E_g + 5A_u + 5E_u$	10	12	0
$\Gamma_{acoustic} = A_u + E_u$	-	-	-

---

[a] A_g and E_g vibrations are Raman active. A_u and E_u vibrations are infrared active.

Table 1.4

Correlation table and vibrational representations of ice IX

Correlation tables for ice IX

Molecules of type 1

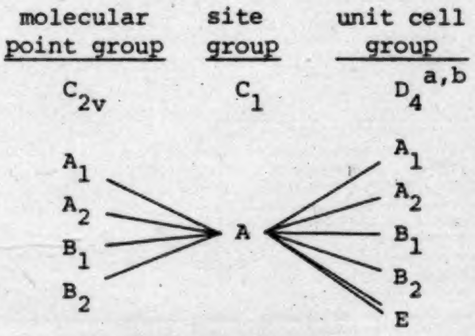
molecular point group
site group
unit cell group
C_{2v}
C_1
D_4 [a,b]
A_1
A_2
B_1
B_2
A
A_1
A_2
B_1
B_2
E

Molecules of type 2

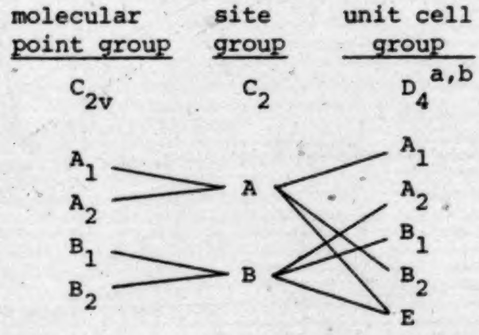
molecular point group
site group
unit cell group
C_{2v}
C_2
D_4 [a,b]
A_1
A_2
B_1
B_2
A
B
A_1
A_2
B_1
B_2
E

Vibrational representations of ice IX

	no. of active vibrations		
	infrared active[a]	Raman active[a]	ir and Raman active
$\Gamma_{OH} = 3A_1 + 3A_2 + 3B_1 + 3B_2 + 6E$	9	15	6
$\Gamma_{\nu_2} = 2A_1 + A_2 + B_1 + 2B_2 + 3E$	4	8	3
$\Gamma_R = 4A_1 + 5A_2 + 5B_1 + 4B_2 + 9E$	14	22	9
$\Gamma_T = 4A_1 + 4A_2 + 5B_1 + 4B_2 + 8E$	12	21	8
$\Gamma_{acoustic} = A_2 + E$	-	-	-

---

[a] A_2 and E vibrations are infrared active. All except A_2 vibrations are Raman active.

[b] C_2'' of D_4 is at 45° to the a axis of Reference 39.

$\Gamma = A_1 + B_2 + E$ under the unit-cell group and those with symmetry B_1 or B_2 under C_{2v} (i.e. ν_3, T_x, T_y, R_x and R_y) yield $\Gamma = A_2 + B_1 + E$ under the unit-cell group. The total vibrational representations for ice IX and the number of vibrations that are active in the infrared and Raman are given in Table 1.4.

As noted above, the $\underline{k}$=0 selection rule, on which the above unit-cell-group symmetry analysis is based, is an approximation to the correct $\underline{k}=\underline{K}$ selection rule, where $\underline{K}$ is the wavevector of the incident light. A clear indication that this approximation is imperfect is the observation of longitudinal optic-transverse optic splitting in the Raman scattering by vibrations that are infrared active. If $\underline{k}$=0 the vibration wave does not propagate through the crystal. If $\underline{k}=\underline{K}$ the vibration wave does propagate in the direction of $\underline{K}$, even though $\underline{K}$ is very small, and the dipole moment change that accompanies an infrared-active vibration can be either parallel to $\underline{k}$, yielding a longitudinal optic mode, or perpendicular to $\underline{k}$, yielding a transverse optic mode. Because of the interaction between the oscillating dipole moments, which extends over a long range, the frequency of the longitudinal optic mode is greater than that of the transverse optic mode. Specifically, for cubic crystals, $\nu_{LO}^2 - \nu_{TO}^2 \propto (\partial\underline{\mu}/\partial Q)^2$, i.e. to the infrared intensity. The longitudinal optic mode is not infrared active because $\underline{k}$ is parallel to $\underline{K}$ in all absorption processes and therefore the dipole moment change accompanying the vibration is parallel to $\underline{K}$ for a longitudinal optic mode and it cannot interact with the electric vector of the radiation that is perpendicular to $\underline{K}$. The dipole moment change accompanying vibrations excited in Raman scattering, however, may be perpendicular or parallel to $\underline{k}$. Thus both the longitudinal and transverse optic modes are Raman active under certain polarizations and, of course, appear as separate peaks in the spectrum instead of the single peak predicted by the unit-cell-group analysis. It should be noted that this definition of longitudinal optic and transverse optic modes is quite different from that used to describe branches of the dispersion curve diagram due to translational vibrations (Figure 1.5), which is based on the direction of displacement of the oscillating masses being parallel or perpendicular to $\underline{k}$.

The approach taken in the treatment of the vibrations of an orientationally disordered crystal depends on whether the potential energy governing the form of the vibrations is periodic (regular) or irregular. The approximately regular positioning of the molecular centers of mass in an orientationally disordered crystal indicates that the part of the intermolecular potential energy that determines the molecular positions in the crystal is approximately periodic. Since this part of the potential energy also determines the translational lattice vibrations, then as long as the translational vibrations do not couple significantly with other vibrations of the crystal they must be approximately mechanically regular, and can be represented as plane waves and described by a wavevector. It is therefore expected that the translational vibrations of an orientationally disordered crystal, and hence the dispersion curves of the translational vibrations, are approximately the same as those of the ordered crystal that has the diffraction structure of the orientationally disordered one. The other vibrations of an orientationally disordered crystal, i.e. the rotational and intramolecular vibrations, are determined by an irregular, or non-periodic, potential energy and thus are mechanically irregular vibrations that can neither be characterized by a wavevector nor described by a dispersion curve. A much different approach must therefore be taken for these vibrations.

The following theory of mechanically regular vibrations in orientationally disordered crystals, which was first described by Whalley and Bertie,[75] has been used to treat the translational vibrations of an orientationally disordered crystal, e.g. in Ref. 63. According to the theory, the infrared or Raman spectrum of the translational vibrations of an orientationally disordered crystal is the combination of an order-allowed spectrum and a disorder-allowed spectrum. The order-allowed spectrum results from the regular part of the dipole moment or polarizability derivative, and is confined to the zero-wavevector vibrations of the diffraction structure that are allowed by the diffraction symmetry of the crystal. The disorder-allowed spectrum arises from the irregular part of the appropriate derivative, which activates all $\sim 10^{23}$ vibrations per mole of crystal. The absorption or scattering intensity at frequency ν by these disorder-allowed vibrations is given by I(ν)·g(ν), where g(ν) is the density of states function and I(ν) is the infrared-absorption or Raman-scattering intensity function.

The intensity function I(ν) describes the relative intensity of a disorder-allowed vibration as a function of its frequency and I(ν) describes the intensity of a disorder-allowed vibration relative to that of an order-allowed vibration. The absorption intensity of one disorder-allowed vibration is a first-order effect of the disorder,[76] and is approximately 1/N of the intensity of order-allowed vibrations, where N is the number of unit cells in the crystal. Although each disorder-allowed vibration is weak, so many are active that the absorption intensities of the order-allowed and disorder-allowed portions of the spectrum are expected to be comparable.[75] The scattering intensity of the disorder-allowed spectrum, however, is a second-order effect of the disorder and is expected to be weak compared to the order-allowed spectrum.[76] The Raman spectrum of the translational vibrations of an orientationally disordered crystal is therefore expected to be dominated by the order-allowed spectrum.

Whalley and Bertie[75] showed that to zeroth approximation the intensity of absorption of a disorder-allowed translational vibration with frequency ν is proportional to ν^2. Klug, Wong and Whalley[67,76] showed that to zeroth approximation the intensity of Raman scattering is proportional to ν. Different assumptions during the derivations can lead to other intensity functions[77] but it is clear in all cases that the features in the disorder-allowed spectrum reflect features in the density of states. An approximation to the density of states can thus be obtained by dividing the disorder-allowed Raman or infrared spectrum by ν or ν^2.

The density of states $g(\nu)$ describes the number of vibrational states with frequency ν, and can be found for mechanically-regular vibrations from their dispersion curves. The density of states is in general a slowly varying function but exhibits maxima or abrupt changes of slope (inflection points) at frequencies corresponding to critical points in the Brillouin zone, where a critical point is defined as a position on the dispersion curves where all derivatives $\partial\nu/\partial\underline{k}$ vanish.[78] Thus, a maximum or inflection point in the disorder-allowed spectrum is assigned to a vibration about which the dispersion branch is nearly flat, and this normally occurs at the zone center or at the zone boundary. Minima in the density of states occur between critical points, at frequencies for which there are few or no vibrational states of any wavevector. As a check to the assignments, the frequencies of the vibrations at critical points in the Brillouin zone can be calculated using model potential functions.

The mechanically irregular vibrations of a disordered crystal must be treated quite differently because they are not described by a wavevector so that dispersion curves can not be defined for them. One approach has been[78-81] to calculate the frequencies and normal coordinates of the vibrations of a large, representative sample of an orientationally disordered crystal that has been constructed so that the sample satisfies cyclic boundary conditions similar to those of the unit cell of an ordered crystal. The infrared or Raman intensity of each vibration can then be estimated through the bond moment or bond polarizability approximation. In a successful calculation, the calculated infrared and Raman spectra reproduce the basic features of the observed spectra, and the calculated normal coordinates are then believed to qualitatively reproduce the actual normal coordinates of the crystal to good approximation. Whether this is actually accomplished depends on whether the structural and potential energy models faithfully represent the structure and forces of the crystal. Few such calculations have been reported, and thus the spectra of the mechanically irregular vibrations of orientationally disordered crystals have normally been assigned in a very general, qualitative way.

1.5 The Vibrational Spectra of the Ices

Because of the fundamental significance of ice Ih, its vibrational spectra have been extensively studied, but the interpretation of the spectra has been hampered by the difficulty of treating orientationally disordered and hydrogen-bonded crystals theoretically. The spectra of the other phases of ice are therefore potentially very useful since their spectra must reflect the structure of the ice and may be easier to interpret than those of ice Ih. In particular, the spectra of the ordered ices, II, IX and VIII, hold promise of being understood in detail since the problems arising from disorder are not present. Thus, as the simplest phases of a simple hydrogen-bonded molecule, ices II, IX and VIII are especially important in the attempt to determine the important intermolecular interactions and to understand the spectra of the ices and hydrogen-bonded crystals in general. The experimental facts and the accepted interpretations of the spectra of the ices are summarized in this section. A more complete historical account can be found in various reviews.[3,5,82-84]

The spectra of the gas phase molecule are the starting points for the interpretation of the spectra of condensed phases, so the vibrations of a gaseous water molecule are given in Table 1.5. The band due to the symmetric O-H stretching vibration, ν_1, is strong and the bands due to the H-O-H bending vibration, ν_2, and the antisymmetric O-H stretching vibration, ν_3, are weak in the Raman spectrum while the reverse is true in the infrared.[74] ν_1 and ν_3 have different symmetries in the gas phase, but this is not generally the case in the solid. Because of this and the fact that ν_1 and ν_3 occur at similar frequencies, the ν_1 and ν_3 vibrations are discussed together as the O-H stretching vibrations in this section. The O-H stretching, H-O-H bending,

Table 1.5

The vibrations of a water molecule in the gas phase

	vibration	symmetry (C_{2v})	H_2O[a]	D_2O[a]	HDO[a]
ν_1	symmetric O-H stretch	A_1	3657	2671	2727
ν_2	H-O-H angle bend	A_1	1595	1178	1402
ν_3	antisymmetric O-H stretch	B_1	3756	2788	3707

[a] From Reference 83.

rotational and translational vibrations have quite different frequencies in the ices, ~3250, ~1600, ~800 and ~200 cm^{-1} respectively, as shown in Figure 1.7 for ice Ih, so each type of vibration will be considered separately in this section. The discussion for each type begins with the spectra of the disordered ice Ih and continues with those of the high pressure ices.

The infrared and Raman spectra of the O-H and O-D stretching vibrations of ice Ih consist of broad bands spanning several hundred wavenumbers, as shown in Figure 1.7. There has been much speculation about the origin of the breadth (e.g. Ref. 82) but it is now known to result mainly from strong coupling of the O-H oscillators.[81,83,86] Perhaps the best evidence for this is the much narrower peaks forming the spectra of the uncoupled O-H or O-D oscillators, which occur in dilute mixtures of HDO in D_2O or H_2O ice, and which are described as ν_{OH}(HDO) and ν_{OD}(HDO) for brevity. These are shown in Figure 1.8 for ice Ih and other ices. The spectra of these oscillators have provided an important key to understanding the spectra of the coupled oscillator and are the starting point of this discussion.

A correlation between ν_{OD}(HDO) or ν_{OH}(HDO) and the $O\cdots O$ distance ($R_{O\cdots O}$) in hydrogen-bonded crystals has long been recognized.[60] The most recent study[87] yielded $d\nu_{OH}/dR_{O\cdots O} = 1843$ cm^{-1}/Å and $d\nu_{OD}/dR_{O\cdots O} = 1362$ cm^{-1}/Å [88] for $R_{O\cdots O} = 2.76$ Å, the separation in ice Ih. The frequency increases with the distance due to an increase in the O-H or

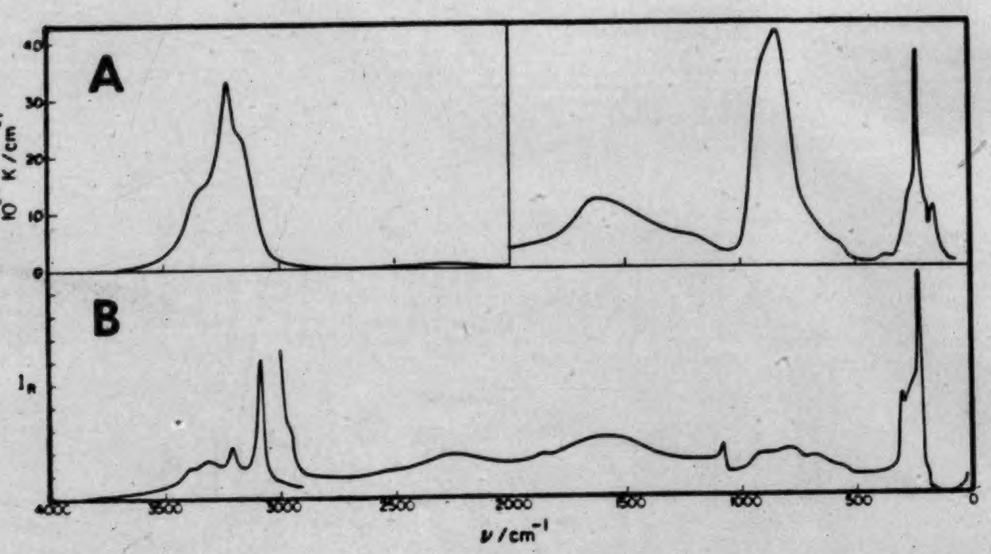

Figure 1.7 The vibrational spectra of H_2O ice Ih at 100 K. A) Infrared spectrum. B) Raman spectrum. From Reference 85.

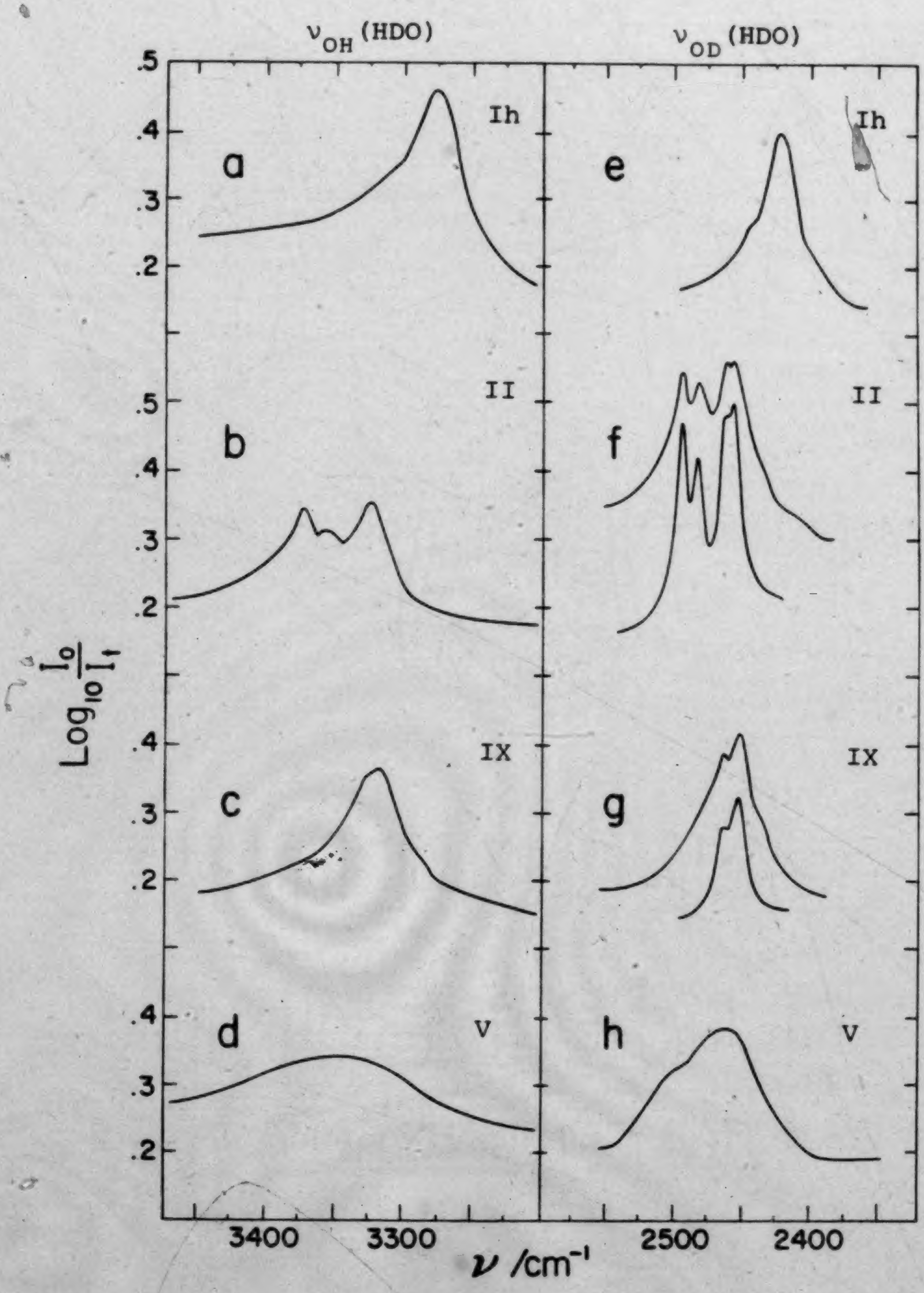

Figure 1.8 ν_{OH}(HDO) and ν_{OD}(HDO) of ice Ih, ice II, ice IX and ice V at 100 K. From Reference 41.

O-D bond strength at the expense of the H···O or D···O hydrogen bond strength.

The appearance of a single peak due to ν_{OH}(HDO) and a single peak due to ν_{OD}(HDO) of ice Ih (Figure 1.8) implies a single O···O distance and hence that all oscillators are equivalent, even though the diffraction symmetry predicts a difference between O-H···O bonds parallel and inclined to the c-axis. The spectroscopic evidence actually agrees with the structure since the predicted difference is known to be small.[5] The HDO frequencies and bandwidths for ice Ih at three temperatures are given in Table 1.6. The infrared absorption by ν_{OH}(HDO) below 100 K has not been reported, but the measurements so far have indicated that ν_{OH}(HDO) is broader than ν_{OD}(HDO) at all temperatures, in both the infrared and Raman spectra. It should be noted that ν_{OH}(HDO) and ν_{OD}(HDO) are broader in the infrared than in the Raman. The 25 cm^{-1} halfwidth of the absorption by ν_{OD}(HDO) in ice Ih must be compared with its halfwidth of ~5 cm^{-1} in the ordered ices, II and IX.[1,41] The greater halfwidth in ice Ih has been attributed to the small range of O···O distances in ice Ih that must be present because of the disorder.[83,86] From the correlations between ν_{OX} and $R_{O\cdots O}$, the halfwidths of ν_{OH}(HDO) and of ν_{OD}(HDO) suggest a range of O···O distances of ~0.015 Å, which is consistent with the results of the diffraction experiments.[31] The increase in ν_{OH}(HDO) and in ν_{OD}(HDO) with temperature has been attributed to an increase in the O···O separation, resulting from the thermal expan-

Table 1.6

HDO frequencies[a] (bandwidths[a]) in ice Ih

	Infrared		Raman	
	ν_{OH}(HDO)	ν_{OD}(HDO)	ν_{OH}(HDO)	ν_{OD}(HDO)
10 K		2413.5 (25)[b]	3264.8 (25.8)[c]	2413.2 (17.3)[c]
100 K	3270 (35)[d]	2416 (20)[d]	3272.2 (27.0)[c]	2418.4 (18.0)[c]
269 K	3300 (60)[d]	2445 (40)[d]	3314 (58)[e]	2448 (31)[e]

[a] Units in cm^{-1}. Bandwidth is the full width at half height.

[b] Reference 2. 2% HDO.

[c] Reference 88. 1.5 to 2% HDO.

[d] Read from graphs in Reference 89. 0.3 to 0.5% HDO.

[e] Reference 90. Bandwidths estimated from spectra. 3% HDO.

sion.[5,88] The increase in the halfwidth with temperature has not been satisfactorily explained, but it is likely due to anharmonic effects.

It may be noted here that Scherer snd Snyder observed two weak features to high frequency of the $\nu_{OH}(HDO)$ and $\nu_{OD}(HDO)$ peaks in the Raman spectrum that maintain the same intensity relative to the main peak for concentrations up to 25% HDO.[90] They attributed these peaks to combinations of $\nu_{OH}(HDO)$ or $\nu_{OD}(HDO)$ with translational lattice vibrations. This is the only reasonably definitive evidence that such combinations influence the spectra of ice, although the structure associated with X-H stretching bands in hydrogen-bonded X-H···Y systems has long been attributed to combinations of the type $\nu(XH) \pm \nu(X\cdots Y)$, an assignment that is definitive for gaseous complexes[91] but much less so in solids.[92]

Haas and Hornig[93] studied the infrared absorption by HDO as a function of HDO concentration, at -190°C. At 18% HDO in H_2O they observed two distinct shoulders at 2393 cm^{-1} and 2442 cm^{-1}, symmetrically displaced about the main peak at 2416 cm^{-1}. The shoulders were attributed to the in-phase and out-of-phase vibrations of coupled O-D oscillators on neighbouring HDO molecules. From the frequencies and relative intensities Haas and Hornig deduced that the intermolecular O-D···O-D coupling constant for ice Ih is -0.123 mdyne Å^{-1}.

In summary, the studies of $\nu_{OH}(HDO)$ and $\nu_{OD}(HDO)$ in ice Ih showed that all of the oscillators are essentially equivalent, and yielded the frequency of the inter- and intramolecularly uncoupled oscillator. The strength of the O-H or O-D bond was found to increase with temperature, and there was evidence of combination bands of ν_{OH} or ν_{OD} with translational vibrations. Finally, the value of the intermolecular O-D···O-D coupling constant for ice Ih was found to be -0.123 mdyne $\mathring{A}^{-1}$.

Ritzhaupt, Thornton and Devlin[94] recently prepared intermolecularly uncoupled D_2O in H_2O ice Ic by simultaneous codeposition of a dilute beam of D_2O with a dense stream of H_2O molecules onto a thin film of H_2O ice Ic held at 135 K. Uncoupled H_2O in D_2O ice Ic was prepared by a similar method[95] and the infrared and Raman spectra of both samples have been reported.[94,95] The peaks that were observed at 3200 and 3270 cm^{-1} in the spectrum of uncoupled H_2O at 90 K (2367 and 2444 cm^{-1} for D_2O) were assigned[94,95] to ν_1 and ν_3 respectively, and the peak at 1732 cm^{-1} (1230 cm^{-1} for D_2O) has been assigned[94,95] to ν_2. The frequency difference between ν_3 and ν_{OH}(HDO) at 3270 cm^{-1} at 90 K (2418 cm^{-1} for ν_{OD}(HDO))[95] suggests, after allowance is made for anharmonic effects, that the harmonic intramolecular stretch-stretch interaction force constant $k_{rr'}$ is ~0.06 mdyne $\mathring{A}^{-1}$[95,96] in ice I, which compares to -0.101 mdyne $\mathring{A}^{-1}$ for the gaseous water molecule.[96] The asymmetric splitting of ν_1 and ν_3 about ν_{OH}(HDO) and ν_{OD}(HDO) has been attributed to Fermi resonance of $2\nu_2$ with ν_1[95,96] and this is the only direct evidence that Fermi resonance does influence the spectra of the ices. The results of this experiment were not available for any of the calculations that are discussed in this section, but the results support the previous indications[1,2,81] of a more positive value of $k_{rr'}$ in the ices than in the gaseous molecule.

The O-H or O-D stretching bands in the spectrum of H_2O or D_2O ice Ih arise from the coupled H_2O or D_2O stretching vibrations, and are described as $\nu_{OH}(H_2O)$ and $\nu_{OD}(D_2O)$. The vibrations are mechanically irregular, as explained in Section 1.4, so the interpretation of their spectra has been largely qualitative, speculative and simplistic, although two assignments based on calculations have been reported.[80,81] The current status of the interpretation of $\nu_{OH}(H_2O)$ and $\nu_{OD}(D_2O)$ is presented next, first for the qualitative approach and then for the quantitative approach. Finally the behavior of the frequencies and halfwidths of the stretching vibrations is discussed.

In the most detailed of the qualitative studies, Whalley[84] correlated features in the spectra of disordered ices to the features in the spectra of corresponding (and sometimes hypothetical) ordered ices, on the justification that he expected unit-cell-group-allowed vibrations to dominate the spectra of even the disordered ices, with the disorder-allowed vibrations broadening the peaks and contributing to a broad, weak, continuum underlying the main features. The identification and correlation of specific features in the spectra were based on relative intensities in the infrared and Raman spectra, depolarization ratios of the Raman bands, and isotope ratios. The principal features in the O-H and O-D stretching bands of ice Ih can be seen in Figure 1.9, and Whalley's assignments are listed in Table 1.7, where the bands are assumed to be due to mixtures of vibrational types, and the assignments merely indicate the principal component of the band. The assignment of the 3083 cm^{-1} Raman peak to the in-phase ν_1 vibration, i.e. to the crystal vibration in which all of the molecules undergo their symmetric stretching motion in phase, is consistent with the long-accepted assignment of the peak to a component of ν_1[83,97] but the assignment of one feature to the longitudinal optic and one to the transverse optic vibrations due to ν_3 has not been proposed before. It has been disputed[81] and defended,[98] and is of uncertain reliability. The discrepancy between the frequencies of corresponding peaks in the infrared and Raman spectra was explained by Wong and Whalley,[99] who argued that maxima in the infrared intensity occur when the amplitudes of the molecular displacements are strongly correlated with the molecular orientations, whereas maxima in the Raman intensity occur where the molecules vibrate as nearly as possible in phase.

The only attempt to assign the O-H and O-D stretching bands on the basis of calculation has resulted from a classical mechanical calculation of the vibrational frequencies and intensities of a disordered model of ice Ih, carried out by McGraw, Madden, Bergren, Rice and Sceats.[81] The model consisted of a 64 molecule proton-disordered sample satisfying cyclic boundary conditions, having no net dipole moment,

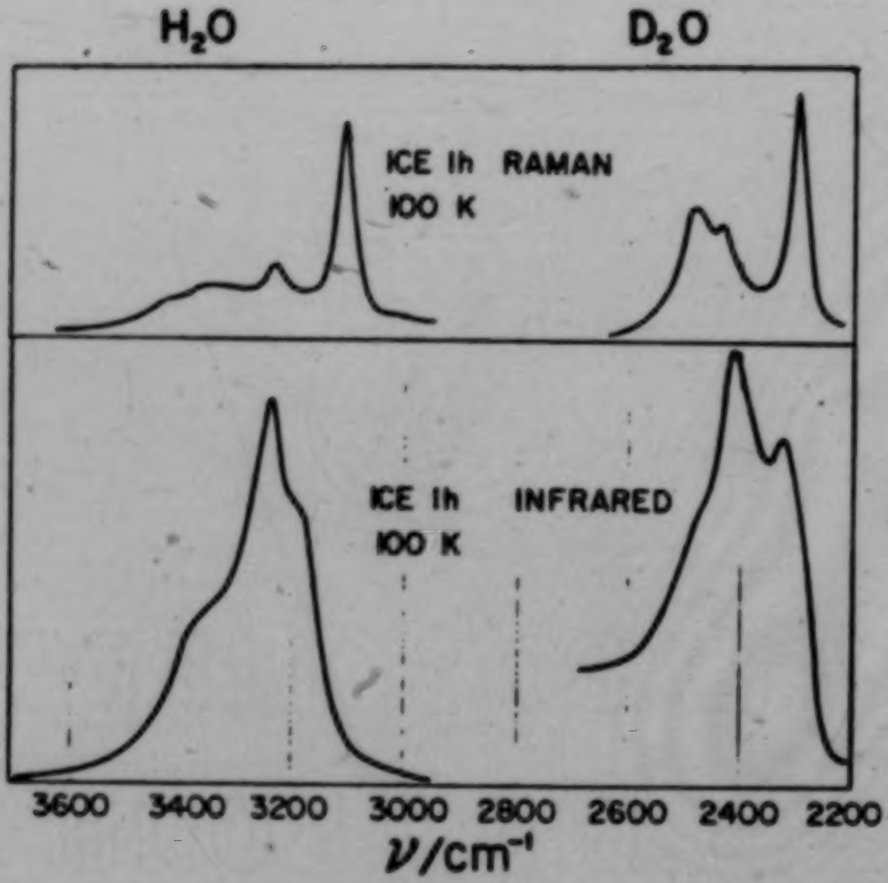

Figure 1.9 Raman and infrared spectra of H_2O and D_2O ice Ih in the O-H and O-D stretching regions, at 100 K. From Reference 84.

Table 1.7

Features of the O-H and O-D stretching bands of ice Ih [a]

H_2O		D_2O		
Raman	infrared	Raman	infrared	Whalley's assignment [a]
3083	3150	2295	2332	ν_1 in-phase
3209	3220	2427	2425	ν_3 TO
3323	3380		2485	ν_3 LO
3420		2547		ν_1 out-of-phase

[a] Reference 84.

and including tetrahedral hydrogen-bonding about each molecule. Their treatment, which they called the 'reduced vibrational model', included only the stretching displacements of each molecule, and the force field included intramolecular, nearest-neighbour intermolecular, and long-range intermolecular, coupling between oscillators. The O-H and O-D stretching force constants were known from studies of ν_{OH}(HDO) and ν_{OD}(HDO), the nearest-neighbour intermolecular coupling constant was set to -0.15 mdyne $\mathring{A}^{-1}$, which they argued was within the experimental error of the observed value, -0.123 mdyne $\mathring{A}^{-1}$ [93] and the long-range intermolecular coupling constants were calculated by assuming the O-H bonds to be point dipoles, so that the potential energy (and its derivatives) was calculable for each configuration of O-H oscillator pairs in the model. The only parameter left to be varied was the intramolecular coupling force constant, which could not be established by independent data at that time. The density of states for the 128 vibrations was found through the Wilson (or GF) formulation of the molecular normal mode problem,[56] and the infrared and Raman spectra were obtained from bond moment and bond polarizability calculations. There was good agreement between the observed and calculated Raman spectra, but agreement was less good with the infrared spectra. They argued that this resulted from approximations that are not as reliable as those in bond polarizability calculations,[81] so that the poorer agreement with the infrared spectra arose principally from the intensity, and not the frequency, calculation. The results suggest that the calculated density of states is representative of that of the true crystal, and that the character of vibrations in ice Ih can be assigned by analogy with the character of the calculated vibrations. The calculated eigenvectors indicated that the lowest frequency band is due to the in-phase ν_1 vibration, in agreement with the accepted assignment, but with varying amplitude from one oscillator to another. All of the other vibrations are mixtures of symmetric, ν_1, and antisymmetric, ν_3, molecular vibrations, and therefore cannot be simply assigned to either ν_1 or ν_3. However, the vibrations at both ends of the frequency range of the density of states mainly involve ν_1, while the vibrations in the middle (near 3270 cm^{-1} in H_2O) mainly involve ν_3.

The breadth of the O-H and O-D bands calculated by Rice et al[81] resulted mainly from intermolecular coupling, as was long believed to be the case,[86] while the distribution of frequencies within the range was strongly affected by the intramolecular coupling constant. The long-range intermolecular coupling appeared to have little effect on the spectra, except possibly to add to their diffuseness, thus implying that longitudinal optic-transverse optic splitting had little effect on the spectrum, in contrast to Whalley's suggestion.[84] A weak, broad shoulder about 100 cm^{-1} to low frequency of the main peak in the Raman spectrum, which increased in relative intensity with the temperature,[88] was assigned to a difference combination transition with a ν_T vibration, $\nu_{OH} - \nu_T$,[81,88] but all of the other features in the infrared and Raman spectra of the O-H and O-D stretching vibrations were assigned to fundamental transitions.[81]

$\nu_{OH}(H_2O)$ and $\nu_{OD}(D_2O)$ of ice Ih increase with temperature for the same reason that $\nu_{OH}(HDO)$ and $\nu_{OD}(HDO)$ do, i.e. because of thermal expansion. The increase in temperature is also accompanied by a broadening of the peaks and features in the spectra. For example, the halfwidth of the main Raman peak is 19 cm^{-1} (13 cm^{-1} for D_2O) at 10 K,[88] 44 cm^{-1} (26 cm^{-1}) at 130 K,[88] and 154 cm^{-1} (72 cm^{-1}) at 269 K.[90] The increase between 10 and 150 K was attributed to scattering of the symmetric O-H stretching vibration by optical phonons of effective frequency $\bar{\nu} \approx 200$ cm^{-1} to combination states of frequency $\nu_{OH} + \bar{\nu}$.[88] Above 150 K some additional mechanism seems to contribute to the breadth.[90]

Thus, the origin and behavior of the features in the infrared and Raman spectra of the O-H and O-D stretching vibrations of ice Ih appear to be reasonably well understood. The interpretation of the spectra of ice Ic is likely to be similar since the spectra of ice Ic are identical to those of ice Ih in all but the absorption by the translational vibrations.[100] Indeed, the similarity between the spectra of ices Ih and Ic has often been an important feature in qualitative interpretations of the spectra of ice Ih (e.g. Ref. 84).

None of the high pressure ices has been studied as extensively as ice Ih. As a result, their spectra are only qualitatively interpreted, with the exceptions of ice II and ice IX for which normal coordinate and intensity calculations have been used to interpret the infrared spectra of the O-D stretching vibrations,[1,2] and the simplest phase, ice VIII, whose Raman spectrum has been assigned largely on symmetry considerations.[101]

The infrared spectra of the uncoupled ν_{OH}(HDO) and ν_{OD}(HDO) vibrations in ice II, ice IX and ice V, which are shown in Figure 1.8 (p. 45), are typical of the high pressure ices. The peaks occur 50 cm^{-1} or more to high frequency of the ice Ih peak,[41] which indicates slightly weaker hydrogen bonding in the high pressure ices in agreement with the diffraction result of greater nearest-neighbour O···O distances in the high pressure ices. The uncoupled vibrations have not been observed for the ordered ice VIII, but for the other ordered ices, II and IX, four and three peaks respectively, with halfwidths of ~5 cm^{-1}, were observed in the infrared spectra.[41] The multiple peaks reflect site splitting or multiple site splitting only, i.e. they reflect the number of non-equivalent hydrogen bonds in the structure. They are assigned to the O-H···O bonds of different lengths so that the frequency increases as the length increases.[1,2,34,41] The peaks in the spectra of ice V have halfwidths of ~150 cm^{-1} for ν_{OH}(HDO) and ~80 cm^{-1} for ν_{OD}(HDO),[41] so are even broader than those in the spectra of ice Ih, probably reflecting both the multiple site splitting and the broadening due to slight variations in the O···O distances as a result of disorder.

The Raman spectra of the coupled O-H and O-D stretching vibrations of ices Ih, II, IX, V, VI and VIII are shown in Figure 1.10. Each Raman spectrum is dominated by a strong, low-frequency peak near 3150 cm^{-1} (2350 cm^{-1} in the D_2O ices) and contains one or more higher-frequency features of lower intensity. In all of the ices the low-frequency Raman peak has an isotope ratio $\nu_{OH}(H_2O)/\nu_{OD}(D_2O)$ of 1.35 to 1.37, is intense in the Raman spectrum, and occurs in a region of low absorption in the infrared spectrum.[97,102] Thus, the low-frequency Raman peak has similar properties to that of ν_1 in gaseous water, and therefore is generally assigned to the in-phase ν_1 vibration of the ice. The higher-frequency O-H or O-D stretching bands in the Raman spectra of the high-pressure ices have been interpreted in detail only for ice VIII. In this case the symmetric, ν_1, and antisymmetric, ν_3, vibrations of a water molecule are completely uncoupled, by symmetry, and the 3477 cm^{-1} and 3448 cm^{-1} peaks of H_2O ice VIII were assigned to ν_1 and ν_3 respectively, on the basis of isotope ratios of 1.365 and 1.342 respectively.[101] The isotope ratio of higher-frequency features in the other high-pressure ices is typically ~1.33,[97,102] suggesting that they are due to mainly ν_3 vibrations, but symmetry does not restrict mixing of ν_1 and ν_3 vibrations in these ices.

There have been only two previous reports of the Raman spectra of ice II and ice IX (or quenched ice III). Taylor and Whalley[97] reported the mercury-arc-excited Raman spectra

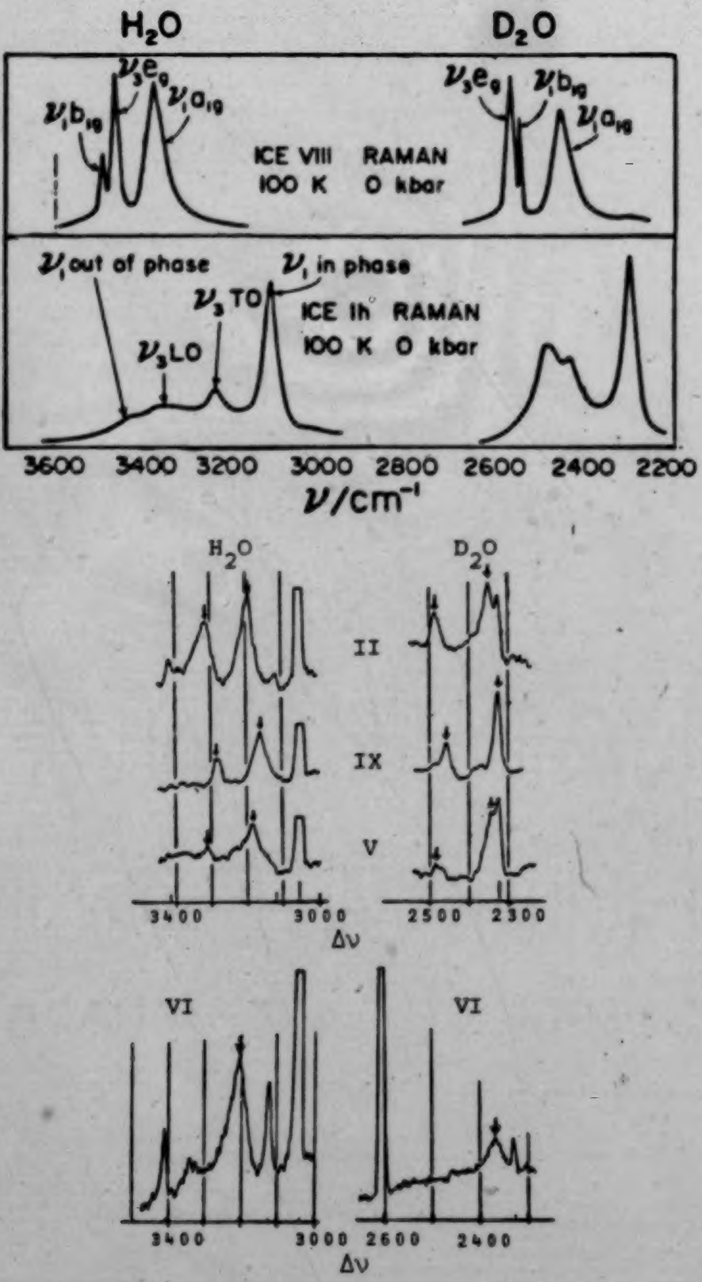

Figure 1.10 Raman spectra in the O-H and O-D stretching regions of ices VIII and Ih[84]; ices II, IX and V[97]; and ice VI,[102] from top to bottom. At 100 K. The Raman peaks of ices II, IX, V and VI are indicated by arrows.

of the O-H and O-D stretching vibrations of ice II and ice IX quenched to 77 K and atmospheric pressure, and the spectra are reproduced in Figure 1.10. Peaks were observed at 3194 (2353) cm^{-1} and 3314 (2489) cm^{-1} in the spectrum of H_2O (D_2O) ice II, and at 3159 (2327) cm^{-1} and 3281 (2457) cm^{-1} in the spectrum of H_2O (D_2O) ice IX (reported as ice III before the phase was identified as ice IX). The peaks were assigned[97] as above. Kennedy et al[103] reported laser-excited survey Raman spectra of the D_2O ices II and III at temperatures and pressures within their regions of stability. The frequencies were not listed, but two peaks were observed in each spectrum at frequencies normally assigned to O-D stretching vibrations. The peaks were of equal intensity in the spectrum of D_2O ice II, but the low-frequency peak was stronger in the spectrum of D_2O ice III. The spectra were not interpreted.

The infrared spectra of the O-H or O-D stretching vibrations of ices Ih, II, IV, V, VI and IX are shown in Figure 1.11. The infrared spectrum of each ice phase contains a strong, broad band centered near 3250 cm^{-1} in the H_2O ices and near 2400 cm^{-1} in the D_2O ices. In general, the spectra of the ordered ices show more structure than those of the disordered ices, and the spectrum of a D_2O ice is better resolved than that of the corresponding H_2O ice. Thus, between 2340 and 2550 cm^{-1}, six bands were observed in the infrared spectrum of D_2O ice II and five bands in the infrared spectrum of D_2O ice IX[1,2,41] and similar structure was observed in the infrared spectra of H_2O ice II and ice IX,

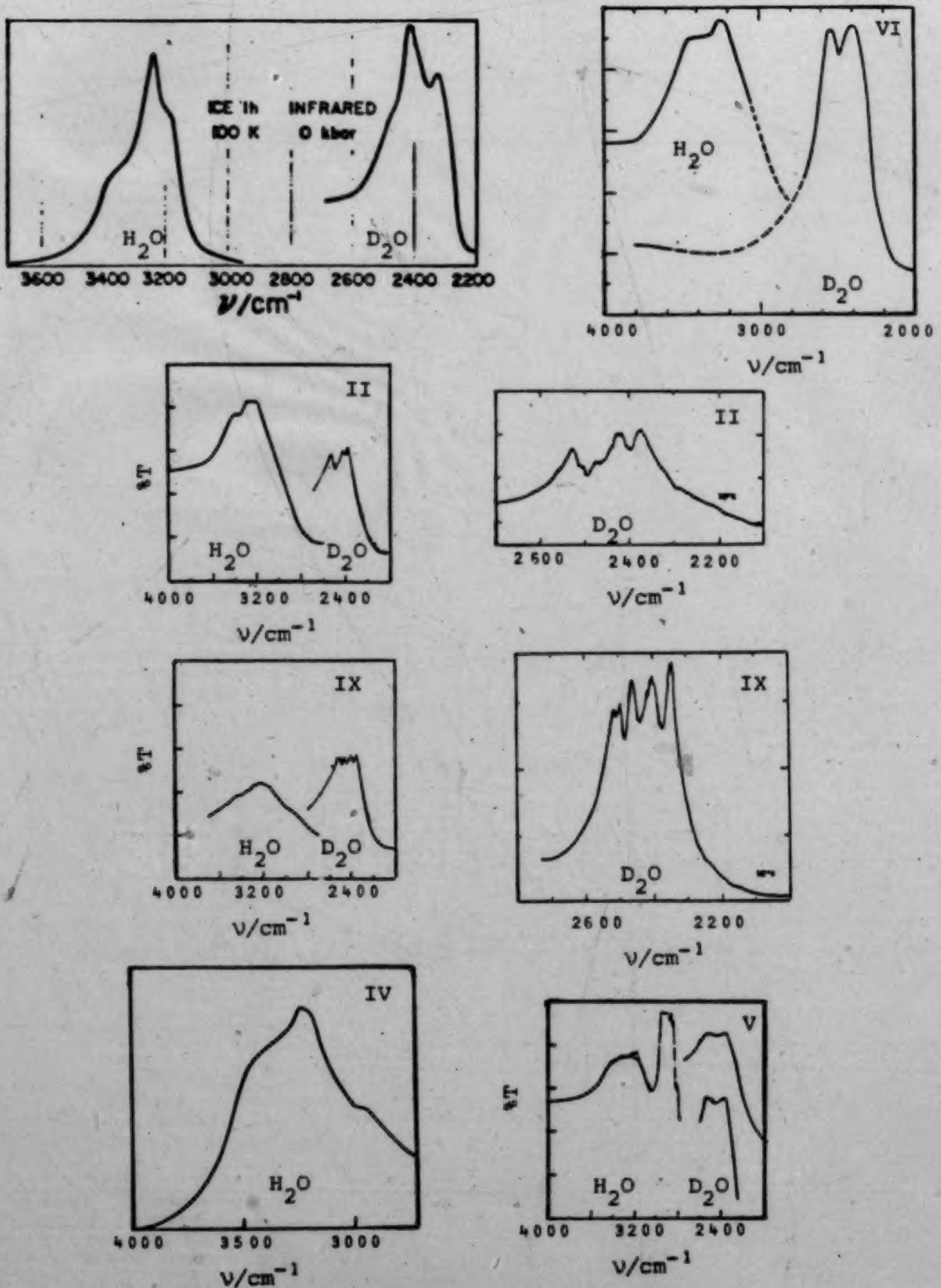

Figure 1.11 Infrared spectra in the O-H and O-D stretching regions of H_2O and D_2O ices Ih, II, IX, IV, V and VI. From References 2, 27, 41, 43 and 84. At 100 K unless noted. Absorbance, unless noted.

although the bands were not as well resolved.[41] Only two, broad features were observed in the spectra of ices IV, V and VI between 3100 and 3500 cm^{-1} in the H_2O ices and between 2300 and 2600 cm^{-1} in the D_2O ices.[27,41,43]

The infrared spectra of the O-H and O-D stretching vibrations of the disordered high-pressure ices have not been interpreted, the only qualitative assignment being for H_2O ice IV, which Engelhardt and Whalley suggested[27] was dominated by ν_3 with important contributions from ν_1, particularly in the wings of the band, following Whalley's assignment[84] of the infrared spectra of the O-H stretching vibrations of ice Ih.

In contrast to the necessarily inconclusive assignment of the spectra of the high-pressure disordered ices, the O-H and O-D stretching bands in the infrared spectra of the ordered ices should be due to the vibrations of one unit cell, and therefore are much more suitable for calculations. For example, Bertie and Bates[1,2] interpreted in detail the infrared spectra of the O-D stretching vibrations of D_2O ice II and D_2O ice IX through calculation of the zero-wavevector normal coordinates and frequencies and the relative intensities of the O-D stretching vibrations. Their calculation model included only O-D stretching displacements, and the force field included intramolecular and nearest-neighbour intermolecular interactions. The intramolecular coupling constants were determined from the FS correlation.[104, 105] The nearest-neighbour intermolecular coupling constants were calculated by the method that Rice et al[81] later used to calculate the long-range intermolecular interaction constants of ice Ih, as described earlier, but Bertie and Bates scaled the calculated coupling constants by the factor necessary to correct the value calculated for the nearest-neighbour O-D···O-D interaction in ice Ih to the observed[93] value, -0.123 mdyne $\mathrm{\AA}^{-1}$. The infrared intensity patterns for ice II and ice IX that were determined through bond moment calculations agreed well with experiment if the diffuse breadth of the observed bands was ignored. The eigenvectors indicated that almost all of the O-D stretching vibrations that absorbed appreciably were mixtures of symmetric and antisymmetric stretching vibrations, and so only one feature could be assigned simply to ν_1 or ν_3: the very strong peak at 2462 cm^{-1} in the spectrum of ice IX at 10 K, which was assigned to the strongly absorbing ν_3 vibration calculated at 2464 cm^{-1}. The infrared spectrum of ice VIII, the only other ordered ice, has never been reported, but should contain only two peaks, one due to a ν_1 vibration of A_{2u} symmetry and the other due to a ν_3 vibration of E_u symmetry.[84] Hence the infrared spectra of the O-H and O-D stretching vibrations of ice VIII should be particularly easy to interpret.

The bending, or ν_2, vibrations of the ices are considered next. Features near 1650 cm^{-1} (1200 cm^{-1}) in the infrared and Raman spectra of the H_2O (D_2O) ices have been attributed to the H-O-H (D-O-D) bending vibrations, by analogy with the spectra of water vapor (Table 1.5), and from the ratio of the frequencies of the H_2O and D_2O ices, which is 1.362

for an uncoupled water molecule with an H-O-H angle of 104.5°. The infrared and Raman spectra of the ν_2 vibrations of H_2O ice Ih, shown in Figure 1.7 (p. 44), are typical of those of both ordered and disordered ices, in that the bands are weak, broad and generally featureless. The region of the spectrum is further complicated by a probable overlap of the bands due to ν_2 vibrations with overtone and combination bands of the lattice vibrations, particularly $2\nu_R$. As a result, there have been no detailed interpretations of this region for any of the ices.

The spectra of the rotational lattice vibrations are observed between 450 and 1000 cm^{-1} for the H_2O ices and between 350 and 725 cm^{-1} for the D_2O ices. The observed ratios of the peak frequencies of H_2O and D_2O are in the range 1.34 to 1.41,[41,43,90,99,101] in good agreement with the isotope ratios calculated for the three rotational vibrations of an uncoupled water molecule, which are the inverse ratios of the square roots of the appropriate moments of inertia. The good agreement suggests that the peaks are due to vibrations that are almost purely rotational in character, with little or no translational character.

The spectra of the rotational lattice vibrations of H_2O ice Ih are shown in Figure 1.7 (p. 44). The infrared spectrum is a broad band with poorly resolved shoulders and a halfwidth of ~175 cm^{-1}, and the Raman spectrum is similar. These characteristics are typical of the spectra of the rotational vibrations of the disordered ices. The spectra of the rotational vibrations of the ordered ices, however, show considerable structure, with peaks as sharp as 5 cm^{-1} in halfwidth in the Raman spectrum of ice VIII and as sharp as 10 cm^{-1} in halfwidth in the infrared spectra of D_2O ice II and ice IX.[1,2,41] The frequencies of the peaks due to the rotational vibrations of D_2O ice II and ice IX decrease by 4 to 8 cm^{-1} as the temperature increases from 10 to 100 K. The peaks also broaden slightly with increasing temperature, resulting in poorer resolution at higher temperatures.[1,2]

Because of the complexity of the spectra and of the structures, the spectra of the rotational vibrations have not been interpreted in detail for any ice. In fact, apart from Bertie and Whalley's assignment of the sharp features in the spectra of ices II and IX to zero-wavevector fundamentals[41] the only assignment of the rotational vibrations that exists is for the simplest phase, ice VIII. There are only three Raman-active rotational vibrations of ice VIII,[101] of symmetry $B_{2g} + 2E_g$ under D_{4h}, and Wong and Whalley[101] have assigned the 548.4 cm^{-1} (398.9 cm^{-1}) peak in the Raman spectrum to the B_{2g} vibration on the basis of the isotope ratio. Two other sharp peaks appear in the Raman spectrum of the rotational vibrations of ice VIII and were assigned to the two E_g rotational vibrations.[101]

The translational vibrations of the ices give rise to the features between 10 and 325 cm^{-1} in the far-infrared and low-frequency Raman spectra of the ices. The translational vibrations result from the oscillations of the molecular centers of mass about their equilibrium positions in the lattice. The frequency is therefore inversely proportional to the square root of the molecular mass, and the ratio of the peak frequencies of H_2O and D_2O is calculated to be 1.054 for the hypothetical harmonic vibrations. The observed isotope ratios are 1.02 to 1.05,[42,43,63,101] indicating that the vibrations are almost purely translational in character. The departure from the ratio of the harmonic vibrations has been attributed in part to different effective intermolecular potential constants of H_2O and D_2O.[42]

The far-infrared spectra of the translational vibrations of ices Ih, Ic, V, VI, II and IX and the Raman spectra of the translational vibrations of ices Ih and VIII are shown in Figure 1.12. The appearance of sharp features in this region, which can be seen in the spectra of ices II, IX and VIII, is clearly characteristic of the ordered phases, while the spectra of the disordered ices are typically broad. It should be mentioned here that the only known difference between the vibrational spectra of ice Ih and ice Ic occurs in the far-infrared spectra of the translational vibrations, where a doublet near 160 cm^{-1} in the spectrum of ice Ih at 4.3 K corresponds to a singlet at 160 cm^{-1} in the spectrum of ice Ic[100] (Figure 1.12).

The far-infrared and Raman spectra of the translational vibrations of ice Ih are quite similar. Corresponding features in the two spectra have almost the same frequencies[76,100,108] although the relative intensities differ considerably

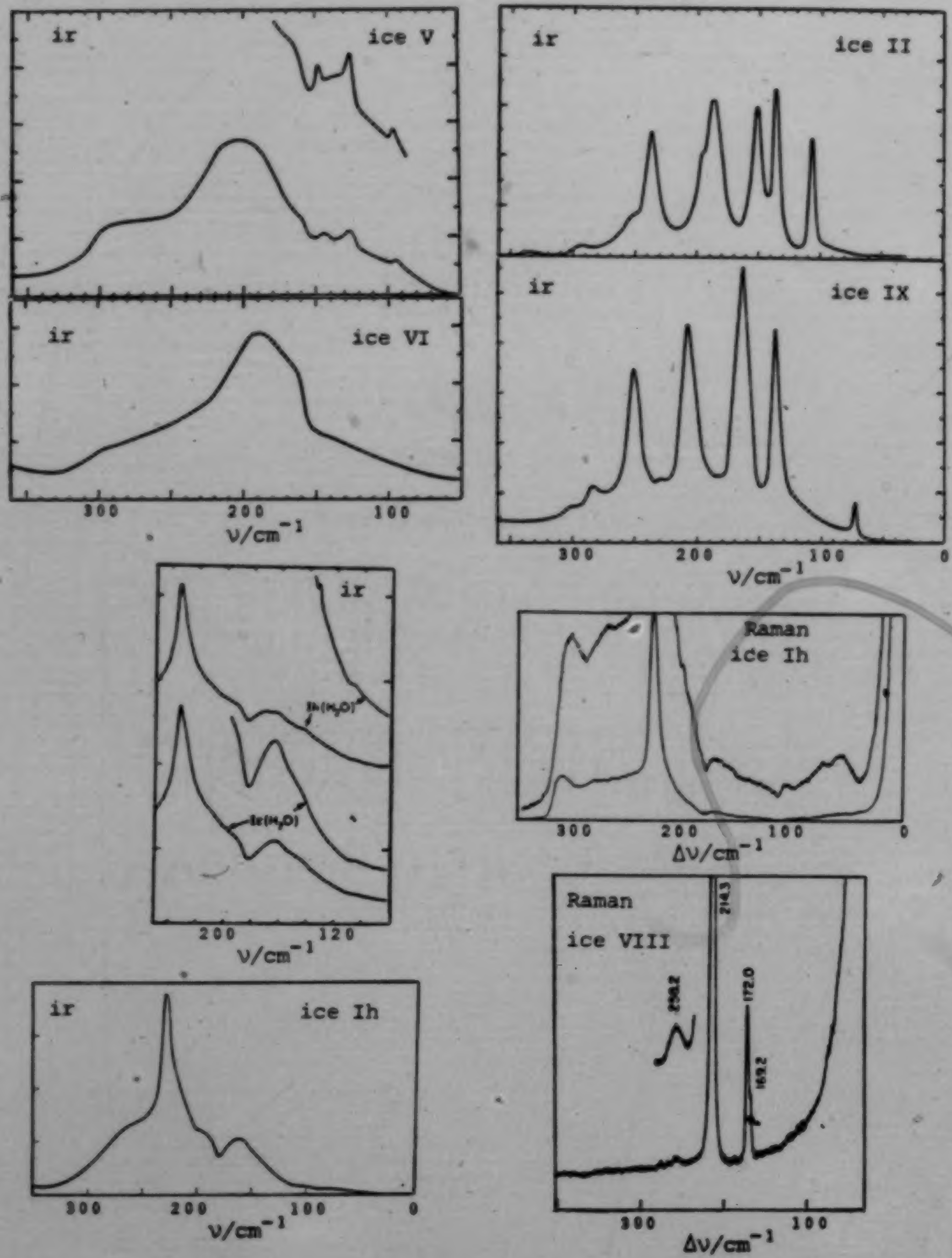

Figure 1.12 Infrared and Raman spectra of the translational vibrations of H_2O ices Ih, Ic, V, VI, II, IX and VIII. From References 42, 43, 100, 101 and 106. At 100 K.

(Figure 1.12) particularly above 240 cm^{-1}. According to Klug, Wong and Whalley,[76, 108] the frequency of the strongest peak due to the translational vibrations is the same in the infrared and Raman spectra within experimental error. However, Bertie and Jacobs[100] suggested that the frequency of the strongest peak in the far-infrared spectrum is closer to that of the shoulder at 229 cm^{-1} in the Raman spectrum and therefore that the origin of these two features is the same.

The theory of the translational vibrations of orientationally disordered crystals that is described in Section 1.4 is particularly suitable for interpretations of the spectra of the disordered ices, since the isotope ratios indicate that the translational vibrations are totally uncoupled from the rotational vibrations. In fact, it was in the first application of this theory that Bertie and Whalley[63] interpreted the far-infrared spectra of ice Ic and ice Ih. The zero-wavevector vibrations of each crystal are inactive in the infrared but some are active in the Raman, under the diffraction symmetry. Therefore the far-infrared absorption by ice Ic or ice Ih is solely the disorder-allowed absorption, but the low-frequency Raman scattering by ice Ic or ice Ih combines both the disorder-allowed and the order-allowed scattering.

Bertie and Whalley[63] identified the maxima, minima and inflection points in the far-infrared spectra of ice Ic, and assigned the frequencies of maxima and inflection points to critical points in the Brillouin zone. The frequencies were fitted to a simple harmonic potential function which included only force constants for nearest-neighbour O···O bond-stretching and O···O···O angle-bending, from which the frequencies of the critical points were calculated through relations available for the diamond structure. The calculated and experimental frequencies agreed well below 240 cm^{-1}, but there was no explanation for the fundamental vibrational states between 240 and 325 cm^{-1}.

The far-infrared spectrum of ice Ih was analyzed in a similar way.[63] The relations between the frequencies of critical points and the force constants were not then known for the wurtzite structure except at the zone center, but an exact correspondence exists between the zone center frequencies of wurzite and the frequencies at the zone center and the zone boundary of diamond. Therefore, the peaks in the ice Ih spectrum were assigned to critical points at the zone center for ice Ih, and the frequencies were calculated using the same potential energy function as for ice Ic. Again the agreement below 240 cm^{-1} was good, but the interpretation failed to explain the existence of translational vibrations above 240 cm^{-1}.

The features below 240 cm^{-1} in the Raman spectrum of ice Ih are also well explained by this theory. Under the D_{6h} diffraction symmetry, three zero-wavevector vibrations, of A_{1g}, E_{1g} and E_{2g} symmetry, are Raman active and therefore give rise to an order-allowed spectrum. Wong and Whalley[76] argued that the strong Raman peak at 227.7 cm^{-1} must result from some of these vibrations, since the order-allowed Raman spectrum is expected to be considerably more prominent than the disorder-allowed Raman spectrum (Section 1.4). The scattering below 200 cm^{-1} is very weak and likely due to disorder-allowed vibrations. Accordingly, the features below ~100 cm^{-1} [76] and the shoulder at 229 cm^{-1}, the frequency of the strongest peak in the infrared spectrum,[100] were assigned to critical points in the Brillouin zone. Just as for the infrared spectrum, however, the Raman scattering above 240 cm^{-1} was not explained by the dispersion curves.

There have been two basic approaches to the interpretation of the absorption and scattering of ice Ih between 240 and 325 cm^{-1}. One approach has been to vary the force constants and to include additional ones to increase the frequencies at the Brillouin zone center and Brillouin zone boundary.[64,65,68,71,75] This usually resulted in an improved fit to the features above 240 cm^{-1} but required potential functions that were unrealistic when applied to other physical measurements such as the compressibility.[106] In the other approach, the vibrations above 240 cm^{-1} have been attributed[76,106–108] to long-range, generally electrostatic, forces, as had been originally suggested by Bertie and Whalley.[63] To implement this, Faure et al have used one model that includes ordering of the hydrogen bonds along the c-axis [107] and another model that places equal but opposite charges on neighbouring molecules,[108] but there is no supporting evidence for either model. Wong and Whalley noted that "the scattering intensity above ~240 cm^{-1} is relatively strong, (which) suggests, but certainly does not prove, that it is connected in some way with the order-allowed A_{1g}, E_{1g} and E_{2g} vibrations."[76] They argued that the coupling constants between neighbouring O···O bonds due to transition moment interaction can account for order-allowed vibrations both at 310 cm^{-1} and at 220 cm^{-1}, and they suggested that longitudinal optic-transverse optic splitting is not possible in disordered solids. Klug and Whalley[106] suggested that the model used by Wong and Whalley[76] may be too crude, withdrew the suggestion that longitudinal optic-transverse optic splitting is not possible in disordered solids, and argued that the Raman scattering at 310 and 275 cm^{-1} and the infrared absorption above 240 cm^{-1} are due to longitudinal optic vibrations corresponding to transverse optic vibrations comprising the strong Raman peak at 229 cm^{-1}.

There is considerable discussion[98,106] about the significance of the terms longitudinal optic and transverse optic modes for disordered crystals. In ordered crystals the longitudinal optic-transverse optic splitting arises from the long-range interactions of transition dipoles, which are spatially periodic.[57,59] In disordered crystals the same interactions exist, but the transition dipoles can not be periodic because of the disorder and the effect on the frequencies of such interactions is unclear. On the other hand, from a phenomenological definition[109] longitudinal optic and transverse optic modes necessarily exist for any strongly absorbing vibration in any condensed phase. Further, calculations for liquid systems have indicated that intramolecular vibrations in liquids can sometimes yield vibration frequencies ranging from near to the gas phase frequency to several tens of wavenumbers above it, due to long-range transition dipole-transition dipole interactions,[110] thus being similar to the effect that Klug and Whalley called longitudinal optic-transverse optic splitting in ice I.

There have been no attempts to interpret the spectra of the translational vibrations of disordered ices other than ices Ih and Ic, but treatments similar to those used for the spectra of ices Ih and Ic would apply to them. The treatment of ices Ih and Ic also suggests that the initial attempts to explain the spectra of the translational vibrations of the ordered ices by calculation should use potential fields that consider nearest-neighbour O···O stretching and O···O···O angle bending coordinates, but that long-range electrostatic forces may cause longitudinal optic-transverse optic splitting which would manifest itself by yielding two Raman bands for vibrations that also absorb strongly. Longitudinal optic-transverse optic splitting may be seen in the Raman spectrum of ice IX, since the E vibrations are both infrared and Raman active, but this cannot be seen in the Raman spectra of ices II and VIII since they are centrosymmetric and Raman-active vibrations are inactive in the infrared.

The spectra of the translational vibrations of the ordered ices have not been interpreted in detail except for the Raman spectra of ice VIII. Wong and Whalley[101] observed four peaks below 300 cm^{-1} in the Raman spectrum of H_2O ice VIII, at 258.2, 214.3, 172.0 and 169.2 cm^{-1}. These were tentatively assigned to an overtone, superimposed B_{1g} and E_g fundamentals, an A_{1g} fundamental, and to the second E_g fundamental, respectively, on the basis of isotope shifts and relative intensities. The far-infrared spectra of ices II and IX are sharp and show considerable structure, with nine features observed in the spectrum of ice II and eight in the spectrum of ice IX.[42] The Raman spectra of the translational vibrations of ices II and IX are relatively poorly characterized. Taylor and Whalley[97] observed two peaks below 300 cm^{-1} in the Raman spectrum of H_2O (D_2O) ice II at 77 K, at 151 (146) cm^{-1} and 261 cm^{-1} and a peak at 166 cm^{-1} in the Raman spectrum of D_2O ice IX at 77 K. Several sharp features can be seen below 500 cm^{-1} in the Raman spectrum of D_2O ice II reported by Kennedy et al,[103] but the frequencies were not listed.

1.6 Objectives of this Work

The ordered ices provide the opportunity to study the vibrational spectra of hydrogen-bonded crystals of the very simple water molecule, without the complications due to the orientational disorder in normal ice. The infrared spectra of ice II and ice IX have been well determined[1,2,42] and

Bertie and Bates[1,2] have interpreted in detail the infrared spectra of deuterated ice II and ice IX in the O-D stretching region. The Raman spectra of ice II and ice IX are comparatively poorly known and are interpreted only qualitatively.[97]

The first objective of the present work was to examine in detail the laser-excited Raman spectra of quenched samples of normal and deuterated ice II and ice IX. Improved experimental procedures and spectroscopic equipment were expected to result in spectra that are vastly better than the arc-excited spectra of Taylor and Whalley.[97] The methods and apparatus are described in Chapter Two, and the experimental results, which fulfilled the expectations, are presented in Chapter Three.

The second objective was to determine whether the model used by Bertie and Bates[1,2] to explain the infrared spectra of the O-D stretching vibrations of ice II and ice IX also explains the Raman spectra. This is discussed in Chapter Four.

Whalley has explained the spectra of the O-H and O-D stretching vibrations of ice Ih through longitudinal optic-transverse optic splitting of the antisymmetric stretching vibrations,[84,98] but this interpretation has been disputed.[81] It should be easier to positively identify the influence of longitudinal optic vibrations in the Raman spectra of the ordered ice II and ice IX. Thus the third objective of this work was to determine the influence of the longitudinal optic vibrations on the Raman spectrum of ices II and IX and, thus, their likely influence on that of ice I.

The final objective was to try to interpret the spectra of the rotational and translational vibrations of ice II and ice IX. A successful interpretation of the spectra of the lattice vibrations of the ordered phases should also provide valuable clues to the interpretation of the spectra of ice Ih and the other disordered phases. This work is described in Chapter Five.

CHAPTER TWO

EXPERIMENTAL TECHNIQUES

2.1 Introduction

The major experimental goals in this work were the measurement of the Raman spectra of normal and deuterated ice II and ice IX and of the temperature dependence of the frequencies of the spectral features. The experimental procedures and apparatus used are presented in this chapter.

2.2 Preparation of Ice II and Ice IX

Samples of ice II and ice IX were prepared by methods described elsewhere,[11] using apparatus developed for previous studies,[1,2] with small modifications. Briefly, ice Ih was cooled to an appropriate temperature (about 200 K to prepare ice II and about 245 K for ice IX) and pressurized to 3 kbar to transform the sample to ice II or ice III. The transformed sample was quenched to 77 K and the pressure was released. Ice III transformed to ice IX in cooling,[22] and the product was ice II or ice IX metastable at atmospheric pressure and 77 K.

Since the probability of nucleation and the rate of transformation increase with temperature, ice samples for Raman studies were prepared at as low a temperature as possible. This enabled the sample to transform slowly about a small number of nucleating centers,[4] which generally resulted in a better optical sample. As seen in the phase diagram (Figure 1.1), ice II can be formed between 180 and

241 K without uncertainty, and a good, semi-transparent sample was prepared by pressurizing ice Ih at 200 K. Ice III can be formed between 241 and 253 K. The recovered ice IX samples from preparations at 245 K were white and easily crumbled, and there was no noticeable optical improvement in the ice IX samples successfully prepared closer to 241 K. The attempts closer to 241 K often resulted in ice II instead of ice IX, because of the temperature uncertainty. Bridgman reported the preparation of clear ice IX,[16] apparently by taking advantage of the extension of the Ih-III equilibrium line into the region of stability of ice II to as low as 210 K. This is possible as long as ice III is present before entering the region and ice II has not been present in the sample recently.[16]

The apparatus used to prepare the samples is shown in cross-section in Figure 2.1. The pressure vessel was a 19 mm i.d. cylinder, C, with matching pistons, A and B, and brass back-up rings, D. The cylinder, the pistons, the spacer, H, and the retaining block, E, were made of Vascomax 350 18% nickel maraging steel, heat-treated to a hardness of 54 Rockwell C. The pressure-distributing plates, F and J, were soft steel, while the thermostat can, G, and its lid were stainless steel.

The first samples were prepared as described previously.[1,2,11] The retaining block, which held the cylinder, the bottom piston and its back-up ring, rested on a pressure-distributing plate in the thermostat can. Liquid nitrogen

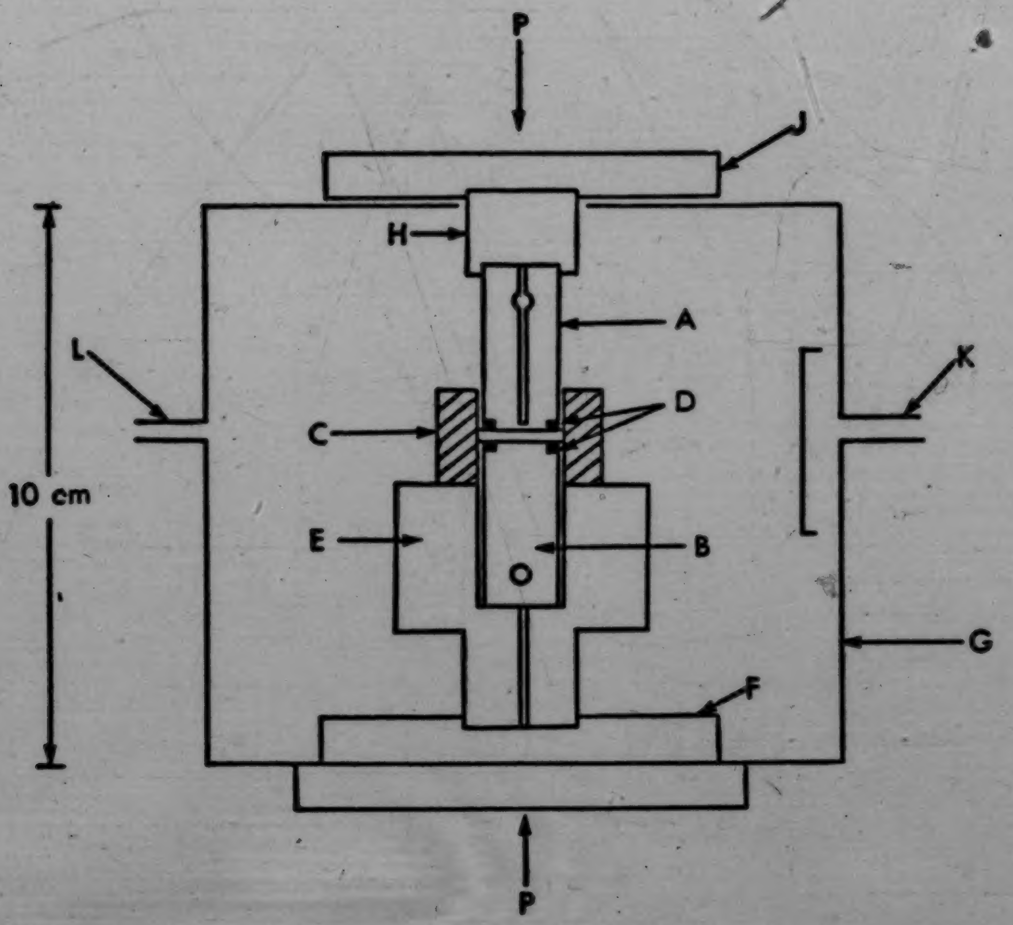

Figure 2.1 Pressure apparatus: A, top piston; B, bottom piston; C, cylinder; D, back-up rings; E, retaining block; F, pressure-distributing plate; G, thermostat can; H, spacer; J, pressure-distributing plate; K, gas entrance port; L, gas exit port.

was poured into the thermostat can to cool the cylinder and piston. One ml of water was syringed into the pressure vessel and froze almost immediately on contact without leaking past the bottom piston. The top piston with its back-up ring in place was inserted to complete the pressure vessel. A copper-constantan thermocouple was inserted into the hole running along the axis of the top piston to within one millimeter of the piston face in contact with the ice sample. The lid was positioned on the thermostat can, and the spacer was placed on the top piston through the hole in the lid. A pressure-distributing plate was placed on the spacer. The pressure apparatus was centered, on a fibreglass plate, on the bottom platen of the press, and another fibreglass plate was inserted between the apparatus and the top platen, for thermal insulation from the press. Styrofoam around the thermostat can helped to thermally insulate it. The entrance port of the thermostat can was connected to a tube that carried the cold gas from boiling liquid nitrogen. The temperature was changed by varying the voltage applied to a pencil heater in the liquid nitrogen, and once set was constant to ±2 K.

The temperature was adjusted to 245 K in the ice IX preparations or 200 K in ice II preparations. The pressure at the sample was increased to 2.1 kbar and maintained for 30 minutes to ensure that heat generated by the compression was dissipated. The pressure was then slowly increased to 3.0 kbar to transform the ice Ih to ice III or ice II, with a reduction in volume of about 20%[4,16] at nearly constant pressure. The transformation to ice III is fast at all temperatures between 241 and 253 K, so one hour at 245 K and 3 kbar was sufficient time to ensure that the sample had completely transformed. The transformation to ice II is slow at 200 K; therefore the sample was allowed to warm up slowly, typically over one to two hours, from 200 to 225 K at 3 kbar to ensure complete transformation.

The transformed ice sample was rapidly quenched to 77 K by passing liquid nitrogen into the thermostat jacket while maintaining the pressure at 3 kbar. After one-half hour at 77 K the pressure was released, and the pressure vessel was moved to the cold can.

The cold can is an uninsulated metal can that contains a work table and boiling liquid nitrogen around the table, to provide a dry atmosphere for handling samples at 77 K.[111] The sample is handled from above the can, with extended tweezers and 30 cm long spatulas. In the cold can, the pistons were removed from the cylinder with a piston extractor that fastens to one of the pistons and twists and pulls the piston relative to the cylinder. The sample was removed by pushing it through the cylinder, which caused it to crack badly. Pieces cut to fit the Raman sample tube were fractured further, yielding poor samples for Raman studies.

The modification of the preparation introduced in this work consisted of Teflon pieces placed in the pressure vessel to shape the sample during preparation and to support the sample as it was pushed out of the cylinder. The Teflon pieces are illustrated in Figure 2.2a. The two Teflon semicircles and the small Teflon blocks were placed on the bottom piston as shown in Figure 2.2b, forming a 1.9×1.9×17 mm rectangular cavity. The cylinder and bottom piston were pre-cooled as before, and water was syringed into the cavity where it froze. The Teflon disk was placed over the cavity, and water was syringed into the one millimeter hole through the disk and on top of the disk, where it froze to provide a pressure linkage between the top piston and the ice in the rectangular cavity.

The remainder of the preparation proceeded as above. The pistons were extracted as before and the back-up rings were removed. The top piston was re-inserted into the cylinder, which was placed on top of a metal cup inside the cold thermostat can. Liquid nitrogen was added to the thermostat can, which was taken to a hand press and the sample was pushed out. The pressure necessary to push the sample out of the cylinder badly fractured the ice against the top piston, but the ice in the rectangular cavity was protected by the Teflon pieces. Some tissues in the bottom of the cup prevented the falling sample from breaking. The Teflon pieces were then separated from the ice sample with little disturbance to the sample, since the adhesion of ice to Teflon is weak. There was no need to cut the samples to size since the rectangularly-shaped chunks of ice fitted into the square glass tubing that was used to contain the

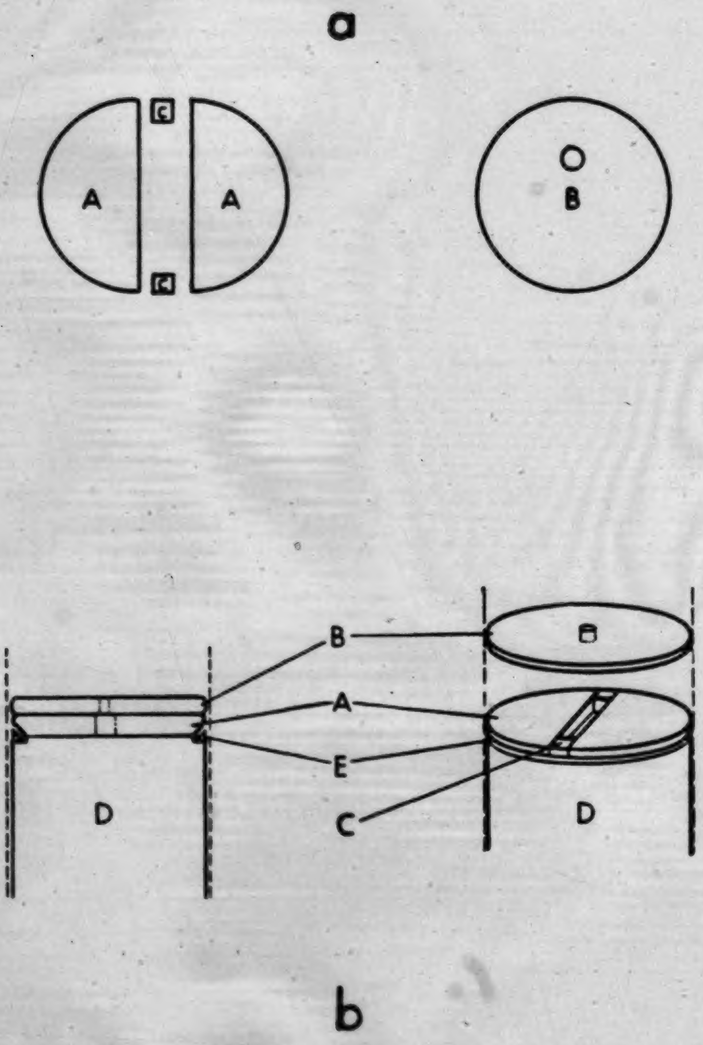

Figure 2.2 a) The Teflon pieces A to C used to shape the sample in the pressure vessel. b) The assembly of the Teflon pieces in the pressure vessel. D is the bottom piston and E the back-up ring.

Raman sample. Therefore, the use of the Teflon pieces during preparation resulted in better Raman samples of both ice II and ice IX than those prepared without the Teflon.

2.3 Characterization of the Ices

The samples of ice were characterized by their behavior during transformation, by their appearance once quenched, by their powder X-ray diffraction patterns, and by their Raman spectra.

The behavior of the sample during the transformation from ice Ih at 2.1 kbar to the high pressure ice at 3 kbar was characteristic of the phase formed. The transformation between 200 and 240 K to ice II began at 2.0 to 2.3 kbar, and the pressure remained constant during compression until the ice was totally transformed. During the preparation of ice III (which yielded ice IX) at 245 K, however, the pressure increased to 2.5 kbar, then fell abruptly when the transformation started, to 2.1 kbar where it stayed until the ice was totally transformed to ice III and the pressure increased again.

Further evidence of the phase prepared was the appearance of the sample after the pressure vessel was disassembled at 77 K. Ice II appeared clear to translucent unless it was subjected to a mechanical shock which shattered it; the crystal separated into thin plates, rather than chunks, during handling and manipulation with the spatulas. Ice IX, however, was always white, and crushed easily into a powder during handling.

The samples were most definitively characterized by their powder X-ray diffraction patterns. The detailed method of preparing and transferring X-ray samples has been described elsewhere.[1] Briefly, a portion of each early preparation was ground at liquid-nitrogen temperature using a stainless steel mortar and pestle, and loaded into a 0.5 millimeter i.d Lindeman glass capillary. The capillary was transferred to a goniometer head that was mounted on a Jarrell-Ash precession camera set at zero degrees precession, and which was precooled by a stream of cold nitrogen gas to produce a temperature of 100 K at the position of the sample. The patterns produced on the flat-plate powder X-ray photographs were compared to the patterns in the literature[11] to verify the ice phase prepared.

Once the Raman spectra of ices II and IX were established for ice samples that had been identified through powder X-ray photographs, the phase of a sample was identified by its Raman spectrum. This identification agreed with that deduced from the behavior of the sample under pressure and from the appearance of the quenched sample.

2.4 The Raman Cryostat

The Raman cryostat (Figure 2.3) was a modification of a design by Dr. S.M. Jacobs. The cryostat consisted of a liquid helium storage dewar, A, a flexible liquid-helium transfer tube, C, the optical cell, E, and two flowmeters, F. The sample was held in a short length of glass tubing on the end of a sample holder-rotator, which fitted into the optical

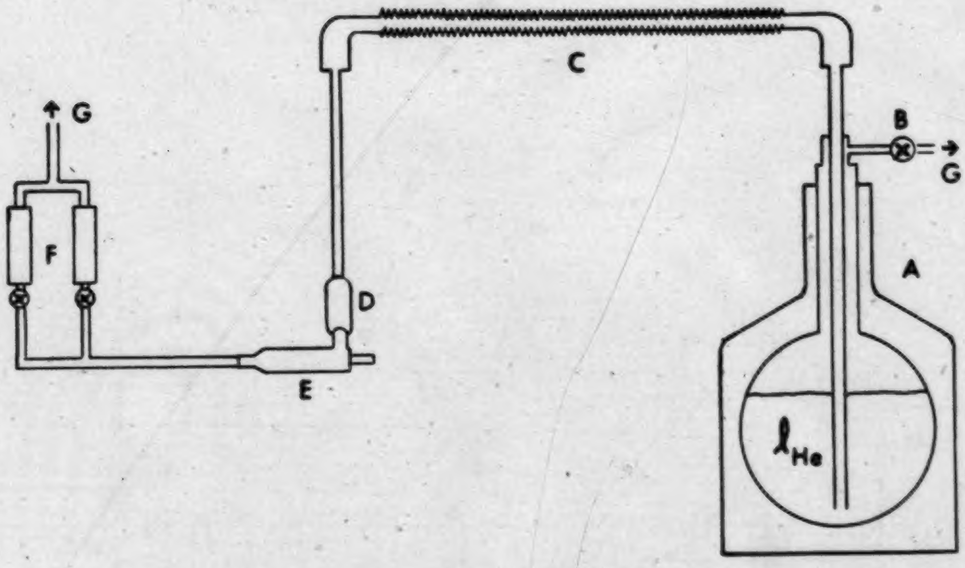

Figure 2.3 Schematic view of the Raman cryostat: A, 50 ℓ liquid-helium storage dewar; B, Hoke valve; C, flexible liquid-helium transfer tube; D, Dewar adapter; E, optical cell; F, flow meters.

cell. The optical cell was cooled by cold helium gas flowing through the transfer tube from the liquid helium storage dewar. The two flowmeters were used to measure the helium gas flow rate, which determined the temperature of the sample and which was controlled by the valves on the flowmeters and by the pressure in the dewar. The Raman spectrum was excited by a laser beam which was focussed on the sample though a flat glass wall of the optical cell, and the light that was scattered at 90° was collected and analyzed by a SPEX spectrometer.

Two different types of glass tubes were used to contain the sample. They were 2.5 cm long and either 2 mm i.d. round Pyrex tubing or 2 mm square Pyrex tubing, and were sealed at one end, rinsed in methanol and dried thoroughly before use.

The sample holder-rotator is shown in Figure 2.4. It consisted of an adapter, A, to hold the glass tube and a rotator, C, which fitted into a Teflon sheath, B, and was used to rotate and position the sample during the Raman experiment.

The adapter was a 6 cm length of 5.5 mm diameter Delrin, with one end machined to snugly fit into the rotator and the other end machined to accept the sample tube. The glass tube extended 1 cm into the adapter and was held in place by frozen oil or water. The adapter extended 4 mm into the sample rotator and was held in place by friction.

The sample rotator was made of Delrin and screwed into a Teflon sheath that fastened to the Raman optical cell and

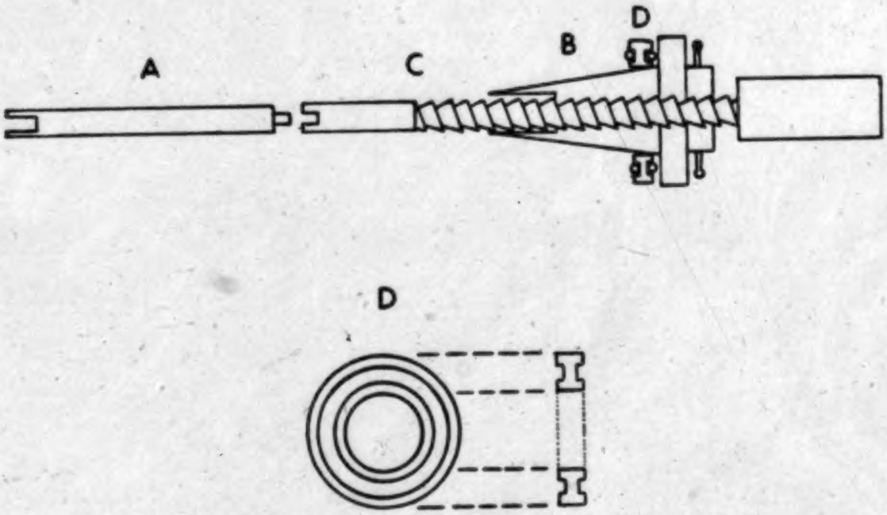

Figure 2.4 Sample holder-rotator and junction ring: A, adapter; B, Teflon sheath; C, rotator; D, junction ring.

had a threaded hole along its axis. The 7 cm long screw (¼" - 20 A.N.C.) enabled the sample to be translated by 3 cm. The maximum diameter of Delrin extending into the optical cell was less than 7 mm.

The Teflon sheath was tapered to seal against the 10/30 ground glass female cone in the original design of the optical cell (Figure 2.5a). Elastic bands held the sheath in place in the cone and this provided a good seal. However, the different thermal expansions of glass and Teflon caused the sheath to be pressed further into the hole as the cell cooled and to become stuck, or to break the cell, when the cell warmed. To overcome this problem, the optical cell was modified (Figure 2.5b), with an o-ring seat replacing the ground glass female cone. A Teflon junction ring (D, Figure 2.4), which had a groove on each side to take a #112 fluorosilicone o-ring formed the seal between the Teflon sheath and the optical cell, with the elastic bands again holding the sheath onto the cell. Fluorosilicone was found to be the best o-ring material available, since it would form a seal at temperatures as low as 210 K.

The Raman optical cell, shown in Figure 2.5b, was an unsilvered dewar cell constructed by the glass shop in this Department. The inner wall of the cell was 10 mm square and round Pyrex and the outer wall was 27 mm square and 28 mm round Pyrex tubing. The space between the two walls was permanently evacuated, and the sample and helium gas went inside the inner tube.

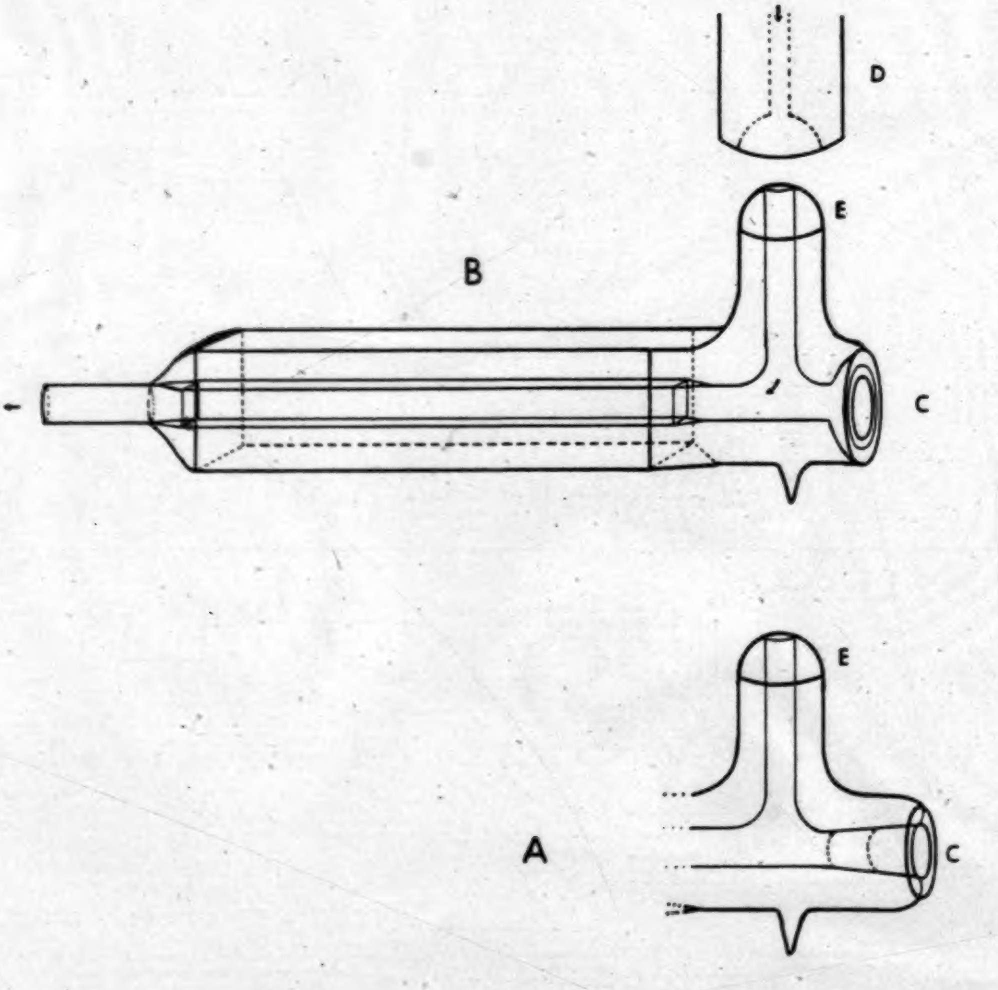

Figure 2.5 Original (A) and modified (B) Raman optical cell with ground-glass female cone and o-ring seat at end C, respectively. D is the Dewar adapter and E is a 8/19 ground-glass ball joint.

In operation, the optical cell was firmly clamped in the sample compartment of the spectrometer, and was oriented with the ground glass ball (E in Figure 2.5) pointing up to receive the transfer tube (Figure 2.3). The transfer tube was connected to the optical cell by a silvered-glass dewar adapter, which contained a 8/19 socket at its lower end and was stuck to the transfer tube at its upper end with silicone rubber cement. Silicone grease on the ball joint sealed the optical cell to the transfer tube adapter.

To control the sample temperature through the helium gas flow rate, the pressure in the liquid-helium storage dewar (A in Figure 2.3) was controlled by the Hoke valve, B, and the flow rate was further controlled by the valves on the flowmeters, F (Matheson 604). The flow rate was adjustable from 0 to 80 ℓ/min. The temperature at the sample position was monitored by a copper-constantan thermocouple and by a germanium resistance thermometer (Scientific Instruments Inc., model no 2G(3-L)) located 1 cm downstream from the laser beam. The sensitivity of a copper-constantan thermocouple increases nearly linearly from 0.017 V/K at 85 K to 0.036 V/K at 250 K, and the junction potential could be read to ±0.002 V. The sensitivity of a germanium resistance thermometer increases with decreasing temperature much faster than linearly, from 0.2 Ω/K at 100 K to 1.2 Ω/K at 50 K, 4.5 Ω/K at 25 K, and greater than 400 Ω/K at 4 K, and the resistance was measured to 0.1 Ω. The copper-constantan thermocouple was used above 85 K, while the germanium resistance thermometer was used between 1.5 and 100 K with high sensitivity at low temperatures and lower sensitivity near 100 K. Temperatures were controlled to ±1 K at 25 K, rising to ±3 K between 40 and 100 K.

2.5 Sample-Handling Procedures

The procedures for loading the Raman samples into the low-temperature cell are described in this section. The sample was loaded into a glass tube in the cold can, attached to the adapter of the sample holder-rotator and stored in liquid-nitrogen. The Raman cryostat was precooled to 100 K and the sample was transferred to it. After the cryostat temperature had been adjusted, Raman spectra of the sample were recorded.

To load the sample into the glass tube, the cold can and table were cooled with liquid nitrogen, and a glass Petri dish containing the empty glass tube was placed on the table and allowed to cool. The ice sample was poured into the Petri dish with the liquid nitrogen from the sample bottle, and a chunk of sample was selected. When necessary, the chunk was cut with the edge of a cold spatula or with a cold X-Acto knife to the diameter of the glass tube; the cut faces were irregular, not smooth. The ice was loaded into the tube with a spatula, which was bent into a right angle 5 mm from its tip to form a horizontal platform when the spatula was held in its normal, vertical position. The ice sample was placed on the platform of the spatula and a second spatula was used to push the ice into the tube, which lay on its side in the Petri dish. The tube was carefully lifted by its open end so that the sample slid into the tube. Often a second piece of ice was put into the glass tube, for a total sample length of 5 to 10 mm. The tube was then positioned vertically in a brass stand on the table. A Teflon core, 1.5 mm diameter and about 1.5 cm in length, was pushed into the tube to wedge the sample in place. The core protruded a few millimeters out of the tube.

The recessed end of the adapter (Section 2.4 and Figure 2.4) was moistened and the excess water was shaken out. The warm adapter was quickly pushed as far as it would go over the open end of the sample tube in the cold can. Within several seconds the water in the adapter froze, bonding the two pieces together. The adapter and sample tube were then immersed in a pool of liquid nitrogen in the table to finish cooling the plastic adapter to 77 K. The sample and adapter could then be stored in a bottle under liquid nitrogen indefinitely, or could be used immediately.

When ready to examine the sample, the junction ring and the two o-rings (Section 2.4 and Figure 2.4) were fastened to the pre-assembled rotator and sheath of the sample rotator, and the rotator was pushed onto the adapter in the cold can. The sample was then immersed in an unsilvered dewar of liquid nitrogen, which had been placed in the cold can so that no condensation onto the sample tube occurred during the transfer. The dewar was then removed from the cold can. The sample holder-rotator was positioned in the dewar with the sample in the liquid nitrogen and the Teflon junction ring and o-rings above the rim of the dewar, so that the o-rings did not freeze.

Before the sample was transferred from the dewar to the cryostat, the cryostat was precooled to 100 K using the following procedure. The cryostat was assembled as in Figure 2.3, but without the transfer tube. The o-ring end of the optical cell (Figure 2.5) where the sample holder-rotator eventually sat was capped by a 25 mm Teflon disk with a 13 mm groove and matching fluorosilicone o-ring, which was held in place by elastic bands looped around glass projections on the cell. Silicone grease was applied to the ball of the dewar cell. One end of the transfer tube was inserted into the liquid helium storage dewar, slowly, to flush the transfer tube and to cool it efficiently. When the dewar adapter (Figure 2.5) on the transfer tube reached the level of the optical cell, the socket of the dewar adapter was placed over the ball of the cell and fastened with elastic bands.

The Hoke valve was just cracked at this point and the valve on each flowmeter was opened about 1.5 turns. Initially the helium gas flow was erratic, but when the cell had cooled to a steady state the gas flow stabilized. The pressure in the storage dewar was adjusted to yield a steady temperature in the cell of 100 K. The pressure could, of course, be decreased by opening the Hoke valve and it spontaneously increased quite rapidly when the Hoke valve was closed. If the temperature was too low the o-rings on the sample rotator froze before sealing. The flowmeters were not adjusted at this point. When the correct temperature was reached the gas flow registered about 30 on a scale of 150 on the meter, indicating a flow of about 4 ℓ/min. through each meter. The cryostat was then ready for the sample.

The success of the sample transfer from the dewar of liquid nitrogen to the cryostat depended largely on the speed of the operation. The elastic bands that held the Teflon cap and o-ring to the Raman optical cell were released, while the cap was held in place. The elastic band holding the junction ring and o-rings to the sheath of the rotator was removed, while the ring was held in place. The Teflon cap and o-ring were then quickly removed from the optical cell and the sample was inserted so that the o-rings and the junction ring resealed the optical cell. It was essential to prevent condensation onto the sample tube as far as possible. Further, if this step was done too slowly, the cold gases froze the o-rings before the seal was made, causing a gas leakage about the o-ring that usually spoiled the attempt to obtain spectra.

After the sample was inserted into the cell, the sample holder-rotator was secured to the cryostat with elastic bands. Any liquid nitrogen on the sample tube quickly evaporated and was flushed away by helium gas at 100 K.

The sample temperature and its steadiness depended on the rate and steadiness of the helium gas flow through the cell, and therefore on the storage dewar pressure and its stability. However, unless enough gas was bled from the storage dewar the pressure in it tended to increase steadily which caused a steady decrease in sample temperature. The Hoke valve (B in Figure 2.3) was used to avoid this. For a particular storage dewar pressure the flowmeter valves could be adjusted to yield the minimum constant temperature possible for that pressure. For any higher temperature the gas flow was more greatly restricted and the excess pressure evolved in the dewar was bled through the Hoke valve.

The lowest temperature that was reached by this procedure was 25 K, considerably higher than the 4.3 K temperature of boiling liquid helium, because gross fluctuations in the gas flow rate increased with the dewar pressure and resulted in considerable variation in the sample temperature. Therefore, spectra were recorded with the sensor temperature between 25 and 100 K in this work.

2.6 Raman Instrumentation

The Raman instrumentation consisted of a laser as the exciting line source, optics to filter, direct and focus the laser beam onto the sample, optics to focus onto the monochromator slit the light scattered by the sample at 90° to the exciting beam, a double monochromator, a detector and photon-counting electronics to measure the intensity of light of each frequency. An iodine filter[112-114] was sometimes used to reduce the intensity of radiation at the laser wavelength from the scattered beam, i.e. to reduce stray light and thus to improve the visibility of Raman features at low frequency shifts.

The excitation line source was a Coherent Radiation CR-5 Ar^+ laser, fitted with a CR-6 or a CR-8 laser tube. The exciting lines were the 4880 Å and 5145 Å Ar^+ lines, which have vacuum wavenumbers of 20486.608 cm^{-1} [115,116] and 19429.73 cm^{-1} [116,117] respectively. The laser was single-moded with a Coherent Radiation model 423 Fabry-Perot etalon when the iodine filter was used. The laser power was normally set to 100 to 200 mW at the sample, although occasionally 400 mW was used. In single-moded operation the maximum laser power that could be obtained was used, i.e. 100 to 150 mW at the sample.

Light from the laser passed through a beam expander (SPEX 1452) and then through a Claassen filter (SPEX 1453) which consists of a prism and a slit to spatially separate lines of different frequencies, in order to remove non-lasing emissions from the laser. The filtered exciting light was then focussed onto the sample. Light scattered by the sample at 90° to the incident beam was collected and focussed through a polarization analyzer, when desired, and through a polarization scrambler onto the entrance slit of the monochromator. When the iodine absorption cell was used it was placed between the polarization scrambler and the entrance slit. The iodine cell was a 10 cm glass cell containing iodine solid and vapor at 70°C.

The monochromator was a SPEX 1401 double monochromator consisting of two 0.75 meter monochromators in series, each fitted with a 1221 grooves/mm ruled grating, with a spatial filter (SPEX 1478) between the exit slits of the two monochromators. The intensity of light leaving the second monochromator was measured with a photomultiplier tube (RCA C31034) which was cooled to -30°C. Harshaw photon-counting electronics converted the signal from the photomultiplier tube to a voltage proportional to the number of photons detected in unit time, and consisted of a preamplifier, an amplifier, a pulse-height analyzer and a linear ratemeter. The voltage output from the ratemeter was recorded with a Hewlett-Packard 7100B strip chart recorder.

Spectral resolution was typically 0.5 to 4 cm^{-1} and the ratemeter integration time constant was 0.5 or 2 seconds. The scanning speed was 5 to 25 cm^{-1}/min and was less than $R/(4 \cdot T)$, where R is the spectral resolution and T the time constant.

2.7 Calibration of the Raman Spectrometer

A Raman spectrum is a plot of the intensity of light that is scattered at each frequency in the spectral range. The Raman spectrum that is obtained from a conventional Raman spectrometer can be converted to the true spectrum by calibrating the spectrometer, that is by correcting the frequencies provided on the wavenumber scale of the spectrometer, which are accurate to only a few wavenumbers, and by determining the way in which the intensity response of the instrument varies with frequency. This latter correction is often neglected.

To obtain accurate frequencies the emission spectrum of neon or Ar^+ was superimposed on the Raman spectrum and the vacuum wavenumber of a Raman line was determined from the known vacuum wavenumbers of the twelve to fifteen emission lines of neon or Ar^+ [115-118] by interpolation. The neon line source was an Oriel C-13-41 pen lamp, while the Ar^+ lines appeared in Raman spectra when the Claassen filter was not used. The intensity center of a Raman or reference line was determined by bisecting the peak at different heights, drawing a line through the points and extrapolating the line until it cut the curve at the peak. The absolute frequency, ν_R, of the Raman line was determined from the chart scale and the distance from a reference line to the Raman line (equation 1, Figure 2.6). This frequency, ν_R, was then subtracted from the vacuum wavenumber, ν_o, of the exciting line to give the Raman shift (equation 2, Figure 2.6). The shift of each Raman line was measured with respect to as many reference lines as possible, and the average and standard deviation of the measurements was found (equation 3, Figure 2.6). Measurements for each Raman line were made relative to between three and eight reference lines on each of three or four spectra.

Two methods for determining the chart scale are indicated in Figure 2.6. In Method 1 it is assumed that the chart scale is constant over the recorded spectrum, which does not take account of the small variations in the chart scale over short frequency ranges. In Method 2 it is assumed that the chart

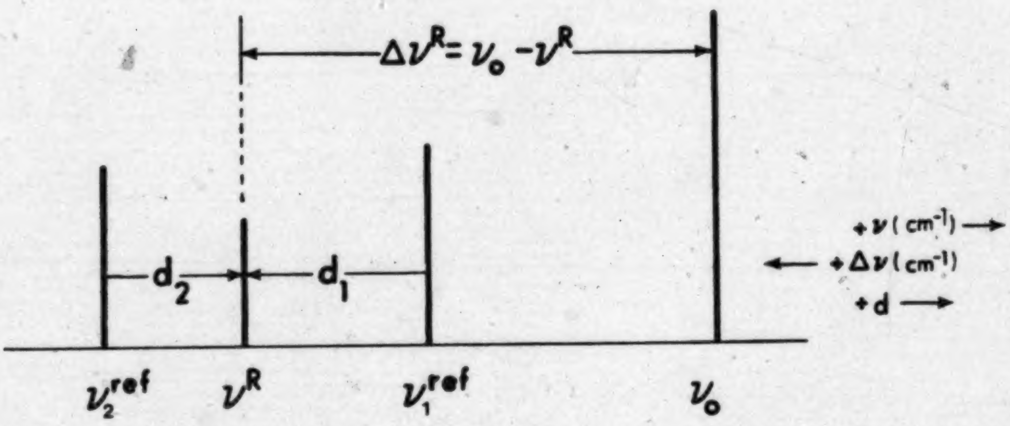
$\Delta\nu^R = \nu_o - \nu^R$
$+\nu\,(\mathrm{cm}^{-1})$
$+\Delta\nu\,(\mathrm{cm}^{-1})$
$+d$
d_2
d_1
ν_2^{ref}
ν^R
ν_1^{ref}
ν_o

$$\nu_i^R = \nu_i^{ref} + d_i \cdot (\text{chart scale}) \qquad (1)$$

$$\Delta\nu_i^R = \nu_o - \nu_i^R \qquad (2)$$

$$\Delta\nu^R = \frac{1}{N} \sum_i \Delta\nu_i^R \qquad i = 1 \text{ to } N \qquad (3)$$

Method 1

$$\text{chart scale } (\mathrm{cm}^{-1}/\mathrm{in}) = \frac{\text{scan speed } (\mathrm{cm}^{-1}/\mathrm{min})}{\text{chart speed } (\mathrm{in}/\mathrm{min})}$$

Method 2

$$\text{chart scale } (\mathrm{cm}^{-1}/\mathrm{in}) = \frac{\nu_1^{ref} - \nu_2^{ref} \;(\mathrm{cm}^{-1})}{d_2 - d_1 \;(\mathrm{in})}$$

Figure 2.6 Methods for frequency calibration of Raman spectrometer. ν_o, ν^R, ν_1^{ref}, and ν_2^{ref} are the vacuum wavenumbers of the exciting line, the Raman line, and the two reference lines. N is the number of reference lines. d_i is the signed distance from reference line i to the Raman line.

scale is constant between any two reference lines, which is probably better than the assumption in Method 1 but is still not perfect because the chart scale over a given frequency region varies with the pair of reference lines used to calculate it. In practice the average frequencies from the two methods were almost identical while the standard deviations were only about 0.1 cm^{-1} smaller from Method 2 than from Method 1.

The frequency dependence of the intensity response of the instrument was determined by recording the spectrum of a lamp for which the intensity was known as a function of the frequency. The spectrum that is recorded in a Raman experiment describes the number of photons scattered in unit time by the sample at each frequency *as measured by the detector*, but the true Raman spectrum describes the *actual* number of photons scattered in unit time at each frequency. The intensity of scattered light is proportional to the number of photons scattered in unit time, through $h \cdot f$, where h is Planck's constant and f is the frequency. The detected light intensity depends not only on the intensity of light that is scattered but also on the response of the monochromator and photomultiplier tube to radiation of different frequencies. The response of the monochromator and the photomultiplier tube together is called the intensity response of the instrument. Once determined, the intensity response of the instrument is used to correct the observed absolute or relative intensities of spectral features to the true absolute or relative intensities. However, the relative intensities are easier to obtain than the absolute intensities, and are also the quantities normally of interest in Raman spectroscopy.

The standard lamp was supplied by the manufacturer with a listing of the power, P, emitted by the lamp in a 10 Å interval about each spectral wavelength, under certain constant conditions that are not important for relative intensity determinations. It can be shown that $B(\nu)$, the intensity emitted by the standard lamp in unit wavenumber interval at wavenumber ν, is proportional to P/ν^2. $C'(\nu)$, the relative intensity response function of the instrument, is thus

$$C'(\nu) = k'[I_{sl}(\nu)/B(\nu)] \qquad (2.1)$$

where $I_{sl}(\nu)$ is the intensity of the standard lamp measured by the detector, and k' is an arbitrary constant. The relative intensity correction function, $C(\nu)$, is the reciprocal of the relative intensity response of the instrument at ν, $C'(\nu)$. The detected Raman intensity, $R_r(\nu)$, is then multiplied by the relative intensity correction function to yield the true relative Raman intensity, $R(\nu)$. Thus

$$R(\nu) = R_r(\nu) \cdot C(\nu) = R_r(\nu) \cdot k \cdot [B(\nu)/I_{sl}(\nu)] \qquad (2.2)$$

where $k^{-1} = k'$. Thus, through equation (2.2), the true intensity spectrum, i.e. the energy that is scattered by the sample through unit area in unit time at each frequency, was calculated from the observed spectrum, i.e. the number of photons scattered at each frequency as modified by the instrument response.

CHAPTER THREE

EXPERIMENTAL RESULTS

3.1 Introduction

The experimental results of this work are described in this chapter. The ice phase that was obtained in a preparation, and its purity, were determined from its powder X-ray diffraction pattern and its Raman spectrum, as discussed in Section 3.2. Section 3.3 describes the corrections that were applied to the temperature indicated by the germanium resistance thermometer, to give the true temperature of the Raman sample. Section 3.4 describes the intensity response of the instrument, which was applied to the recorded spectra to obtain the true relative Raman intensities. Section 3.5 presents the frequencies, half-widths and relative intensities of the features in the Raman spectra of H_2O and D_2O ice II and ice IX for samples between 35 and 100 K at atmospheric pressure, and polarized spectra of ice II.

3.2 Characterization of the Samples

The four ices examined in this study were H_2O and D_2O ice II, and H_2O and D_2O ice IX. At least two samples of each ice were prepared, and the powder X-ray diffraction pattern and the Raman spectrum were obtained for at least one sample of each ice. Other samples of the same ice were then identified through their Raman spectra. The amount of hydrogen isotope impurity in the liquid D_2O starting material was determined from the O-H stretching region of the Raman spectra of two samples of D_2O ice.

The X-ray diffraction pattern of a powdered sample consists of a set of concentric circles, and each circle results from X-ray diffraction by particular crystal planes. The interplanar spacings, called the d-spacings, were calculated from the circle diameters and compared to the listings in the literature.[1,11] The d-spacings are temperature dependent but vary slowly enough that precise knowledge of the temperature was unnecessary for identification of the phase. In two experiments, however, the temperature was accurately measured before and after recording the X-ray pattern. In the first experiment, two photographs of one sample of H_2O ice II were recorded, each was measured once, and the average d-spacings were determined. Each d-spacing was assigned to the most intense X-ray reflection contributing to the circle[1] and the cell parameters were refined with the program DREFINE to fit the d-spacings. The parameters of the hexagonal cell of ice II refined to a = 12.95 Å and c = 6.25 Å for a sample at 115±1 K. This compares well with the previous determinations of the cell parameters by Bertie, Calvert and Whalley[11] (a = 12.92 Å, c = 6.23 Å at ~90 K), Kamb[46] (a = 12.97 Å, c = 6.25 Å at 123 K), and Bates[1] (a = 12.91 Å, c = 6.24 Å at 100 K). In the second experiment, one photograph of a sample of D_2O ice IX at 118±3 K was recorded and the d-spacings were measured once. The parameters of the tetragonal cell of ice IX refined to a = 6.75 Å and c = 6.81 Å, which compares well with the cell parameters determined by Bertie, Calvert and

Whalley[11] (a = 6.75 Å, c = 6.79 Å at ~90 K), Kamb and Prakash[52] (a = 6.73 Å, c = 6.83 Å at 98 K), and Bates[1] (a = 6.74 Å, c = 6.77 Å at 100 K).

The most likely contaminants of ice II or ice IX are ice Ih, ice Ic, and either ice IX or ice II, and the strongest reflections of these impurities should be readily observable in the X-ray patterns if the contaminants are present in sufficient quantity. No evidence of impurity was observed for the ice II samples, but the 111 reflection of ice Ic was present very weakly in the diffraction pattern of the ice IX samples. This trace of ice Ic was detected in both samples of ice IX tested by this method.

Ice Ic impurity in ice IX at 100 K would affect the Raman spectrum most noticeably at the frequencies of its most intense Raman lines, 3083 and 227.6 cm^{-1} for H_2O [76,99] and 2295 and 218.6 cm^{-1} for D_2O.[76,99] The lower frequency peaks, with half-widths of ~10 cm^{-1},[76] are much sharper than the higher frequency peaks, and occur in spectral regions where ice II and ice IX scatter very little. However, no scattering was observed at 227.6 cm^{-1} in H_2O ice IX and 218.6 cm^{-1} in D_2O ice IX, even in the spectra of those samples that were shown by the X-ray evidence to contain traces of ice Ic. It is concluded, therefore, that either ice Ic formed while the X-ray samples were prepared or ice Ic was present in the samples in spectroscopically undetectable amounts.

The hydrogen isotope content of the liquid D_2O that was used to prepare the ice samples was 0.5 ± 0.1% H,[119] but the hydrogen content of each D_2O ice sample could be somewhat higher because the liquid was exposed to atmospheric water vapor during the preparation. The hydrogen content of two deuterated ice samples was tested by measuring the intensity of $\nu_{OH}(HDO)$, the band due to the uncoupled O-H oscillator, relative to that of $\nu_{OD}(D_2O)$, the band due to the coupled O-D oscillators. $\nu_{OH}(HDO)$ absorbs at 3326 cm^{-1}, 3318 cm^{-1} and 3288 cm^{-1} in D_2O ice IX at 100 K,[41] and the corresponding Raman scattering is expected at the same frequencies. A very weak, broad peak was observed at ~3315 cm^{-1} in the Raman spectrum of a sample of D_2O ice IX with an area that was ~1.6% of the integrated area of the $\nu_{OD}(D_2O)$ band. Since scattering by an O-H oscillator is twice as intense as that by an O-D oscillator, the sample contained ~0.8% H. The same experiment was performed with a D_2O ice II sample but the scattering by $\nu_{OH}(HDO)$, which is expected at 3373 cm^{-1}, 3357 cm^{-1} and 3323 cm^{-1},[41] was not observed, so the hydrogen content of that sample was presumably close to 0.5% H, the value for the starting liquid. It is clear that the preparation of the ice samples did not introduce a significant amount of hydrogen into the D_2O samples.

3.3 Determination of the Sample Temperature

The accuracy with which the germanium resistance thermometer indicated the true temperature of the sample was checked by comparing the temperature it gave with the temperature obtained from the relative intensity of a corresponding pair of Stokes and anti-Stokes Raman lines. The Stokes/anti-Stokes intensity ratio is given by

$$\frac{I_s}{I_{as}} = \left(\frac{\nu_s}{\nu_{as}}\right)^n \cdot e^{\frac{hc\Delta\nu}{kT}} \qquad (3.1)$$

where n=3 if the spectrum is a plot of the number of photons scattered at frequency ν per second, and n=4 if the spectrum is a plot of the scattered intensity at ν. The intensity ratio I_s/I_{as} is the ratio of the areas under the Stokes and anti-Stokes peaks, Δν is the Raman shift of each peak, ν_s and ν_{as} are the absolute frequencies of the Stokes and anti-Stokes peaks, and T is the absolute temperature of the sample. The ratio k/hc, of the Boltzmann constant to Planck's constant times the velocity of light in vacuum, equals 0.6950 $\mathrm{cm}^{-1}\cdot\mathrm{K}^{-1}$. Equation (3.1) can be rearranged to

$$T_{s/as} = \frac{\Delta\nu/0.6950}{\ln\left(\frac{I_s}{I_{as}}\right) - n\cdot\ln\left(\frac{\nu_s}{\nu_{as}}\right)}, \qquad (3.2)$$

where $T_{s/as}$ is the Stokes/anti-Stokes temperature, that is the sample temperature determined from the Stokes/anti-Stokes intensity ratio.

The intensity ratio, I_s/I_{as}, can be measured most accurately, and thus yields the most accurate temperatures, if it is less than ~10. For temperatures below 100 K this requires that strong Raman peaks below 100 cm^{-1} be used. For ice II

(Section 3.5) the most favorable peak occurs at ~71 cm (~ 69 cm^{-1} for D_2O) and, although less favorable, the peak at ~103 cm^{-1} (~100 cm^{-1} for D_2O) can be used. For ice IX (Section 3.5) the optimum peak occurs at ~73 cm^{-1} (~70 cm^{-1} for D_2O), since the 35 cm^{-1} peak (34 cm^{-1} for D_2O) is normally difficult to measure accurately, due to intense Rayleigh scattering.

$T_{s/as}$ and T_{Ge} are compared in Table 3.1 and Figure 3.1 for thirteen determinations at eleven temperatures between 40 and 100 K. The average of up to six measurements of $I_{s/as}$ was used to calculate $T_{s/as}$. The standard deviation of $I_{s/as}$ was about 10% of $I_{s/as}$, so the standard deviation of $T_{s/as}$ is less than 1 K at 40 K, and about 3 K at 100 K. The data were fitted by an unweighted least-squares analysis to the straight line

$$T_{corr} = 0.819 \cdot T_{Ge} + 15.5 \text{ K}, \qquad (3.3)$$

which is shown in Figure 3.1. The standard errors of the slope and the intercept are 0.064 and 4.6 K respectively, and the covariance of the slope and intercept is -0.284 K. The correct temperature, T_{corr}, for each value of T_{Ge} is given in Table 3.1 with its standard error. The temperatures quoted for spectral samples in this thesis are the correct temperatures.

A necessary concern of Raman spectroscopists is laser heating of the sample, which occurs if the frequency of the exciting laser line coincides with an absorption band of the

Table 3.1

Results of the calibration of the germanium resistance thermometer

T_{Ge}[a]/K	$T_{s/as}$[b]/K	T_{corr}[c]/K
40	49.1	48.2(2.2)
41	44.0	49.0(2.1)
46	53.9	53.1(1.9)
50	55.6	56.4(1.7)
60	67.0	64.6(1.3)
71	69.3	73.6(1.2)
75	76.0	76.9(1.3)
79	84.0	80.1(1.4)
82	88.4	82.6(1.5)
82	85.5	82.6(1.5)
91	90.2	90.0(1.9)
98	86.5	95.7(2.2)

[a] Temperature indicated by the germanium resistor.

[b] Temperature determined from the Stokes/anti-Stokes intensity ratio.

[c] $T_{corr} = 0.819 \cdot T_{Ge} + 15.5$ K. The standard error is given in parentheses.

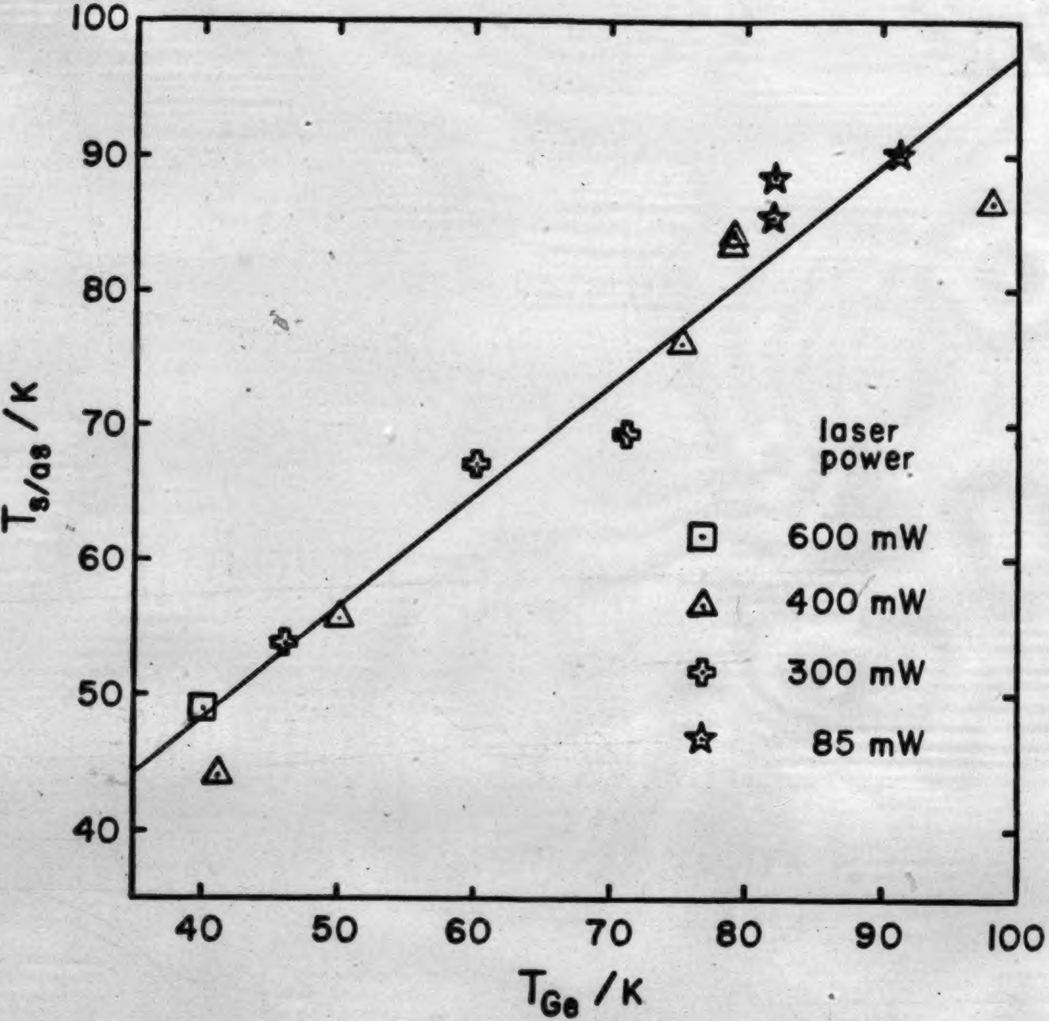

Figure 3.1 The temperature of Raman samples measured from the intensity ratio of Stokes and anti-Stokes lines plotted against the temperature measured by a germanium resistance thermometer.

sample. The Napierian absorption coefficient, $\alpha = \ell^{-1} \cdot \ell n(I_o/I_t)$, where I_o and I_t are the intensities of light before and after traversing the distance ℓ in the sample, of ice Ih is only 0.0008 cm^{-1} at 20487 cm^{-1},[120] so that less than 0.02% of 4880 Å exciting radiation is absorbed by a 2 mm thick sample of ice Ih. The visible absorption coefficients of ice II and ice IX have never been reported, but they are likely similar to that of ice Ih. Therefore laser heating of ice II or ice IX is expected to be small, but not zero.

To test this experimentally, the spectra used for temperature calibration were excited with four different power levels between 85 and 600 mW. If laser heating had been a problem, the points obtained with higher laser powers would be consistently above those obtained with lower laser powers in Figure 3.1, and this is not observed. Thus laser heating of the sample appears not to have been significant even at a power of 600 mW.

3.4 The Intensity Response of the Instrument

The spectrum of a standard lamp was recorded between 21000 and 11500 cm^{-1}, at a constant slit width of 50 μm. The relative intensity response function of the instrument, $C'(\nu)$, and the relative intensity correction, $C(\nu)$, (Section 2.7) that were calculated from the spectrum are given in Figure 3.2, where k and k' of equations (2.1) and (2.2) have been adjusted to give $C'(\nu) = C(\nu) = 1.0$ at 20487 cm.$^{-1}$ The observed spectrum was multiplied by $C(\nu)$ to correct the

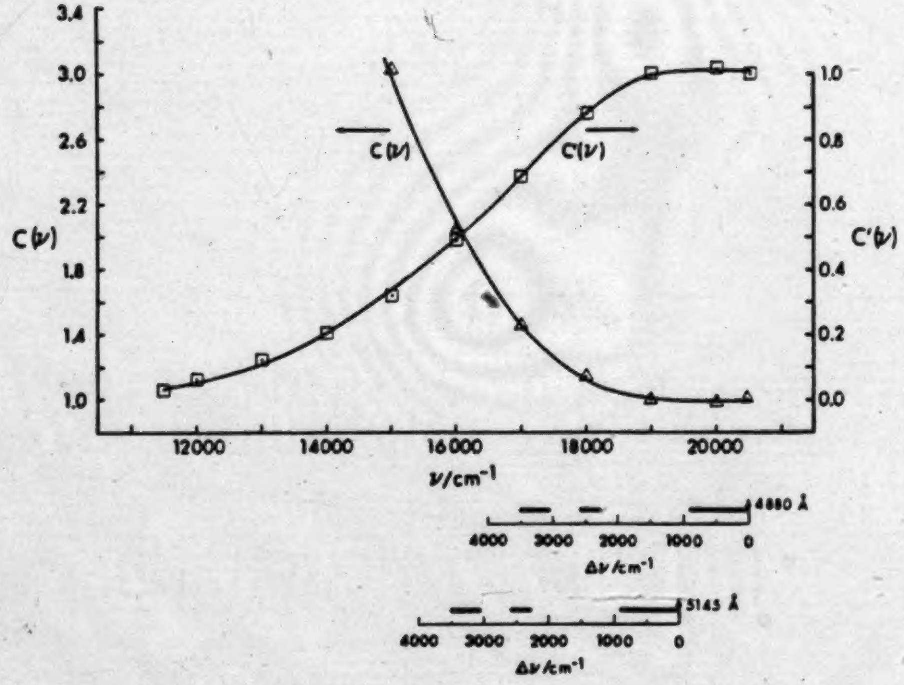

Figure 3.2 The intensity response C'(ν) of the Raman instrument and its reciprocal, the relative intensity correction curve C(ν). $I_{corr} = I_{obs}\ C(\nu)$.

relative intensities for the instrument response. The values of C'(ν) are accurate to within 15%, judging from the noise on the spectrum of the standard lamp. Those portions of the curves that apply to Stokes Raman spectra excited with 4880 and 5145 Å laser lines are indicated under the wavenumber axis, and the wavenumber ranges over which spectra of ice were recorded in this work are indicated by horizontal bars.

It is concluded from Figure 3.2 that the correction function C(ν) is constant to within 3% between 0 and 900 cm^{-1}, and to within 10% between 2300 and 2600 cm^{-1}. Thus the uncorrected relative intensities of features within either of these ranges are correct within experimental error. However, between 3100 and 3500 cm^{-1} away from 4880 or 5145 Å excitation, C(ν) increases by 15 or 20% respectively. Thus data within this range must be corrected.

It is further concluded from Figure 3.2 that the value of the correction function is ~1.0 at 900 cm^{-1}, ~1.1 at 2400 cm^{-1} and ~1.35 at 3300 cm^{-1} for 4880 Å excitation, but ~1.4 at 2400 cm^{-1} and ~1.9 at 3300 cm^{-1} for 5145 Å excitation. Therefore the intensity of scattering by the O-D or O-H stretching vibrations relative to that by the lattice vibrations must be corrected.

The figures reported in Section 3.5 have not been corrected for the instrument response, but corrections that are larger than 15% have been applied to the relative intensities reported in the tables of Section 3.5.

3.5 The Raman Spectra of Ice II and Ice IX

The Raman spectra of H_2O and D_2O ices II and IX between 35 and 100 K at atmospheric pressure are reported in this section. The features of the spectra are assigned to O-H or O-D stretching vibrations, H-O-H or D-O-D bending vibrations, rotational lattice vibrations, and translational lattice vibrations based on the ratios of the frequencies of the corresponding features of the H_2O and D_2O ice, i.e. on the isotope ratio, and on the previous assignments for other ices (Section 1.5). The strongest Raman band of each of the four ices lay between 3100 and 3500 cm^{-1} for the H_2O ices and between 2300 and 2600 cm^{-1} for the D_2O ices. This band is assigned to the O-H and O-D stretching vibrations. A series of weaker and sharper peaks was observed between 30 and 325 cm^{-1} for each ice and is assigned to the translational vibrations. A much weaker series of peaks of various widths was observed between 480 and 900 cm^{-1} in the spectra of the H_2O ices and between 350 and 700 cm^{-1} in the spectra of the D_2O ices, and is assigned to the rotational vibrations. Weak scattering that was observed between 1000 and 2000 cm^{-1}, but is not reported here because of its non-reproducibility, is likely due to the H-O-H bending vibrations.

The spectra changed little between 35 and 100 K. The most pronounced effects were small frequency shifts and a sharpening of features as the temperature decreased, so that the weaker features were better defined and the components of the closely-spaced doublets were better resolved at lower temperatures. Therefore the spectrum of each of the ices is summarized for a sample temperature of 35 K, the lowest temperature attained, and the temperature dependence of the frequency and half-width of the well-defined features is given in separate tables, with the other features expected to behave similarly. The relative intensities of the features are tabulated for a crushed sample. The spectra of ice II presented in the figures, however, are largely of uncrushed samples that are believed to be near-single crystals.

The Raman spectra of H_2O and D_2O ice II are shown in Figures 3.3, 3.4 and 3.5, and are summarized for a sample temperature of 35 K in Table 3.2. The corresponding features in the spectra of the two isotopic species are usually readily identified. Exceptions to this are the highest frequency features due to the O-H and O-D stretching vibrations, but these features can be related with the aid of the polarized spectra of near-single crystals, which are reported later in this section.

Seven features are assigned to O-H or O-D stretching vibrations of ice II (Table 3.2). Between 35 and 100 K the frequencies increased by ~0.2%, as shown in Table 3.3 and Figure 3.6, and the half-widths increased by ~30%, as shown in Table 3.3. As a result of this broadening, the bands of the D_2O doublet at 2476/2486 cm^{-1} became unresolvable above ~80 K. The features were underlain by very broad, weak Raman scattering that extended from ~3000 (2220) to ~3700 (2700) cm^{-1} for H_2O (D_2O) ice II at 90 K.

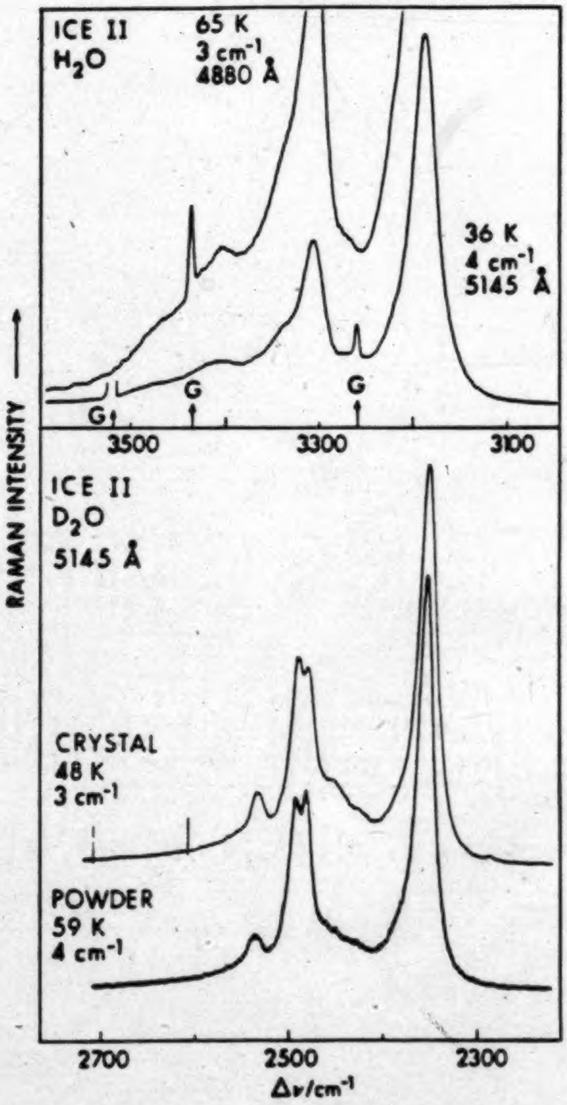

Figure 3.3 Raman spectra of O-H and O-D stretching vibrations of ice II crystals (H_2O and upper curve for D_2O) and powder (lower curve for D_2O) under Y(Z,Z+Y)X scattering geometry. The sample temperature, resolution and exciting line are shown. Features marked G are due to grating ghosts.

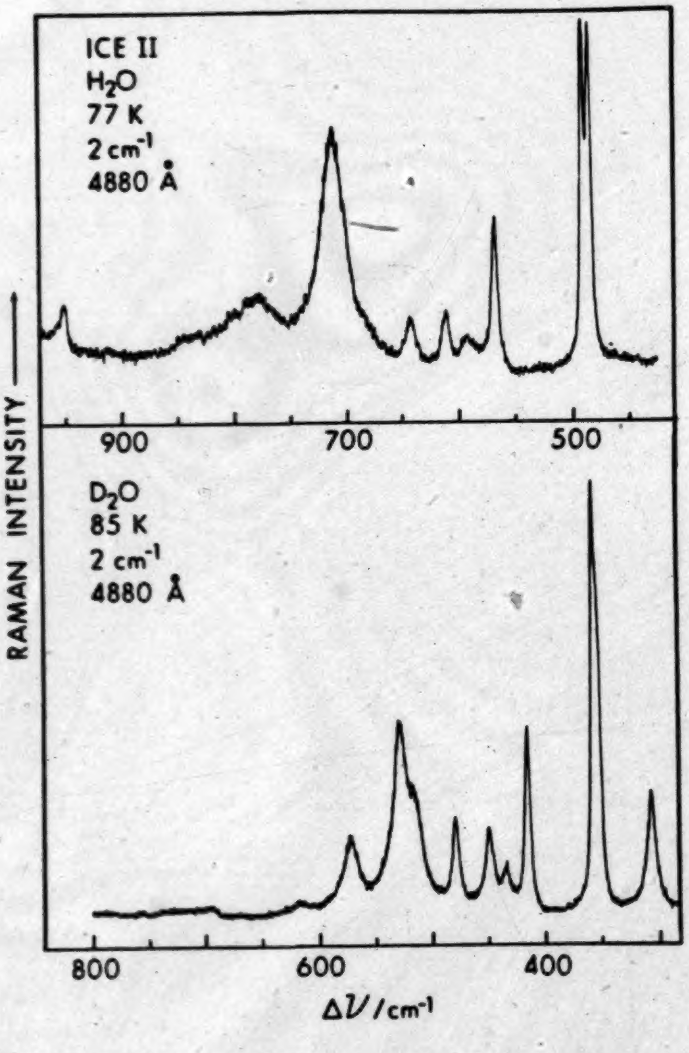

Figure 3.4 Raman spectra of rotational lattice vibrations of ice II crystals under Y(Z,Z+Y)X scattering geometry. The sample temperature, resolution and exciting line are shown.

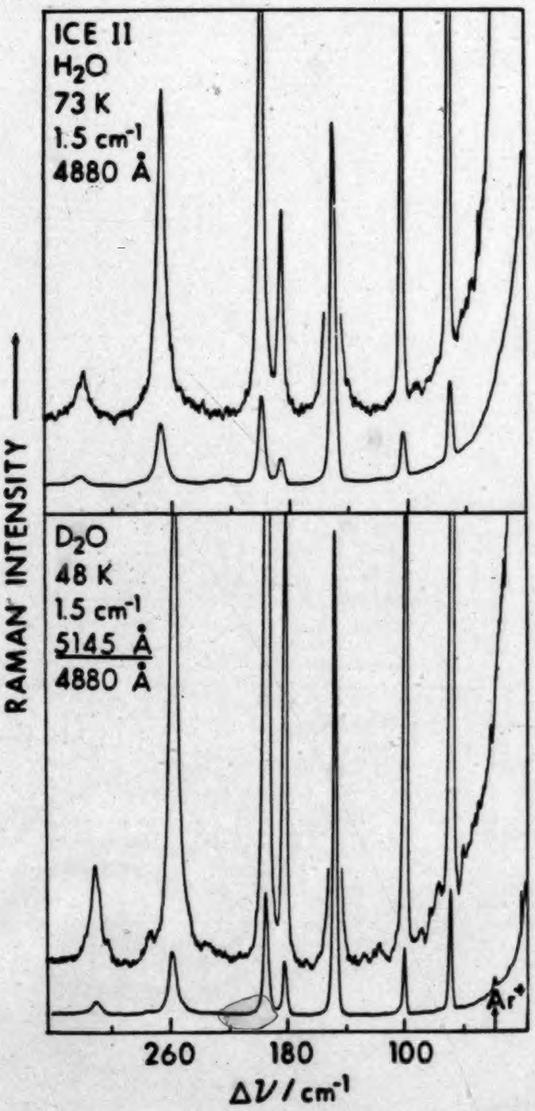

Figure 3.5 Raman spectra of translational lattice vibrations of ice II crystals under Y(Z,Z+Y)X scattering geometry. The sample temperature, resolution and exciting line are shown. The feature marked Ar^+ is due to an argon ion plasma line.

Table 3.2 Features of the Raman scattering by ice II at 35 K.[a]

H_2O				D_2O					
	Intensity[b]				Intensity[b]				
ν/cm^{-1}	height	area	FWHM[c]/cm^{-1}	ν/cm^{-1}	height	area	FWHM[c]/cm^{-1}	ν_{OH}/ν_{OD}	Assignment
3465(10)	10	30	br. sh.					1.369	$\nu_1(A_g) + \nu_9(E_g)$
3400(5)	19		>20	2530.5(1.5)	13		26	1.344(3)	
3340	35	60	sh	2475.9(1)	48	50	<10	1.349(3)	$\nu_2(A_g)$
3306.0(0.4)	64		29	2486.1(1)	46		<10	1.3296(7)	$\nu_{10}(E_g)$
				2445(5)	15		sh		$\nu_{11}(E_g)$
3270	21			2420(5)	11		sh	1.351(3)	$\nu_{12}(E_g)$
~3225	vw		31	2380(5)	<18		sh	1.355(3)	$\nu_3(A_g)$
3188.8(0.4)	100	100		2349.8(0.4)	100	100	19	1.3571(4)	$\nu_4(A_g)$
~950	~10		~5	~695	vw		br	1.37	A_g?
~845?	~5		sh	~620	vw			1.36	$\nu_R(A_g?)$
~775	~15		36±10	~575	15	25	12	1.348	$\nu_R(E_g(+A_g?))$
				544			sh		ν_R
				530.3(0.5)	55	100	12	1.349(2)	$\nu_R(E_g)$
714.8(0.5)	40	85	22	518.8(0.5)	35	50	12	1.378(2)	$\nu_R(A_g)$
685	~15		sh						ν_R
648.1(0.5)	7	5	8	482.9(0.5)	15	15	5	1.342(2)	$\nu_R(A_g)$
617.0(0.5)	13	8	6.7	452.6(0.5)	20	25	7	1.363(3)	$\nu_R(E_g)$
597(0.7)	6	7	7½	438(0.6)	15	10	6½	1.363(4)	$\nu_R(A_g)$
572.6(0.5)	23	15	4½	418.6(0.5)	45	40	4½	1.368(3)	$\nu_R(E_g(+A_g?))$
495.2(0.5)	100	100	4	360.0(0.4)	100	100	7½	1.376(3)	$\nu_R(A_g)$
489.0(0.5)	100		3.7	~357(1.0)				1.370(5)	$\nu_R(E_g)$
322.1(1.0)	<5	10	6½	310(1.0)	5	8	6	1.039(7)	$\nu_T(E_g(+A_g?))$
				272.8(0.4)	<5		6		$\nu_T(A_g)$
268.2(0.3)	20	25	5½	257.1(0.4)	20	35	5½	1.043(3)	$\nu_T(E_g)$
262	5		sh	245	2		sh		ν_T
199.8(0.3)	35	37	2.7	194.6(0.4)	35	50	2½	1.027(4)	$\nu_T(A_g)$
186.5(0.3)	20	20	2½	181.9(0.4)	20	20	2½	1.025(4)	$\nu_T(E_g(+A_g?))$
151.5(0.3)	100	100	2	147.5(0.4)	100	100	1½	1.026(5)	$\nu_T(E_g)$
104(1.0)	20	20	<3	100.2(0.4)	30	20	1½	1.04(1)	$\nu_T(E_g(+A_g?))$
71.6(0.3)	45	35	1.7	69.1(0.4)	50	30	1½	1.035(10)	$\nu_T(E_g)$

---

[a] The uncertainty in the last place is in parentheses.

[b] Intensities for polycrystalline samples, measured as the heights or areas of the features above the scattering to either side of the feature, relative to the strongest peak in each region as 100.

[c] Full width at half-maximum intensity, measured or, for imperfectly resolved bands, estimated. Slit width was 2 cm^{-1} for bands due to O-H or O-D stretching vibrations and rotational vibrations; 1 cm^{-1} for bands due to translational vibrations. Units are cm^{-1}.

Table 3.3

Temperature dependence of the frequencies and half-widths of the well-defined features in the Raman spectra of ice II.

	Frequencies (half-widths)/cm^{-1} [a]				
	10 K[b]	35 K	60 K	80 K	100 K
$\nu_{OH}(H_2O)$	3305.8	3306.0 (29)	3307.0 (32)	3309.1 (39)	3313.0 (48)
	3188.7	3188.8 (31½)	3189.8 (33.7)	3191.9 (38)	3195.4 (42½)
$\nu_R(H_2O)$	715.6	714.8 (22)	713.8	712.6	711.2 (27)
	649.6	648.1 (8)	646.2	644.5	642.7 (11½)
	618.4	617.0 (6.7)	515.0	613.0	610.9 (9½)
	573.4	572.6 (4½)	571.2	569.4	567.4 (7)
	495.8	495.2 (4)	491.5	490.8	489.8 (5½)
	490.0	489.0 (3.7)	487.7	486.2	484.0 (5.7)
$\nu_T(H_2O)$	322.5	322.1 (6½)	321.5	320.8	319.9 (10)
	268.4	268.2 (5½)	267.8	267.4	266.7 (7½)
	199.9	199.8 (2.7)	199.5	199.2	198.9 (4½)
	186.7	186.5 (2½)	186.3	186.0	185.6 (3½)
	152.0	151.5 (2)	150.0	150.3	149.7 (3½)
	~104	~103.8 (<3)	103.4	102.9	102.4 (3)
	71.6	71.6 (1.7)	71.6	71.6	71.6 (2½)
$\nu_{OD}(D_2)$	2484.4	2486.1 (<10)	2487.8	2489.1	2490.4
	2481.3[c]	2481.4[c]	2482.1[c]	2483.6[c]	2486.5[c]
	2474.6	2475.9 (<10)	2477.2	2478.2	2479.3
	2349.6	2349.8 (18½)	2350.6 (20)	2352.3 (21½)	2354.9 (22½)
$\nu_R(D_2O)$	531.0	530.3 (12)	529.5	528.7	527.8 (14)
	519.8	518.8 (12)	517.5	516.4	515.1 (14½)
	484.2	482.9 (5)	481.5	480.2	478.8 (8.7)
	453.7	452.6 (7)	451.3	450.1	448.6 (9)
	419.8	418.6 (4½)	417.4	416.2	414.8 (6½)
	360.7	360.0 (~5½)	358.8	357.7	356.2 (5½?)
$\nu_T(D_2O)$	257.3	257.1 (5½)	257.0	256.9	256.8 (6.7)
	194.9	194.6 (2½)	194.1	193.6	192.9 (4½)
	182.4	181.9 (2½)	181.4	180.8	180.0 (3½)
	148.2	147.5 (1½)	146.9	146.2	145.6 (3)
	100.4	100.2 (1½)	100.2	99.8	99.6 (2)
	69.2	69.1 (1½)	69.0	68.9	68.8 (2)

[a] The frequencies are believed accurate to ±0.5 cm^{-1}, except for the components of the doublet (2476/2486) of D_2O ice II which are believed accurate to ±1 cm^{-1}. The half-widths are believed accurate to ±10%.

[b] Frequencies obtained by extrapolation.

[c] These frequencies are the center of the partially resolved doublet.

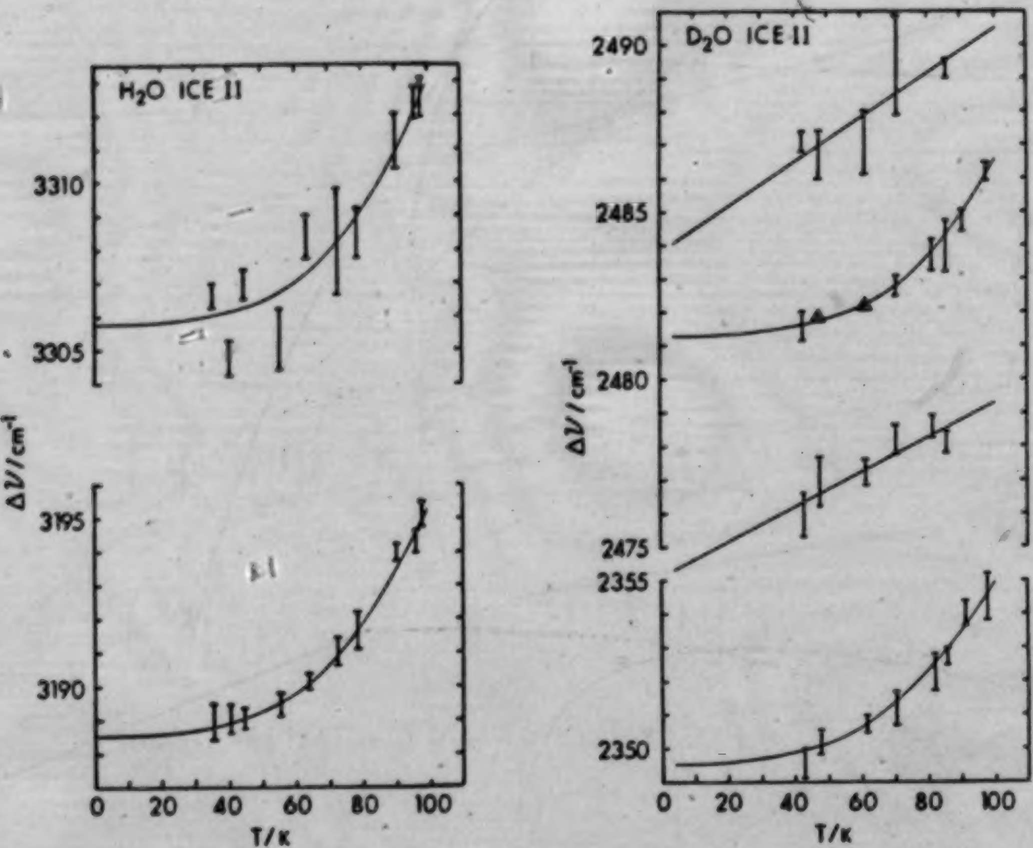

Figure 3.6 The temperature dependence of the frequencies of the well-defined Raman features due to the O-H and O-D stretching vibrations of ice II. The triangles indicate frequencies obtained with single measurements. The error bars represent the average of ten to thirty measurements ± one standard deviation. The D_2O curve at 2481 cm^{-1} at 0 K is for the average frequency of the observed doublet.

Ten features in the Raman spectrum of H_2O ice II and eleven features in the spectrum of D_2O ice II are assigned to rotational vibrations (Table 3.2). Between 35 and 100 K their frequencies decreased by -1% (Table 3.3 and Figure 3.7), and their half-widths increased by ~25% (Table 3.3). The H_2O doublet at 489/495 cm^{-1} was resolved between 35 and 100 K but the corresponding D_2O doublet at 357/360 cm^{-1} was not resolved above 65 K.

Eight features in the spectrum of H_2O ice II and nine features in the spectrum of D_2O ice II are assigned to translational vibrations (Table 3.2). Between 35 and 100 K their frequencies decreased by 0.5 to 1% (Table 3.3 and Figure 3.8) and their half-widths increased by ~50% (Table 3.3). The weak D_2O feature at 272 cm^{-1} was well-defined, particularly in the spectra of single crystals with polarized light, but the corresponding H_2O feature was not observed.

Taylor and Whalley[97] observed four peaks, at 3314, 3194, 261 and 151 cm^{-1}, in the spectrum of H_2O ice II and three peaks, at 2489, 2353 and 146 cm^{-1}, in the spectrum of D_2O ice II, at 77 K. Thus they saw the most intense peaks found in this work, except for those that must have been hidden by a mercury line at 186 cm^{-1}.[97]

The relative intensities of the spectral features of D_2O ice II, and to a lesser extent of H_2O ice II, varied markedly when uncrushed samples were examined; they varied with the sample, with the position of the sample in the beam, and with the polarization of the exciting light. In contrast,

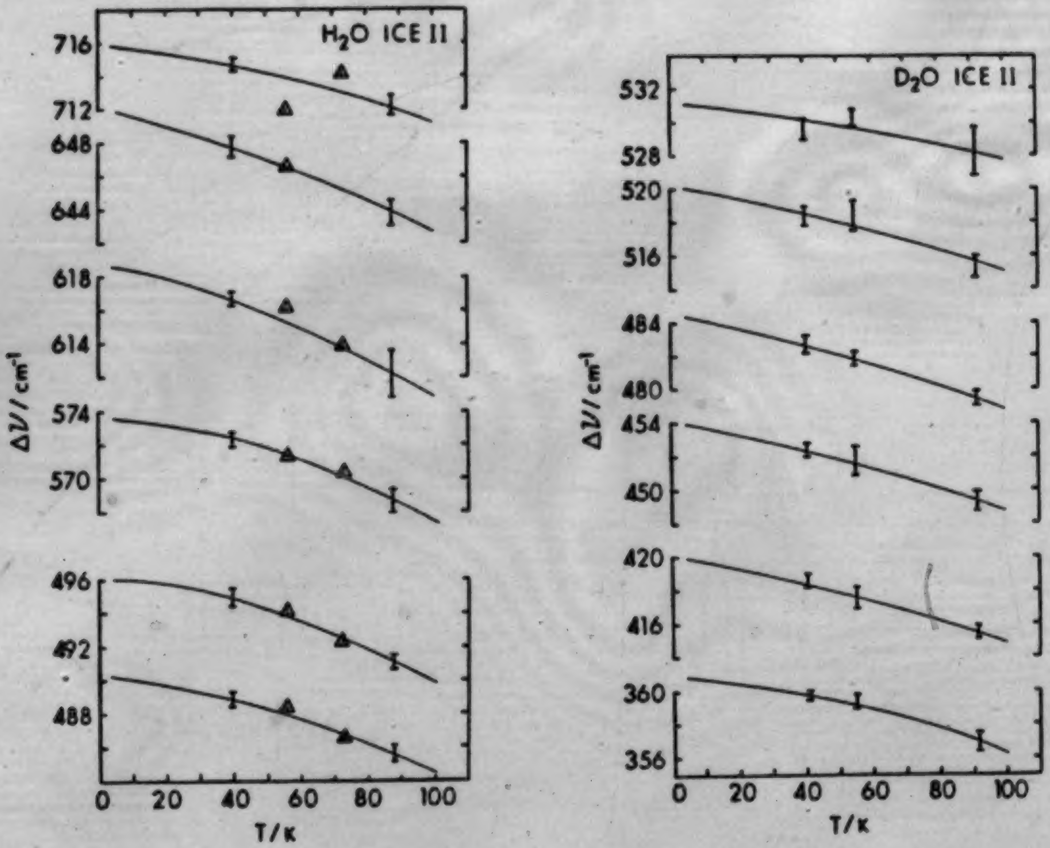

Figure 3.7 The temperature dependence of the frequencies of the well-defined Raman features due to the rotational vibrations of ice II. The triangles indicate frequencies obtained with single measurements. The error bars represent the average of twelve to thirty-two measurements ± one standard deviation.

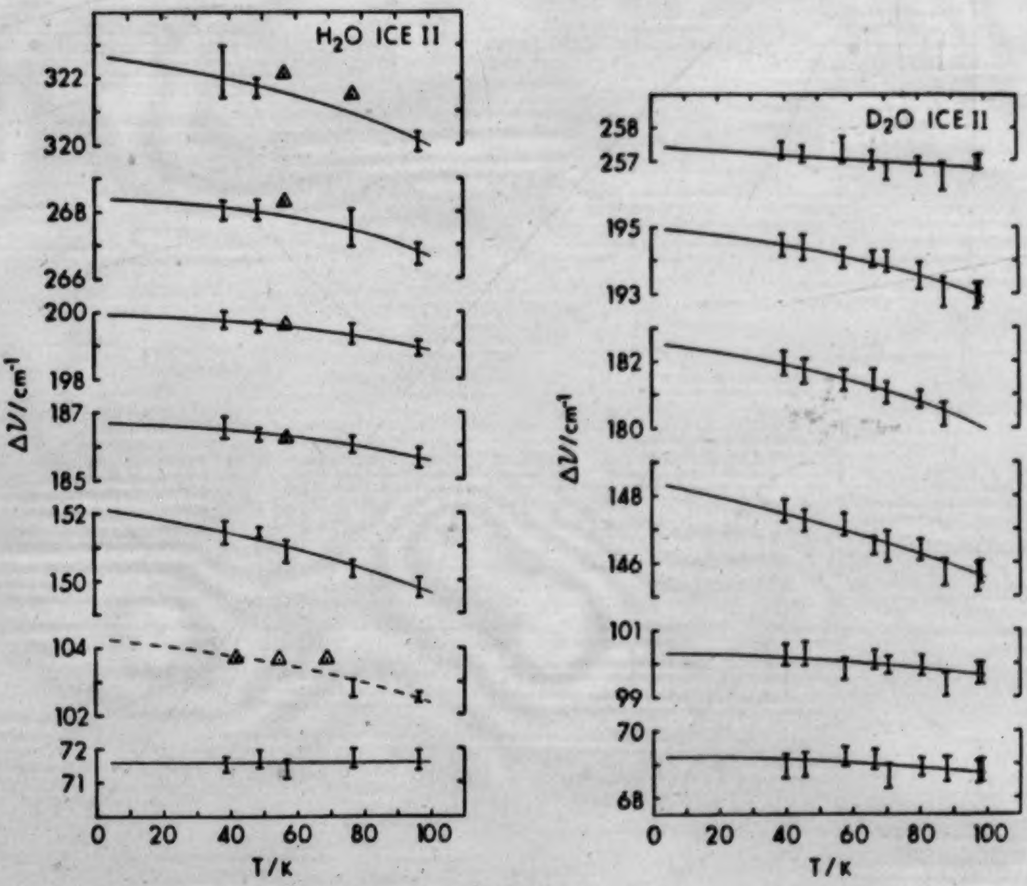

Figure 3.8 The temperature dependence of the frequencies of the well-defined Raman features due to the translational vibrations of ice II. The triangles indicate frequencies obtained with single measurements. The error bars represent the average of five to twenty measurements ± one standard deviation.

the spectra of crushed samples were independent of the sample, its position in the beam and the polarization. Thus the uncrushed samples contained single crystals of sufficient size to yield polarization data. The qualitative usefulness of this can be seen in Figure 3.3, where the shoulders at 2420 and 2445 cm^{-1} are barely visible in the spectrum of the D_2O powder but are well defined in the spectrum of the crystal. The differences between spectra of uncrushed samples recorded with different polarizations of the incident and scattered light were sometimes even more informative, and are reported next. The scattering geometries are denoted by the Porto notation,[121] $Y(\alpha\beta)X$, where Y and X are the propagation directions of the incident and collected light and α and β are their respective polarizations, with reference to orthogonal laboratory axes. In this work α is either Z or X while β is Z or Y, or $Z+Y$ when the polarization of the collected light was not analyzed.

The spectra of D_2O ice II under $Y(Z,Z+Y)X$ and $Y(X,Z+Y)X$ polarizations are shown in Figures 3.9, 3.10 and 3.11 for the O-D stretching vibrations, the rotational vibrations, and the translational vibrations. The spectra in Figures 3.9 and 3.11 were recorded on one sample at one orientation. The sample was unavoidably moved before the spectra of Figure 3.10 were recorded, but was realigned to nearly reproduce the spectra of Figure 3.11 before Figure 3.10 was recorded. Thus the orientation of the sample for Figure 3.10 is believed to be very close to that for Figures 3.9 and 3.11.

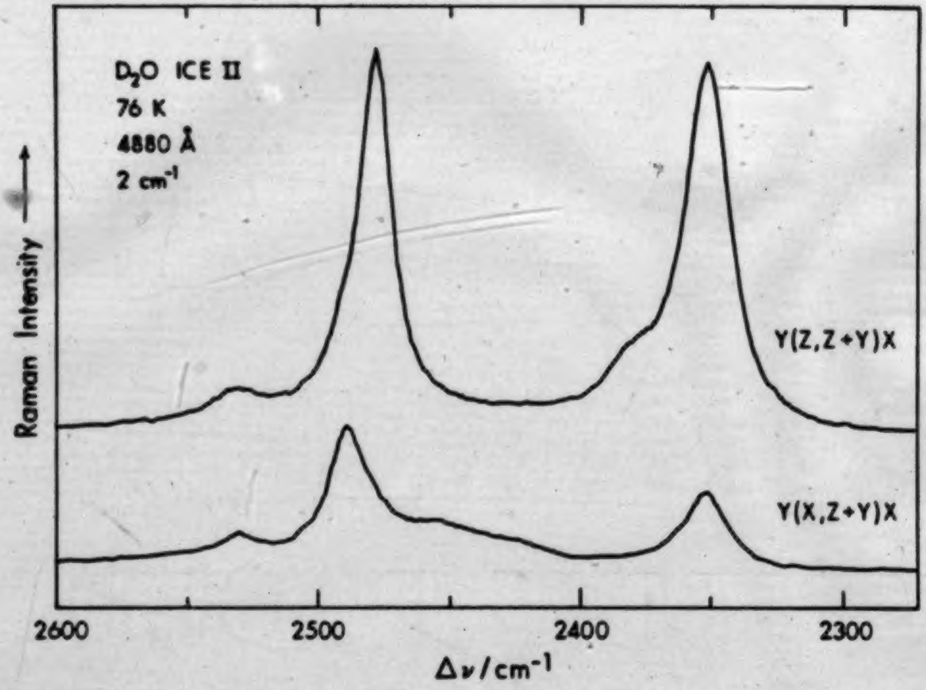

Figure 3.9 Raman spectra of the O-D stretching vibrations of a single crystal of D_2O ice II under different polarizations. The sample temperature, resolution, and exciting wavelength are shown.

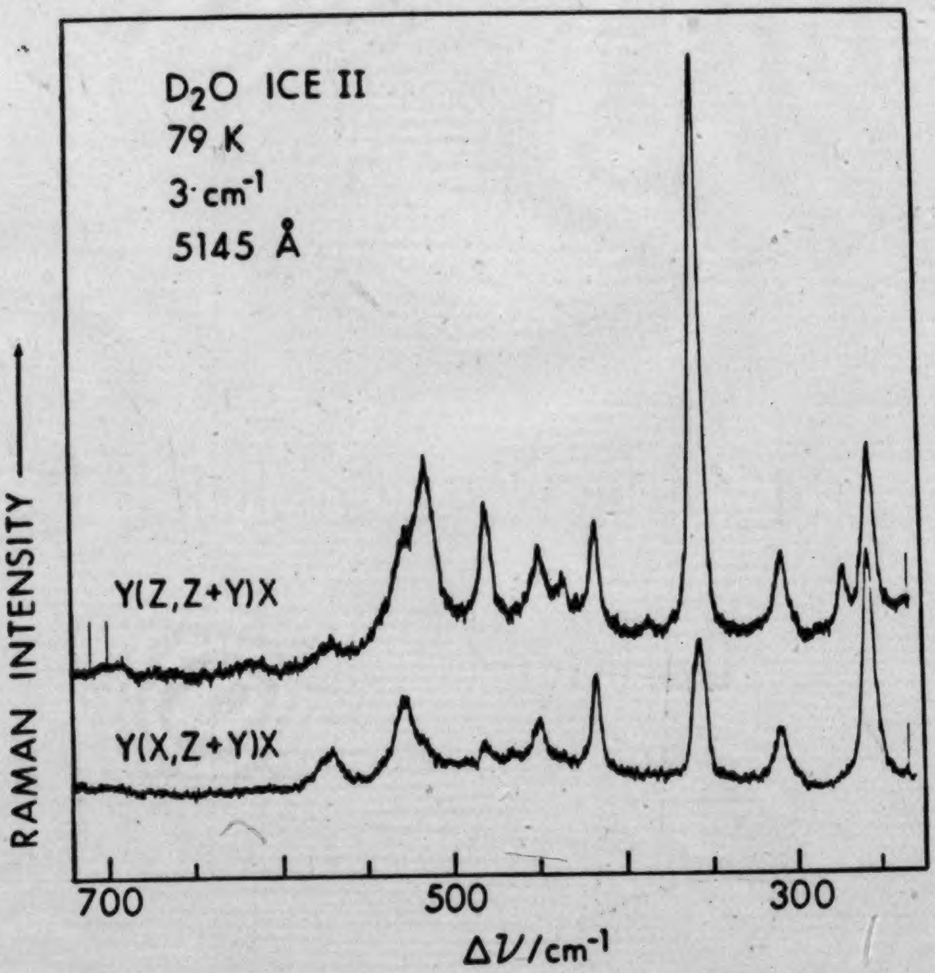

Figure 3.10 Raman spectra of the rotational lattice vibrations of a single crystal of D_2O ice II under different polarizations. The sample temperature, resolution, and exciting wavelength are shown.

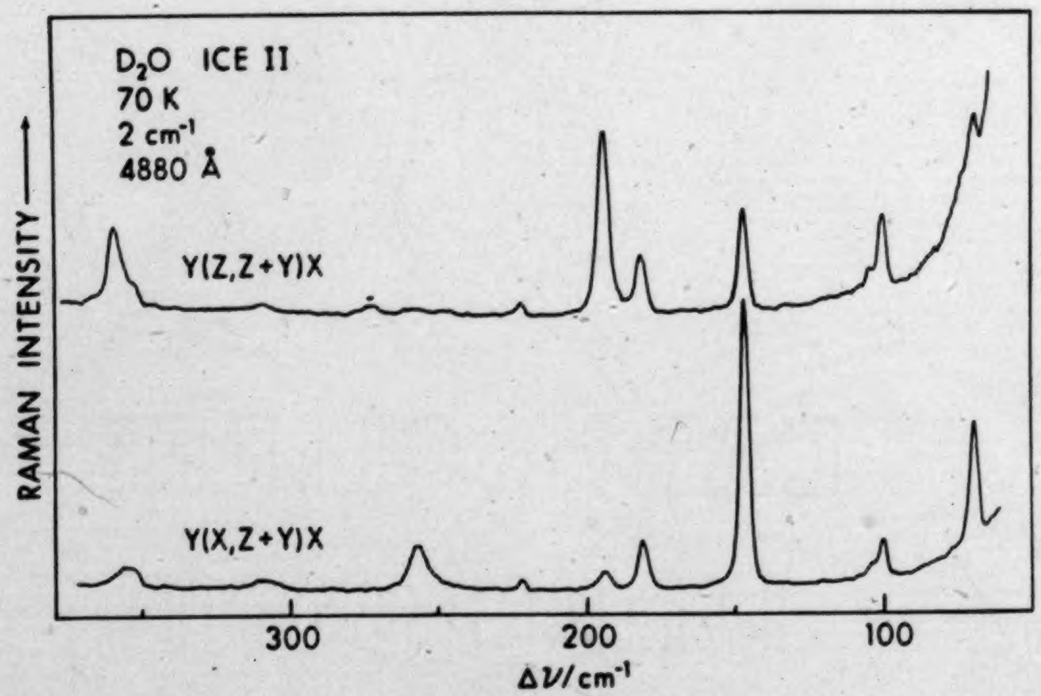

Figure 3.11 Raman spectra of the translational lattice vibrations of a single crystal of D_2O ice II under different polarizations. The sample temperature, resolution, and exciting wavelength are shown.

The sample was clearly a near-single crystal since nearly complete extinction of some spectral peaks was seen when the polarization of the incident light was rotated by 90°. The spectra were not examined with the analyzer and therefore the information that is obtained is potentially ambiguous. Nevertheless, under the two polarizations of the incident light many of the features exhibited one of two behaviours. Thus the features at 2476, 2380, 2350, 519, 483, 438, 360, 273, and 195 cm^{-1} were strongest under Z,Z +Y polarization but weak or nearly extinguished under X,Z +Y. In contrast the features at 2531, 2486, 2445, 2420, 575, 530, 453, 419, 357, 310, 257, 182, 148 and 69 cm^{-1} were either equally intense under all polarizations, or were more intense under X,Z +Y polarizations. The features at 695 and 620 cm^{-1} were too weak to be classified, and the feature at 100 cm^{-1} was only slightly weaker under X,Z + Y and so did not fall into either classification. It should be noted that the shape of the feature at 2531 cm^{-1} is slightly different under the two polarizations (Figure 3.9). The spectra that are presented represent the most definitive polarization data that was obtained for D_2O ice II. All of the other, less definitive, polarization data also indicated the result that is clear from Figures 3.9, 3.10 and 3.11.

The polarized spectra of the O-H stretching vibrations and of the rotational lattice vibrations of H_2O ice II are shown in Figures 3.12 and 3.13. A different sample was used for each region. It is clear from these spectra that the

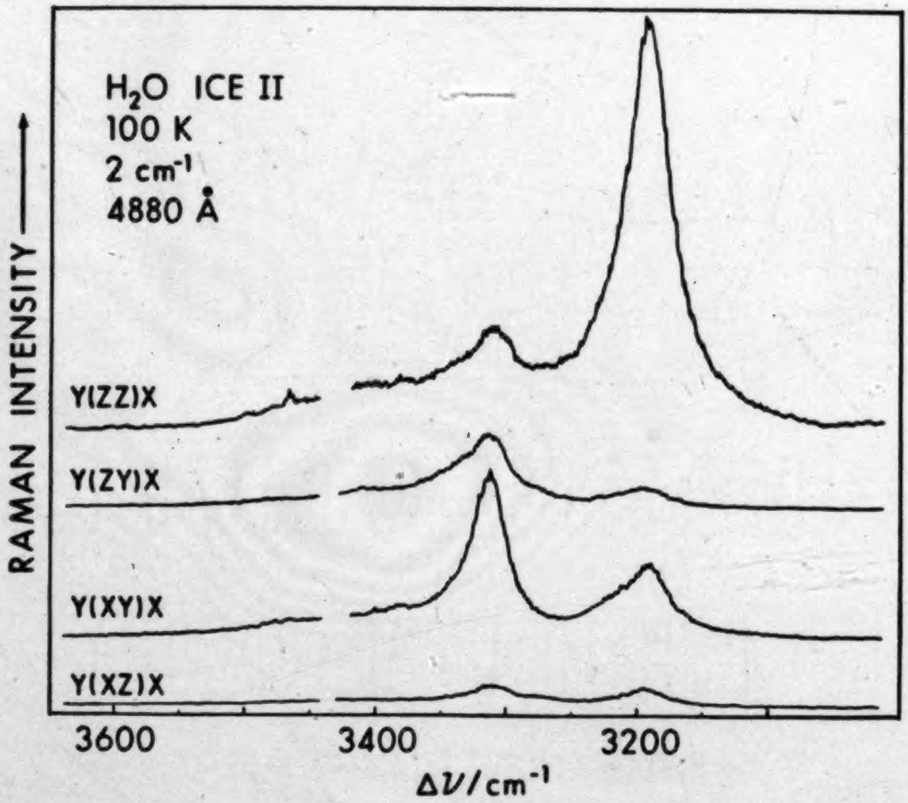

Figure 3.12 Raman spectra of the O-H stretching vibrations of a single crstal of H_2O ice II under different polarizations. The sample temperature, resolution and exciting wavelength are shown.

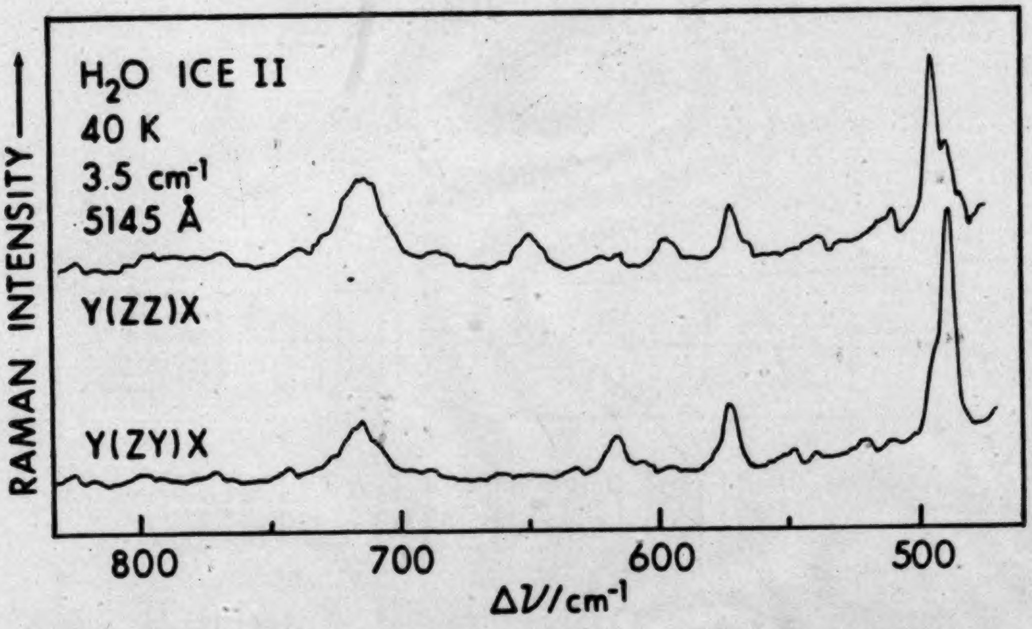

Figure 3.13 Raman spectra of the rotational lattice vibrations of a single crystal of H_2O ice II under different polarizations. The sample temperature, resolution and exciting wavelength are shown.

features at 3189, 648, 597 and 495 cm^{-1} are strongest under parallel (ZZ) polarization, while the features at 617, 489, and, possibly, 573 cm^{-1} are strongest under the perpendicular polarizations. Somewhat ambiguous behaviour was observed for the peak at 3306 cm^{-1} but there seems little doubt that it is perpendicularly polarized. No useful polarization data were obtained for the translational lattice vibrations of H_2O ice II.

The polarized spectra of ice II were often of marginal quality, mainly because the conditions of good extinction, which indicated that the sample was a near-single crystal, were met largely by chance. Definitive polarized Raman spectra would be recorded with an analyzer, and the orientation of the crystal axes with respect to the laboratory axes would be known. The spectra would also be corrected for the convergence error,[90] which causes light of the wrong polarization to appear in a spectrum and is caused by the focussing of the laser beam on the sample and by the finite collection aperture. Clearly the spectra of Figures 3.9 to 3.13 are not definitive, but they are the best that were recorded and a good deal of useful information can still be obtained from them.

The Raman spectra of H_2O and D_2O ice IX are shown in Figures 3.14, 3.15, and 3.16, and are summarized for 35 K in Table 3.4. The corresponding features in the spectra of H_2O and D_2O ice IX are readily identified in all three regions of the spectra. Unlike the case of ice II, the relative

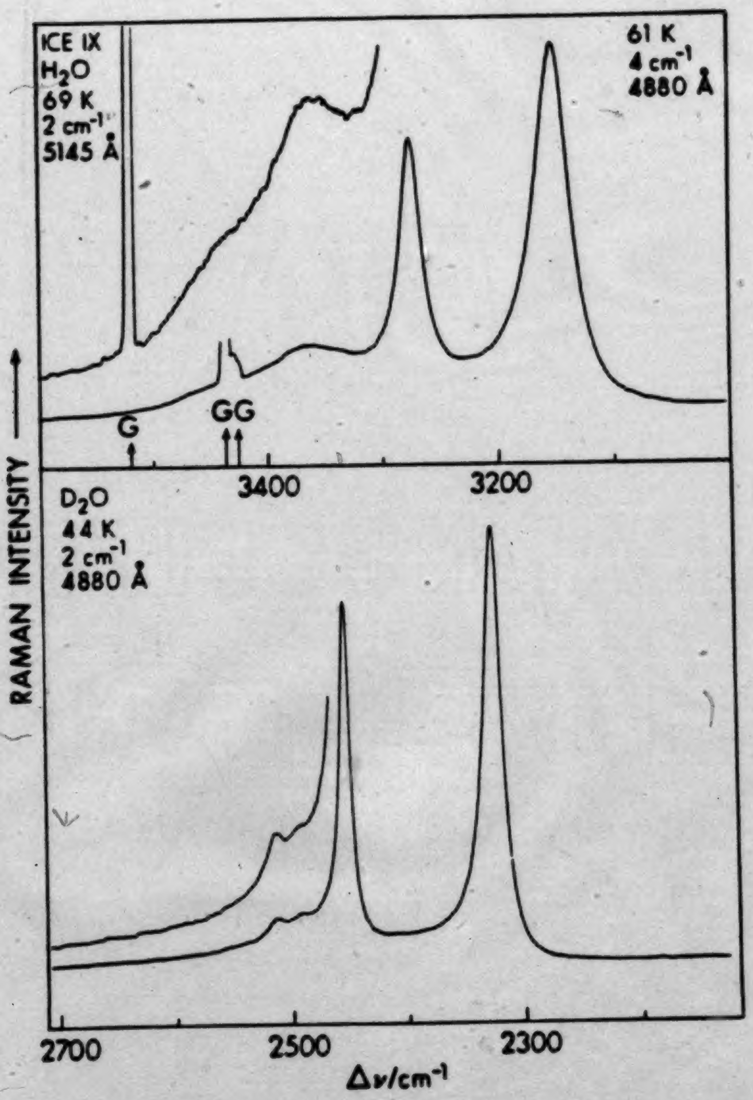

Figure 3.14 Raman spectra of the O-H and O-D stretching vibrations of polycrystalline ice IX under Y(Z,Z+Y)X scattering geometry. The sample temperature, resolution, and exciting wavelength are shown. Features marked G are due to grating ghosts.

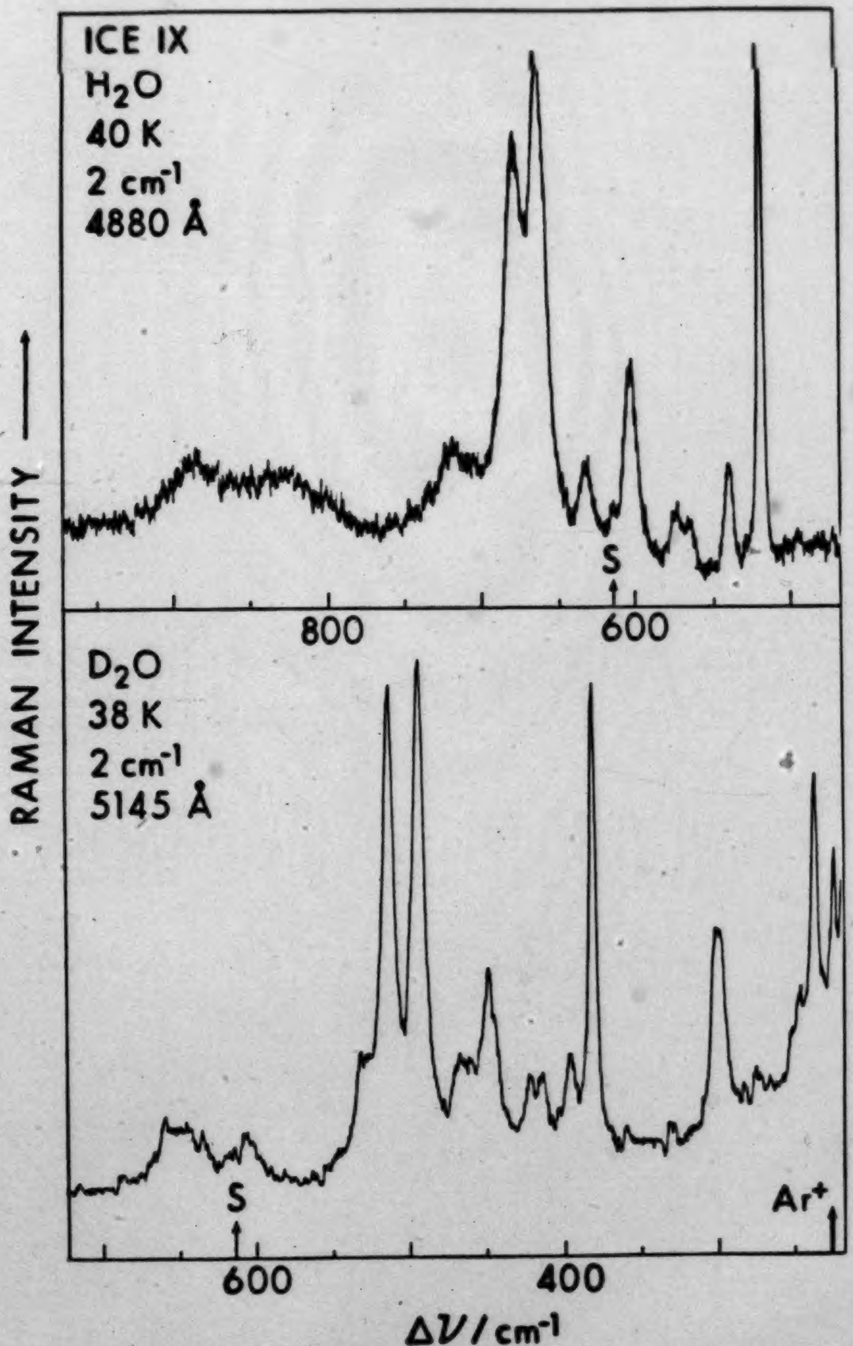

Figure 3.15 Raman spectra of the rotational vibrations of polycrystalline ice IX under Y(Z,Z+Y)X scattering geometry. The sample temperature, resolution, and exciting wavelength are shown. Features marked S are spurious.

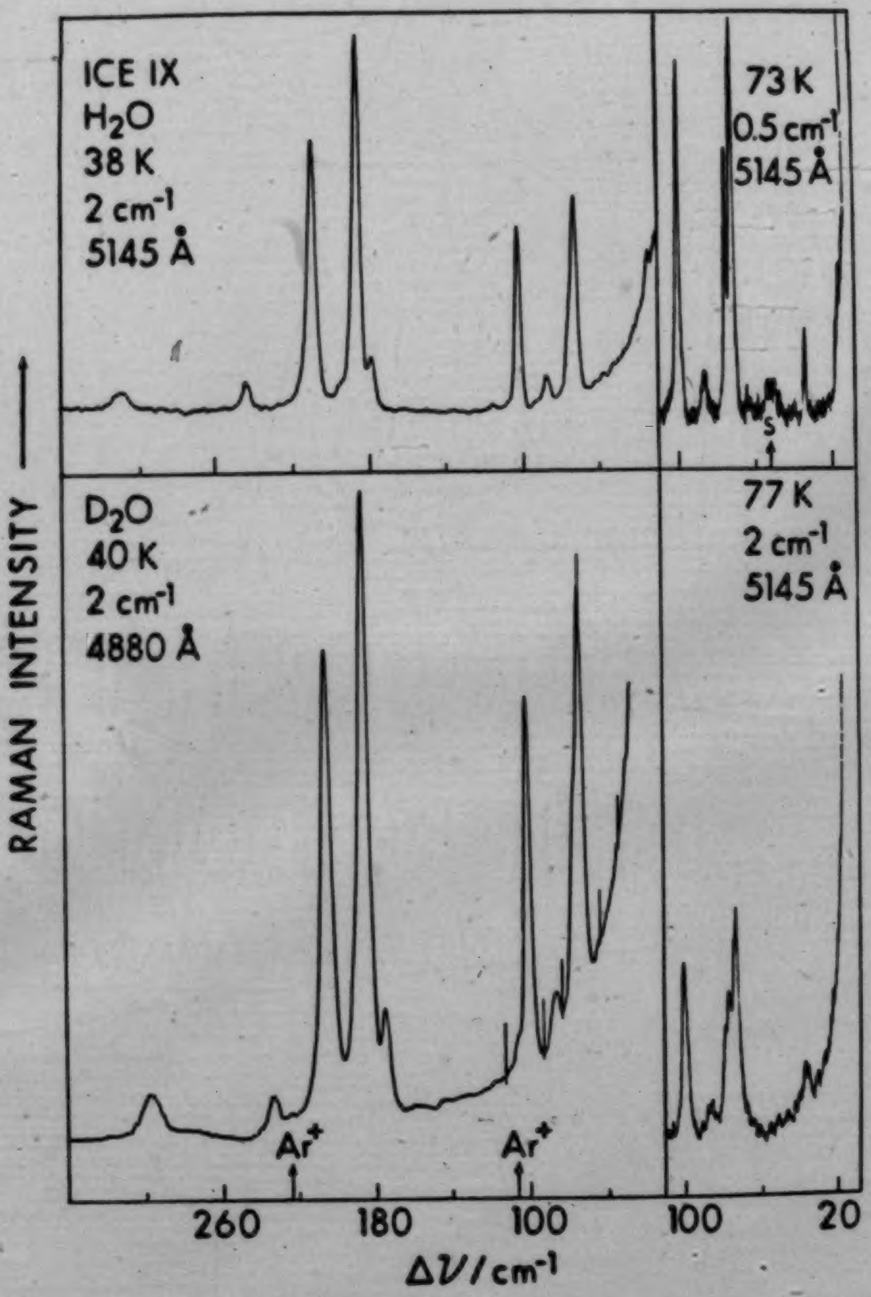

Figure 3.16 Raman spectra of the translational vibrations of polycrystalline ice IX under Y(Z,Z+Y)X scattering geometry. The sample temperature, resolution, and exciting wavelength are shown. Features marked S are spurious.

Table 3.4

Features of the Raman scattering by ice IX at 35 K.[a]

H_2O				D_2O					
	Intensity[b]				Intensity[b]				
ν/cm^{-1}	heights	area	FWHM[c]/cm^{-1}	ν/cm^{-1}	height	area	FWHM[c]/cm^{-1}	ν_{OH}/ν_{OD}	Assignment
3440(5)	10	40	br. sh.	2513(1)	9		>15	1.369(3)	$\nu_1(A_1),\nu_7(B_1),$ $\nu_{10}(B_2),\nu_{13}(E)$
3360(5)	17		>40	2492(3)	9		sh	1.348(4)	$\nu_{14}(E)$
3274.0(0.4)	70	50	20½	2454.0(0.4)	85	50	10	1.3342(4)	$\nu_8(B_1),\nu_{11}(B_2),$ $\nu_{15}(E),\nu_{16}(E)$
3151.2(0.4)	100	100	31	2325.4(0.4)	100	100	17	1.3552(4)	$\nu_3(A_1)$
885	15	25	21	650	15	55	35	1.362	
820	15	50	45	605	10	25	22	1.355	$\nu_R(E)$
717(1.5)	15	40	30	531	20	25	9½	1.350(5)	ν_R
679.7(0.8)	80	95	16	510.3(0.3)	95	105	9½	1.332(2)	ν_R
664.7(0.7)	100	100	13	490.9(0.3)	100	100	8	1.354(2)	ν_R(E?)
632(1.5)	15	10	9½	462(3)	10	10	10±4	1.37(1)	ν_R
604.4(0.5)	35	30	10½	444.9(0.6)	35	40	10	1.358(3)	$\nu_R(E)$
574.6(0.4)	12	8	8½	418.5(0.6)	15	10	6½	1.373(3)	ν_R
565(1)	12	8	8½	411.0(0.6)	15	10	6½	1.375(4)	$\nu_R(E)$
539.8(0.3)	20	10	6½	392(1.5)	20	20	8	1.377(6)	$\nu_R(E)$
519.2(0.4)	100	35	5	378.4(0.5)	100	55	4½	1.372(3)	ν_R
310(1)	5	10	10	297(1)	5	13	10	1.044(7)	$\nu_T(E)$
245(0.4)	10	15	5½	234.3(0.5)	7	6	3	1.045(4)	ν_T
209.6(0.3)	65	80	3½	204.2(0.3)	80	80	3½	1.026(3)	$\nu_T(E)$
195.4(0.3)	10		sh	189.6(0.3)	20		sh	1.031(3)	ν_T
186.8(0.3)	100	100	3½	184.2(0.3)	100	100	3½	1.014(3)	ν_T
179(0.3)	20	13	2½	173.6(0.3)	15	12	2½	1.031(4)	ν_T
103.0(0.3)	90	45	1½	99.0(0.3)	60	37	2	1.040(6)	ν_T
87.0(0.3)	15	10	3	84.9(0.3)	10	10	4	1.025(7)	ν_T
76.6(0.3)	45	18	1½	74.4(0.3)	30	20	2	1.030(8)	ν_T
73.5(0.4)	90	50	2	71.0(0.3)	65	45	2½	1.035(10)	$\nu_T(E)$
35.6(0.4)	20	8	1½	34.3(0.3)	15	10	3?	1.04(2)	ν_T

[a] The uncertainty in the last place is in parentheses.

[b] Intensities for polycrystalline samples, measured as the heights or areas of the features above the scattering to either side of the feature, relative to the strongest peak in each region as 100.

[c] Full width at half-maximum intensity, measured or, for imperfectly resolved bands, estimated. Slit width was 2 cm^{-1} for bands due to O-H or O-D stretching vibrations and rotational vibrations; 1 cm^{-1} for bands due to translational vibrations. Units are cm^{-1}.

intensities in the spectra of ice IX were virtually independent of the sample orientation and the polarization of the laser so the samples of ice IX were clearly polycrystalline.

Four features are assigned to O-H or O-D stretching vibrations (Table 3.4). Between 35 and 100 K their frequencies increased by ~0.2% as shown in Table 3.5 and Figure 3.17 for the two prominent features, whose half-widths increased by ~30 to 50% (Table 3.5). The features were underlain by weak Raman scattering that extended from 3000 (2220) to 3650 (2850) cm^{-1} for H_2O (D_2O) ice IX at 90 K.

Eleven features are assigned to rotational vibrations (Table 3.4). Between 35 and 100 K, the frequencies of the main features decreased by 1% (Figures 3.18 and Table 3.5). The weak H_2O doublet at 565/575 cm^{-1} usually appeared as a single broad band above 50 K, while the corresponding D_2O doublet at 411/419 cm^{-1} (Figure 3.15) was split even at 90 K. Similarly the H_2O doublet at 664/679 cm^{-1} was barely resolved above 60 K, while the corresponding D_2O doublet at 491/510 cm^{-1} was well resolved even at 100 K.

Eleven features are assigned to the translational vibrations of ice IX (Table 3.4). Between 35 and 100 K, their frequencies decreased by ~1% (Table 3.5 and Figure 3.19) and their half-widths increased by ~30% (Table 3.5). The splitting of the doublet at 74/77 cm^{-1} (71/74 cm^{-1} for the D_2O) was strongly dependent on the spectral slit width, with the features being unresolved with a slit width of 2 cm^{-1} but resolved with slit widths of 1 cm^{-1} or less.

Table 3.5

Temperature dependence of the frequencies and half-widths of the well-defined features in the Raman spectra of ice IX.

	Frequencies (half-widths) /cm^{-1} [a]				
	10 K[b]	35 K	60 K	80 K	100 K
$\nu_{OH}(H_2O)$	3273.9	3274.0 (20½)	3275.2 (22.7)	3277.5 (26.7)	3280.9 (31)
	3149.9	3151.2 (31)	3152.7 (33)	3155.9 (37½)	3161.0 (42)
$\nu_R(H_2O)$	681.4	679.7 (16)	677.1	674.6	672 (18)
	666.1	664.7 (13)	662.8	660.4	657 (17)
	605.9	604.4 (10)	601.7	599.0	595 (12½)
	520.0	519.2 (4½)	518.0	516.0	512.5 (6)
$\nu_T(H_2O)$	210.0	209.6 (3½)	209.1	208.4	207.3 (6)
	187.2	186.8 (3½)	186.2	185.6	184.7 (5)
	103.5	103.0 (1½)	102.3	101.7	100.8 (2½)
	76.7	76.6 (1½)	76.4	76.2	75.9 (2)
	73.5	73.5 (2)	73.3	73.1	72.8 (2½)
$\nu_{OD}(D_2O)$	2453.7	2454.0 (10)	2454.9 (11)	2456.1 (12½)	2457.6 (14)
	2325.0	2325.4 (17)	2326.8 (18½)	2328.7 (20)	2330.9 (22)
$\nu_R(D_2O)$	510.8	510.3 (9½)	509.2	507.5	504.3 (15)
	492.2	490.9 (8)	489.2	487.8	485.8 (13½)
	445.9	444.9 (9½)	443.7	442.5	441.0 (12)
	378.8	378.4 (4½)	377.7	376.7	374.9 (6.7)
$\nu_TD_2O)$	234.5	234.3 (3)	233.7	232.7	230.5 (4½)
	204.6	204.2 (3½)	203.7	203.0	202.0 (4½)
	184.5	184.2 (3½)	183.8	183.2	182.4 (4½)
	99.2	99.0 (2)	98.6	98.0	97.0 (2½)
	74.5	74.4 (2)	74.2	73.9	73.6 (2½)
	71.1	71.0 (2½)	70.9	70.6	70.2 (3)

[a] The frequencies are believed accurate to ±0.5 cm^{-1}. The half-widths are believed accurate to ±10%.

[b] Frequencies obtained by extrapolation.

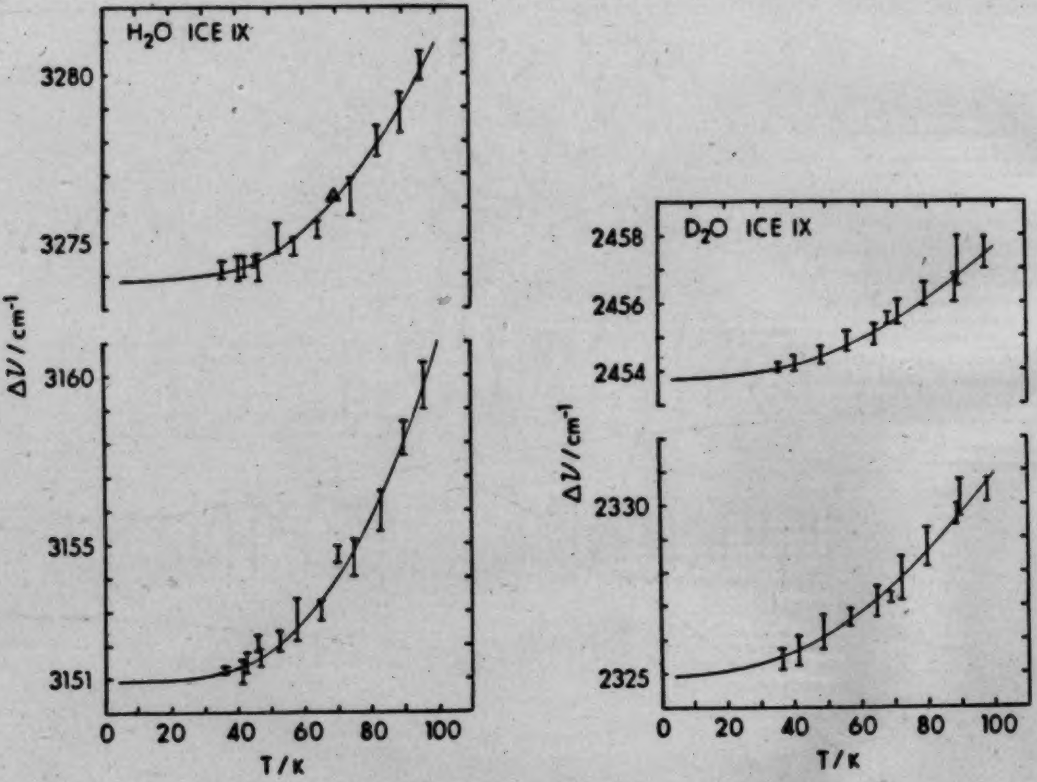

Figure 3.17 Temperature dependence of the frequencies of the well-defined Raman features due to the O-H and O-D stretching vibrations of ice IX. The triangle indicates a frequency obtained with a single measurement. The error bars represent the average of six to twenty-four measurements ± one standard deviation.

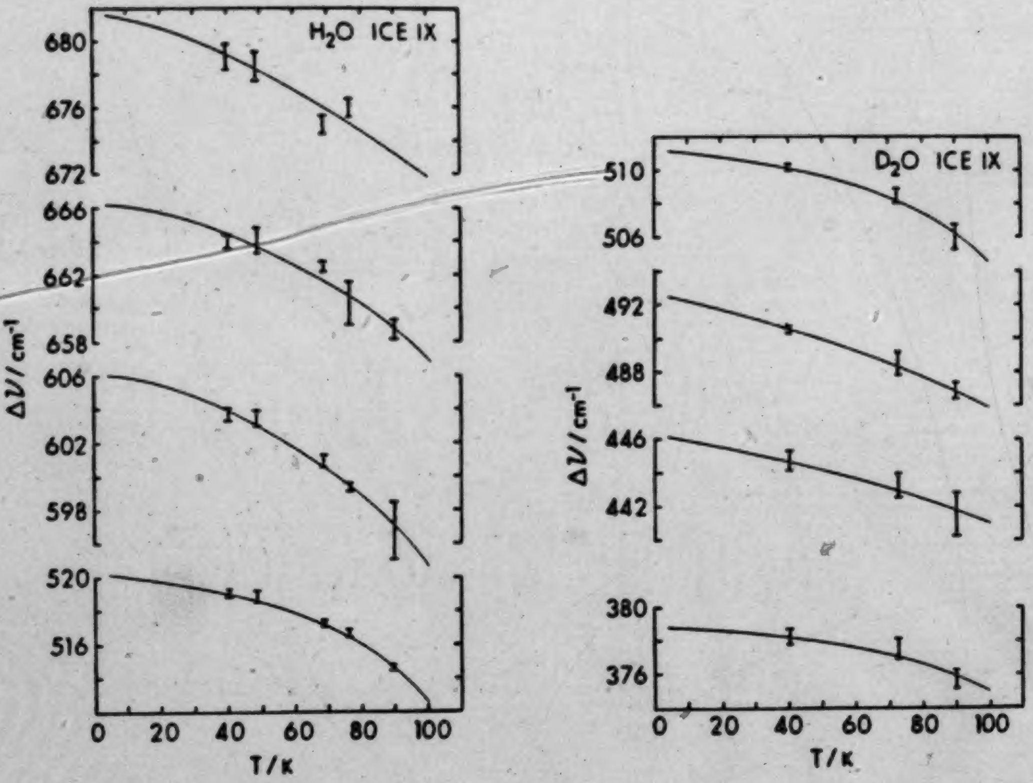

Figure 3.18 Temperature dependence of the frequencies of the well-defined Raman features due to the rotational vibrations of ice IX. The error bars represent the average of nine to twelve measurements ± one standard deviation.

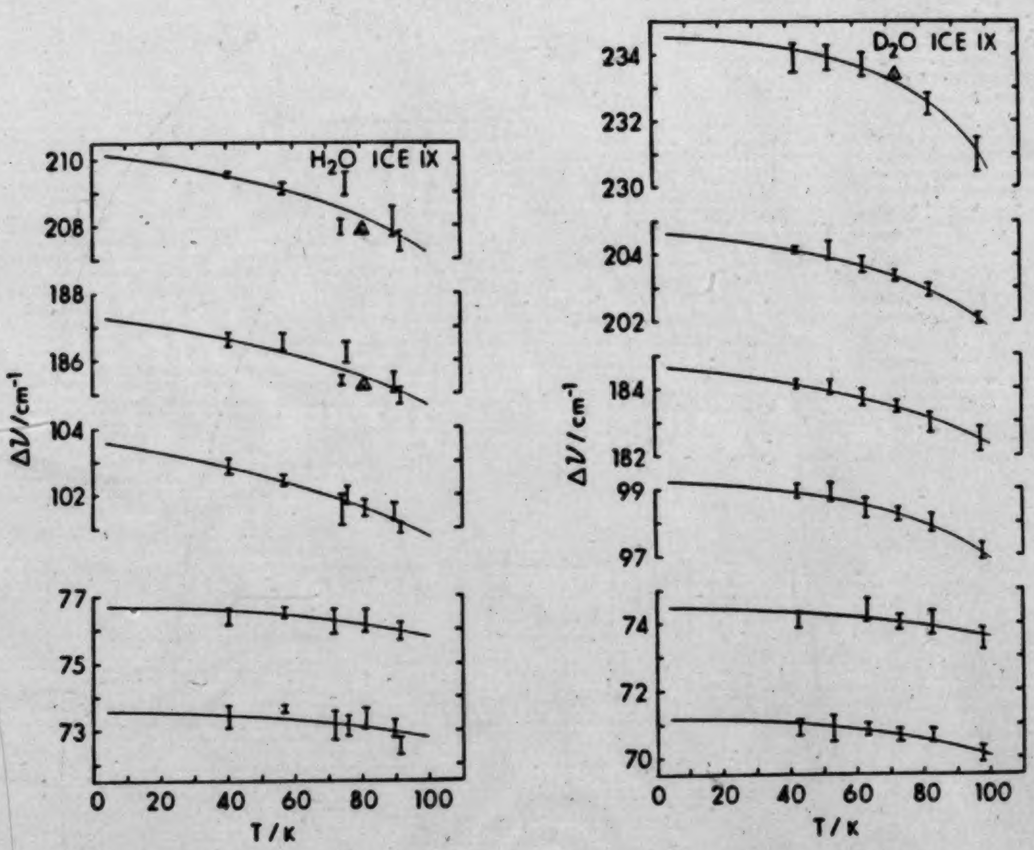

Figure 3.19 Temperature dependence of the frequencies of the well-defined Raman features due to the translational vibrations of ice IX. A triangle indicates a frequency obtained with a single measurement. The error bars represent the average of six to twenty measurements ± one standard deviation.

Taylor and Whalley[97] observed two peaks, at 3281 and 3159 cm^{-1}, in the spectrum of H_2O ice IX and three peaks, at 2457, 2327 and 166 cm^{-1}, in the spectrum of D_2O ice IX, at 77 K. Clearly the strongest peak due to the translational vibrations (Table 3.4), at 183 cm^{-1} at 80 K (Table 3.5), must have been masked in their spectra by the mercury emission at 186 cm^{-1}.[97] Their peak reported at 166 cm^{-1} [97] must have been an artifact of this mercury emission or of the noise on their spectrum.

All of the features that are reported here for ice II and ice IX (Tables 3.2 and 3.4) were observed at all temperatures between 35 and 100 K, and there is no doubt of their existence. Other, very weak features may exist, particularly due to rotational lattice vibrations which scatter weakly and typically had low signal-to-noise ratios. Any undetected feature due to translational vibrations must either be unresolved at 35 K or must have a height that is less than 0.01 of the height of the peak at 152 cm^{-1} of H_2O ice II or at 187 cm^{-1} of H_2O ice IX, or less than 0.02 of the height of the corresponding peak of the D_2O ices.

The intensity of the scattering in each region of the Raman spectra of ices II and IX relative to that of the O-H or O-D stretching region, corrected for the instrument response, is given in Table 3.6. The relative areas are independent of temperature between 40 and 100 K within experimental error. Further, the intensity of scattering by the translational lattice vibrations and by the rotational

Table 3.6

Relative intensities of the Raman scattering due to the O-H or O-D stretching vibrations, the translational vibrations and the rotational vibrations of ice II.

	Relative areas			Relative heights (peak frequency/cm^{-1})		
	$\nu_{OH/OD}$	ν_T	ν_R	$\nu_{OH/OD}$	ν_T	ν_R
H_2O ice II	100	7.3	3.0	100 (3189)	50 (152)	8.9 (492)
D_2O ice II	100	7.3	3.3	100 (2350)	30 (148)	4.4 (358)
H_2O ice IX	100	7.5	2.3	100 (3151)	39 (187)	4.1 (519)
D_2O ice IX	100	8.3	3.2	100 (2325)	22 (184)	2.4 (378)

lattice vibrations is 7.6 ± 1.2 % and 3.0 ± 0.7 % respectively of that of the O-H or O-D stretching vibrations for all four ices.

The relative heights of the strongest features in each region are also given in Table 3.6, since these are more easily compared visually than are relative areas. It must be noted, however, that it is the area and not the height of a feature that is of theoretical significance.

The baselines used to obtain the intensities reported in Table 3.2, 3.4 and 3.6 were found by interpolation of the scattering to either side of the overall band of overlapping features. This was sometimes clearly unsatisfactory for the rotational vibrations because a broad and non-reproducible band frequently underlaid the sharper Raman peaks and shoulders. Therefore the uncertainty in the relative areas is ~15% for the O-H or O-D stretching vibrations and the translational vibrations, but is ~20% for the rotational vibrations.

CHAPTER FOUR

DISCUSSION OF THE RAMAN SPECTRA OF THE O-H AND O-D STRETCHING VIBRATIONS OF ICE II AND ICE IX

4.1 Introduction

The Raman spectra of the O-H and O-D stretching vibrations of ice II and ice IX were reported in Chapter Three. Seven features were observed for ice II and four for ice IX, and there was a weak, broad scattering underlying the prominent features in each of the spectra. The relative intensities of the peaks and shoulders are independent of temperature between 35 and 100 K, which supports the assignment of these features to fundamental vibrations.

In Section 4.2 the Raman spectra of the O-D stretching vibrations of the D_2O ice II and IX are assigned from the results of the normal coordinate analyses[1,2] that explained[1,2] the infrared spectra of these ices, and the polarized spectra of D_2O ice II are considered in light of this assignment. The spectra of the H_2O ices II and IX are assigned by analogy. The Raman intensities of the O-D stretching vibrations have been calculated under the bond polarizability approximation and are reported in Section 4.3. The force fields used in the normal coordinate analyses were altered to correct slight frequency mismatches, and the results of these attempts are discussed in Section 4.4. The effects of disorder, longitudinal optic-transverse optic splitting, and Fermi resonance on the Raman spectra of ices II and IX are discussed in

Section 4.5.

4.2 Assignment of the Raman Spectra of the O-H and O-D Stretching Vibrations of Ice II and Ice IX

Bertie and Bates[1,2] used normal coordinate and bond moment calculations to interpret the infrared spectra of the O-D stretching vibrations of deuterated ice II and ice IX (Section 1.5). The normal coordinates were described in terms of the symmetric, ν_1, and antisymmetric, ν_3, O-D stretching displacements of the twelve water molecules in the unit cell of each ice, and the force fields were constructed using O-D stretching force constants, intramolecular O-D,O-D' interaction constants, and nearest neighbour intermolecular O-D•••O'-D' interaction constants. The force fields that were used for each ice differed slightly in the interaction constants. The frequencies and eigenvectors were calculated using the Wilson GF method,[56] as implemented in the computer program VSEC,[122] and the relative absorption intensities of the vibrations were calculated under the bond moment approximation,[123],[124] through the program DMUDQ written by J.E. Bertie. The details of these calculations are found elsewhere.[1,2]

The vibrational representation of the O-D stretching vibrations of ice II is $4A_g + 4A_u + 4E_g + 4E_u$ (Table 1.3), with the A_u and E_u vibrations infrared active and the A_g and E_g vibrations Raman active. The vibrational frequencies, relative absorption intensities, and eigenvectors that were calculated [1,2] for D_2O ice II using two force fields are reproduced in Table 4.1 and the experimental and calculated spectra are compared in Figure 4.1. The effect of the interaction constants of the force field on the calculated infrared spectrum is significant (Table 4.1 and Figure 4.1), but the results demonstrate that the spectrum of ice II is characteristic of the structure and not of the force field. This result was also found[1,2] for the spectrum of ice IX. The intensity distribution and features of the spectrum of D_2O ice II are well described by the calculated spectrum, with the most serious discrepancy being the calculation near the observed minimum at ~2400 cm^{-1} of an intense absorption which is believed[1,2] to contribute to the peak at ~2418 cm^{-1}.

The Raman spectrum of D_2O ice II, which was not well known when the normal coordinate analysis was published,[2] must also be explained by the calculations. The seven features that were observed in the Raman spectrum can be readily assigned as in Table 3.2 from the calculated[1,2] frequencies (Table 4.1). From the eigenvectors (Table 4.1), it can be seen that $\nu_4(A_g)$, the vibration to which the intense lowest-frequency peak is assigned (Table 3.2), is the in-phase symmetric O-D stretching vibration of ice II, an assignment that is consistent (Section 1.5) with that of the intense lowest-frequency peak in the Raman spectra of ice Ih,[81,84] ice VIII,[101] and amorphous ice.[125] This assignment of the Raman spectrum (Table 3.2) is supported by the polarization data for D_2O ice II (Figure 3.9, p. 126) in which the

Table 4.1

The calculated frequencies, infrared and Raman relative intensities, and assignments, of the $\underline{k} = 0$, O-D stretching vibrations of ice II at 10 K.

	Force Field A[a]			Force Field B[b]			
Mode	ν/cm^{-1}	Raman[c] intensity	Infrared[d] intensity	ν/cm^{-1}	Raman[c] intensity	Infrared[d] intensity	Assignment[e]
$\nu_1(A_g)$	2534	4	0	2527	12	0	$-0.1s_1+0.2s_2+0.4as_1-0.6as_2$
$\nu_2(A_g)$	2487	17	0	2483	18	0	$0.6as_1+0.4as_2$
$\nu_3(A_g)$	2398	6	0	2399	11	0	$0.5s_1-0.5s_2+0.1as_1-0.3as_2$
$\nu_4(A_g)$	2360	100	0	2350	100	0	$0.5s_1+0.5s_2$
$\nu_5(A_u)$	2544	0	15	2568	0	8	$0.5s_1+0.2s_2+0.4as_1-0.4as_2$
$\nu_6(A_u)$	2522	0	9	2517	0	11	$0.3s_1+0.5s_2-0.4as_1+0.3as_2$
$\nu_7(A_u)$	2487	0	2	2474	0	0.2	$0.1s_1-0.1s_2+0.5as_1+0.6as_2$
$\nu_8(A_u)$	2397	0	48	2410	0	55	$-0.5s_1+0.5s_2+0.3as_1-0.1as_2$
$\nu_9(E_g)$	2546	10	0	2554	9	0	$0.2s_1-0.2s_2+0.2as_1-0.2as_2$
$\nu_{10}(E_g)$	2504	38	0	2494	40	0	$0.1s_1-0.1s_2+0.2as_1+0.2as_2$
$\nu_{11}(E_g)$	2445	6	0	2454	12	0	$-0.2s_1-0.3s_2-0.1as_1+0.2as_2$
$\nu_{12}(E_g)$	2415	11	0	2416	10	0	$0.3s_1-0.2s_2-0.2as_1-0.1as_2$
$\nu_{13}(E_u)$	2520	0	31	2518	0	46	$0.1s_1+0.1s_2+0.2as_1-0.4as_2$
$\nu_{14}(E_u)$	2502	0	26	2494	0	6	$0.1s_1-0.1s_2+0.3as_1+0.2as_2$
$\nu_{15}(E_u)$	2428	0	26	2431	0	20	$-0.3s_1+0.3s_2+0.1as_1+0.2as_2$
$\nu_{16}(E_u)$	2374	0	59	2370	0	70	$-0.3s_1+0.3s_2+0.1as_1-0.1as_2$

---

[a] $F_1 = 6.3518$, $F_2 = 6.5184$, $F_3 = 6.4557$, $F_4 = 6.3259$, $F_5 = 0.04$, $F_6 = -0.02$, $F_7 = 1.029 \cdot F_8 = 0.850 \cdot F_9 = 0.964 \cdot F_{10} = 1.019 \cdot F_{11} = 0.982 \cdot F_{12} = 0.931 \cdot F_{13} = 0.915 \cdot F_{14} = -0.108$, $F_{15} = 0.09$, $F_{16} = 0.076$. Units are mdyne Å^{-1}. The force field is defined in References 1 and 2.

[b] As force field A, except $F_5 = 0.11$, $F_6 = 0.013$, $F_7 = F_8 = F_{10} = F_{11} = F_{12} = -0.10$, $F_9 = -0.16$, $F_{13} = F_{14} = -0.18$, $F_{15} = 0.04$, $F_{16} = 0.12$.

[c] Arbitrary units; $RP = \alpha_1'/\alpha_2' = 7.5$. The intensities of the two components of the degenerate modes have been added.

[d] $d_k \cdot (\partial\mu/\partial Q_k)^2$, where d_k is the degeneracy of vibration k and the units of $\partial\mu/\partial Q_k$ are $\text{D} \cdot \text{Å}^{-1} \cdot \text{amu}^{-\frac{1}{2}}$.

[e] Eigenvector elements, $\partial S_i/\partial Q_k$, for force field A, where S_i is a symmetry coordinate. The magnitude of the a and b symmetry coordinates have been added for the E_g and E_u modes.

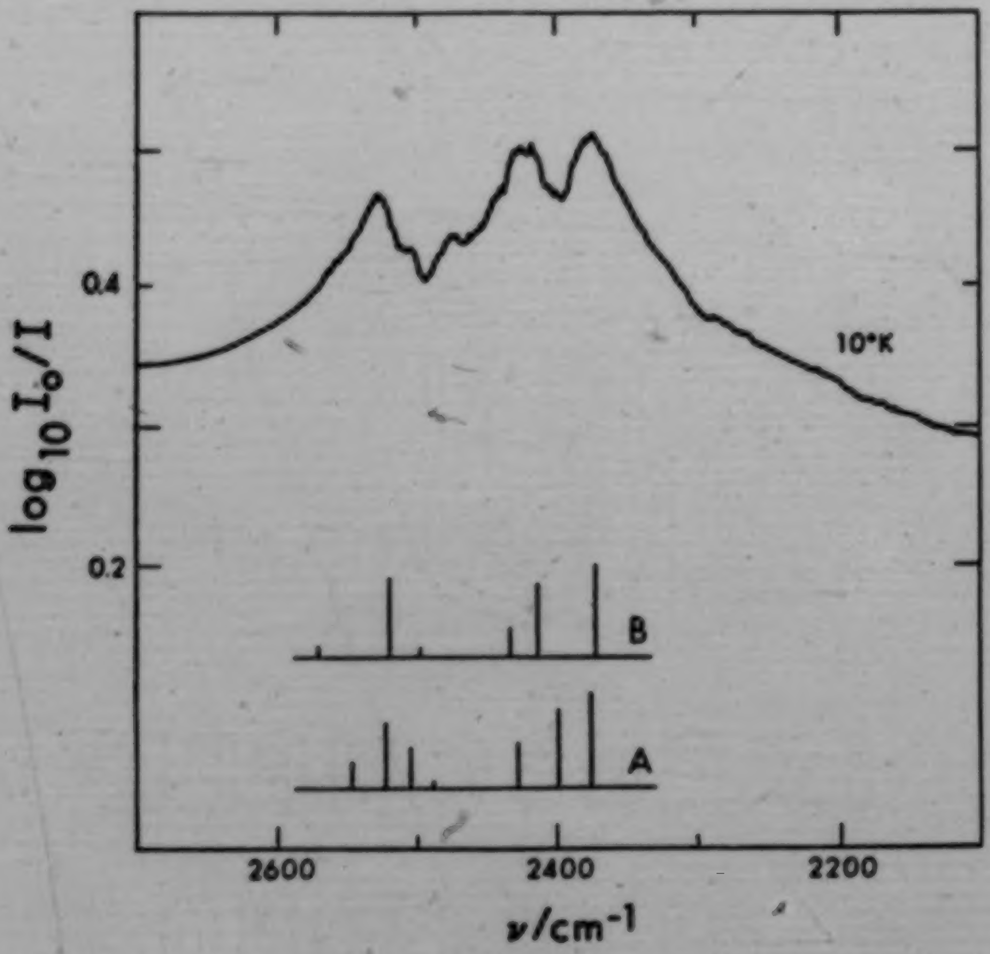

Figure 4.1 Comparison of the calculated and observed infrared absorption by $\nu_{OD}(D_2O)$ of ice II, reproduced from References 1 and 2.

features at 2350, 2380 and 2476 cm^{-1} were more intense under Y(ZZ)X polarization than under perpendicular polarization. This data suggests that these three features should be assigned to A_g vibrations, since the A_g vibrations of ice II are active under xx, yy and zz polarizations[56,57] while the four E_g vibrations are active under all but zz polarization, where z is the direction of the $\bar{3}$ axis of the crystal and lower case letters refer to crystal axes.

It is obvious from Figure 3.3 (p. 116) that the intense, lowest-frequency peak at 3189 cm^{-1} in the spectrum of H_2O ice II corresponds to the peak at 2349 cm^{-1} in the spectrum of D_2O ice II, and therefore can be assigned to an A_g vibration. The relation of the other features is not so apparent, but is aided by the opposite polarization (Figure 3.12) of the 3306 cm^{-1} feature to that of the 3189 cm^{-1} peak, which suggests its assignment to an E_g vibration. Thus the 3306 cm^{-1} peak corresponds to the high frequency, E_g, component of the 2476/2486 cm^{-1} doublet in the spectrum of D_2O. The polarization data does not exclude the possibility that the peak at 3306 cm^{-1} contains an A_g component in addition to the E_g component, and in fact allows little more to be said about the symmetries of the features. A definitive assignment of the remaining H_2O features would require better polarization data from a crystal of known orientation, but on the basis of the available information a tentative assignment is proposed in Table 3.2. The H_2O analogue of the low-frequency, A_g, component of the D_2O doublet at 2476/2486 cm^{-1} is believed to coincide with the 3306 cm^{-1} peak, based on the relative intensity of the D_2O feature. Alternately, the D_2O peak could be related to the H_2O shoulder at 3340 cm^{-1}, but this is considered less likely because of the differences in intensities and half-widths. Some of the polarized spectra of H_2O ice II suggest that the features at 3306 and 3270 cm^{-1} are both of E_g symmetry. However this is not clear in Figure 3.12, which contains the best polarized spectra of H_2O ice II that were obtained, and therefore the symmetry of the 3270 cm^{-1} feature is uncertain. The feature at 3270 cm^{-1} is believed to be related to the 2420 cm^{-1} shoulder of D_2O, with the H_2O analogue of the 2445 cm^{-1} shoulder presumably being buried in the broad peak at 3306 cm^{-1}. The H_2O features at 3465 and 3400 cm^{-1} appear to be both derived from the D_2O feature at 2530 cm^{-1}. The isotope ratios of the vibrations of ice II are thus between 1.33 and 1.37 (Table 3.2) and therefore are consistent with those found for other forms of ice.[81,84,97,101,125]

The vibrational representation of the $\underline{k} = 0$ O-D stretching vibrations of ice IX is $3A_1 + 3A_2 + 3B_1 + 3B_2 + 6E$, with the A_2 and E vibrations infrared active, and all but the A_2 vibrations Raman active. The vibrational frequencies, relative absorption intensities, and eigenvectors that were calculated[1,2] for D_2O ice IX are given in Table 4.2 as Force Field A, and the experimental and calculated absorption spectra are compared in Figure 4.2. The agreement is considered[1,2] to be excellent. The four features that were observed

Table 4.2

The calculated frequencies, infrared and Raman relative intensities, and assignments, of the $\underline{k} = 0$, O-D stretching vibrations of ice IX at 10 K.

	Force Field A[a]			Force Field B[b]			
Mode	ν/cm^{-1}	Raman[c] intensity	Infrared[d] intensity	ν/cm^{-1}	Raman[c] intensity	Infrared[d] intensity	Assignment[e]
$\nu_1(A_1)$	2522	8	0	2521	8	0	$0.3s_1-0.4s_2-0.6as_1$
$\nu_2(A_1)$	2417	2	0	2416	0.7	0	$0.3s_1-0.5s_2+0.5as_1$
$\nu_3(A_1)$	2341	100	0	2325	100	0	$0.6s_1+0.4s_2$
$\nu_4(A_2)$	2497	0	24	2500	0	33	$0.1s_1-0.3as_1-0.7as_2$
$\nu_5(A_2)$	2464	0	31	2461	0	23	$0.7as_1-0.3as_2$
$\nu_6(A_2)$	2357	0	4	2356	0	3	$0.7s_1+0.1as_1+0.1as_2$
$\nu_7(B_1)$	2527	0.2	0	2533	0.01	0	$0.4s_1+0.3as_1-0.5as_2$
$\nu_8(B_1)$	2468	30	0	2468	27	0	$0.6as_1+0.4as_2$
$\nu_9(B_1)$	2412	4	0	2422	8	0	$0.6s_1-0.3as_1+0.3as_2$
$\nu_{10}(B_2)$	2513	3	0	2511	4	0	$0.2s_1-0.3s_2+0.6as_1$
$\nu_{11}(B_2)$	2457	0.7	0	2463	0.06	0	[illegible]$s_1+0.2as_1$
$\nu_{12}(B_2)$	2401	0.5	0	2396	0.6	0	[illegible]$_2+0.3as_1$
$\nu_{13}(E)$	2516	6	12	2520	10	7	[illegible]$_1+0.2s_2-0.4as_1-0.5as_2$
$\nu_{14}(E)$	2492	7	24	2486	6	15	$0.1s_1+0.2s_2-0.9as_1+0.3as_2$
$\nu_{15}(E)$	2464	13	0.3	2466	2	5	$0.1s_1+0.9as_1-0.4as_2$
$\nu_{16}(E)$	2462	11	9	2461	20	0.07	$-0.5s_1+0.5s_2+0.3as_1+0.1as_2$
$\nu_{17}(E)$	2395	2	48	2402	0.8	54	$0.7s_1+0.2as_1+0.2as_2$
$\nu_{18}(E)$	2360	0.04	65	2353	0.08	76	$0.5s_1+0.5s_2+0.2as_1-0.1as_2$

---

[a] $F_1 = 6.2950$, $F_2 = 6.3053$, $F_3 = 6.3518$, $F_4 = 0.03$, $F_5 = 0.01$, $F_6 = 1.113 \cdot F_7 = 0.967 \cdot F_8 = 0.983 \cdot F_9 = 1.073 \cdot F_{10} = F_{11} = -0.118$, $F_{12} = 0.074$, $F_{13} = 1.081 \cdot F_{12}$. Units are mdyne$\cdot$Å^{-1}. The force field is defined in References 1 and 2.

[b] As force field A, except $F_4 = 0.0894$, $F_5 = 0.0023$, $F_6 = -0.1388$, $F_{12} = 0.0389$.

[c] Arbitrary units; $RP = \alpha_1'/\alpha_2' = 7.5$. The intensities of the two components of the degenerate modes have been added.

[d] $d_k \cdot (\partial\mu/\partial Q_k)^2$, where d_k is the degeneracy of vibration k, and the units of $\partial\mu/\partial Q_k$ are $D \cdot Å^{-1} \cdot amu^{-\frac{1}{2}}$.

[e] Eigenvector elements, S_i/Q_k, for force field A, where S_i is a symmetry coordinate. The magnitude of the eigenvector elements of the a and b symmetry coordinates have been added for the E modes.

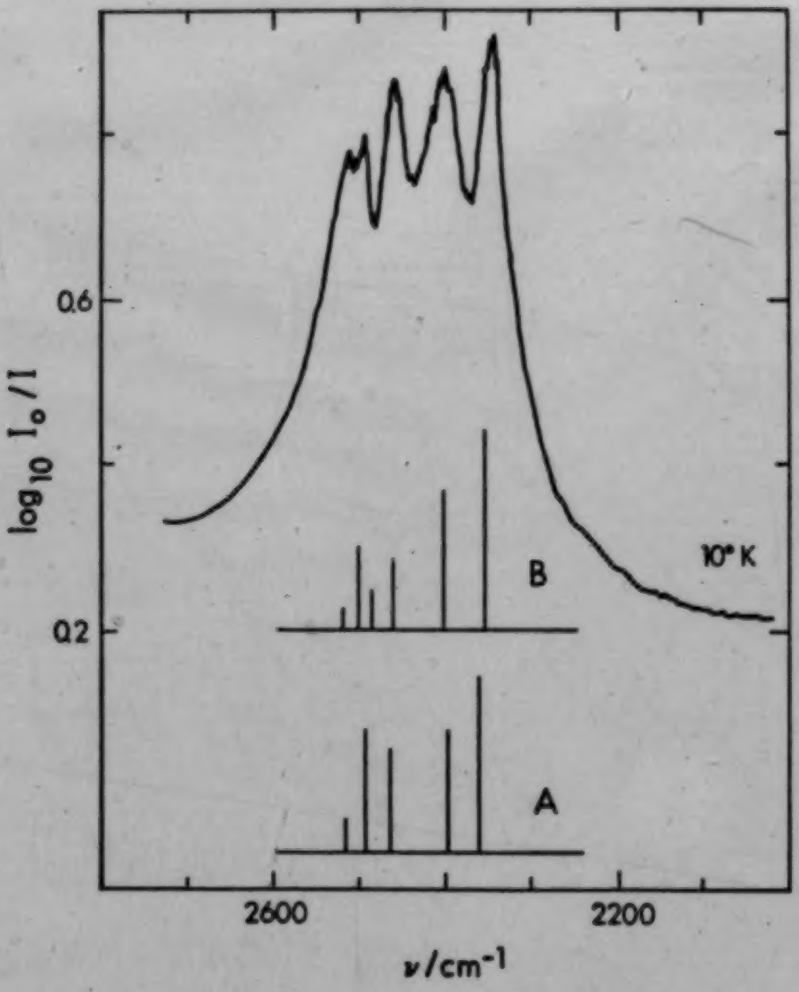

Figure 4.2 Comparison of the calculated and observed infrared absorption by $\nu_{OD}(D_2O)$ of ice IX. The observed spectrum and bar graph A are reproduced from References 1 and 2.

in the Raman spectrum of D_2O ice IX can be assigned as in Table 3.4 from the calculated[1,2] frequencies in Table 4.2, provided that $\nu_2(A_1)$, $\nu_9(B_1)$, $\nu_{12}(B_2)$, $\nu_{17}(E)$ and $\nu_{18}(E)$ are sufficiently weak in the Raman spectrum to explain the absence of distinct features between 2417 and 2360 cm^{-1}. The assignment of the four Raman features of H_2O ice IX is made by comparison with those for D_2O ice IX, and the isotope frequency ratios (Table 3.4) are consistent with those reported for other ice phases.[81,84,97,101,125] Once again, the intense, lowest-frequency peak, at 2325 cm^{-1} in the spectrum of D_2O and at 3151 cm^{-1} for H_2O, is assigned (Table 3.4) to the in-phase O-D or O-H stretching vibration, which is an A_1 vibration in ice IX (Table 4.2).

It is clear from Figures 3.3 and 3.14 that for ice II and ice IX the Raman spectrum of the D_2O ice consists of sharper, better resolved features than that of the H_2O ice, as is the case for the infrared spectra.[41] This must result from the greater effect of anharmonicity on the spectra of the H_2O ices, and indicates that interpretation by calculations based on harmonic force fields and first derivatives of the dipole moment and polarizability with respect to normal and internal coordinates is more suitable for the spectra of D_2O ices than for H_2O ices. Accordingly, these calculations are used to interpret the spectra of the D_2O ices (Sections 4.3 and 4.4) and the spectra of the H_2O ices are not discussed further here.

4.3 Calculation of the Raman Spectra of the O-D Stretching Vibrations of Ice II and Ice IX

To further test the reliability of the assignments given in Tables 3.2 and 3.4 the relative Raman intensities of the O-D stretching vibrations of polycrystalline samples of D_2O ice II and D_2O ice IX have been calculated under the bond polarizability approximation. In this approximation the polarizability derivatives with respect to a normal coordinate are expressed as the sum of the polarizability derivatives with respect to displacement of the O-D bonds weighted by the eigenvectors. The mathematical expression of the bond polarizability approximation is

$$\frac{\partial \underset{\sim}{\alpha}}{\partial Q_k} = \sum_i \frac{\partial \underset{\sim}{\alpha}}{\partial r_i} \cdot \frac{\partial r_i}{\partial Q_k} = \sum_i \frac{\partial \underset{\sim}{\alpha}}{\partial r_i} \cdot \ell_{ik} \tag{4.1}$$

where $\underset{\sim}{\alpha}$ is the polarizability tensor of the crystal, ℓ_{ik} is the i^{th} element of the eigenvector of the k^{th} normal coordinate Q_k of the crystal, and the summation is over all internal coordinates r_i, which in the present case are the displacements of the O-D bonds. In such calculations, the eigenvectors of the crystal vibrations, which describe the displacements of the bonds in the crystal during each vibration, and a model for the dependence of the polarizability of each bond on the displacement of the bond are needed. The bond polarizability approximation has been applied with good success to the vibrations of single crystal ice Ih by Scherer and Snyder[90] and to polycrystalline ice Ih by Rice et al.[81]

The change in the polarizability of the bond with displacement of the bond may be represented by $\underset{\sim}{\alpha}'$, a 3 × 3 tensor called the polarizability derivative tensor of the bond. The xy element of $\underset{\sim}{\alpha}'$, $(\alpha')_{xy} = \partial\alpha_{xy}/\partial r_i$, describes the change in the xy polarizability of the bond with unit displacement r_i of the bond. The x, y and z axes of bond i are the principal axes of the polarizability ellipsoid[74] of bond i, and are different for each bond.

The direction cosine matrix $\underset{\sim}{T}_i$ of bond i is given by

$$\underset{\sim}{T}_i = \begin{pmatrix} \cos(X,x) & \cos(Y,x) & \cos(Z,x) \\ \cos(X,y) & \cos(Y,y) & \cos(Z,y) \\ \cos(X,z) & \cos(Y,z) & \cos(Z,z) \end{pmatrix} \tag{4.2}$$

where X, Y and Z are the crystal axes, and cos(X,y) is the cosine of the angle between the X axis of the crystal and the y axis of bond i. $\underset{\sim}{T}_i$ and its transpose $\underset{\sim}{T}_i^{\dagger}$ are used to transform $\underset{\sim}{\alpha}'$ to $\underset{\sim}{\alpha}_i'$ through

$$\underset{\sim}{\alpha}_i' = \underset{\sim}{T}_i^{\dagger}\cdot\underset{\sim}{\alpha}'\cdot\underset{\sim}{T}_i. \tag{4.3}$$

The XY element of $\underset{\sim}{\alpha}_i'$, $(\underset{\sim}{\alpha}_i')_{XY} = \partial\alpha_{XY}/\partial r_i$, gives the change in the XY polarizability of the crystal with unit displacement of bond i. $\underset{\sim}{\alpha}_i'$ depends on the orientation of bond i with respect to the crystal axes, and so may be different even for bonds with the same polarizability derivative tensor $\underset{\sim}{\alpha}'$.

$(\underset{\sim}{\alpha}')_j$ is the polarizability derivative tensor of the crystal with respect to normal coordinate j, and the XY component is given by

$$(\alpha_{XY}')_j = \sum_i (\alpha_i')_{XY} \cdot \ell_{ij} = \sum_i \frac{\partial \alpha_{XY}}{\partial r_i} \cdot \frac{\partial r_i}{\partial Q_j} \qquad (4.4)$$

where the summation is over all bonds i of the crystal. The ℓ_{ij} are the eigenvector elements for normal coordinate Q_j and are available from normal coordinate analyses. A similar summation is carried out to find each of the nine components of the polarizability derivative tensor for the crystal for each normal coordinate Q_j of the crystal.

In this application of the bond polarizability approximation to ice II and ice IX, the z-principal axis of the polarizability ellipsoid of each bond is assumed to be coincident with the bond axis, so that all off-diagonal elements of the polarizability derivative tensor $\underset{\sim}{\alpha}'$ are zero. Further, the ellipsoids are assumed to be cylindrically symmetrical, so that the xx and yy elements of the polarizability derivative tensor are equal and have the value α_2'. Thus, the only unique elements of $\underset{\sim}{\alpha}'$ are α_1', the component parallel to the bond, and α_2', the value of each of the two components perpendicular to the bond. The polarizability derivative tensor $\underset{\sim}{\alpha}'$ is assumed to be the same for all O-D bonds in the crystal, even though there are four non-equivalent types of O-D bond in ice II and three in ice IX. Thus the ratio $RP = \alpha_1'/\alpha_2'$ is the only variable in the calculation of the relative Raman intensities under a particular force field for each ice.

The Raman intensity of vibration j is related to the components of $(\underset{\sim}{\alpha}')_j$, the polarizability derivative tensor of the crystal with respect to the normal coordinate, in a way which depends on the orientations of the polarizations of the incident and scattered light with respect to the crystal axes. For a sample of randomly oriented crystallites the incident light may be totally scrambled with respect to polarization and propagation direction on passing through the sample.[126] If this happens, the spectrum is the same under parallel and perpendicular polarizations. This was experimentally observed for crushed samples of ice II and for all samples of ice IX (Section 3.5). For this case, the intensity $I(\nu_j)$ of vibration j is given by[126]

$$I(\nu_j) \propto \frac{[(\nu_o - \nu_j)^4/\nu_j]}{[1 - \exp(-h\nu_j/kT)]} \cdot [45(\bar{\alpha}_j')^2 + 10(\gamma_j')^2] \qquad (4.5)$$

where $\bar{\alpha}_j'$ and γ_j' are the isotropic and anisotropic invariants of the polarizability derivative tensor for vibration j at frequency ν_j, ν_o is the Raman excitation frequency, T is the absolute temperature, and h and k are the Planck and Boltzmann constants. The isotropic invariant is defined as

$$\bar{\alpha}' = \frac{1}{3}(\alpha_{XX}' + \alpha_{YY}' + \alpha_{ZZ}') \qquad (4.6)$$

and the anisotropic invariant is defined as

$$(\bar{\gamma}') = \tfrac{1}{2}\{(\alpha_{XX}' - \alpha_{YY}')^2 + (\alpha_{YY}' - \alpha_{ZZ}')^2 + (\alpha_{ZZ}' - \alpha_{XX}')^2$$
$$+ 6(\alpha_{XY}'^2 + \alpha_{YZ}'^2 + \alpha_{ZX}'^2)\} . \qquad (4.7)$$

$\bar{\alpha}'$, γ', and the scattering intensities of the vibrations, given by equation (4.5), relative to that of the in-phase symmetric O-D stretching vibration, are given in Appendix I for RP = 5.6, 7.5, 10, 20 and 50 for force fields A and B of D_2O ice II[1,2] (Table 4.1), and for force field A of D_2O ice IX[1,2] (Table 4.2) and for force field B of D_2O ice IX, which is described in the following section.

The scattering intensities of the O-D stretching vibrations of ices II and IX are plotted as a function of RP in Figures 4.3 and 4.4, where it can be seen that the intensity of each vibration increases relative to that of the symmetric O-D stretching vibration of each ice as RP increases. The value of RP was chosen to give the best fit to the relative intensities of the three strongest peaks of ice II and the two strongest peaks of ice IX. For a polycrystalline sample of D_2O ice II the integrated area of the doublet at 2476/2486 cm^{-1} ($\nu_2(A_g)/\nu_{10}(E_g)$) is 0.52 ± 0.1 times that of the bands at 2350 cm^{-1} ($\nu_4(A_g)$), and for polycrystalline ice IX the integrated area of the band at 2454 cm^{-1} ($\nu_8(B_1)$, $\nu_{11}(B_2)$, $\nu_{15}(E)$, $\nu_{16}(E)$) is 0.52 ± 0.1 times that of the band at 2325 cm^{-1} ($\nu_3(A_1)$). From Figure 4.3 the calculated intensity ratio for ice II is 0.5 at RP=6.7 for force field A and at 6.3 for force field B, and the ranges of RP that span the experimental uncertainty are 5.4 to 9.4 for force field A and 5.0 to 8.3 for force field B. From Figure 4.4, the calculated intensity ratio for ice IX is 0.5 at RP = 6.7 for force field A and at RP = 7.6 for force field B, and the experimental range is

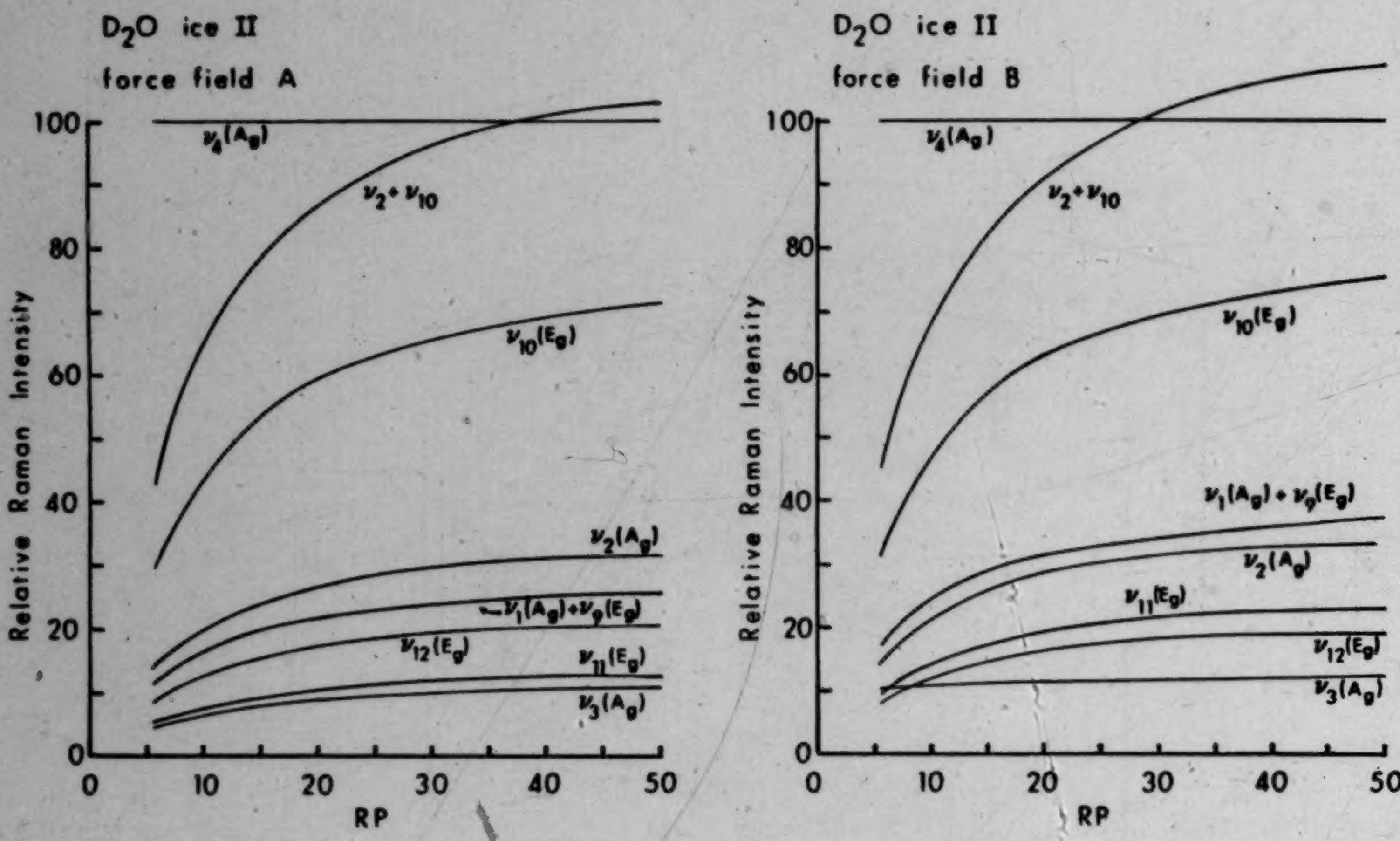

Figure 4.3 Calculated relative Raman intensities of the O-D stretching vibrations of D_2O ice II as a function of RP.

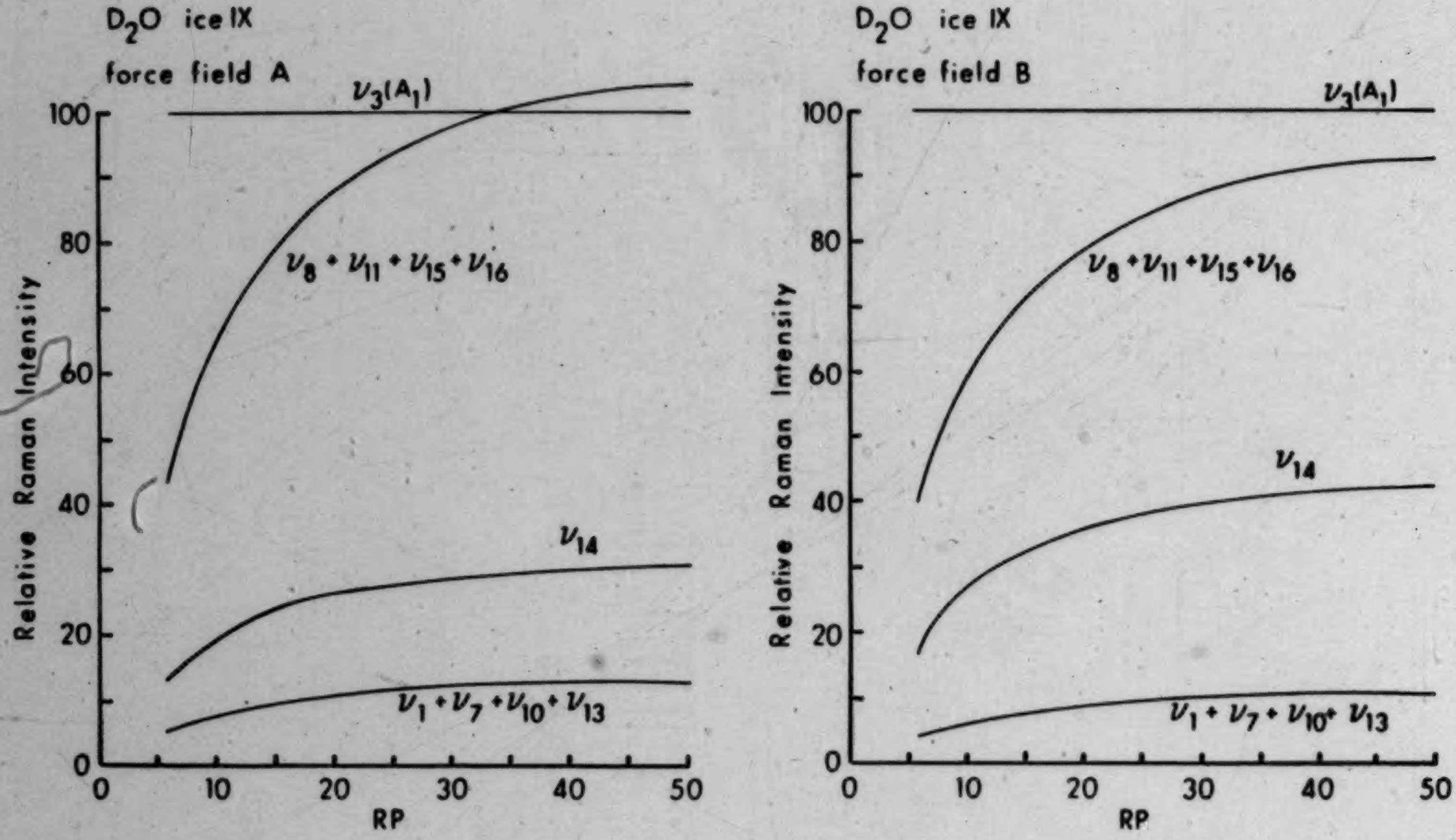

Figure 4.4 Calculated relative Raman intensities of the O-D stretching vibrations of D_2O ice IX as a function of RP.

spanned by RP = 5.2 to 9.0 for force field A and 6.0 and 11.0 for force field B. The average of the four values of RP that give an intensity ratio of 0.5 for the two ices is 6.8, and the average of the eight values of RP that reproduce the extremes of the experimental ranges of the intensity ratio is 7.4.

The relative intensities that were calculated with the ratio RP = 7.5 are listed in Tables 4.1 and 4.2, and the relative intensities calculated with RP = 50 are shown as bar graphs in Figures 4.5 and 4.6. The relative peak heights in the Raman spectra of D_2O ices II and IX are rather well reproduced by the intensities calculated with RP = 50, but the relative peak areas are better reproduced with RP = 7.5. It is, of course, the peak areas that are theoretically important. It is encouraging that the Raman spectra are explained rather well by the normal coordinate and bond polarizability calculations that use the force fields described earlier[1,2] to explain the infrared spectra. It is particularly impressive that the calculations that have[1,2] explained the infrared spectrum of ice IX so well indicate why only four features are observed in the Raman spectrum of ice IX when 15 O-D stretching vibrations are Raman active.

The calculation of the Raman intensities allows the Raman features of ice IX to be assigned in more detail, by assignment of the observed features to the vibrations with the largest calculated scattering intensities. These assignments of the Raman features and the assignments[1,2] of the

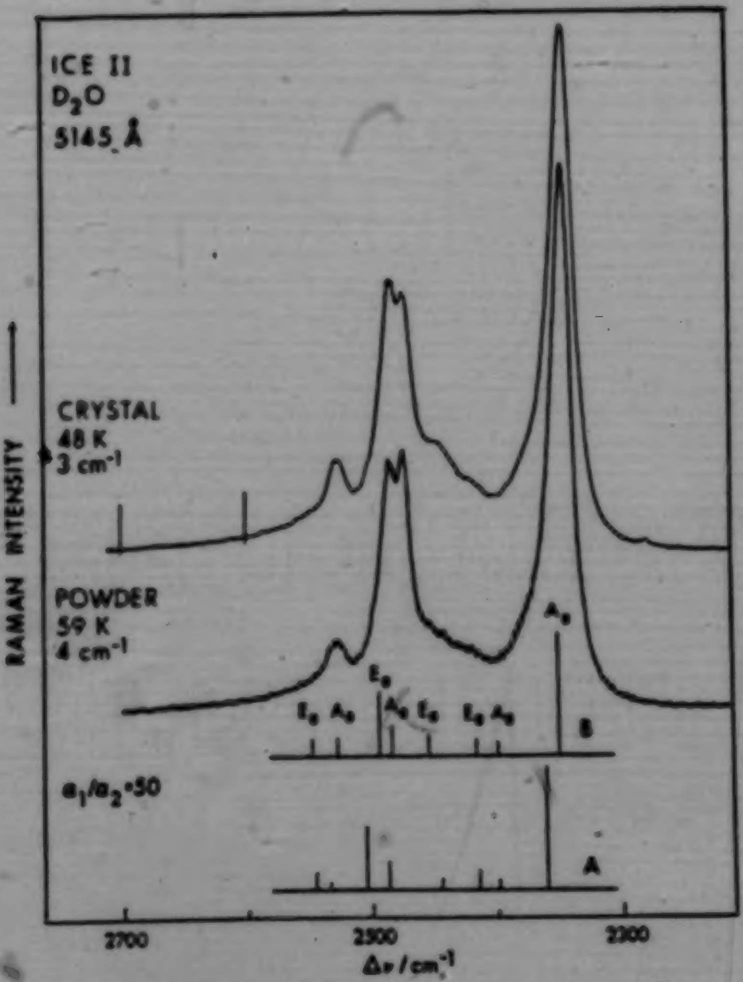

Figure 4.5 Observed and calculated Raman spectra of the O-D stretching vibrations of D_2O ice II.

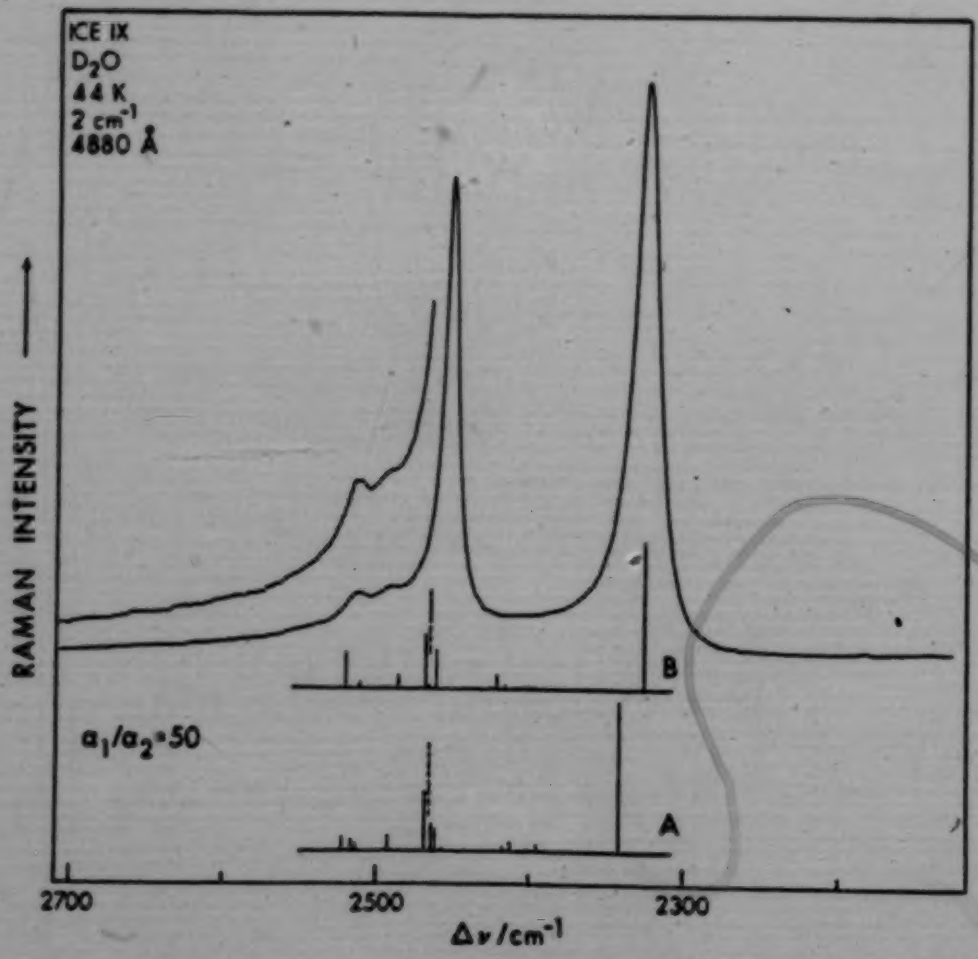

Figure 4.6 Observed and calculated Raman spectra of the O-D stretching vibrations of D_2O ice IX.

infrared spectrum are given in Table 4.3. The modes in parentheses in the table undoubtedly contribute to the assigned feature but are weak enough (Table 4.2) that they do not determine its frequency. The intensities of the vibrations $\nu_2(A_1)$, $\nu_6(A_2)$, $\nu_7(B_1)$, $\nu_9(B_1)$, $\nu_{11}(B_2)$ and $\nu_{12}(B_2)$ appear to be too small to allow any experimental indication of their frequencies.

The assignment of the Raman spectrum of D_2O ice II is that given in Table 3.2, and is combined with the assignment of the infrared spectrum[1,2] in Table 4.4.

The values of RP found previously in studies of the Raman spectra of gaseous water vapor and single crystal and polycrystalline ice Ih should be compared to those found here. Murphy found[127] 3.1 to be the most probable value of RP for gaseous H_2O. Scherer and Snyder[90] found the value RP = 5.6±1 from a least-squares refinement of the relative integrated intensities, under various polarizations, of the Raman scattering by O-H and O-D stretching modes of HDO molecules isolated in single-crystal, D_2O or H_2O, ice Ih at -4°C. The uncertainty in RP resulted from the uncertainty in the intensity measurements and from the approximations of harmonic oscillator theory which cannot simultaneously explain the intensities of O-H and O-D oscillators precisely, due to the effects of electrical and/or mechanical anharmonicity. Rice et al[81] found that the value RP = 5.6 gave the intense, lowest-frequency Raman peak due to the O-H or O-D motion in H_2O or D_2O ice Ih an integrated area that is three times too large

Table 4.3

Assignments of the features due to the O-D stretching vibrations in the infrared and Raman spectra of D_2O ice IX at 10 K.

ν/cm^{-1}		
Infrared	Raman[a]	Assignment
2517		$\nu_{13}(E)$
	2513	$\nu_1(A_1)$ [+ $\nu_7(B_1)$ + $\nu_{10}(B_2)$ + $\nu_{13}(E)$]
2499		$\nu_4(A_2)$ [+ $\nu_{14}(E)$]
	2492	$\nu_{14}(E)$
2462		$\nu_5(A_2)$ [+ $\nu_{15}(E)$ + $\nu_{16}(E)$]
	2453.9	$\nu_8(B_1)$ [+ $\nu_{11}(B_2)$ + $\nu_{15}(E)$ + $\nu_{16}(E)$]
2403		$\nu_{17}(E)$
2348		$\nu_{18}(E)$ [+ $\nu_6(A_2)$]
	2325.1	$\nu_3(A_1)$

[a] Extrapolated from frequencies at higher temperatures.

Table 4.4

Assignments of the features due to the O-D stretching vibrations in the infrared and Raman spectra of D_2O ice II at 10 K.

ν/cm^{-1}		
Infrared	Raman [a]	Assignment
2550		$\nu_5(A_u)$
	2530.5	$\nu_1(A_g) + \nu_9(E_g)$
2524		$\nu_6(A_u) + \nu_{13}(E_u)$
2501		$\nu_{14}(E_u)$
	2485.8	$\nu_{10}(E_g)$
	2475.5	$\nu_2(A_g)$
2470		$\nu_7(A_u)$
	2445	$\nu_{11}(E_g)$
	2420	$\nu_{12}(E_g)$
2418		$\nu_{15}(E_u) + \nu_8(A_u)$
	2380	$\nu_3(A_g)$
2370		$\nu_{16}(E_u)$
	2349.6	$\nu_4(A_g)$

[a] Extrapolated from frequencies at higher temperatures.

relative to that of the higher-frequency part of the band, but did not explore the effect of changing RP. It is concluded that the value of RP found here for ices II and IX is definitely larger than that of gaseous water[127] and is comparable to the averaged value of 5.6 found for ice Ih.[90]

4.4 Refinement of the Force Fields for D_2O Ices II and IX

Force fields A and B for D_2O ice II and A for D_2O ice IX were reported[1,2] as those that best reproduced the infrared frequencies of the O-D stretching vibrations. Only the two strongest Raman features of each ice had been observed at that time, and their frequencies were not well known. It is therefore not surprising that the agreement between the frequencies that were calculated[1,2] for the Raman-active vibrations and the observed Raman frequencies is not perfect. An attempt was therefore made to refine the force fields to improve the fit to the infrared and Raman data for each ice (Tables 4.3 and 4.4).

The main deficiency of the calculations for ice IX is that the frequencies of the two strong Raman peaks are calculated about 15 cm^{-1} too high. The diagonal, O-D stretching, force constants are known with certainty from the spectrum of ν_{OD}(HDO) in H_2O ice IX, and therefore were not varied. The intermolecular coupling constant between two bonds, r_i and r_j, on different molecules was calculated[1,2] as $\partial^2V/\partial r_i\partial r_j$, where V is the potential energy of interaction of effective charges on the deuterium atoms of r_i and r_j. The coupling constant between the two oscillators was then evaluated from their local geometry. Force contants F_6 to F_{11} arise from the configuration in which one oscillator is hydrogen bonded to the molecule containing the oscillator with which it is interacting. Force constants F_{12} and F_{13} account for the interaction of two oscillators that are hydrogen bonded to a common atom. In varying the intermolecular coupling constants in this work, the relative values[1,2] of F_6 to F_{11} were assumed to be correct, but the scaling factor that determines their absolute values was adjusted; the same approach was taken with the intermolecular coupling constants of the second type (F_{12} and F_{13}). Finally, the values of the two intramolecular coupling constants (F_4 and F_4) were adjusted independently. Thus, four parameters were adjusted to improve the fit to nine frequencies (Table 4.3) by the program FPERT.[122] The resulting force constants, frequencies, and infrared and Raman intensities are shown in Table 4.2, under Force Field B, and the calculated spectra are compared with those from force field A[1,2] and with the observed infrared and Raman spectra in Figures 4.2 and 4.6. The eigenvectors calculated with force field B are similar to those given in Table 4.2 for force field A. Force field B does correct the frequency mismatch for $\nu_3(A_1)$ at 2325 cm^{-1} but still predicts the second intense Raman peak, at 2454 cm^{-1}, to be about 10 cm^{-1} too high, and does not explain the infrared spectrum quite as well as does force field A (Figure 4.2). This could not be improved further.

For ice II, the calculated frequencies of $\nu_9(E_g)$ and

$\nu_3(A_3)$ are ~15 cm^{-1} higher than the observed frequencies, and those of $\nu_{10}(E_g)$ and $\nu_2(A_g)$ are ~10 cm^{-1} too high (Tables 4.1 and 4.4). Various attempts were made to improve the agreement between the observed and calculated frequencies, without improving on the results given by force field B (Table 4.1).

The sets of force constants that provided the best agreement between the calculated and observed spectra of D_2O ices II and IX are those given in References 1 and 2 and in Tables 4.1 and 4.2. The agreement can be considered to be excellent in view of the limited force fields and harmonic theory. However it must be recognized that other sets of force constants that are similar to those presented (Tables 4.1 and 4.2) are able to reproduce the spectra nearly as well, and that under somewhat expanded force fields the individual force constants would likely be somewhat different. Therefore no undue significance should be attached to values of individual force constants given here.

4.5 Discussion of the Effects of Disorder, LO-TO Splitting and Fermi Resonance on the Spectra of Ice II and Ice IX

Ice II is centrosymmetric and fully ordered, but ice IX is non-centrosymmetric and is ~4% orientationally disordered. The spectrum of ice IX could therefore be affected by longitudinal optic-transverse optic (LO-TO) splitting, and the disorder could conceivably broaden the peaks in the spectra of ice IX relative to those of ice II. These effects are discussed in this section. The broad absorption underlying the infrared spectra of the O-D stretching vibrations of ice

II and ice IX has been attributed[1,2] to Fermi resonance of the fundamentals with high-order overtone and combination states, and this explanation is now discussed in light of the Raman spectra of these ices.

Orientational disorder of a crystal should broaden the peaks of the vibrational spectra because of the destruction of the $\underline{k} = 0$ selection rules, and therefore the peaks in the Raman spectrum of ice IX might be expected to be broader than those of ice II. However, from Tables 3.2 and 3.4 it can be seen that the strongest peak in the Raman spectra of the O-H and O-D stretching vibrations of both ice II and ice IX have the same half-widths, i.e. ~30 cm^{-1} for H_2O and ~18 cm^{-1} for D_2O ice at 35 K and ~40 and ~22 cm^{-1} respectively at 100 K. Further, the half-width of the strongest peak of ice Ih, which is as disordered as is possible, is 19 cm^{-1} for H_2O and 13 cm^{-1} for D_2O at 20 K,[88] and 36 cm^{-1} [99] (or 48 cm^{-1})[90] for H_2O and ~25 cm^{-1} [90] (or 32 cm^{-1})[99] for D_2O at ~100 K, and the half-widths of the two strongest peaks of the fully-ordered ice VIII[101] at 100 K are 50 and 20 cm^{-1} for H_2O and 48 and 14 cm^{-1} for D_2O. Thus, there does not seem to be a correlation between the breadth of the strong, low-frequency peak in the Raman spectrum of the O-H or O-D stretching vibrations and the degree of order of the ice. It is true that the Raman spectra of the ordered ices VIII, II and IX show sharper features in the high-frequency part of the band than does the spectrum of the disordered ice Ih,[99] but these high-frequency features in the Raman spectra of ice II and ice IX are of comparable breadth (Figures 3.3 and 3.14). A comparison of the Raman and infrared (Figures 4.1 and 4.2) spectra of ices II and IX and the success with which they have been interpreted indicates that no effect of the slight disorder in ice IX can be identified at present in the infrared and Raman bands due to the O-H or O-D stretching vibrations.

Ice IX is non-centrosymmetric, and so the E vibrations of ice IX are active in both the infrared and Raman. Accordingly, the longitudinal optic (LO) mode of the E vibrations may be considerably higher in frequency than the transverse optic (TO) mode, and both the longitudinal optic and transverse optic E modes are potentially observable in the Raman spectrum of ice IX. The frequencies of longitudinal optic and transverse optic modes derived from the zero-wavevector normal mode k of an isotropic material are related by[128]

$$(\nu_k^{LO})^2 - (\nu_k^{TO})^2 = \frac{N}{\pi c^2}\cdot\left(\frac{n\,n^*+2}{3n}\right)^2\cdot\left(\frac{\partial\mu}{\partial Q_k}\right)^2 . \qquad (4.8)$$

The number density of oscillators, N, which may be calculated from the diffraction data, is 3.23×10^{21} cm^{-3} for ice IX and 3.29×10^{21} cm^{-3} for ice II, c is the velocity of light in vacuum and n is the refractive index at the frequency of vibration k. The squared derivative of the dipole moment with respect to the zero-wavevector normal coordinate k, $(\partial\mu/\partial Q_k)^2$, was calculated under the bond moment approximation for ices II and IX, and can be obtained by dividing the infrared intensities reported in Tables 4.1 and 4.2 by d_k, the degeneracy of vibration k. In fact, ice II and ice IX are uniaxial, not isotropic, crystals, but equation (4.8) gives a useful estimate of the splitting. The refractive indices are not known for ices II and IX, but n varies between 1.0 and 1.9 for radiation between 2800 and 3600 cm^{-1} in H_2O ice Ih and between 2000 and 2700 cm^{-1} in D_2O ice Ih,[3] and the range of the refractive index is likely similar in ice II and ice IX. Between $n = 1.0$ and $n = 2.0$ the function $[(n^2 + 2)/3n]$ varies by only ~11% and is a minimum at $n = \sqrt{2}$. Therefore $n = \sqrt{2}$ is used here to calculate the minimum LO-TO splittings of the infrared-active vibrations of ice II and IX. Thus, for ice IX equation (4.8) becomes

$$(\nu_k^{LO})^2 - (\nu_k^{TO})^2 = 6120 \cdot (\partial\mu/\partial Q_k)^2 \qquad (4.9)$$

and for ice II it becomes

$$(\nu_k^{LO})^2 - (\nu_k^{TO})^2 = 6230 \cdot (\partial\mu/\partial Q_k)^2 \qquad (4.10)$$

where the units of $(\partial\mu/\partial Q_k)^2$ are $D^2\ \text{Å}^{-2}\ \text{amu}^{-1}$. In Table 4.5, the frequencies of the transverse optic vibrations of the infrared-active O-D stretching fundamentals are the observed infrared and Raman frequencies, and the longitudinal optic frequencies are estimated from equations (4.9) and (4.10). The longitudinal optic frequencies are, of course, only as reliable as the intensity calculations.

Large LO-TO splittings are calculated for some of the infrared-active vibrations of ice II and for the A_2 vibrations

Table 4.5

Calculated LO-TO splittings of the infrared-active O-D stretching vibrations of D_2O ices II and IX.

	Mode	$d_k \cdot (\partial\mu/\partial Q_k)^2$ [a]	I_{Raman}	ν^{TO}	ν^{LO}	$\nu^{LO} - \nu^{TO}$
ice II	$\nu_5(A_u)$	12	0	2550	2564(4)	14
	$\nu_6(A_u)$	10	0	2524	2536(2)	12
	$\nu_7(A_u)$	1	0	2470	2472(2)	2
	$\nu_8(A_u)$	52	0	2418	2484(5)	66
	$\nu_{13}(E_u)$	38	0	2524	2547(5)	23
	$\nu_{14}(E_u)$	16	0	2501	2511(6)	10
	$\nu_{15}(E_u)$	23	0	2418	2433(2)	15
	$\nu_{16}(E_u)$	65	0	2370	2412(4)	42
ice IX	$\nu_4(A_2)$	28	0	2499	2534(6)	35
	$\nu_5(A_2)$	27	0	2462	2495(5)	33
	$\nu_6(A_2)$	4	0	2350	2355(1)	5
	$\nu_{13}(E)$	10	10	2517	2522(2)	5
	$\nu_{14}(E)$	20	8	2492	2504(3)	12
	$\nu_{15}(E)$	3	10	2460	2462(2)	2
	$\nu_{16}(E)$	5	20	2460	2463(3)	3
	$\nu_{17}(E)$	51	2	2403	2435(2)	32
	$\nu_{18}(E)$	70	0.1	2348	2394(4)	46

[a] The values of $d_k \cdot (\partial\mu/\partial Q_k)^2$ given here are the averages of those calculated from force fields A and B for each ice.

of ice IX. However all of these vibrations are forbidden in the Raman spectrum and only the transverse optic mode can be observed in the infrared spectrum. The E vibrations of ice IX are active in both the infrared and Raman spectra. However only ν_{14}(E) is totally responsible for a feature in the Raman spectrum, the weak feature at 2492 cm^{-1} (Table 3.4), while ν_{13}(E), ν_{15}(E) and ν_{16}(E) are expected to contribute to the Raman features at 2513 cm^{-1} and 2454 cm^{-1}, and ν_{17}(E) and ν_{18}(E) appear to be too weak to be observed in the Raman spectrum.

The only peak in the Raman spectrum of ice IX to which the longitudinal mode of ν_{14}(E) could contribute is the weak peak at 2513 cm^{-1}, but this peak is equally well assigned to $\nu_1(A_1)$ with contributions from other vibrations (Table 4.3). It is more likely that the longitudinal optic mode of ν_{14}(E) contributes to the Raman scattering near 2504 cm^{-1}, i.e. to the region between the weak Raman features at 2492 and 2513 cm^{-1}, and therefore cannot be assigned to any specific feature. The longitudinal optic mode of ν_{13}(E) is calculated to be only 5 cm^{-1} higher in frequency than the TO mode, so both modes probably contribute to the 2513 cm^{-1} feature. ν_{15}(E) and ν_{16}(E) are relatively intense in the Raman, but they are calculated to have negligible LO-TO splitting. Thus, no specific features in the Raman spectrum of D_2O ice IX can be assigned to a longitudinal optic mode, and all of the Raman features of ice IX can be readily assigned without invoking the influence of longitudinal optic modes. This is, however, a direct result of the low Raman intensity of strongly absorbing vibrations, which may be peculiar to the case of ice IX, and therefore one should be cautious in taking this as evidence of the probable influence of longitudinal modes on the Raman spectra of other phases of ice.

The breadth of the infrared absorption peaks due to the O-D stretching vibrations of D_2O ice II and D_2O ice IX and a broad absorption that underlies the peaks (Figures 4.1 and 4.2) have been attributed[1,2] to broadening of the O-D stretching fundamental transitions by Fermi resonance between the fundamental states and the continuum of isoenergetic, high-order overtone and combination states of the lower frequency translational, rotational and, possibly, D-O-D bending modes. The Fermi resonance interaction between fundamentals and combinations (or overtones) that influences the infrared spectrum must also influence the Raman spectrum, although the effect on the intensities in the two spectra can differ. However, the peaks in the Raman spectra of ice II and ice IX are much sharper than those in the infrared spectra, and the broad underlying feature is about ten times less intense relative to the peaks in the Raman spectra than in the infrared spectra. The question is whether such large differences between the spectra can be explained by reasonable differences in the factors that determine the degree of Fermi-resonance enhancement of the intensities of the combination and overtone transitions.

The differences that can occur between the two spectra can be estimated through degenerate perturbation theory.[129,130] If Ψ^+ and Ψ_u are the wavefunctions of the perturbed and unperturbed higher energy states, and Ψ^- and Ψ_ℓ are the perturbed and unperturbed lower energy states, then

$$\Psi^+ = \sqrt{\frac{\Delta E_o + \Delta E}{2\Delta E}}\,\Psi_u \pm \sqrt{\frac{\Delta E - \Delta E_o}{2\Delta E}}\,\Psi_\ell \tag{4.11}$$

and

$$\Psi^- = \sqrt{\frac{\Delta E - \Delta E_o}{2\Delta E}}\,\Psi_u \mp \sqrt{\frac{\Delta E_o + \Delta E}{2\Delta E}}\,\Psi_\ell \tag{4.12}$$

where $\Delta E_o = E_u - E_\ell$, the difference between the unperturbed energies, and $\Delta E = E^+ - E^-$, the difference between the perturbed energies, and it is assumed that $<\Psi_u|H'|\Psi_u> = <\Psi_\ell|H'|\Psi_\ell> = 0$. Then I^+/I^-, the ratio of the intensities of the upper and lower perturbed states, is given by

$$\frac{I^+}{I^-} = \frac{(\Delta E_o + \Delta E)\cdot\left(\frac{M_u}{M_\ell}\right)^2 + (\Delta E - \Delta E_o) \pm 2\cdot\left(\frac{M_u}{M_\ell}\right)\cdot\sqrt{\Delta E^2 - E_o^2}}{(\Delta E - \Delta E_o)\cdot\left(\frac{M_u}{M_\ell}\right)^2 + (\Delta E + \Delta E_o) \mp 2\cdot\left(\frac{M_u}{M_\ell}\right)\cdot\sqrt{\Delta E^2 - E_o^2}} \tag{4.13}$$

where $M_u = <\Psi_u|M|\Psi_o>$ and $M_\ell = <\Psi_\ell|M|\Psi_o>$. In equations (4.11) to (4.13), the upper signs are used if $W_{fc} = <\Psi_u|H'|\Psi_\ell>$ is positive, and the lower signs are used if W_{fc} is negative. Thus, the intensity gained by a combination or overtone transition through Fermi resonance depends on M_u/M_ℓ, the ratio of the moment of the transition to the unperturbed combination or overtone state to that of the transition to the fundamental state. The intensity ratio I^+/I^- was calculated for various values of M_u/M_ℓ with $\Delta E/\Delta E_o$ between 15 and 1.25, and the results are tabulated in Appendix II.

To account for the observed differences between the breadths of the infrared and Raman spectra of the ices by Fermi resonance, the ratio of the infrared intensities of the perturbed combination (or overtone) bands to that of the perturbed fundamental band must be ten times larger than the corresponding ratio of Raman intensities. From Appendix II this requires the infrared intensity of the unperturbed fundamental transition to be greater than ten times that of the unperturbed combination or overtone, and the Raman intensity of the unperturbed fundamental to be only one to three times the intensity of the unperturbed combination. Normally, however, the unperturbed intensities of combinations or overtones are much weaker than those of fundamentals. It is therefore unlikely that the unperturbed combination transitions are so intense in the Raman, and in such a situation the bands would be broad anyway, even without Fermi resonance. For the more normal situation in which the unperturbed fundamental transition is greater than about ten times as intense as the unperturbed combination transition, the calculations reveal that I^+/I^- varies at most by a factor of two for the cases considered. It is concluded that no reasonable difference in M_u/M_ℓ will explain the observed differences between the infrared and Raman spectra, and thus that Fermi resonance is probably not the cause of the breadth in the infrared spectrum.

The significant LO-TO splittings estimated in Table 4.5 suggest that at least part of the breadth of the infrared bands may be due to reflection effects associated with large changes in the refractive index in the region of the absorption bands, as described by classical dispersion theory.[131] Unfortunately the infrared reflection spectra of ice II and ice IX have not been reported. These reflection effects would not, of course, affect the breadth of the Raman bands because the radiation involved in the Raman spectrum is not at the frequency of the absorption bands.

CHAPTER FIVE

DISCUSSION OF THE RAMAN SPECTRA OF THE LATTICE VIBRATIONS OF ICE II AND ICE IX

5.1 Introduction

The translational and rotational lattice vibrations of ices II and IX are discussed in this chapter. In Section 5.2 the Raman spectra of the lattice vibrations are assigned from the polarization data for ice II and from the coincident infrared and Raman frequencies of ice IX, but the assignment is necessarily incomplete. The remainder of the chapter deals with the normal coordinate calculations used to further the interpretation. In Section 5.3 the method of calculation of the lattice vibrations used in this work is described and compared with the method used for the molecular vibrations of free molecules. In Section 5.4 the calculations that are reported in this chapter are discussed in general terms, and the models for the structure and potential energy of each calculation are defined.

It was anticipated that it would be much easier to calculate the frequencies of the translational vibrations alone than to calculate the frequencies of both the translational and rotational vibrations from the same force field. Thus two sets of calculations are reported in this chapter. In Section 5.5 calculations of the frequencies and intensities of the translational vibrations of ices II and IX are reported, and detailed assignments are made on the basis of these calculations. In Sections 5.6 and 5.7 frequency calculations of both the translational and rotational vibrations of ices II and IX are reported for several sets of coordinates, in exploratory work whose aim is to find a very simple model to describe the potential energy of the lattice of the ices.

5.2 Discussion of the Low-Frequency Raman Spectra of Ices II and IX

The features below 1000 cm^{-1} in the Raman spectra of ices II and IX are assigned in this section on the basis of their frequencies, isotope ratios and the polarized spectra. The frequencies of rotational vibrations of the ices are expected to be between 450 and 1000 cm^{-1} for H_2O and between 350 and 700 cm^{-1} for D_2O, and the ratio of frequencies of corresponding rotational vibrations of H_2O and D_2O, i.e. the isotope ratio, is calculated from the moments of inertia to be about 1.35 (Section 1.5). Features due to the translational vibrations are expected below 325 cm^{-1}, with isotope ratios of about 1.05 (Section 1.5).

Based on these criteria, twelve features in the Raman spectrum of ice II are assigned in Table 3.2 to rotational vibrations, and nine features are assigned to translational vibrations. The relative intensities of these features are independent of temperature within experimental error and therefore all of the observed features are assigned to transitions from the ground state to fundamental states. The sharp feature at ~950 cm^{-1} (~695 cm^{-1} in D_2O) (Figure 3.4) is presumably analogous to the sharp peak that was observed[99] at 1085 cm^{-1} in the Raman spectrum of H_2O ice Ih and was tentatively assigned[99] to the rotational band. This frequency is, however, rather high for a rotational vibration,[99] and this assignment is not definitive. The unobserved H_2O analogue of the D_2O peak at 273 cm^{-1} presumably is buried under the H_2O peak at 268 cm^{-1} (Figure 3.5).

The symmetries of the Raman peaks due to the translational and rotational vibrations are assigned in Table 3.2 by the arguments used in Section 4.2 for the O-D stretching vibrations. Thus in the unanalyzed polarized spectra (Figures 3.9 to 3.11) both A_g and E_g vibrations are active in the Y(Z,Z+Y)X spectrum while only E_g vibrations are active in the Y(X,Z+Y)X spectrum. In the analyzed spectra (Figures 3.12 to 3.13) only A_g components should appear in the ZZ spectrum, if it is assumed that the crystal c-axis was nearly aligned with the Z laboratory axis. Through the convergence error[90] E_g components could appear in the ZZ spectrum, but presumably they would be stronger in the perpendicularly-polarized spectrum than in the ZZ spectrum.

Thus, of the nine features assigned to translational vibrations of ice II, six of E_g symmetry and two to five of A_g symmetry have been identified (Table 3.2). Of the features assigned to rotational vibrations, five of E_g symmetry and four to seven of A_g symmetry have been identified (Table 3.2). The observed number of vibrations of each symmetry is therefore in fair agreement with the numbers predicted (Table 1.3), $6\,A_g + 6\,E_g$ for the rotational vibrations and 6 A_g + 6 E_g for the translational vibrations.

The frequencies of the lattice vibrations observed in the Raman and absorption[1,2,41,42,132] spectra of D_2O ice II are combined in Tables 5.1 and 5.2. Twelve[1,2] features in the infrared spectrum of D_2O ice II have been assigned to rotational vibrations,[1,2,41] and ten[132] features have been assigned to translational vibrations.[42,132] The symmetry, A_u or E_u, of the vibration responsible for a particular absorption is unknown.[1,2,41,42,132] There is at present no evidence that any of the features listed in Table 5.1 are due to overtone or combination transitions so they are all assigned to fundamental transitions.

For ice IX, eleven Raman features are assigned to rotational vibrations and eleven Raman features are assigned to translational vibrations in Table 3.4, on the basis of their frequencies and isotope ratios. As for ice II, all of these are assigned to fundamental transitions. Thus the number of observed Raman transitions of ice IX is much less than the number predicted, that is twenty-two rotational and twenty-one translational vibrations.

No polarization information was obtained for ice IX, because the samples were polycrystalline (Section 3.5), so the Raman spectra give no indication of the symmetries of the vibrations responsible for the observed features. However, the E vibrations are active in both the infrared and Raman spectra, so coincident peaks in the two spectra are tentatively assigned accordingly.

Table 5.1

Summary of observed Raman and infrared frequencies of the rotational vibrations of D_2O ice II.

Raman			infrared		
10 K[a]	35 K	100 K	10 K[b]	35 K[c]	100 K[b]
			713 ± 5	713	705 ± 5
~695	~695				
~620	~620				
			610 ± 2	609	606 ± 2
			595 ± 2	595	592 ± 2
~577	~575	~570			
			563 ± 2	563	559 ± 2
~545	~544	~543			
531.0	530.3 ± 0.5	527.8 ± 0.5			
			528 ± 3	528	528 ± 3
519.8	518.8 ± 0.5	515.1 ± 0.5			
			511 ± 2	510	507 ± 2
484.2	482.9 ± 0.5	478.8 ± 0.5			
			476 ± 2	476	471 ± 2
453.7	452.6 ± 0.5	448.6 ± 0.5			
			444 ± 2	443	439 ± 2
439	438 ± 0.6	~434			
419.8	418.6 ± 0.5	414.8 ± 0.5			
			407 ± 3	405	402 ± 3
			365 ± 3	364	361 ± 3
360.7	360.0 ± 0.4	356.2 ± 0.5	360 ± 3		
358	~357	~353			
			328 ± 3	328	324 ± 3

[a] Extrapolated value.

[b] Reference 2.

[c] Interpolated value.

Table 5.2

Summary of observed Raman and infrared frequencies of the translational vibrations of D_2O ice II.

Raman			infrared	
10 K[a]	35 K	100 K	4.3 K[b]	100 K[c]
~311	310 ± 1	307±1.5		
			284.5 ± 0.5	279.6 ± 0.5
~273	272.8 ± 0.4	272 ± 1		
257.3	257.1 ± 0.4	256.8 ± 0.5		
~245	~245 (sh)		248.5 ± 0.5	242.5 ± 0.5
			233.6 ± 0.5	229.9 ± 0.5
			205 ± 1 (sh)	
194.9	194.6 ± 0.4	192.9 ± 0.5	195 ± 0.5 (sh)	191 ± 1 (sh)
			185.5 ± 0.5	
182.4	181.9 ± 0.4	180.0 ± 0.5	182.5 ± 0.5	180.4 ± 0.5
			149.0 ± 0.5	146.6 ± 0.5
148.2	147.5 ± 0.4	145.6 ± 0.5		
			135.0 ± 0.5	133.0 ± 0.5
			106.0 ± 0.5	104.3 ± 0.5
100.4	100.2 ± 0.4	99.6 ± 0.5	—	
69.2	69.1 ± 0.4	68.8 ± 0.5		

[a] Extrapolated value.

[b] Reference 132.

[c] Reference 42.

The features in the infrared[1,2,41,42,132] and Raman spectra of D_2O ice IX that are assigned to rotational and translational vibrations are collected in Tables 5.3 and 5.4. An unassigned absorption peak may result from either an A_2 vibration or an E vibration that scatters too weakly to be observed in the Raman spectrum. An unassigned Raman peak may result from an A_1, B_1 or B_2 vibration, a transverse optic E vibration that is too weak to be observed in the infrared, or a longitudinal optic E mode (Sections 1.4 and 4.4). The spectra of the lattice vibrations of ice IX cannot be assigned further from the available experimental evidence.

A discussion of the relative Raman intensities of the rotational, translational, and bond-stretching vibrations in H_2O and D_2O ice II and ice IX concludes this section. The relative integrated scattering intensities, corrected from observed counts-per-second to calibrated energy per square centimeter per second, are reported in Section 3.5. The integrated scattering intensity of the rotational vibrations relative to that of the bond-stretching vibrations is 0.030 ± 0.007, while that of the translational vibrations relative to that of the stretching vibrations is 0.076 ± 0.012, for both H_2O and D_2O ices II and IX.

The near equality of this ratio for the translational vibrations of an ice is unexpected, based on the theory of absolute scattering intensities. Under the harmonic approximation the scattering intensity of a vibration is proportional to $(\partial \underset{\sim}{\alpha}/\partial Q_k)^2$,[56] where Q_k is the mass-weighted normal

Table 5.3

Summary of observed Raman and infrared frequencies of the rotational vibrations of D_2O ice IX.

Raman			infrared			
10 K[a]	35 K	100 K	10 K[b]	35 K[c]	100 K[b]	
			678 ± 3	678	674 ± 3	
~651	~650	~635				
			633 ± 4	632	627 ± 4	
~606	~605	~600	607 ± 3	607	602 ± 3	E
			595 ± 3			
			549 ± 2	548	545 ± 2	
~532	~531	~525				
510.8	510.3 ± 0.3	504.3 ± 0.5				
492.2	490.9 ± 0.3	485.8 ± 0.5	489 ± 2	488	485 ± 2	E ?
~463	462 ± 3	~459				
445.9	444.9 ± 0.6	441.0 ± 0.5	445 ± 2	444	441 ± 2	E
~420	418.5 ± 0.6	~411	421 ± 2			
~412	411.0 ± 0.6		412 ± 2	411	408 ± 2	E
~393	392 ± 1½	389	393 ± 2	392	389 ± 2	E
378.8	378.4 ± 0.5	374.9 ± 0.5				

[a] Extrapolated value.

[b] Reference 2.

[c] Interpolated value.

Table 5.4

Summary of observed Raman and infrared frequencies of the translational vibrations of D_2O ice IX.

Raman			infrared		
10 K[a]	35 K	100 K	4.3 K[b]	100 K[c]	
~298	297 ± 1	~292	295 ± 1	295 (sh)	E
			274.8 ± 0.5	270.2 ± 0.4	
			246.5 ± 0.5	242.8 ± 0.9	
234.5	234.3 ± 0.5	230.5 ± 0.5	234 ± 1 (?)		E
			208 (sh)		
204.6	204.2 ± 0.3	202.0 ± 0.5	205.3 ± 0.5	201.5 ± 0.7	E
~190	189.6 ± 0.3	~187			
			187 (sh)		E ?
184.5	184.2 ± 0.3	182.4 ± 0.5			
~175	173.6 ± 0.3	~172			
			161.5 ± 0.5	159.9 ± 0.1	
			159 (sh) (?)		
			136.8 ± 0.5	134.7 ± 0.1	
99.2	99.0 ± 0.3	97.0 ± 0.5			
~85	84.9 ± 0.3	~83			
74.5	74.4 ± 0.3	73.6 ± 0.5			
71.1	71.0 ± 0.3	70.2 ± 0.5	70.8 ± 0.5	70.2 ± 0.7	E
~35	34.3 ± 0.3	~34.3			

[a] Extrapolated value.

[b] Reference 132.

[c] Reference 2.

coordinate. Thus, to good approximation for the vibrations of molecules or crystals, the intensity of scattering by a vibration is proportional to the G-matrix element of the principal coordinate contributing to the normal mode.[56]

The appropriate G-matrix elements for the bond-stretching, rotational and translational vibrations are the reduced masses of the O-H and O-D oscillators, the inverse moments of inertia, and the inverse molecular masses respectively. Therefore the absolute scattering intensities of the bond-stretching and rotational vibrations of a D_2O ice are expected to be about 0.5 of those of the corresponding H_2O ice, while those of the translational vibrations of the H_2O and D_2O ice should be almost equal. It follows that the intensity of the rotational vibrations relative to that of the bond-stretching vibrations should be the same for the H_2O and D_2O ice, and the intensity of the translational vibrations relative to that of the bond stretching vibrations of the D_2O ice should be almost twice that for the H_2O ice. As noted above, this is not observed.

Marechal et al observed a similar anomaly in the absolute absorption intensities of the isotopic forms of gaseous dimers of carboxylic acids[133] and of crystalline formic acid.[134] They attributed[133] this behavior to the effects of the mechanical and electrical anharmonicities of the hydrogen bond.

5.3 The Normal Coordinate Calculation of Lattice Vibrations

In the previous chapter the absorption and scattering of radiation by the O-D stretching modes was interpreted in large measure by the results of normal coordinate and intensity calculations. There is little doubt that the interpretation is essentially correct, although imperfect, because the calculations were based on a simple force field whose force constants were given values that are known to be of the correct magnitude. Further, the intensity calculations were based on the simplest model that is undoubtedly correct in essence if not in detail. In short, the interpretation is the more credible because simple models that used physically reasonable parameters were used.

In this chapter the spectra of the translational and rotational vibrations are investigated theoretically in the same way. As will be seen, the infrared and Raman spectra due to the translational vibrations are quite well explained by simple models for the forces and intensities. However it has not been possible to find a simple short-range force field that reproduces the correct isotope ratios when the rotational and translational vibrations are treated together, yet still generates the correct ranges of frequencies of the translational and rotational vibrations.

In the calculations of the previous chapter the potential energy was written as a function of internal coordinates $\underset{\sim}{R}$ by supplying parameters to represent the force constants, i.e. the second derivatives of the potential energy with respect to the internal coordinates. These parameters formed the $\underset{\sim}{F}$ matrix and the kinetic energy was written as a function of the internal coordinates through the $\underset{\sim}{G}$ matrix, following the GF matrix method of Wilson, Decius and Cross.[56] The GF matrix was then diagonalized to give the frequencies and eigenvectors, the latter relating the internal and normal coordinates.

Algebraically the method can be summarized as

$$2\,V = \underset{\sim}{R}^{\dagger}\,\underset{\sim}{F}\,\underset{\sim}{R} \tag{5.1}$$

$$2\,T = \underset{\sim}{P}^{\dagger}\,\underset{\sim}{G}\,\underset{\sim}{P} \tag{5.2}$$

where $\underset{\sim}{R}^{\dagger}$ is the transpose of $\underset{\sim}{R}$, and $\underset{\sim}{P}$ is the matrix of momenta conjugate to the internal coordinates. The secular equation is

$$|\underset{\sim}{G}\,\underset{\sim}{F} - \underset{\sim}{E}\,\underset{\sim}{\lambda}| = 0 \tag{5.3}$$

where $\underset{\sim}{E}$ is a unit matrix and $\underset{\sim}{\lambda}$ is a diagonal matrix of the eigenvalues. Solution of the secular equation yields the frequencies and the eigenvectors, which form the $\underset{\sim}{L}$ matrix in $\underset{\sim}{R} = \underset{\sim}{L}\,\underset{\sim}{Q}$, where $\underset{\sim}{Q}$ is the vector of normal coordinates. The $\underset{\sim}{G}$ and $\underset{\sim}{F}$ matrices may, if desired, be transformed to their symmetrized forms

$$\underset{\sim}{G}_s = \underset{\sim}{U}\,\underset{\sim}{G}\,\underset{\sim}{U}^{\dagger} \tag{5.4}$$

$$\underset{\sim}{F}_s = \underset{\sim}{U}\,\underset{\sim}{F}\,\underset{\sim}{U}^{\dagger} \tag{5.5}$$

where $\underset{\sim}{U}$ is defined by $\underset{\sim}{S} = \underset{\sim}{U}\,\underset{\sim}{R}$, and $\underset{\sim}{S}$ is the column vector of symmetry coordinates. Thus the secular equation $|\underset{\sim}{G}_s\,\underset{\sim}{F}_s - \underset{\sim}{E}\,\underset{\sim}{\lambda}| = 0$ may be solved to yield the eigenvectors $\underset{\sim}{L}_s = \underset{\sim}{U}^{\dagger}\,\underset{\sim}{L}$

in terms of the symmetry coordinates, so that $\underset{\sim}{S} = \underset{\sim}{L}_s \underset{\sim}{Q}$. This use of symmetry is, however, a convenience, not an essential part of the method.

The normal coordinate calculations of lattice vibrations are based on the same principles, but appear to be more complex because the potential energy is most easily written in terms of one set of coordinates but the eigenvectors are more useful if the matrices that are diagonalized are written in terms of a different set. The coordinates in which the matrix to be diagonalized, and hence the eigenvectors, are written are called the problem coordinates in this thesis.

The problem coordinates of the calculations of this chapter make use of a simple approximation called the rigid molecule approximation.[135] Under this approximation the molecules are treated as rigid bodies that can translate and rotate but cannot deform. Thus the lattice vibrations are calculated without consideration of the intramolecular vibrations. The rigid molecule approximation is particularly well suited to calculations for the ices, for it is well established (Section 1.5) that the intermolecular vibrations are virtually independent of the intramolecular vibrations because their frequencies are so different.

The problem coordinates of these calculations are then the normal coordinates $\underset{\sim}{Q}_{TR}$ that represent rotation and translation of the rigid molecules. Since the calculations are restricted to zero wavevector vibrations in this work, $\underset{\sim}{Q}_{TR}$

is of dimension 6 times the number of molecules in the cell. Thus we seek the matrices $\underset{\sim}{F}_Q$ and $\underset{\sim}{G}_Q$ which are defined by

$$2V = \underset{\sim}{Q}_{TR}^{\dagger} \underset{\sim}{F}_Q \underset{\sim}{Q}_{TR} \tag{5.6}$$

$$2T = \underset{\sim}{P}_Q^{\dagger} \underset{\sim}{G}_Q \underset{\sim}{P}_Q \tag{5.7}$$

where $\underset{\sim}{P}_Q$ is the vector of the momenta conjugate to the normal coordinates of the rigid molecules. Then the secular equation $|\underset{\sim}{G}_Q \underset{\sim}{F}_Q - \underset{\sim}{E}\underset{\sim}{\lambda}| = 0$ is solved to find the frequencies and the eigenvectors, which form the matrix $\underset{\sim}{L}_Q$ defined by $\underset{\sim}{Q}_{TR} = \underset{\sim}{L}_Q \underset{\sim}{Q}_C$ where $\underset{\sim}{Q}_C$ is the column vector of the normal coordinates of the crystal. Again, symmetry may be used during this procedure if desired.

The matrix $\underset{\sim}{G}_Q$ is trivial by the definition of normal coordinates,[56] being the unit matrix $\underset{\sim}{E}$. To find the $\underset{\sim}{F}_Q$ matrix one chooses a model to define the forces that act in the crystal when certain selected distances and angles change. These selected distances and angles are intermolecular, and their displacements from equilibrium form a set of coordinates that is here designated by the vector $\underset{\sim}{D}$ and called the intermolecular coordinates. The potential energy is then written as

$$2V = \underset{\sim}{D}^{\dagger} \underset{\sim}{F}_D \underset{\sim}{D} \quad . \tag{5.8}$$

The construction of $\underset{\sim}{F}_D$ is usually done in one of two ways, which may be mixed. First, the elements of $\underset{\sim}{F}_D$ can be regarded as parameters that are chosen to have physically reasonable values. This approach is the dominant one in this work. It is limited by the number of parameters for which one can choose physically reasonable values with confidence, and is usually restricted to short-range forces, as in this work. The second method of constructing $\underset{\sim}{F}_D$ is to use interatomic potential functions, which are most commonly of the types[136]

$$V = -A/r^6 + B\exp(-C\,r) \tag{5.9}$$

or

$$V = -A/r^6 + B/r^{12} \tag{5.10}$$

The force constants in $\underset{\sim}{F}_D$ which correspond to changes in, say, intermolecular hydrogen-hydrogen distances can be calculated from such a function for all equilibrium distances, thus greatly reducing the number of parameters at the expense of the assumption that the form of the potential function is correct. This method is also used in this work, using a potential function for a pair of water molecules calculated by Clementi et al[137] from the results of ab initio calculations. This method is more complicated than the first one, because the chosen parameters or the crystal structure must be adjusted to ensure that the energy of the crystal given by the function is a minimum with respect to the variables in $\underset{\sim}{D}$ at the geometry chosen.

The conversion of $\underset{\sim}{F}_D$ to $\underset{\sim}{F}_Q$ is as follows. The matrix $\underset{\sim}{B}$, defined by $\underset{\sim}{D} = \underset{\sim}{B}\,\underset{\sim}{Y}$, defines the coordinates $\underset{\sim}{D}$ in terms of crystal-fixed Cartesian displacement coordinates of the atoms, $\underset{\sim}{Y}$, so that the potential energy in terms of these coordinates is given by

$$2\,V = \underset{\sim}{Y}^{\dagger}\ \underset{\sim}{B}^{\dagger}\underset{\sim}{F}_{D}\ \underset{\sim}{B}\ \underset{\sim}{Y} \tag{5.11}$$

The normal coordinates of the rigid molecule can be related to the $\underset{\sim}{Y}$ through Cartesian displacement coordinates of each atom based on molecule-fixed axes. Thus, $\underset{\sim}{L}_{X}^{TR}$ relates the normal coordinates of the rigid molecule $\underset{\sim}{Q}_{TR}$ to Cartesian displacement coordinates of the atoms with respect to the inertial axes of the molecule, $\underset{\sim}{X}$, through $\underset{\sim}{X} = \underset{\sim}{L}_{X}^{TR}\ \underset{\sim}{Q}_{TR}$. The elements of $\underset{\sim}{L}_{X}^{TR}$ are the same for all equivalent molecules in the crystal. The molecule-fixed and crystal-fixed Cartesian coordinates are related by $\underset{\sim}{Y} = \underset{\sim}{T}\,\underset{\sim}{X}$, where $\underset{\sim}{T}$ is different for each molecule in the cell. Thus $\underset{\sim}{Y} = \underset{\sim}{T}\ \underset{\sim}{L}_{X}^{TR}\ \underset{\sim}{Q}_{TR}$, so that

$$\begin{aligned} 2\,V &= \underset{\sim}{Q}_{TR}^{\dagger}\ [\ (\underset{\sim}{L}_{X}^{TR})^{\dagger}\ \underset{\sim}{T}^{\dagger}\ \underset{\sim}{B}^{\dagger}\ \underset{\sim}{F}_{D}\,\underset{\sim}{B}\ \underset{\sim}{T}\ \underset{\sim}{L}_{X}^{TR}\ ]\ \underset{\sim}{Q}_{TR} \\ &= \underset{\sim}{Q}_{TR}^{\dagger}\ \underset{\sim}{F}_{Q}\ \underset{\sim}{Q}_{TR} \end{aligned} \tag{5.12}$$

When symmetry-adapted linear combinations of the normal coordinates of the rigid molecules, defined by $\underset{\sim}{S}^{TR} = \underset{\sim}{U}^{TR}\,\underset{\sim}{Q}_{TR}$, are used, as in this work, the expression for the potential energy in terms of these coordinates is

$$\begin{aligned} 2\,V &= (\underset{\sim}{S}^{TR})^{\dagger}\ [\underset{\sim}{U}^{TR}\ (\underset{\sim}{L}_{X}^{TR})^{\dagger}\ \underset{\sim}{T}^{\dagger}\ \underset{\sim}{B}^{\dagger}\underset{\sim}{F}_{D}\,\underset{\sim}{B}\ \underset{\sim}{T}\,\underset{\sim}{L}_{X}^{TR}\ (\underset{\sim}{U}^{TR})^{\dagger}]\ \ \underset{\sim}{S}^{TR} \\ &= (\underset{\sim}{S}^{TR})^{\dagger}\ \underset{\sim}{F}_{QS}\ \underset{\sim}{S}^{TR} \end{aligned} \tag{5.13}$$

Calculation of $\underset{\sim}{F}_{Q}$ or $\underset{\sim}{F}_{QS}$ by this method assumes that the transformation from $\underset{\sim}{R}$ to $\underset{\sim}{Y}$ is linear. It has been suggested that this is an objection to the method[138,139] and programs that do not make this assumption have been written.

In some tested cases[138] little difference between the two methods has been noted, although for α-N_2 the error in the frequencies of the rotational vibrations ranges from 25 to 44 %.[138-141] The error can, of course, be effectively corrected by adjusting the parameters of the potential model,[138] although the physical meaning of the revised force constants may be decreased by this procedure.

The method described above is applied to the calculations reported in this chapter through the programs AXSMZ and LSMX written by Shimanouchi and his colleagues.[142] The programs were tested with a calculation of the lattice vibrations of crystalline benzene, which crystallizes in the space group Pbca (D_{2h}^{15}) with four molecules in the unit cell, on C_i sites.[143] The changes in the intermolecular hydrogen-hydrogen distances whose equilibrium lengths are 3.0 Å or less formed the set of intermolecular coordinates. The atomic positions, $\underset{\sim}{T}$ matrices and intermolecular force constants were given by Harada and Shimanouchi,[144] and the $\underset{\sim}{L}_X^{TR}$ matrices[135] were computed from their data. The values of the parameters were therefore the same as those used by Harada and Shimanouchi in their calculation[144] of the intramolecular and lattice vibrations of crystalline benzene. The effect of the intramolecular normal coordinates on the intermolecular normal coordinates, which they included,[144] is expected[145] to be small, and therefore the calculated frequencies from the two calculations should be very similar. The results are compared in Table 5.5. The small differences

Table 5.5

Comparison of calculated frequencies of
the lattice vibrations of benzene at 269 K.

	This work	Harada and Shimanouchi[a]		This work	Harada and Shimanouchi[a]
A_g	78.6	79	A_u	61.2	58
	60.0	57		49.8	49
	28.3	28		26.6	26
B_{1g}	103.1	100	B_{1u}	44.8	44
	70.2	72		31.1	30
	64.3	60		0.0	-
B_{2g}	78.5	76	B_{2u}	60.8	57
	67.8	69		31.7	31
	57.2	56		0.0	-
B_{3g}	105.5	102	B_{3u}	60.0	58
	70.0	70		33.8	34
	36.0	33		0.0	-

[a] Reference 144.

between the two sets of frequencies can be attributed to the combined effects of the inclusion of intermolecular-intramolecular vibrational interactions by Harada and Shimanouchi,[144] and a probable difference in precision between their reported[144] and actual numbers used in the calculation. The reasonable agreement in Table 5.5 strongly suggests that the programs AXSMZ and LSMX implemented in this work function as intended.

Harada and Shimanouchi's vibrational calculation for benzene[144] was the first "full molecule" treatment of benzene, and has been followed by reports of a number of similar calculations, differing in the method of calculation, the crystal structure and the potential function. The far-infrared[146] and low-frequency Raman[147] spectra were also re-examined. Our understanding of the lattice vibrations has therefore progressed beyond Harada and Shimanouchi's interpretation, the results of which appear in Table 5.5. The calculation by Califano et al[145] for benzene at 138 K was particularly successful. Their method was similar to that of Harada and Shimanouchi,[144,148] but they extended the interaction radius from 3.14[148] to 6 Å and made use of two intermolecular atom-atom potentials empirically obtained by Williams.[149,150] The results of Califano et al[145] were similar to those of Harada and Shimanouchi[148] for benzene at 138 K and were in good agreement with the experimental results.[146,147]

5.4 General Discussion of the Calculations of the Lattice Vibrations of Ices II and IX

The magnitudes of the force constants used in any normal coordinate calculations are of obvious importance in determining the frequencies and eigenvectors. Another important aspect is the matrix that transforms the $\underset{\sim}{G}\,\underset{\sim}{F}$ or $\underset{\sim}{F}$ matrix from the internal or intermolecular coordinates to the problem coordinates. For the lattice vibrational calculations reported here, this transformation matrix is defined by the matrices $\underset{\sim}{B}$, $\underset{\sim}{T}$, $\underset{\sim}{L}_X^{TR}$ and $\underset{\sim}{U}^{TR}$ (equation (5.13)). The structural model for the crystal and the model for the potential energy, i.e. the choice of intermolecular coordinates, determines $\underset{\sim}{B}$,[56] the structural model alone determines $\underset{\sim}{T}$ and $\underset{\sim}{L}_X^{TR}$ (Appendix III), and the choice of problem coordinates, i.e. the choice of symmetry coordinates, determines $\underset{\sim}{U}^{TR}$ (Appendix III). In this section the structural model, the set of intermolecular coordinates and the symmetry coordinates are defined for each normal coordinate calculation that is reported in Sections 5.5 to 5.7.

The calculations reported in this chapter are summarized in Table 5.6. The calculations in the first group were restricted in $\underset{\sim}{U}^{TR}$ to only those symmetry coordinates that describe translational degrees of freedom of the molecules. These will be called the translational symmetry coordinates. These calculations are reported in Sections 5.5. The second group of calculations used the full $\underset{\sim}{U}^{TR}$ matrix, i.e. both the rotational and translational symmetry

ONLY COPY AVAILABLE
SEULE COPIE DISPONIBLE

Table 5.6

Summary of normal coordinate calculations of lattice vibrations of ices II and IX. Location of discussion and frequency tabulations for each force field.

Translational vibrations

true structure model (Section 5.5)	point mass model (Section 5.5)
A^{OX}: O··O stretch O··O··O deformation O··O', O··O' interaction ice II: p.205; Tables 5.7, 5.8 (intensities: Table 5.9) ice IX: p.216; Table 5.11 (intensities: Table 5.12)	A^{M}: M··M stretch M··M··M deformation ice II: p.205; Table 5.7 ice IX: p.216; Table 5.11
A^{D}: H··O stretch O··O··O deformation ice II: p.205; Table 5.7	

Translational and rotational vibrations

true structure model (Section 5.6)	linear structure model (Section 5.6)
A^{OX}(H··O-H): O··O stretch O··O··O deformation H··O-H deformation ice II: p.225; Table 5.15 ice IX: p.227; Appendix VI	A^{OX}(H··O-H): O··O stretch O··O··O deformation H··O-H deformation ice IX: p.227; Appendix VI
A^{OX}(O··O-H): O··O stretch O··O··O deformation O··O-H deformation ice II: p.228; Table 5.16 ice IX: p.230; Appendix VI	
A^{OX}(H-H'): O··O stretch O··O··O deformation H-H' interaction ice II: p.231; Table 5.17 ice IX: p.231; Appendix VI	A^{OX}(O-H··O, H-H'): O··O stretch O··O··O deformation O-H··O linear angle bend H-H' interaction ice IX: p.233; Table 5.18
(Section 5.7) CP: H-H', H-M^-, H-O, O-O, M^--M^- ice II: p.237; Table 5.19	

coordinates. These calculations are reported in Sections 5.6 and 5.7.

The calculations for which the problem coordinates were the translational symmetry coordinates are discussed first in this section. One structural model that was used is the true structure of the ice[34,39] assuming the molecules to be rigid. The mass of each molecule is distributed over all three atoms, but the model in fact behaves as if the total mass of each molecule is concentrated at the position of the oxygen atom, particularly with intermolecular coordinates involving only interactions between the oxygen atoms. In the other model, which is called the point mass model, the total mass of each molecule was placed at M, the position of the center of mass of the molecule in the true structure. Under the point mass model, therefore, the structural models for H_2O and D_2O crystals of the same ice are not identical, but the differences are in fact small.

For these calculations, the potential energy due to the translational vibrations was given by

$$2\,V_T = \sum_i (k_r)_i\, r_i^2 + \sum_{ij} (k_{rr'})_{ij}\, r_i r_j + \sum_{k\ell} (H_\theta)_{k\ell}\, a_k a_\ell\, \theta_{k\ell}^2 \tag{5.14}$$

where the intermolecular coordinates r_i and $\theta_{k\ell}$ must still be specified for each force field. In equation (5.14) r_i is the displacement of distance i, $\theta_{k\ell}$ is the change in the angle formed by the two distances of equilibrium lengths

a_k and a_ℓ, $(k_r)_i$ and $(H_\theta)_{k\ell}$ are the stretching and angle deformation force constants, and $(k_{rr'})_{ij}$ is the interaction force constant between two stretching coordinates. Two sets of coordinates were used with the true structure model (Table 5.6). In coordinate set A^{OX} the r_i were O··O stretching coordinates and the $\theta_{k\ell}$ were O··O··O angle deformation coordinates. In coordinate set A^D the $\theta_{k\ell}$ were as in A^{OX}, but the r_i were H··O stretching coordinates. Under the point mass model the coordinate set A^M, which is analogous to A^{OX}, is used. Thus, the r_i were M··M stretching coordinates and the $\theta_{k\ell}$ were M··M··M angle deformation coordinates.

The suitability of each of these force fields depends on its ability to reproduce the translational lattice motions of an ice without introducing significant rotational character into the eigenvectors even when the problem coordinates include the rotational symmetry coordinates. Rotational motion is not possible under the point mass model. It is, however, possible under the true structure model, and therefore both coordinate sets A^{OX} and A^D were tested (Section 5.5) by including the rotational as well as translational symmetry coordinates in $\underset{\sim}{U}^{TR}$.

The calculations of the translational and rotational vibrations together are reported in Sections 5.6 and 5.7. In the true structure model (Table 5.6), the rigid H_2O or D_2O molecules had the equilibrium molecular configurations of the true crystal structure,[34,39] and thus the hydrogen bonds were distorted from linearity by 2 to 14° for ice II and by 5 to 15° for ice IX. In the linear structure model, each hydrogen or deuterium atom was repositioned by up to 0.015 Å so that it lay on the line joining the oxygen atoms of the donor and acceptor molecules of the hydrogen bond.

To ensure that the calculated rotational vibrations are uncoupled from the translational vibrations, as is observed experimentally (Section 3.5), the potential energy due to the rotational vibrations must be written in terms of intermolecular coordinates that reorient the H_2O or D_2O molecules but do not significantly translate them. It was not obvious which coordinates meet this requirement. Four sets of coordinates were constructed by combining the coordinate set A^{OX}, which was found to be adequate to describe purely translational motion, with intermolecular coordinates chosen for their abilities to reorient molecules.

Coordinate set $A^{OX}(H\cdot\cdot O\text{-}H)$, in which the $H\cdot\cdot O\text{-}H$ angle deformation coordinates were the intermolecular coordinates for reorientation, was used with both structural models. Coordinate set $A^{OX}(O\cdot\cdot O\text{-}H)$, which used the set of $O\cdot\cdot O\text{-}H$ angle deformation coordinates, was tested with the true structure model only. Under both $A^{OX}(H\cdot\cdot O\text{-}H)$ and $A^{OX}(O\cdot\cdot O\text{-}H)$ the rotational potential energy was given by

$$2\,V_R = \sum_{k\ell} a_k\, a_\ell\, (H_\phi)_{k\ell}\, \phi_{k\ell}^2 \qquad (5.15)$$

where $\phi_{k\ell}$ is the angle deformation coordinate and the meanings of the symbols are the same as in equation (5.14).

Coordinate set A^{OX}(O-H··O; H-H') used the O-H··O linear angle deformation coordinates and the set of nearest-neighbour H-H' interactions and can only be applied to the linear structure model. Under this model the potential energy was given by

$$2 V_R = \sum_{k\ell} (H_\Delta)_{k\ell} \, \phi_{k\ell}^2 + \sum_i k_i^H r_i^2 \qquad (5.16)$$

where r_i is the change in the distance between the i^{th} pair of hydrogen atoms on nearest-neighbour water molecules, $\phi_{k\ell}$ is the O-H··O angle deformation coordinate, and k_i^H and $(H_\Delta)_{k\ell}$ are the corresponding force constants. $(H_\Delta)_{k\ell}$ has the dimensions of energy in equation (5.16).

Coordinate set A^{OX}(H-H'), with the set of nearest-neighbour H,H' interactions, was used with the true structure model. The expression for the rotational potential energy under A^{OX}(H-H') was thus the second summation in equation (5.16). The calculations using these four coordinate sets are reported in Section 5.6.

A fifth coordinate set, CP, expressed all of the intermolecular forces as interactions between the oxygen atoms, hydrogen atoms and the centers of negative charge (M^-) of hydrogen-bonded nearest-neighbour water molecules. The expression given by Clementi et al[137] for the potential energy of interaction of two water molecules was used for this calculation, and therefore the H-H', H-M^-, H-O, O-O' and M^--M^- interactions were considered. The expression for the potential energy due to translational and rotational vibrations was thus

$$2V = \sum_i k_i r_i^2 \qquad (5.17)$$

where r_i is the change in the interatomic distance, k_i is the second derivative of the potential energy with respect to the interatomic distance of interest, and the summation is over all interactions.

5.5 Discussion of the Calculations of the Translational Vibrations of Ice II and Ice IX

5.5.1 Ice II

Ice II crystallizes with twelve molecules in the unit cell, on two non-equivalent six-fold sites of C_1 symmetry (Section 1.3). Thus the structure contains four non-equivalent types of hydrogen bonds and twelve non-equivalent types of O··O··O angles in each unit cell.

The simplest force field is considered first. In force field T_1^{II} a single force constant $k_r = 0.22$ mdyne Å^{-1} was associated with all twenty-four hydrogen-bond stretching coordinates and a second force constant $H_\theta = 0.0075$ mdyne Å^{-1} associated with all seventy-two angle deformation coordinates (equation (5.14)); the stretch-stretch interaction force constant $k_{rr'}$ was set to zero. The frequencies that were calculated for ice II with two structural models and three coordinate sets A^{OX}, A^{D} and A^{M} are listed in Table 5.7. The problem coordinates were limited to the translational symmetry coordinates. For this and all other calculations of the lattice vibrations of ice II the normal coordinates

Table 5.7

Calculated frequencies for ice II, with A^{ox}, A^{D} and A^{M} and with translational problem coordinates.

		true structure model				point mass model		
		A^{ox}		A^{D}		A^{M}		
force field[a]		$k_{O\cdot O}=0.22$		$k_{D\cdot O}=0.22$		$k_{M\cdot M}=0.22$		
T_1^{II}		$H_{O\cdot O\cdot O}=0.0075$		$H_{O\cdot O\cdot O}=0.0075$		$H_{M\cdot M\cdot M}=0.0075$		
	no.	H_2O	D_2O	H_2O	D_2O	H_2O	D_2O	ν_H/ν_D
A_g	7	278.6	264.2	278.2	263.9	279.4	265.8	1.051
	8	208.5	197.8	206.4	195.7	209.0	198.6	1.052
	9	164.5	156.0	164.3	155.8	163.4	153.9	1.062
	10	102.8	97.5	100.9	95.7	102.6	97.1	1.057
	11	87.3	82.8	87.4	82.9	88.2	84.5	1.044
	12	78.6	74.6	79.3	75.2	78.8	74.9	1.052
A_u	19	297.8	282.5	299.6	284.1	297.6	282.1	1.055
	20	254.0	240.9	254.3	241.2	254.9	242.5	1.051
	21	222.0	210.5	222.0	210.6	220.9	208.5	1.059
	22	154.4	146.4	156.2	148.2	154.2	145.9	1.057
	23	122.9	116.6	121.6	115.3	122.2	115.1	1.062
	24	0	0	0	0	0	0	-
E_g	31	286.0	271.3	287.7	272.9	286.5	272.2	1.053
	32	237.8	225.5	237.4	225.2	237.7	225.3	1.055
	33	196.4	186.3	194.9	184.8	196.0	185.5	1.057
	34	177.3	168.2	179.1	169.8	176.5	166.6	1.059
	35	94.4	89.5	94.0	89.1	94.2	89.2	1.056
	36	66.7	63.2	66.3	62.9	66.7	63.2	1.055
E_u	43	249.3	236.4	251.4	238.5	249.8	237.5	1.052
	44	241.5	229.1	239.0	226.7	242.4	230.8	1.050
	45	190.7	180.9	189.9	180.1	190.0	179.4	1.059
	46	134.9	127.9	133.7	126.8	133.9	126.1	1.062
	47	110.5	104.8	110.7	105.0	110.5	104.8	1.054
	48	0	0	0	0	0	0	-

[a] Units are mdyne $\mathring{A}^{-1}$.

that are numbered from 1 to 12 are of A_g symmetry, those from 13 to 24 are of A_u symmetry, those from 25 to 36 are of E_g symmetry, and those from 37 to 48 are of E_u symmetry. Under the true structure model, the isotope ratios ν_H/ν_D are, and must be, equal to $(m^{H_2O}/m^{D_2O})^{\frac{1}{2}} = 1.0544$ where m^{H_2O} is the total mass of an H_2O molecule. Under the point mass model the isotope ratios are 1.05 ± 0.01, the range apparently resulting from the different positions of the center of mass in H_2O and D_2O. Clearly (Table 5.7) the calculated translational frequencies are nearly the same under all of the structural models and coordinate sets considered here.

By extending the set of problem coordinates to include the rotational symmetry coordinates, the molecules are allowed to respond to forces that tend to reorient them. The effect of this is shown in Table 5.8, with force field T_1^{II}. When no reorienting forces are included in a force field the first six frequencies in each block should be exactly zero and the other frequencies should be the same with and without the rotational symmetry coordinates. This was, and must be, the case with the point mass model, and was nearly the case with coordinate set A^{OX} under the true structure model, but it was far from true with coordinate set A^D under the true structure model. Thus coordinate set A^{OX} was used in the remainder of the calculations of the translational vibrations, since it approached a description of purely translational motion and, in contrast to coordinate set A^M under the point mass model, could be expanded to include

ONLY COPY AVAILABLE
SEULE COPIE DISPONIBLE

Table 5.8

Calculated frequencies and isotope ratios for ice II, with A^{OX} and A^{D} and with translational and rotational coordinates.

	A^{OX}			A^{D}				A^{OX}			A^{D}		
	$k_{O\cdot O}=0.22$			$k_{D\cdot O}=0.22$				$k_{O\cdot O}=0.22$			$k_{D\cdot O}=0.22$		
	$H_{O\cdot O\cdot O}=0.0075$			$H_{O\cdot O\cdot O}=0.0075$				$H_{O\cdot O\cdot O}=0.0075$			$H_{O\cdot O\cdot O}=0.0075$		
no.	H_2O	D_2O	ν_H/ν_D	H_2O	D_2O	ν_H/ν_D	no.	H_2O	D_2O	ν_H/ν_D	H_2O	D_2O	ν_H/ν_D
A_g							E_g						
1	1.4	1.6		68.7	50.1	1.371	25	1.9	1.3		41.4	31.6	1.310
2	*	*		39.8	30.6	1.301	26	1.4	*		28.8	21.3	1.35
3	*	*		14.4	10.5	1.371	27	*	*		14.0	10.1	1.39
4	*	*		3.9	2.8	1.4	28	*	*		3.4	2.5	1.4
5	*	*		*	*	-	29	*	*		*	*	-
6	*	*		*	*	-	30	*	*		*	*	-
7	282.0	270.6	1.042	306.3	285.0	1.075	31	288.3	275.6	1.046	305.4	286.9	1.064
8	216.4	212.3	1.019	258.8	241.4	1.072	32	242.3	234.1	1.035	266.6	248.2	1.074
9	171.4	168.7	1.016	185.5	178.7	1.038	33	203.7	199.7	1.020	226.2	214.5	1.055
10	106.7	104.7	1.019	106.8	104.5	1.022	34	181.6	175.4	1.035	211.0	194.9	1.083
11	87.8	83.5	1.051	93.4	86.6	1.079	35	97.8	95.6	1.023	99.9	96.8	1.032
12	80.8	78.4	1.031	87.1	82.6	1.054	36	69.3	67.9	1.021	69.8	68.0	1.026
A_u							E_u						
13	2.2	2.1		55.0	42.0	1.310	37	2.1	1.8		49.7	38.2	1.301
14	1.0	1.3		36.1	26.7	1.352	38	1.4	*		38.8	28.6	1.357
15	*	*		12.1	8.7	1.39	39	*	*		22.6	16.3	1.39
16	*	*		4.3	3.1	1.4	40	*	*		6.8	4.8	1.4
17	*	*		*	*	-	41	*	*		*	*	-
18	*	*		*	*	-	42	*	*		*	*	-
19	297.9	282.6	1.054	309.0	289.1	1.069	43	253.3	244.3	1.037	287.9	266.6	1.080
20	257.9	248.1	1.040	278.3	258.4	1.077	44	246.1	237.3	1.037	271.7	254.9	1.066
21	230.8	226.8	1.018	255.0	243.7	1.046	45	196.3	190.7	1.029	211.5	200.0	1.058
22	161.0	158.4	1.016	196.0	182.6	1.073	46	140.6	138.3	1.017	156.3	147.2	1.062
23	127.5	124.7	1.022	128.5	125.8	1.021	47	113.9	110.8	1.028	115.4	112.0	1.030
24	0	0	-	0	0	-	48	0	0	-	0	0	-

* less than 1 cm^{-1}.

Units of force constants are mdyne $\mathring{A}^{-1}$.

intermolecular coordinates for rotational motion.

The infrared and Raman intensities of the normal coordinates of translation were calculated with BMBP, the program described in Section 4.3. The eigenvectors $\underset{\sim}{L}_R$ required for use with BMBP are given by

$$\underset{\sim}{R} = \underset{\sim}{L}_R \underset{\sim}{Q} = (\underset{\sim}{B}\ \underset{\sim}{T}\ \underset{\sim}{L}_X^{TR}\ (\underset{\sim}{U}^{TR})^{\dagger})\ \underset{\sim}{L}_S \underset{\sim}{Q} \qquad (5.18)$$

where the matrix in parentheses is given by the program AXSMZ, $\underset{\sim}{L}_S$ is the eigenvector matrix from LSMX and is defined by $\underset{\sim}{S} = \underset{\sim}{L}_S \underset{\sim}{Q}$, $\underset{\sim}{R}$ and $\underset{\sim}{S}$ are the vectors of intermolecular and symmetry coordinates, and $\underset{\sim}{Q}$ is the vector of the normal coordinates of the crystal.

The infrared intensities calculated under force field T_1^{II} for D_2O ice II are given in Table 5.9 for $\mu'(r) = 1.44$ D Å^{-1} and $\mu'(\theta) = 0.0$ D, and for $\mu'(r) = 1.44$ D Å^{-1} and $\mu'(\theta) = 0.26$ D, where $\mu'(r)$ is the dipole moment derivative with respect to bond stretching coordinates r and $\mu'(\theta)$ is that resulting from the angle deformation coordinate θ. Whalley[151] has estimated that $\mu'(r)$ is about 1.44 D Å^{-1}. If the dipole moment change on displacement of an oxygen atom parallel to the O··O bond, $\mu'(r)$, is an order of magnitude larger than that for motion perpendicular to the bond,[152] then $\mu'(\theta)$ is about 0.26 D per radian. The direction of $\mu'(\theta)$ was taken to be along the bisector of the O··O··O angle and $\mu'(r)$ was assumed to point along the bond.

The polarizability ellipsoids were assumed to be cylindrically symmetrical about the bonds and about the

ONLY COPY AVAILABLE
SEULE COPIE DISPONIBLE

Table 5.9

Calculated frequencies and infrared and Raman intensities for D_2O ice II, with A^{ox} and two force fields.

		Force field T_1^{II}: k_r=0.22 mdyne Å^{-1}, k_θ=0.0075 mdyne Å^{-1}					Force field T_2^{II}: k_r=0.22 mdyne Å^{-1}, k_θ=0.0075 mdyne Å^{-1} $k_{rr'}$=-0.022 mdyne Å^{-1}				
			Calculated intensities[a]					Calculated intensities[a]			
			infrared		Raman			infrared		Raman	
	no.	ν_{calc}	μ(r)	μ(r) +μ(θ)	α(r)	α(r) +α(θ)	ν_{calc}	μ(r)	μ(r) +μ(θ)	α(r)	α(r) +α(θ)
A_g	7	264.2	0	0	42.0	18.8	285.8	0	0	36.5	17.4
	8	197.8	0	0	45.1	28.3	213.4	0	0	43.6	30.0
	9	156.0	0	0	1.20	1.30	143.6	0	0	0.76	1.07
	10	97.5	0	0	0.74	2.09	96.6	0	0	0.84	2.17
	11	82.8	0	0	2.51	0.15	81.8	0	0	2.07	0.18
	12	74.6	0	0	5.82	0.69	74.7	0	0	5.15	0.41
A_u	19	282.5	0.003	0.004	0	0	308.4	0.004	0.005	0	0
	20	240.9	0.014	0.016	0	0	262.4	0.012	0.014	0	0
	21	210.5	0.231	0.228	0	0	227.8	0.226	0.223	0	0
	22	146.4	0.497	0.429	0	0	137.2	0.498	0.426	0	0
	23	116.6	0.003	0.016	0	0	116.5	0.008	0.024	0	0
	24	0	0	0	0	0	0	0	0	0	0
E_g	31	271.3	0	0	44.4	26.5	294.0	0	0	36.9	24.3
	32	225.5	0	0	100.	100.	238.5	0	0	100.	100.
	33	186.3	0	0	20.2	27.9	184.8	0	0	24.5	37.3
	34	168.2	0	0	43.1	47.9	157.2	0	0	35.0	45.9
	35	89.5	0	0	2.15	21.0	89.4	0	0	2.08	22.0
	36	63.2	0	0	0.29	7.6	63.3	0	0	0.25	8.3
E_u	43	236.4	0.180	0.180	0	0	252.9	0.154	0.172	0	0
	44	229.1	0.030	0.032	0	0	241.4	0.240	0.216	0	0
	45	180.9	0.966	0.948	0	0	170.1	0.736	0.724	0	0
	46	127.9	0.482	0.442	0	0	112.3	0.526	0.484	0	0
	47	104.8	0.002	0.004	0	0	104.8	0.004	0.006	0	0
	48	0	0	0	0	0	0	0	0	0	0

[a] The intensities reported in the column headed μ(r) were calculated with μ(r)=1.44 D Å and with μ(θ)=0.0 D. Those in the column headed μ(r) + μ(θ) were calculated with μ(r) = 1.44 D Å and μ(θ) = 0.26 D. The Raman intensities in the column headed α(r) were calculated with RP(r) = 10 and $\alpha_{\parallel}(\theta) = \alpha_{\perp}(\theta) = 0$. Those in the column headed α(r) + α(θ) were calculated with RP(r) = RP(θ) = 10 and $\alpha_{\parallel}(r) = \alpha_{\parallel}(\theta) = 1$.

bisectors of the O••O••O angles. There is at present no indication of the magnitudes of the elements of $\underset{\sim}{\alpha}'(r)$ and $\underset{\sim}{\alpha}'(\theta)$, the polarizability derivative tensors with respect to bond stretching and angle deformation coordinates. The relative Raman intensities calculated for D_2O ice II under force field T_1^{II} are given in Appendix IV for RP(r) = 2, 5, 10 and 20 with $\alpha_{\parallel}'(\theta) = \alpha_{\perp}'(\theta) = 0.0$, where $RP(r) = \alpha_{\parallel}'(r) / \alpha_{\perp}'(r)$. It is clear from Appendix IV that the relative intensities were rather insensitive to RP(r) for RP(r) between 5 and 20. A value of RP(r) = 10 was somewhat arbitrarily chosen for further calculations, and the same value was assumed for RP(θ). The calculated Raman intensities are given in Table 5.9 for RP(r) = 10 with $\alpha_{\parallel}'(\theta) = \alpha_{\perp}'(\theta) = 0.0$, and for RP(r)=RP(θ) = 10 with $\alpha_{\parallel}'(r) = \alpha_{\parallel}'(\theta)$.

Force field T_2^{II} is the same as T_1^{II}, but the stretch-stretch interaction force constant $k_{rr'}$ was -0.022 mdyne Å^{-1}. Only the interactions between O••O bonds with a common oxygen atom were considered, and the seventy-two of these in ice II were assumed to be equivalent. The frequencies and the infrared and Raman intensities calculated for D_2O ice II are given in Table 5.9. The range of frequencies above ~120 cm^{-1} in each block was greater by 26 to 33 % under T_2^{II} than under T_1^{II} but the intensities under T_1^{II} and T_2^{II} were very similar. In fact, other calculations with k_r between 0.20 and 0.30 mdyne Å^{-1} and H_θ between 0.0050 and 0.0075 mdyne Å^{-1} showed the calculated intensities to be much less sensitive than the calculated frequencies to the force field. The symmetrized eigenvectors calculated with force fields T_1^{II} and T_2^{II} are given in Appendix V and are quite similar.

The observed infrared[132] and Raman spectra of the translational vibrations of D_2O ice II are compared in Figure 5.1 to three of the calculated spectra from Table 5.9. Table 5.10 shows the assignment that is deduced from this comparison, for force fields T_1^{II} and T_2^{II}.

The assignment of the infrared spectrum is largely unambiguous and the simpler force field T_1^{II} fits the data better than T_2^{II}. Differences in detail exist, of course, because the force field and intensity models are exceedingly simple. The only difference that is particularly disturbing is the factor of about 100 between the calculated and experimental intensities at 106 cm^{-1} and a similar factor, about 30, between the intensities at 284 cm^{-1}. Of less, but still some, concern is the inability to explain the shoulders at 185 and 205 cm^{-1}. Otherwise the frequency and intensity fit is good enough to suggest that the assignment under T_1^{II} in Table 5.10 is essentially correct.

The assignment of the Raman spectrum under force field T_1^{II} is also acceptable (Table 5.10). It is usually easy to assign the experimental features to a vibration of the symmetry that was deduced from the polarization measurements. The only major defects are the frequency mismatch of ~13 % between the experimental features at 148, 257 and 310 cm^{-1}, and the calculated frequencies for modes 34, 32 and 31, to which they are assigned. Force field T_2^{II} corrects this

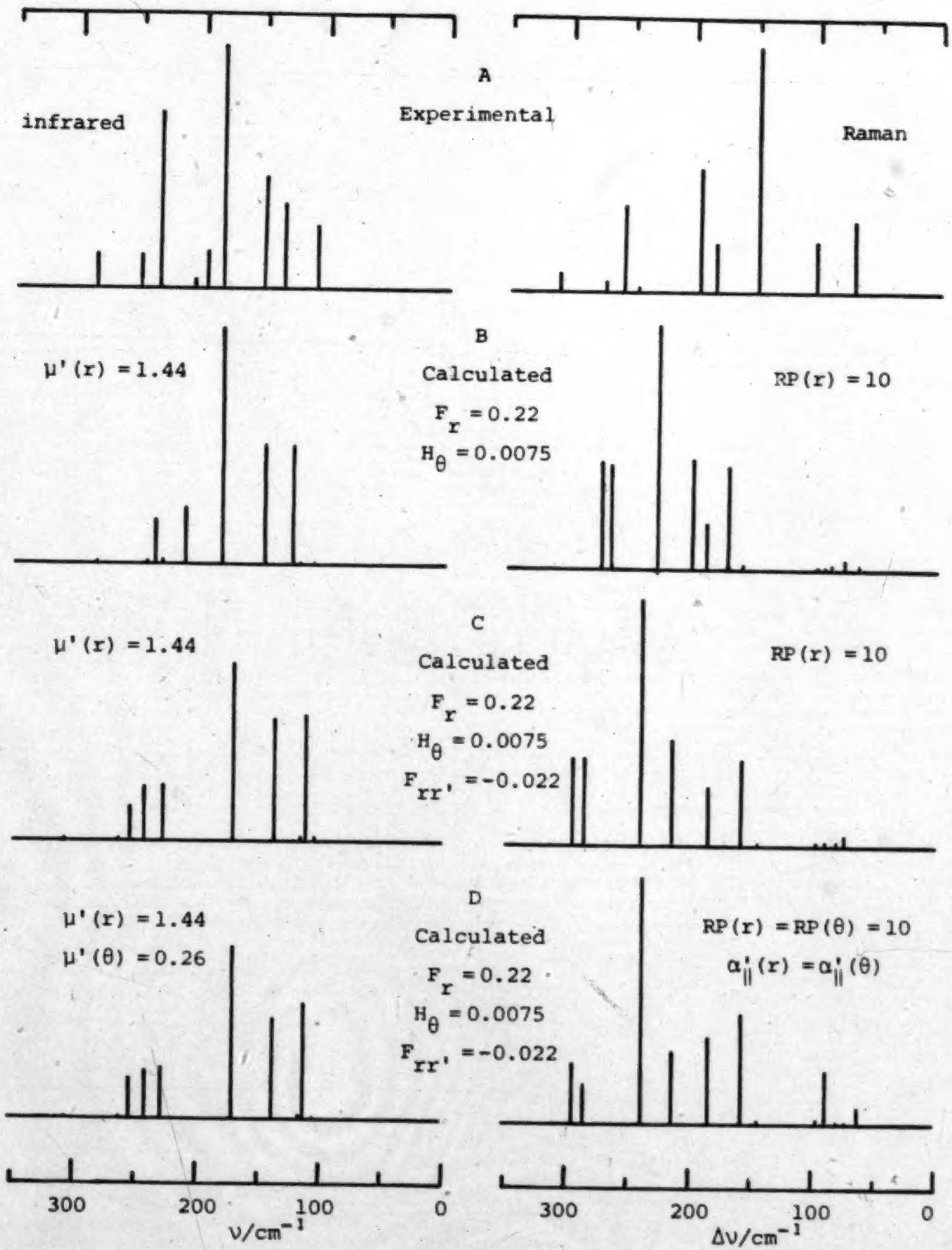

Figure 5.1 Observed and calculated infrared and Raman spectra of the translational vibrations of D_2O ice II.

ONLY COPY AVAILABLE
SEULE COPIE DISPONIBLE

Table 5.10

Assignment of the infrared and Raman spectra due to translational vibrations of D_2O ice II at 10 K.

observed			calculated					
			T_1^{II}			T_2^{II}		
ν/cm^{-1}	intensity	P[a]	mode[b]	ν/cm^{-1}	intensity[c]	mode[b]	ν/cm^{-1}	intensity[c]
infrared:								
106	m		47	105	0.003	47	105	0.005
			23	117	0.01			
135	m		46	128	0.4	46	112	0.5
						23	116	0.01
149	m		22	146	0.4	22	137	0.4
182	s		45	181	1.0	45	170	0.7
185	sh							
195	w		21	210	0.2	21	228	0.2
205	sh							
234	s		44	229	0.03	44	241	0.2
			43	236	0.2			
248	w		20	241	0.01	43	253	0.2
						20	262	0.01
284	w		19	282	0.003	19	308	0.05
Raman:								
69	m	E_g	36	63	0.3 - 8	36	63	0.2 - 8
			12	75	6 - 1	12	75	5 - 0.4
			11	83	2 - 0.1	11	82	2 - 0.2
			35	90	2 - 20	35	89	2 - 20
100	m	$E_g(+A_g?)$	10	98	1	10	97	1
			9	156	1	9	144	1
148	s	E_g	34	168	45	34	157	40
182	m	$E_g(+A_g?)$	33	186	25	33	185	30
195	ms	A_g	8	198	35	8	213	40
245	sh							
257	ms	E_g	32	225	100	32	239	100
273	w	A_g	7	264	30	7	286	25
310	w	$E_g(+A_g?)$	31	271	30	31	294	30

[a] Vibrational symmetry deduced from polarization data.

[b] Modes 7 to 12 are A_g, 19 to 24 are A_u, 31 to 36 are E_g, and 43 to 48 are E_u.

[c] Infrared: $d_k(\partial\mu/\partial Q_k)^2$, where d_k is the degeneracy of the vibration and the units are $D\ \mathring{A}^{-1}\ (amu)^{-\frac{1}{2}}$.

defect to some extent but worsens the overall fit to the two spectra.

It is concluded that the calculated spectra of ice II agree well with the observed spectra in view of the extremely simple force fields and intensity models that were used. Table 5.10 is believed to give an assignment that gives a useful indication of the origin of the spectra even if the details are modified by future, more sophisticated calculations. There is little merit to using more complicated parametric force fields because the values of the parameters can not be supported by independent evidence. Thus future calculations to extend this work will probably be most satisfactory if they are based on one of the many intermolecular potentials for water-water interactions that are being developed by other methods.[137,153,154]

5.5.2 Ice IX

Ice IX contains twelve molecules in the unit cell, on one eight-fold site of C_1 symmetry and one four-fold site of C_2 symmetry (Section 1.3). Thus it has three non-equivalent types of hydrogen bonds and ten non-equivalent types of O••O••O or M••M••M angles. In force field T_1^{IX}, a single force constant $k_r = 0.20$ mdyne $\mathring{A}^{-1}$ was used for all of the three types of hydrogen-bond stretching coordinates and $H_\theta = 0.0075$ mdyne $\mathring{A}^{-1}$ was used for all ten types of angle deformation coordinates.

The frequencies calculated with T_1^{IX} and the translational problem coordinates are given in Table 5.11 for coordinate set A^{OX} under the true structure model and for coordinate set A^{M} under the point mass model. Normal coordinates of ice IX that are numbered from 1 to 8 are of A_1 symmetry, from 9 to 18 are of A_2 symmetry, from 19 to 28 are of B_1 symmetry, from 29 to 36 are of B_2 symmetry, and from 37 to 54 are of E symmetry. The isotope ratios ν_H/ν_D of the translational vibrations of ice IX were 1.0544 under the true structure model, as for ice II, and 1.05 ± 0.02 under the point mass model. The true structure model with coordinate set A^{OX} was used in all further calculations of ice IX reported in this and the following section. The Raman intensities calculated with $RP(r) = 2$, 5, 10 and 20 are given in Appendix IV. As for ice II, the relative Raman intensities were rather insensitive to RP(r) for RP(r) between 5 and 20, and so a value of $RP(r) = 10$ was arbitrarily chosen for further calculations. The infrared and Raman intensities calculated under force field T_1^{IX} and the true structure model are given in Table 5.12, where the values of $\mu'(r)$, $\mu'(\theta)$, $\underset{\sim}{\alpha}'(r)$ and $\underset{\sim}{\alpha}'(\theta)$ were the same as used for ice II in Table 5.9.

Force field T_2^{IX} used a single force constant for the O··O··O angle deformation coordinates, but three force constants for the hydrogen-bond stretching coordinates. To reflect the relative strengths of the hydrogen bonds, those for which the oxygen-oxygen distances are 2.7504 Å, 2.7628 Å, and 2.7971 Å were assigned force constants of 0.21, 0.20 and

Table 5.11

Calculated frequencies for ice IX, with A^{OX} and A^{M} and with translational problem coordinates.

		true structure model			point mass model		
force field[a]		A^{OX}			A^{M}		
T_1^{IX}		$k_{O\cdot\cdot O} = 0.20$			$k_{M\cdot\cdot M} = 0.20$		
		$H_{O\cdot\cdot O\cdot\cdot O} = 0.0075$			$H_{M\cdot\cdot M\cdot\cdot M} = 0.0075$		
	no.	H_2O	D_2O	ν_H/ν_D	H_2O	D_2O	ν_H/ν_D
A_1	5	260.8	247.4	1.054	263.7	252.0	1.046
	6	181.2	171.9	1.054	180.5	170.6	1.058
	7	100.5	95.3	1.055	99.9	94.4	1.058
	8	85.5	81.0	1.056	88.1	85.5	1.030
A_2	14	238.6	226.3	1.054	237.7	224.8	1.057
	15	220.6	209.3	1.054	220.5	209.0	1.055
	16	145.7	138.2	1.054	143.6	134.5	1.068
	17	78.3	74.3	1.054	79.6	76.6	1.039
	18	0	0	-	0	0	-
B_1	24	253.2	240.2	1.054	249.8	234.3	1.066
	25	207.4	196.7	1.054	207.1	197.0	1.051
	26	201.4	191.0	1.054	202.4	191.7	1.056
	27	105.8	100.3	1.055	105.0	99.0	1.061
	28	64.1	60.8	1.054	64.4	61.2	1.052
B_2	33	255.0	241.8	1.055	253.1	238.7	1.060
	34	223.5	212.0	1.054	228.0	219.6	1.038
	35	169.8	161.1	1.054	169.3	160.0	1.058
	36	83.4	79.1	1.054	83.4	79.2	1.053
E	46	254.1	241.0	1.054	255.6	243.8	1.048
	47	246.5	233.8	1.054	246.0	232.7	1.057
	48	225.2	213.6	1.054	224.5	212.4	1.057
	49	213.1	202.1	1.054	213.4	202.9	1.052
	50	168.0	159.3	1.055	167.3	157.9	1.060
	51	150.4	142.6	1.055	150.6	142.7	1.055
	52	92.7	88.0	1.053	91.4	85.6	1.068
	53	75.7	71.8	1.054	76.1	72.5	1.050
	54	0	0	-	0	0	-

[a] Units are mdyne Å^{-1}

Table 5.12

Calculated frequencies and infrared and Raman intensities
of the translational vibrations of D_2O ice IX,
with A^{OX} and two force fields.

		Force field T_1^{IX}:						Force field T_2^{IX}: k_r=0.19 to 0.21				
		k_r=0.20 mdyne $Å^{-1}$, H_θ= 0.0075 mdyne $Å^{-1}$						mdyne $Å^{-1}$, H_θ=0.0075 mdyne $Å^{-1}$				
			Calculated intensities[a]						Calculated intensities[a]			
			infrared		Raman				infrared		Raman	
	no.	ν_{calc}	$\mu(r)$	$\mu(r)+\mu(\theta)$	$\alpha(r)$	$\alpha(r)+\alpha(\theta)$		ν_{calc}	$\mu(r)$	$\mu(r)+\mu(\theta)$	$\alpha(r)$	$\alpha(r)+\alpha(\theta)$
A_1	5	247.4	0	0	32.8	53.6		246.8	0	0	29.7	49.0
	6	171.9	0	0	4.1	1.50		171.3	0	0	3.9	0.78
	7	95.3	0	0	27.3	28.9		95.3	0	0	25.6	26.0
	8	81.0	0	0	26.6	2.3		81.3	0	0	24.2	2.0
A_2	14	226.3	0.234	0.260	0	0		225.2	0.090	0.108	0	0
	15	209.3	1.045	1.005	0	0		208.0	1.197	1.167	0	0
	16	138.2	0.074	0.112	0	0		139.1	0.064	0.099	0	0
	17	74.3	0.008	0.017	0	0		74.1	0.009	0.019	0	0
	18	0	0	0	0	0		0	0	0	0	0
B_1	24	240.2	0	0	0.014	0.096		243.9	0	0	0.006	0.016
	25	196.7	0	0	22.2	13.2		192.8	0	0	66.2	43.2
	26	191.0	0	0	60.2	42.7		191.5	0	0	9.0	7.5
	27	100.3	0	0	0.38	0.16		100.4	0	0	0.31	0.126
	28	60.8	0	0	0.36	4.43		60.8	0	0	0.32	4.0
B_2	33	241.8	0	0	2.1	2.5		245.0	0	0	2.8	2.5
	34	212.0	0	0	10.7	1.18		211.4	0	0	8.6	0.75
	35	161.1	0	0	1.4	0.013		159.6	0	0	1.56	0.019
	36	79.1	0	0	0.057	0.002		79.2	0	0	0.046	0.002
E	46	241.0	0.032	0.036	3.4	6.0		241.5	0.026	0.034	4.3	7.0
	47	233.8	0.050	0.038	3.3	4.7		236.3	0.058	0.044	5.5	7.3
	48	213.6	0.122	0.202	100.	100.		209.9	0.126	0.192	100.	100.
	49	202.1	0.008	0.044	21.5	25.6		201.8	0.006	0.042	8.4	10.7
	50	159.3	1.078	1.152	6.0	1.23		160.3	1.046	1.130	5.3	1.11
	51	142.6	0.276	0.302	0.43	5.6		142.3	0.302	0.332	0.040	3.4
	52	88.0	0.016	0.034	0.41	5.0		88.0	0.014	0.032	0.27	5.1
	53	71.8	0.002	0.001	2.0	25.1		71.8	0.002	0.001	1.86	22.6
	54	0	0	0	0	0		0	0	0	0	0

[a] The infrared intensities in the column headed $\mu(r)$ were calculated with $\mu'(r) = 1.44$ D $Å^{-1}$ and $\mu'(\theta) = 0.0$ D. Those in the column headed $\mu(r) + \mu(\theta)$ were calculated with $\mu'(r) = 1.44$ D $Å^{-1}$ and $\mu'(\theta) = 0.26$ D. The Raman intensities in the column headed $\alpha(r)$ were calculated with RP(r) = 10 and $\alpha'_{\parallel}(\theta) = \alpha'_{\perp}(\theta) = 0$. Those in the column headed $\alpha(r) + \alpha(\theta)$ were calculated with RP(r) = RP(θ) = 10 and $\alpha'_{\parallel}(r) = \alpha'_{\parallel}(\theta) = 1$.

0.19 mdyne Å^{-1} respectively. The frequencies, and infrared and Raman intensities calculated under force field T_2^{IX} are given in Table 5.12. The frequencies and intensities were similar to those calculated under force field T_1^{IX}, with the greatest changes occurring to modes 25 and 26 which apparently switch positions. The symmetrized eigenvectors from force fields T_1^{IX} and T_2^{IX} are given in Appendix V.

The observed infrared[132] (Figure 1.12) and Raman (Figure 3.16) spectra of the translational vibrations of D_2O ice IX are compared in Figure 5.2 with three of the calculated spectra from Table 5.12, and the observed frequencies are assigned in Table 5.13.

The infrared spectrum can be readily assigned up to 250 cm^{-1} except for the shoulders at 159, 187 and 234 cm^{-1}. The two highest-frequency features, at 275 and 295 cm^{-1}, can not be assigned reasonably. The calculated modes that are not assigned to spectral features are calculated to have very low intensities. The main defect in the calculated spectrum is the intensity calculated near 73 cm^{-1}, which should be about ten times larger than it is. Otherwise the main spectral features are reproduced rather well.

All of the features in the Raman spectrum can be readily assigned to calculated modes of the correct relative intensity (within a factor of about 3), except for the highest- and lowest-frequency features, at 297 and 34 cm^{-1}. The latter is a very low-frequency O··O··O deformation vibration in a large unit cell, and it is likely that the omission of

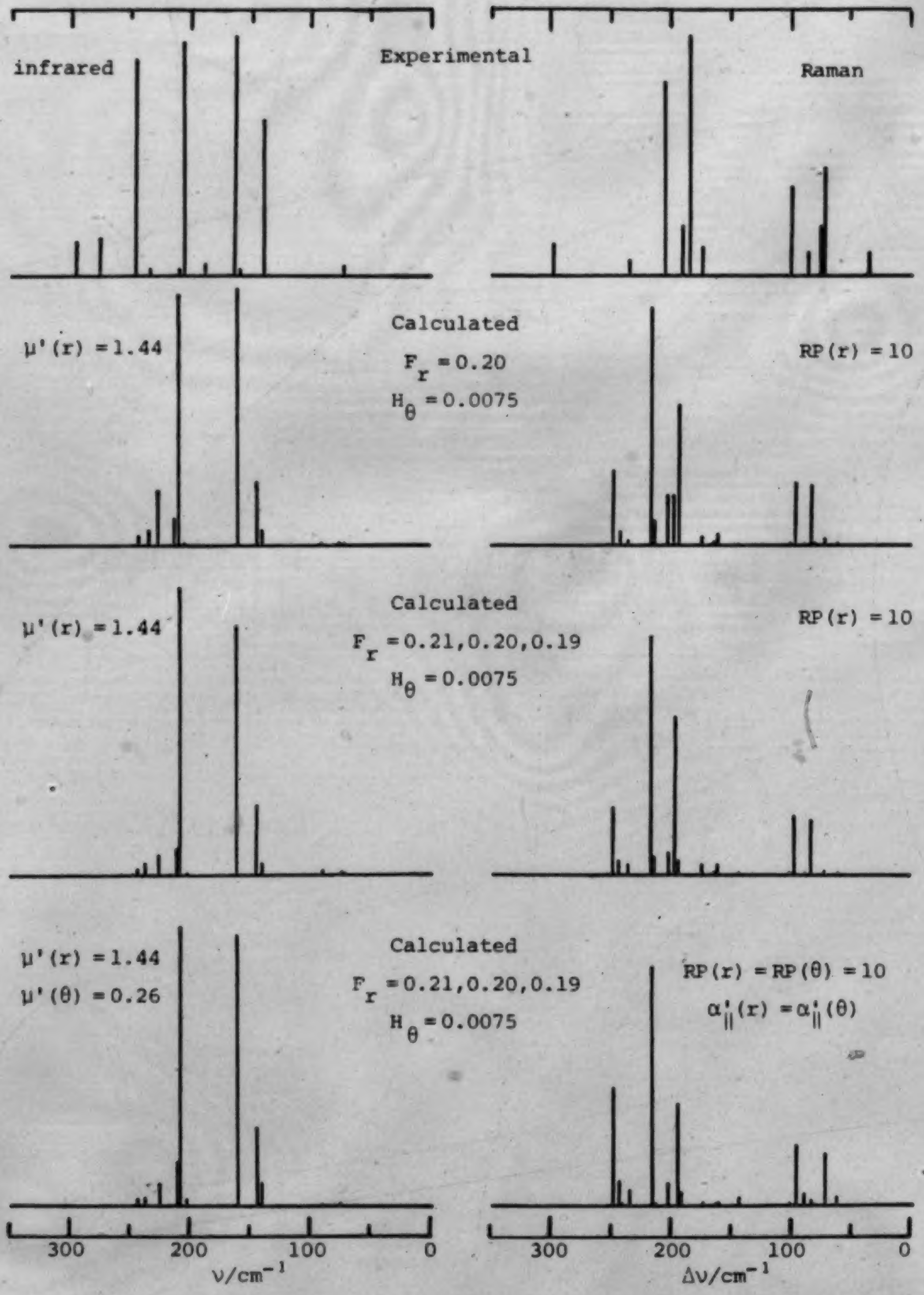

Figure 5.2 Observed and calculated infrared and Raman spectra of the translational vibrations of D_2O ice IX.

ONLY COPY AVAILABLE
SEULE COPIE DISPONIBLE

Table 5.13

Assignment of the infrared and Raman spectra due to translational vibrations of D_2O ice IX at 10 K.

	observed		calculated					
			T_1^{IX}			T_2^{IX}		
	ν/cm^{-1}	intensity	mode[a]	ν/cm^{-1}	intensity[b]	mode[a]	ν/cm^{-1}	intensity[b]
infrared:			53	72	0.002	53	72	0.002
	71	mw	17	74	0.01	17	74	0.01
			52	88	0.02	52	88	0.03
	137	s	16	138	0.1	16	139	0.1
			51	143	0.3	51	142	0.3
	159	sh						
	161	s	50	159	1.1	50	160	1.1
	187	sh						
			49	202	0.02	49	202	0.04
	205	s	15	209	1.0	15	208	1.2
	208	sh	48	214	0.1	48	210	0.2
	234	sh						
	246	s	14	226	0.25	14	225	0.1
			47	234	0.05	47	237	0.06
			46	241	0.04	46	241	0.03
	275	w						
	295	sh or w						
Raman:	34	w						
			28	62	0.4 - 4	28	61	0.3 - 4
	71	m	53	72	2 - 25	53	72	2 - 23
			36	79	0.06	36	79	0.01
	74	mw	8	81	27 - 2	8	81	24 - 2
	85	w	52	88	0.4 - 5	52	88	0.3 - 5
	99	m	7	95	29	7	95	26
			27	100	0.3	27	100	0.2
			51	143	0.4 - 6	51	142	0.04 - 3
			50	159	6 - 1	50	160	5 - 1
			35	161	1 - 0.01	35	160	2 - 0.02
	174	w	6	172	3	6	171	2
	184	s	26	191	50	26	191	8
			25	197	20	25	193	50
	190	sh	49	202	20	49	202	9
	204	s	34	212	11 - 1	48	210	100
			48	214	100	34	211	9 - 0.08
			47	234	4	47	236	6
			24	240	0.1	46	241	5
			46	241	5	24	244	0.01
			33	242	2	33	245	3
	234	w	5	247	40	5	247	40
	297	w						

[a] Modes 5 to 8 have A_1 symmetry, 14 to 18 have A_2, 24 to 28 have B_1, 33 to 36 have B_2, and 46 to 54 have E.

[b] Infrared: $d_k(\partial\mu/\partial Q_k)^2$, where d_k is the degeneracy of mode k. The units are D Å^{-1} (amu)$^{-\frac{1}{2}}$

second- and third-nearest neighbour interactions affects it strongly. The 297 cm^{-1} mode presents the same problem as for ice Ih (Section 1.5), and for ice IX it may or may not be a fundamental. The calculations do explain why twenty-one translational vibrations are not observed spectroscopically, giving very low intensities to several modes and grouping others together.

As was the case for ice II, the calculations are believed to reproduce the spectra very well for such simple models, and to yield a useful assignment. More sophisticated force fields will have to be supported by independent evidence before their use to improve upon the assignment in Table 5.13 is justified.

5.5.3 LO-TO Splitting of the Translational Vibrations of Ices II and IX

The longitudinal optic frequencies of the infrared-active translational vibrations of ice II and IX were calculated from the frequencies of the transverse optic modes, the dipole moment changes with respect to the normal coordinates, and equations (4.9) and (4.10). They are listed in Table 5.14. The frequencies of the transverse optic modes are the observed frequencies, as assigned in Tables 5.10 and 5.13, or were estimated from the calculated frequencies. The dipole moment derivatives that were used are the averages of the four values calculated under two force fields in Tables 5.9 and 5.12. The longitudinal optic modes are observable only in the Raman spectrum, so only the LO modes

Table 5.14

Calculated LO - TO splittings of the infrared-active translational vibrations of D_2O ices II and IX.

	Mode	$\nu^{TO}=\nu_{obs}$	$(\partial\underline{\mu}/\partial Q_k)^2$	ν^{LO}	$\nu^{LO}-\nu^{TO}$
Ice II					
A_u	19	285	0.004	285.0	0
	20	248	0.014	248.2	0
	21	195	0.227	199	4
	22	149	0.463	158	9
	23	116	0.013	116.3	0
	24	0	0		
E_u	43	240	0.086	241	1
	44	234	0.065	235	1
	45	182	0.422	189	7
	46	135	0.242	140.5	5
	47	106	0.004	106	0
	48	0	0		
Ice IX					
A_2	14	246	0.173	248	2
	15	205	1.104	221	16
	16	137	0.087	139	2
	17	71	0.013	71.6	0
	18	0	0		
E	46	298	0.016	298	0
	47	275	0.024	275	0
	48	205	0.080	206	1
	49	190	0.012	190	0
	50	162	0.551	172	10
	51	137	0.151	140	3
	52	85	0.012	85	0
	53	71	0.001	71	0
	54	0	0		

of the E vibrations of ice IX may be observed. However, of these vibrations, LO-TO splittings greater than 1 cm^{-1} occur only for $\nu_{50}(E)$ and $\nu_{51}(E)$, and neither of these was calculated to Raman-scatter strongly enough to contribute to observed peaks in the Raman spectra. Thus, as for the spectra of the O-D stretching vibrations (Section 4.5) no observed feature in the spectra of the translational vibrations of ice IX can be assigned exclusively to a longitudinal optic mode.

In Section 4.5 it was suggested that the breadth of the absorption due to the O-D stretching vibrations of ice II and ice IX is caused by the LO-TO splittings of many of the infrared-active vibrations, which were calculated to be large. The peaks of the far-infrared spectra of these ices, however, are sharper, and in fact the sharpness of these features has served[42] as an indicator of the degree of order of the ice. The calculated LO-TO splittings of the translational vibrations are much smaller than those of the O-D stretching vibrations (Table 4.5), which is consistent. The quantitative usefulness of Table 5.14 is, of course, questionable in light of the obvious defects of the frequency and intensity calculations (Figures 5.1 and 5.2) and the approximations of the bond moment calculations. However the largest calculated LO-TO splitting, which is about 15 cm^{-1}, can be regarded as a reasonable estimate of the maximum splitting that would be observed for any of the infrared-active translational vibrations of ice II or ice IX.

5.6 Calculations of the Translational and Rotational Vibrations of Ices II and IX using Parametrized Potential Functions

For these calculations, the potential energy due to the lattice vibrations was expressed in terms of hydrogen-bond-stretching coordinates, angle-deformation coordinates and interatomic hydrogen-hydrogen interaction coordinates. As discussed in Section 5.4, the four sets of intermolecular coordinates that are reported in this section were constructed from coordinate set A^{OX} (Section 5.5) and a set of intermolecular coordinates that describes mainly rotational motion.

In coordinate set A^{OX}(H••O-H), the reorientational motion was described by the forty-eight H••O-H valence angle bending coordinates of one unit cell of either ice. There are eight different types of H••O-H angles in ice II and six types in ice IX, but the simplest possible force field was assumed. Therefore the same force constant H_ϕ (equation (5.15)) was used for all of the H••O-H deformation coordinates of the ice.

The frequencies that were calculated for ice II under the true structure model and coordinate set A^{OX}(H••O-H) with $H_\phi = 0.160$ mdyne Å^{-1} and k_r and H_θ as in T_1^{II} (Table 5.9) are given in Table 5.15. The isotope ratios of the six highest-frequency normal coordinates of each block are ~1.35, except for modes 5, 6, 17, 18, 29, 30 and 42. The low isotope ratios for these modes, and the eigenvectors, show considerable translational character in addition to the predominantly

Table 5.15

Calculated frequencies of the translational and rotational vibrations of the true structure model of ice II, with coordinate set A^{ox}(H••O-H)

	no.	H_2O[a]	D_2O[a]	ν_H/ν_D		no.	H_2O[a]	D_2O[a]	ν_H/ν_D
A_g	1	1162.0	847.2	1.372	E_g	25	1162.8	837.9	1.388
	2	1133.2	813.6	1.393		26	922.7	690.5	1.336
	3	1015.4	732.5	1.386		27	893.7	671.3	1.331
	4	912.3	673.9	1.354		28	743.8	550.7	1.351
	5	672.2	515.3	1.304		29	651.9	502.0	1.299
	6	514.3	441.0	1.166		30	463.9	364.2	1.274
	7	270.7	247.3	1.095		31	290.3	265.6	1.093
	8	204.0	184.1	1.108		32	240.0	222.7	1.078
	9	160.5	143.4	1.120		33	190.2	173.3	1.098
	10	137.9	128.7	1.071		34	172.8	159.4	1.084
	11	105.1	96.9	1.085		35	94.6	83.0	1.140
	12	75.8	68.4	1.108		36	67.8	62.7	1.081
A_u	13	1065.7	782.2	1.362	E_u	37	1173.5	842.8	1.392
	14	997.3	737.9	1.352		38	1042.0	758.3	1.374
	15	797.4	591.0	1.349		39	1011.7	741.5	1.364
	16	766.4	572.9	1.338		40	803.7	611.6	1.314
	17	560.5	435.2	1.288		41	752.3	567.3	1.326
	18	437.2	355.2	1.231		42	423.9	361.8	1.172
	19	298.6	277.3	1.077		43	250.2	231.7	1.080
	20	256.4	241.0	1.064		44	238.4	218.0	1.094
	21	220.3	199.9	1.102		45	186.6	171.1	1.091
	22	154.5	137.5	1.124		46	143.2	131.4	1.090
	23	99.4	82.3	1.208		47	106.4	88.2	1.206
	24	0	0	-		48	0	0	-

[a] Force field: k_r = 0.22 mdyne $\mathring{A}^{-1}$, H_θ = 0.0075 mdyne $\mathring{A}^{-1}$,
H_ϕ = 0.160 mdyne $\mathring{A}^{-1}$.

rotational nature of these modes. The isotope ratios of ~1.10 of many of the six lowest-frequency normal coordinates of each block, and their eigenvectors, show these normal modes to be predominantly translational but with non-negligible contributions from rotational motion. Similar results were calculated with H_ϕ less than 0.16 mdyne $Å^{-1}$, except that the isotope ratios of the rotational vibrations are lower and those of the translational vibrations are greater than those calculated with $H_\phi = 0.16$ mdyne $Å^{-1}$. With H_ϕ greater than 0.16 mdyne $Å^{-1}$ the isotope ratios might approach the correct values but the range of calculated rotational frequencies would be higher than the observed range of frequencies.

Similar mixing of the normal modes was found for ice IX with A^{OX}(H··O-H). The frequencies and isotope ratios that were calculated with $H_\phi = 0.16$ mdyne $Å^{-1}$ and k_r and H_θ as in T_1^{IX} (Table 5.12) for both the true and linear structure models (Table 5.6) are given in Appendix VI. Frequency differences of up to 45 cm^{-1} for modes 2, 4, 12 and 40, and of up to 20 cm^{-1} for the others, result from the different structural models. Although the calculated frequencies were not independent of the structural model, the isotope ratios in Appendix VI show that the amount of mixing of translational and rotational motions was very similar for both structural models. Thus, calculations with the linear structure model can be useful although the details of the result may be unreliable. This is important because at least one calculation of the lattice vibrations of ice Ih[68,71] has used linear angle deformation coordinates, and a similar coordinate set was used in this work and is reported later in this section.

The above results show that considerable mixing of rotational and translational motion occurs in the normal coordinates of ices II and IX that were calculated with coordinate set A^{OX}(H••O-H) and the force field discussed above. No simple change to the force field can correct this problem, and there is no obvious justification for considerably different and more complex force fields based on coordinate set A^{OX}(H••O-H).

The next coordinate set, A^{OX}(O••O-H), used the set of forty-eight O••O-H angle deformation coordinates of one unit cell of ice II or ice IX, in addition to the intermolecular coordinates of A^{OX}. For the calculations reported here the force constant $H_{\phi'} = 0.060$ mdyne Å^{-1} was used with all eight or six types of O••O-H angle deformation coordinates of ice II or ice IX and the values of k_r and H_ϕ were as in force field T_1^{II} or T_1^{IX} (Tables 5.9 and 5.12). The frequencies and isotope ratios calculated under the true structure model for H_2O and D_2O ice II are given in Table 5.16. No isotope ratios are between 1.28 and 1.11, showing the calculated normal modes to be of nearly pure translational or rotational character and the eigenvalues confirmed this. The calculated rotational frequencies all lie within a range of ~100 cm^{-1}, which is much less than the observed range of ~400 to 500 cm^{-1}

Table 5.16

Calculated frequencies of the translational and rotational vibrations of the true structure model of ice II, with coordinate set A^{OX}(O••O-H)

	no.	H_2O^a	D_2O^a	ν_H/ν_D		no.	H_2O^a	D_2O^a	ν_H/ν_D
A_g	1	624.7	482.7	1.294	E_g	25	634.3	493.4	1.286
	2	614.2	474.1	1.296		26	602.3	463.3	1.300
	3	570.2	422.5	1.350		27	576.3	425.9	1.353
	4	558.8	411.6	1.358		28	563.3	415.6	1.355
	5	549.5	401.0	1.370		29	552.5	399.5	1.383
	6	545.5	387.8	1.407		30	537.7	387.9	1.385
	7	272.3	251.0	1.085		31	280.4	260.0	1.078
	8	200.9	182.6	1.100		32	235.0	218.2	1.077
	9	159.7	146.5	1.090		33	189.1	172.0	1.099
	10	103.5	96.0	1.078		34	173.1	159.4	1.086
	11	93.8	88.1	1.065		35	92.7	85.5	1.084
	12	78.9	73.3	1.076		36	65.8	61.0	1.079
A_u	13	636.1	494.3	1.287	E_u	37	629.2	484.7	1.298
	14	603.1	465.1	1.297		38	606.7	467.9	1.297
	15	575.6	426.9	1.348		39	573.4	427.6	1.341
	16	565.0	413.5	1.366		40	560.1	412.0	1.359
	17	552.0	398.4	1.386		41	550.8	401.6	1.372
	18	534.3	387.0	1.381		42	544.2	388.7	1.400
	19	297.2	280.3	1.060		43	244.9	227.5	1.076
	20	251.8	234.3	1.075		44	236.9	217.1	1.091
	21	214.7	194.7	1.103		45	184.3	168.1	1.096
	22	146.6	132.7	1.105		46	130.7	119.8	1.091
	23	116.5	105.3	1.106		47	110.5	101.2	1.092
	24	0	0	-		48	0	0	-

[a] Force field: k_r = 0.22 mdyne $\mathring{A}^{-1}$, H_θ = 0.0075 mdyne $\mathring{A}^{-1}$, $H_{\phi'}$ = 0.060 mdyne $\mathring{A}^{-1}$.

for H_2O ice II and 200 to 300 cm^{-1} for the D_2O, and, thus, poses a problem. A similar result was observed for ice IX. Thus this force field neglected the mechanism that couples the rotational vibrations. The O··O-H deformations could be coupled more directly through interaction terms in the potential energy or indirectly through the inclusion of intermolecular coordinates such as the interatomic hydrogen-hydrogen interaction, but neither approach was taken with A^{OX}(O··O-H).

In coordinate set A^{OX}(H-H') the ninety-six interactions in one unit cell between hydrogen atoms on nearest-neighbour water molecules were added to the coordinates of A^{OX}. The values of the second derivatives k^H of the potential energy with respect to the distance between hydrogen atoms r_{H-H} (equation (5.16)) were calculated from the function given by Clementi et al[137] for the potential energy of interaction between water molecules. The discussion of Clementi's complete potential function[137] ε is postponed until the following section since only the second derivative with respect to r_{H-H} is of concern here. The expression for k^H is

$$k^H = \partial^2\varepsilon/\partial r^2_{H-H} = 2\,q^2/r^3_{H-H} + a_2\, b_2^2 \exp(-b_1\, r_{H-H}) \quad (5.19)$$

where r_{H-H} is in atomic units of distance and q^2, a_2 and b_2 have values[137] of 0.514783, 1.061887 and 1.460975 a.u. Thus for r_{H-H} = 2.329 A, k^H is 0.01573 a.u. or 0.2449 mdyne Å^{-1}.

For the calculations reported here, similar values of k^H were grouped and the average value was used. In ice II there are sixteen non-equivalent H-H interactions between hydrogen-bonded molecules. The equilibrium H-H distances fall into the groups 2.33 Å, 2.43 to 2.50 Å, 3.16 to 3.38 Å, and 3.70 to 3.93 Å and those in a group were given the force constant values k^H of 0.24, 0.20, 0.072 and 0.044 mdyne $Å^{-1}$ respectively. In ice IX there are twelve non-equivalent H-H interactions. The equilibrium H-H distances fall into the groups 2.24 to 2.26 Å, 2.33 to 2.34 Å, 2.45 to 2.52 Å, 3.33 to 3.52 Å and 3.80 to 3.85 Å and those in a group were given the force constant values k^H of 0.28, 0.24, 0.19, 0.06, and 0.043 mdyne $Å^{-1}$ respectively.

Under the true structure models, the frequencies and isotope ratios that were calculated for ice II with the above values of k^H and force field T_1^{II} (Table 5.9) are given in Table 5.17, and those calculated for ice IX with the above values of k^H and force field T_1^{IX} (Table 5.12) are given in Appendix VI. The hydrogen-hydrogen interaction caused the frequencies of the translational vibrations to be larger than when calculated simply with T_1^{II} or T_1^{IX} (Tables 5.9 and 5.12), and the potential energy distributions showed that the H-H interactions provide the principle restoring forces to many of the translational vibrations. The eigenvectors showed that the vibrations in all of the symmetry blocks were generally mixtures of translational and rotational motions and furthermore, they were often quite different in the H_2O and D_2O ice. These two effects are reflected in the isotope ratios. The mixing of modes was not corrected by

Table 5.17

Calculated frequencies of the translational and rotational vibrations of the true structure model of ice II, with coordinate set $A^{ox}(H\text{-}H')$.

	no.	H_2O^a	D_2O^a	ν_H/ν_D		no.	H_2O^a	D_2O^a	ν_H/ν_D
A_g	1	737.0	543.0	1.357	E_g	25	723.7	532.3	1.360
	2	703.2	507.8	1.385		26	654.7	508.0	1.289
	3	670.5	482.8	1.389		27	601.9	463.6	1.298
	4	582.9	441.0	1.322		28	530.8	434.6	1.221
	5	518.7	417.5	1.242		29	476.6	363.3	1.312
	6	467.8	376.0	1.244		30	452.8	356.2	1.271
	7	402.6	311.1	1.294		31	399.4	308.4	1.295
	8	208.7	191.3	1.091		32	346.5	288.4	1.201
	9	192.7	185.6	1.038		33	213.5	202.8	1.053
	10	125.2	116.6	1.074		34	198.7	182.7	1.088
	11	110.2	104.2	1.058		35	116.7	109.2	1.069
	12	103.7	96.6	1.073		36	76.3	70.6	1.081
A_u	13	719.5	535.2	1.344	E_u	37	738.4	538.6	1.371
	14	657.4	510.9	1.287		38	679.6	509.1	1.335
	15	552.6	475.6	1.162		39	627.4	458.1	1.370
	16	535.3	427.6	1.252		40	584.3	430.4	1.358
	17	512.2	393.7	1.301		41	522.1	414.2	1.261
	18	427.9	339.3	1.261		42	425.6	359.0	1.186
	19	392.7	308.4	1.273		43	383.9	310.2	1.238
	20	334.6	244.4	1.369		44	306.9	246.3	1.246
	21	221.1	201.1	1.099		45	215.6	199.0	1.083
	22	179.3	175.4	1.022		46	168.9	166.2	1.016
	23	144.8	129.5	1.118		47	144.3	137.8	1.047
	24	0	0	-		48	0	0	-

[a] Force field: $k_r = 0.22$ mdyne $\mathring{A}^{-1}$, $H_\theta = 0.0075$ mdyne $\mathring{A}^{-1}$, $k^H = 0.044$ to 0.24 mdyne $\mathring{A}^{-1}$

changing the value of k_r from 0.22 to 0.11 mdyne $\mathring{A}^{-1}$ for ice II, even though the frequencies of modes 8, 9, 19, 21, 22, 31, 33, 34, 42, 44, and 46 decreased by 10 to 40 cm^{-1}.

The results obtained with coordinate set A^{ox}(H-H') clearly do not agree with experiment, and there is no simple way to modify the force field to correct this. The problem seems to arise from the influence of the H-H interaction on the translational vibrations. It might be corrected by varying the potential function and so changing the dependence of $\partial^2\varepsilon/\partial r^2_{H-H}$ on r_{H-H}, but it may also require the inclusion of interactions other than H-H', which were neglected in coordinate set A^{ox}(H-H').

The final coordinate set to be discussed in this section, A^{ox}(O-H··O, H-H'), used A^{ox} for the translational motion and for the reorientational coordinates combined the hydrogen-hydrogen interatomic interaction coordinates discussed above with the set of forty-eight linear angle deformation coordinates of one unit cell. The linear structure model (Section 5.4) was therefore used. There are eight non-equivalent O-H··O deformation coordinates in ice II and six in ice IX, with half of each describing deformation within the planes of the water molecules and half describing deformation in planes perpendicular to those of the water molecules. The force constant (equation (5.16)) $H_\Delta = 0.04$ mdyne $\mathring{A}$ was assigned to all of the O-H··O deformation coordinates, and the values of k^H were determined as discussed above for A^{ox}(H-H').

When the frequencies for ice IX were calculated with force field T_1^{IX} (Table 5.12), $H_\Delta = 0.040$ mdyne Å and all of the H-H' force constants set to zero, the isotope ratios were close to those observed, i.e. 1.32 to 1.41 calculated for the normal modes of rotation and 1.03 to 1.08 for the normal modes of translation. The frequencies of the translational normal modes were normally up to 5 cm^{-1}, but occasionally up to 12 cm^{-1}, higher than those reported in Table 5.12 for force field T_1^{IX} and the true structure model, but most of this difference was probably due to the different structural model used here. The eigenvectors showed little mixing of translational and rotational motion in the normal modes. The problem with this force field was that all of the rotational frequencies were calculated between 409 and 432 cm^{-1} for H_2O ice IX and between 289 and 323 cm^{-1} for D_2O ice IX, in disagreement with the observed ranges (Tables 3.4 and 5.3).

The frequencies given in Table 5.18 are calculated for the linear structure models of H_2O and D_2O ice IX, using $k_r = 0.12$ mdyne $Å^{-1}$, $H_\theta = 0.0025$ mdyne $Å^{-1}$, $H_\Delta = 0.040$ mdyne Å, and the values of k^H set as with coordinate set A^{OX}(H-H'). The O··O stretching force constant k_r and the O··O··O angle deformation force constant H_θ were smaller than when k^H equalled zero to partially offset the increase in the frequencies of the translational normal modes caused by the H-H' interactions. The isotope ratios were similar to those calculated with k^H set to zero, with none between 1.11 and

Table 5.18

Calculated frequencies of the translational and rotational vibrations of the linear structure model of ice IX, with coordinate set A^{OX}(O-H··O, H-H')

	no.	H_2O^a	D_2O^a	ν_H/ν_D		no.	H_2O^a	D_2O^a	ν_H/ν_D
A_1	1	901.4	654.1	1.378	B_2	29	932.1	664.5	1.403
	2	820.4	585.7	1.401		30	880.7	645.6	1.364
	3	725.4	520.9	1.393		31	629.4	455.6	1.381
	4	653.1	481.4	1.357		32	582.3	422.3	1.379
	5	427.3	384.8	1.110		33	405.3	374.4	1.083
	6	226.0	217.0	1.041		34	363.1	337.7	1.075
	7	117.7	114.4	1.029		35	188.6	181.8	1.037
	8	99.5	94.1	1.057		36	97.9	94.0	1.041
A_2	9	976.7	704.1	1.387	E	37	963.8	691.2	1.394
	10	902.2	656.9	1.373		38	915.5	661.5	1.384
	11	740.4	525.5	1.409		39	902.9	650.8	1.387
	12	696.7	494.9	1.408		40	824.3	587.7	1.403
	13	558.9	420.5	1.329		41	778.2	574.8	1.354
	14	324.9	298.6	1.088		42	684.6	495.3	1.382
	15	217.5	210.2	1.035		43	664.4	480.0	1.384
	16	140.9	136.9	1.029		44	621.4	449.1	1.383
	17	98.9	95.2	1.039		45	570.7	414.6	1.377
	18	0	0	-		46	398.1	370.5	1.074
						47	357.7	328.8	1.088
B_1	19	944.2	670.6	1.408		48	330.6	308.5	1.072
	20	855.3	618.5	1.383		49	237.3	224.3	1.058
	21	808.7	589.2	1.373		50	183.5	177.9	1.031
	22	620.5	462.4	1.342		51	160.9	158.6	1.015
	23	612.4	435.4	1.407		52	96.6	93.3	1.035
	24	401.6	375.4	1.070		53	89.0	86.3	1.031
	25	251.1	238.3	1.054		54	0	0	-
	26	207.8	198.6	1.046					
	27	107.5	105.3	1.021					
	28	64.5	61.6	1.047					

[a] Force field: $k_r = 0.12$ mdyne Å^{-1}, $H_\theta = 0.0025$ mdyne Å^{-1}, $H_\Delta = 0.04$ mdyne Å, $k^H = 0.043$ to 0.28 mdyne Å^{-1}.

1.33, but the rotational frequencies ranged from 560 to 975 cm^{-1} for H_2O ice IX and from 420 to 700 cm^{-1} for D_2O ice IX, in much better agreement with experiment. However the frequency range of 0 to 427 cm^{-1} that was calculated for the translational modes is higher than the observed range of 0 to 325 cm^{-1}. This range can only be decreased by decreasing the values of k^H, since the highest translational frequencies were determined mainly by the H-H' interactions, but this would also decrease the calculated range of rotational frequencies. It is not clear how to correct this problem. It is an equally serious problem that the calculated frequencies do not match those that are observed for the rotational vibrations. Such a fit depends on the values of k^H, but these can be meaningfully refined only through the parameters of the potential function (q^2, a_2 and b_2 in Clementi's function and in equation (5.19)). This capability does not exist in the programs that were used here. Of course such a fit would not be physically meaningful if important interactions other than the H-H' interactions were omitted and the refinement would merely compensate for their omission.

The simple parametrized force fields that were examined in this section have been poor to fair in reproducing the observed features of the infrared and Raman spectra due to the rotational vibrations of ices II and IX. More complex parametrized force fields that perform better can undoubtedly be devised, but with the necessary increase in the number of parameters the result is less likely to be physically significant.

5.7 Calculation of the Lattice Vibrations of Ice II using Clementi's Interatomic Interaction Potential Function for Water Molecules

The use in normal coordinate analyses of functions that describe the lattice energy of the crystal in terms of interatomic interactions between the molecules of the crystal has met with good success in the treatment of non-hydrogen-bonded molecular crystals such as benzene (Section 5.3). Therefore in this section a normal coordinate calculation of the lattice vibrations of the true structure model of ice II which used the potential function developed by Clementi et al[137] for the interaction of two water molecules is reported.

Clementi et al[137] calculated the potential energy of two water molecules in sixty-six different geometrical configurations with an ab initio configuration-interaction quantum mechanical method, and they fitted the results to a function of the interatomic distances, i.e.

$$\begin{aligned}\varepsilon = {} & q^2\left(\frac{1}{r_{13}} + \frac{1}{r_{14}} + \frac{1}{r_{23}} + \frac{1}{r_{24}}\right) + \frac{4q^2}{r_{78}} \\ & -2q^2\left(\frac{1}{r_{18}} + \frac{1}{r_{28}} + \frac{1}{r_{37}} + \frac{1}{r_{47}}\right) \\ & + a_1 \exp(-b_1 r_{56}) \\ & + a_2 [\exp(-b_2 r_{13}) + \exp(-b_2 r_{14}) + \exp(-b_2 r_{23}) \\ & \qquad + \exp(-b_2 r_{24})]\end{aligned}$$

$$+ a_3[\exp(-b_3 r_{16}) + \exp(-b_3 r_{26}) + \exp(-b_3 r_{35})$$

$$+\exp(-b_3 r_{45})]$$

$$- a_4[\exp(-b_4 r_{16}) + \exp(-b_4 r_{26}) + \exp(-b_4 r_{45})$$

$$+ \exp(-b_4 r_{45})] \qquad (5.20)$$

This function will be referred to as the Clementi pair potential. Points $i = 1,2,5$ and 7 are on one molecule, points $j = 3,4,6$ and 8 are on the other molecule, and the distances r_{ij} are in atomic units. The hydrogen atoms (1 to 4) carry a charge of $+q$, atoms 5 and 6 are oxygen atoms, and the M^- points (7 and 8) carry a charge of $-2\,q$. The constants q^2, a_i and b_i ($i=1$ to 4) were evaluated[137] for the calculated potential energies including both the inter- and intramolecular correlation energies (ε_{CI}) and also including only the intermolecular correlation energy (ε_{INTER}). There was some evidence that ε_{CI} underestimates the correlation effect at short O-O distances,[137] and therefore the parameters for ε_{INTER} (Appendix VII) were used for these calculations on ice II.

The second derivatives of the Clementi pair potential with respect to the interaction distances are

$$\partial^2\varepsilon/\partial r_{H-H}^2 = 2\,q^2/r_{H-H}^3 + a_2\, b_1^2 \exp(-b_2\, r_{H-H}) \qquad (5.21)$$

$$\partial^2\varepsilon/\partial r_{H-M}^2 = -4\,q^2/r_{H-M}^3 \qquad (5.22)$$

$$\partial^2\varepsilon/\partial r_{H-O}^2 = a_3\, b_3^2 \exp(-b_3\, r_{H-O}) - a_4\, b_4^2 \exp(-b_4\, r_{H-O}) \qquad (5.23)$$

$$\partial^2\varepsilon/\partial r^2_{O-O} = a_1\, b_1^2 \exp(-b_1\, r_{O-O}) \quad (5.24)$$

$$\partial^2\varepsilon/\partial r^2_{M-M} = 8\, q^2/r^3_{M-M} \quad (5.25)$$

Only the interactions between nearest-neighbour water molecules in ice II were considered here, yielding sixteen non-equivalent types each of H-H', M^--H and H-O interactions and four non-equivalent types each of O-O' and M^--M^- interactions, for a total of 56 types of interactions. Because of the S_6 symmetry of the rhombohedral cell of ice II, there are six equivalent interactions for each type of interaction, for a total of 336 interaction coordinates. The 56 interaction distances for the true structure model of ice II and the corresponding interaction constants that were used in the normal coordinate calculation are given in Appendix VII.

The frequencies that were calculated for ice II from the second derivatives of the Clementi pair potential are given in Table 5.19. There are three serious problems with these results. The most obvious of these is the calculation of seven imaginary frequencies. This is a common problem in normal coordinate calculations using interatomic potentials, and occurs because the molecular positions in the crystal are not minima in the potential energy described by the function. To correct this problem either the constants of the potential function or the molecular positions must be refined,[147] but neither is possible with the programs AXSMZ and LSMX. A second problem is the mixing of translational and rotational motions in many of the normal modes,

Table 5.19

Calculated frequencies of the translational and rotational vibrations of the true structure model of ice II, with the Clementi pair potential.

	no.	H_2O^a	D_2O^a	ν_H/ν_D		no.	H_2O^a	D_2O^a	ν_H/ν_D
A_g	1	570.0	404.7	1.408	E_g	25	512.4	371.1	1.381
	2	518.2	370.5	1.400		26	414.6	314.6	1.318
	3	441.7	323.8	1.364		27	349.2	285.2	1.224
	4	348.6	288.3	1.209		28	299.5	259.1	1.156
	5	285.7	246.6	1.159		29	255.1	228.6	1.116
	6	217.0	203.1	1.068		30	220.7	188.7	1.170
	7	158.2	146.3	1.081		31	202.0	176.6	1.144
	8	153.5	131.7	1.166		32	177.2	155.9	1.137
	9	70.2	61.8	1.136		33	117.6	87.1	1.350
	10	27.1	25.6	1.059		34	67.3	63.5	1.060
	11	52.2 i	42.8 i	1.220		35	23.2 i	21.3 i	1.089
	12	86.7 i	67.7 i	1.281		36	147.6 i	106.0 i	1.392
A_u	13	455.2	338.6	1.344	E_u	37	551.0	393.0	1.402
	14	411.9	317.5	1.297		38	476.9	344.1	1.386
	15	323.3	296.1	1.092		39	442.3	327.5	1.351
	16	304.2	256.0	1.188		40	284.2	255.5	1.112
	17	284.7	221.7	1.284		41	258.6	233.3	1.108
	18	254.7	212.0	1.216		42	239.5	210.0	1.140
	19	213.9	184.1	1.162		43	185.8	163.5	1.136
	20	137.1	127.2	1.078		44	167.5	140.4	1.193
	21	96.2	92.6	1.039		45	95.9	79.8	1.202
	22	0	0	-		46	44.5	41.7	1.067
	23	122.8 i	88.1 i	1.394		47	0	0	-
	24	191.7 i	135.7 i	1.413		48	86.3 i	61.4 i	1.406

[a] Force constants are given in Appendix VII.

as shown by the isotope ratios and the eigenvectors. A third problem is that the calculated range of frequencies is considerably less than the observed range.

The results of this calculation are clearly unsatisfactory. Further progress can only be made with the refinement capability discussed above.

5.8 Conclusions

The frequencies and intensities of the translational lattice vibrations of ice II and ice IX have been calculated under the simplest possible models. The reasonable agreement between the calculated and observed infrared and Raman spectra suggests that the assignments made in Section 5.5 are useful and in general correct, though perhaps not in detail.

Similar normal coordinate calculations of the rotational lattice vibrations of ices II and IX have not been successful. The amount of translational and rotational motion in the normal modes was found to depend on the coordinates used to describe the forces which oppose the reorientational motion and therefore several coordinate sets have been tested. With some of the coordinate sets the mixing of translational and rotational motions was much greater than indicated by experiment, while for others the amount of mixing was much nearer to that observed but the observed ranges of the translational and rotational vibrations were not reproduced. Thus the simple force fields assumed here are inadequate to describe the restoring forces that determine the rotational vibrations of the ices. Thus the development of interatomic potential functions to describe the intermolecular forces between water molecules, and the inclusion of such forces between non-nearest neighbours, is likely to yield the greatest progress in calculations of the rotational vibrations of the ices.

REFERENCES

1. F.E. Bates. Ph.D. thesis, University of Alberta, 1978.
2. J.E. Bertie and F.E. Bates. J. Chem. Phys. 67, 1511 (1977).
3. P.V. Hobbs. Ice Physics. Oxford University Press, London, 1974.
4. B. Kamb. Trans. Am. Crystallogr. Assoc. 5, 61 (1969).
5. E. Whalley. In The Hydrogen Bond, Vol. III. Edited by P. Schuster, G. Zundel and C. Sandorfy. North-Holland Publishing Company, Amsterdam, 1976, Chapter 29.
6. B. Kamb. In Physics and Chemistry of Ice. Edited by E. Whalley, S.J. Jones and L.W. Gold. Royal Society of Canada, Ottawa, 1973, p. 28.
7. B. Kamb. In Water and Aqueous Solutions. Edited by R.A. Horn. Wiley-Interscience, New York, 1972, p. 9.
8. E. Whalley. In Physics of Ice. Edited by N. Riehl, B. Bullemer and H. Engelhardt. Plenum Press, New York, 1969, p.19.
9. O. Mishima and S. Endo. J. Chem. Phys. 73, 2454 (1980).
10. H. König. Nachr. Akad. Wiss. Göttingen 1, 1 (1942).
11. J.E. Bertie, L.D. Calvert and E. Whalley. J. Chem. Phys. 38, 840 (1963).
12. J.E. Bertie, L.D. Calvert and E. Whalley. Can. J. Chem. 42, 1373 (1964).
13. G. Tammann. Kristallisieren und Schmelzen. Barth, Leipzig, 1903, pp. 315-344.

14. G. Tammann. Z. Phys. Chem. (Leipzig) 72, 609 (1910).

15. G. Tammann. Z. Phys. Chem. (Leipzig) 69, 569 (1910).

16. P.W. Bridgman. Proc. Am. Acad. Arts Sci. 47, 438 (1912).

17. P.W. Bridgman. J. Chem. Phys. 3, 597 (1935).

18. P.W. Bridgman. J. Chem. Phys. 5, 964 (1937).

19. C.W.F.T. Pistorius, M.C. Pistorius, J.P. Blakey and L.J. Admiraal. J. Chem. Phys. 38, 600 (1963).

20. C.W.F.T. Pistorius, E. Rapoport and J.B. Clark. J. Chem. Phys. 48, 5509 (1968).

21. E. Whalley, D.W. Davidson and J.B.R. Heath. J. Chem. Phys. 45, 3976 (1966).

22. E. Whalley, J.B.R. Heath and D.W. Davidson. J. Chem. Phys. 48, 2362 (1968).

23. L.F. Evans. J. Appl. Phys. 38, 4930 (1967).

24. H. Engelhardt and E. Whalley. J. Chem. Phys. 56, 2678 (1972).

25. K. Nishibata. Jpn. J. Appl. Phys. 11, 1701 (1972).

26. H. Engelhardt and B. Kamb. J. Glaciol. 21, 51 (1978).

27. H. Engelhardt and E. Whalley. J. Chem. Phys. 71, 4050 (1979).

28. G.P. Johari and E. Whalley. J. Chem. Phys. 70, 2094 (1979).

29. W. C. Hamilton, B. Kamb, S.J. LaPlaca and A. Prakash. In Physics of Ice. Edited by N. Riehl, B. Bullemer and H. Engelhardt. Plenum Press, New York, 1969, p. 44.

30. E.F. Burton and W.F. Oliver. Proc. R. Soc. London, Ser. A 153, 166 (1935).

31. A.H. Narten, C.G. Venkatesh and S.A. Rice. J. Chem. Phys. 64, 1106 (1976).

32. E. Whalley and D.W. Davidson. J. Chem. Phys. 43, 2148 (1965).

33. S.W. Peterson and H.A. Levy. Acta Crystallogr. 10, 70 (1957).

34. B. Kamb, W.C. Hamilton, S.J. LaPlaca and A. Prakash. J. Chem. Phys. 55, 1934 (1971).

35. E.D. Finch, S.W. Rabideau, R.G. Wenzel and N.G. Nereson. J. Chem. Phys. 49, 4361 (1968).

36. G.P. Arnold, R.G. Wenzel, S.W. Rabideau, N.G. Nereson and A.L. Bowman. J. Chem. Phys. 55, 589 (1971).

37. W.C. Hamilton, B. Kamb, S.J. LaPlaca and A. Prakash. Unpublished data cited in Ref. 4.

38. S.W. Rabideau, E.D. Finch, G.P. Arnold and A.L. Bowman. J. Chem. Phys. 49, 2514 (1968).

39. S.J. LaPlaca, W.C. Hamilton, B. Kamb and A. Prakash. J. Chem. Phys. 58, 567 (1973).

40. G.J. Wilson, R.K. Chan, D.W. Davidson and E. Whalley. J. Chem. Phys. 43, 2384 (1965).

41. J.E. Bertie and E. Whalley. J. Chem. Phys. 40, 1646 (1964).

42. J.E. Bertie, H.J. Labbé and E. Whalley. J. Chem. Phys. 49, 775 (1968).

43. J.E. Bertie, H.J. Labbé and E. Whalley. J. Chem. Phys. 49, 2141 (1968).

44. D.S. Olander and S.A. Rice. Proc. Natl. Acad. Sci. USA

69, 98 (1972).

45. G.P. Arnold, E.D. Finch, S.W. Rabideau and R.G. Wenzel. J. Chem. Phys. 49, 4365 (1968).

46. B. Kamb. Acta Crystallogr. 17, 1437 (1964).

47. K. Lonsdale. Proc. R. Soc. London, Ser. A 247, 424 (1958).

48. M. Blackman and N.D. Lisgarten. Proc. R. Soc. London, Ser. A 239, 93 (1957).

49. R. Brille and A. Tippe. Acta Crystallogr. 23, 343 (1967).

50. S.W. Rabideau, E.D. Finch and A.B. Denison. J. Chem. Phys. 49, 4660 (1968).

51. W.S. Benedict, N. Gailar and E.K. Plyler. J. Chem. Phys. 24, 1139 (1956).

52. B. Kamb and A. Prakash. Acta Crystallogr. Sect. B 24, 1317 (1968).

53. B. Kamb. Science (Washington, D.C.) 150, 205 (1965).

54. B. Kamb and B.L. Davis. Proc. Natl. Acad. Sci. USA 52 1433 (1964).

55. B. Kamb, A. Prakash and C. Knobler. Acta Crystallogr. 22, 706 (1967).

56. E.B. Wilson, J.C. Decius and P.C. Cross. Molecular Vibrations. McGraw-Hill, New York, 1955.

57. J.C. Decius and R.M. Hexter. Molecular Vibrations in Crystals. McGraw-Hill, New York, 1977.

58. F.A. Cotton. Chemical Applications of Group Theory, 2nd Edition. Wiley-Interscience, New York, 1971.

59. G. Turrell. Infrared and Raman Spectra of Crystals. Academic Press, London, 1972.

60. G.C. Pimentel and A.L. McClellan. Hydrogen Bonding. Freeman, San Francisco, 1960.

61. A. Novak. Struct. Bonding (Berlin) 18, 177 (1974).

62. B. Berglund, J. Lindgren and J. Tegenfeldt. J. Mol. Struct. 43, 179 (1978).

63. J.E. Bertie and E. Whalley. J. Chem. Phys. 46, 1271 (1967).

64. H.J. Prask, S.F. Trevino, J.D. Gault and K.W. Logan. J. Chem. Phys. 56, 3217 (1972).

65. B. Renker. In Physics and Chemistry of Ice. Edited by E. Whalley, S.J. Jones and L.W. Gold. Royal Society of Canada, Ottawa, 1973, p. 82.

66. B. Dorner. J. Glaciol. 21, 231 (1978).

67. P.T.T. Wong, D.D. Klug and E. Whalley. In Physics and Chemistry of Ice. Edited by E. Whalley, S.J. Jones and L.W. Gold. Royal Society of Canada, Ottawa, 1973, p. 87.

68. P. Bosi, R. Tubino and G. Zerbi. In Physics and Chemistry of Ice. Edited by E. Whalley, S.J. Jones and L.W. Gold. Royal Society of Canada, Ottawa, 1973, p. 98.

69. J. Govindarajan and T.M. Hardisan. In Physics and Chemistry of Ice. Edited by E. Whalley, S.J. Jones and L.W. Gold. Royal Society of Canada, Ottawa, 1973, p. 103.

70. D. Jović, M. Davidović and M. Zivanović. Phys. Lett. A 42, 509 (1973).

71. P. Bosi, R. Tubino and G. Zerbi. J. Chem. Phys. 59, 4578 (1973).

72. C. Kittel. Introduction to Solid State Physics, 5th Edition. J. Wiley, New York, 1976, p. 118.

73. W.G. Fateley, F.R. Dollish, N.T. McDevitt and F.F. Bentley. Infrared and Raman Selection Rules for Molecular and Lattice Vibrations: The Correlation Method. Wiley-Interscience, New York, 1972.

74. G. Herzberg. Molecular Spectra and Molecular Structure II. Infrared and Raman Spectra of Polyatomic Molecules. Van Nostrand, New York, 1945.

75. E. Whalley and J.E. Bertie. J. Chem. Phys. 46, 1264 (1967).

76. P.T.T. Wong and E. Whalley. J. Chem. Phys. 65, 829 (1976).

77. D.D. Klug and E. Whalley. J. Chem. Phys. 71, 2903 (1979).

78. L. Van Hove. Phys. Rev. 89, 1189 (1953).

79. R.E. Shawyer and P. Dean. Discuss. Faraday Soc. 48, 102 (1969).

80. R.E. Shawyer and P. Dean. J. Phys. C 5, 1028 (1972).

81. R. McGraw, W.G. Madden, M.S. Bergren, S.A. Rice and M.G. Sceats. J. Chem. Phys. 69, 3483 (1978).

82. N. Ockman. Adv. Phys. 7, 199 (1958).

83. E. Whalley. Dev. Appl. Spectrosc. 6, 277 (1968).

84. E. Whalley. Can. J. Chem. 55, 3429 (1977).

85. E. Whalley. In Physics and Chemistry of Ice. Edited by E. Whalley, S.J. Jones and L.W. Gold. Royal Society of Canada, Ottawa, 1973, p. 73.

86. J.E. Bertie and E. Whalley. J. Chem. Phys. 40, 1637

(1964).

87. M. Falk. In The Chemistry and Physics of Aqueous Gas Solutions. Edited by W.A. Adams et al. The Electrochemical Society, Toronto, 1975, p. 19.

88. T.C. Sivakumar, S.A. Rice and M.G. Sceats. J. Chem. Phys. 69, 3468 (1978).

89. T.A. Ford and M. Falk. Can J. Chem. 46, 3579 (1968).

90. J.R. Scherer and R.G. Snyder. J. Chem. Phys. 67, 4794 (1977).

91. N. Sheppard. In Hydrogen Bonding. Edited by D. Hadzi. Pergammon Press, London, 1959, p. 85; J. Arnold, J.E. Bertie and D.J. Millen. Proc. Chem. Soc., London 121 (1961); J.E. Bertie and D.J. Millen. J. Chem. Soc. 497 (1965); J. Arnold and D.J. Millen. J. Chem. Soc. 503 (1965); J. Arnold and D.J. Millen. J. Chem. Soc. 510 (1965); J.E. Bertie and D.J. Millen. J. Chem. Soc. 514 (1965).

92. A. Novak. J. Chim. Phys. 72, 981 (1975).

93. C. Haas and D.F. Hornig. J. Chem. Phys. 32, 1763 (1960).

94. G. Ritzhaupt, C. Thornton and J.P. Devlin. Chem. Phys. Lett. 59, 420 (1978).

95. G. Ritzhaupt, W.B. Collier, C. Thornton and J.P. Devlin. Chem. Phys. Lett. 70, 294 (1980).

96. M.G. Sceats, M. Stavola and S.A. Rice. J. Chem. Phys. 71, 983 (1979).

97. M.J. Taylor and E. Whalley. J. Chem. Phys. 40, 1660 (1964).

98. E. Whalley and D.D. Klug. J. Chem. Phys. 71, 1513 (1979).

99. P.T.T. Wong and E. Whalley. J. Chem. Phys. 62, 2418 (1975).

100. J. E. Bertie and S.M. Jacobs. J. Chem. Phys. 67, 2445 (1977).

101. P.T.T. Wong and E. Whalley. J. Chem. Phys. 64, 2359 (1976).

102. J.P. Marckmann and E. Whalley. J. Chem. Phys. 41, 1450 (1964).

103. J.M. Kennedy, W.F. Sherman, N. Treloar and G.R. Wilkinson. In Proc. Vth Int. Conf. on Raman Spectrosc., Freiburg. Edited by E.D. Schmid, J. Brandmuller, W. Kiefer, B. Schrader and H.W. Schrotter. Schulz Verlag, Freiburg, 1976; spectra also presented by W.F. Sherman and G.R. Wilkinson. In Advances in Infrared and Raman Spectroscopy Vol. 6. Edited by R.J.H. Clark and R.E. Hester. Heyden, London, 1980, p. 288.

104. R.A. Fifer and J. Schiffer. J. Chem. Phys. 52, 2664 (1970).

105. J. Schiffer, M. Intenzo, P. Hayward and C. Calabrese. J. Chem. Phys. 64, 3014 (1976).

106. D.D. Klug and E. Whalley. J. Glaciol. 21, 55 (1978).

107. P. Faure and A. Chosson. In Proc. 2nd Int. Conf. on Light Scattering in Solids. Edited by M. Balkanski. Flammarion Sciences, Paris, 1971, p. 272.

108. P. Faure and A. Chooson. J. Glaciol. 21, 65 (1978).

109. A.S. Barker Jr. Phys. Rev. B 12, 4071 (1975).

110. M. Yvinec and R.M. Pick. J. Chem. Phys. 71, 3440 (1979).

111. J.E. Bertie and E. Whalley. Spectrochim. Acta 20, 1349 (1964).

112. G.E. Devlin, J.L. Davis, L. Chase and S. Geschwind. Appl. Phys. Lett. 19, 138 (1971).

113. J.L. Lippert, G.W. Hibler, E.W. Small and W.L. Peticolas. In Proc. 2nd Int. Conf. on Light Scattering in Solids. Edited by M. Balkanski. Flammarion Sciences, Paris, p. 342.

114. W.L. Peticolas. Annu. Rev. Phys. Chem. 23, 93 (1972).

115. A.N. Zaidel', V.K. Prokof'ev, S.M. Raiskii, V.A. Slavnyi and E.Ya. Shreider. Tables of Spectral Lines. IFI/Plenum, New York, 1970.

116. C. DeWitt Coleman, W.R. Bozman and W.F. Meggers. Table of Wavenumbers, Vol. I and II. NBS Monogr. (U.S.) 3 (1960).

117. L. Minnhagen. Ark. Fys. 25, 203 (1963).

118. G.R. Harrison. Massachusetts Institute of Technology Wavelength Tables. M.I.T. Press, Cambridge, 1969.

119. M.M. Morrison. M.Sc. thesis, University of Alberta, 1980.

120. F. Sauberer. Wett. Leben 2, 193 (1950). Cited in Reference 3, p. 207.

121. T.C. Damen, S.P.S. Porto and B. Tell. Phys. Rev. 142, 570 (1966).

122. J.H. Schachtschneider. Report number 57-65, Shell Development Co., West Hollow Research Center, P.O. Box

1380, Houston, Texas 77001, U.S.A.

123. D.F. Hornig and D.C. McKean. J. Chem. Phys. 59, 1133 (1955).

124. J. Overend. In Infrared Spectroscopy and Molecular Structure. Edited by M. Davies, Elsevier, Amsterdam, 1963, Chapter X.

125. W.G. Madden, M.S. Bergren, R. McGraw, S.A. Rice and M.G. Sceats. J. Chem. Phys. 69, 3497 (1978).

126. J.E. Cahill and G.E. Leroi. J. Chem. Phys. 51, 97 (1969).

127. W.F. Murphy. Mol. Phys. 36, 727 (1978).

128. C. Haas and D.F. Hornig. J. Chem. Phys. 26, 707 (1957).

129. I.N. Levine. Quantum Chemistry Volume 1: Quantum Mechanics and Molecular Electronic Structure. Allyn and Bacon, Boston, 1970.

130. R.N. Dixon. J. Chem. Phys. 31, 258 (1959).

131. J. Fahrenfort. In Infrared Spectroscopy and Molecular Structure. Edited by M. Davies, Elsevier, Amsterdam, 1963, Chapter XI.

132. J.E. Bertie and S.M. Jacobs. Unpublished data.

133. J. Bournay and Y. Marechal. Spectrochim. Acta 31A, 1351)1975); J. Bournay and Y. Marechal. Chem. Phys. Lett. 27, 180 (1975).

134. H.R. Zelsmann and Y. Marechal. Chem. Phys. 20, 445 (1977).

135. T. Shimanouchi and I. Harada. J. Chem. Phys. 41, 2651 (1964).

136. L. Colombo and J.P. Mathieu. In Molecular Interactions.

Edited by H. Ratajczak and W.J. Orville-Thomas. John Wiley and Sons, New York, 1980, Chapter 11.

137. O. Matsuoka, E. Clementi and M. Yoshimine. J. Chem. Phys. 64, 1351 (1976).

138. O. Schnepp and N. Jacobi. In Dynamical Properties of Solids. Edited by G.K. Horton and A.A. Maradudin. North-Holland Publishing, Amsterdam, 1975, Chapter 3.

139. O. Schnepp and N. Jacobi. Adv. Chem. Phys. 22, 205 (1972).

140. J.E. Cahill and G.E. Leroi. J. Chem. Phys. 51, 1324 (1969).

141. R.V. St. Louis and O. Schnepp. J. Chem, Phys. 50, 5177 (1969).

142. T. Shimanouchi. Private communication.

143. E.G. Cox. Rev. Mod. Phys. 30, 159 (1958).

144. I. Harada and T. Shimanouchi. J. Chem. Phys. 44, 2016 (1966).

145. G. Taddei, H. Bonadeo, M.P. Marzocchi and S. Califano. J. Chem. Phys. 58, 966 (1973).

146. M.P. Marzocchi, H. Bonadeo and G. Taddei. J. Chem. Phys. 53, 867 (1970).

147. H. Bonadeo, M.P. Marzocchi, E. Castellucci and S. Califano. J. Chem. Phys. 57, 4299 (1972).

148. I. Harada and T. Shimanouchi. J. Chem. Phys. 46, 2708 (1967).

149. D.E. Williams. J. Chem. Phys. 45, 3770 (1966).

150. D.E. Williams. J. Chem. Phys. 47, 4680 (1967).

151. E. Whalley. Can. J. Chem. 50, 310 (1972).

152. D.D. Klug and E. Whalley. In Physics and Chemistry of Ice. Edited by E. Whalley, S.J. Jones and L.W. Gold. Royal Society of Canada, Ottawa, 1973, p. 93.

153. M.G. Sceats and S.A. Rice. J. Chem. Phys. 72, 3236 (1980).

154. F.H. Stillinger. Adv. Chem. Phys. 31, 1 (1975).

155. R. Kopelman. J. Chem. Phys. 47, 2631 (1967).

Appendix I

Calculated mean-value and squared anisotropic invariants of the polarizability derivatives, $\bar{\alpha}'$ and $(\gamma')^2$, and relative Raman intensities of the O-D stretching vibrations of ices II and IX

			D_2O ice II force field A				
Mode	ν/cm^{-1}		RP=5.6	RP=7.5	RP=10	RP=20	RP=50
$\nu_1(A_g)$	2534.5	$\bar{\alpha}'$	0.142	0.132	0.126	0.115	0.109
		$(\gamma')^2$	0.393	0.437	0.471	0.525	0.558
		Int.	3.6	4.5	5.2	6.7	7.8
$\nu_2(A_g)$	2487.3	$\bar{\alpha}'$	-0.004	-0.003	-0.003	-0.003	-0.003
		$(\gamma')^2$	1.694	1.883	2.031	2.263	2.408
		Int.	13.2	16.8	20.1	26.7	31.7
$\nu_3(A_g)$	2398.5	$\bar{\alpha}'$	-0.053	-0.049	-0.047	-0.043	-0.041
		$(\gamma')^2$	0.527	0.586	0.632	0.705	0.750
		Int.	4.4	5.6	6.7	8.9	10.6
$\nu_4(A_g)$	2360.2	$\bar{\alpha}'$	-1.624	-1.517	-1.437	-1.317	-1.246
		$(\gamma')^2$	0.013	0.014	0.015	0.017	0.018
		Int.	100	100	100	100	100
$\nu_9(E_g)$	2545.6	$\bar{\alpha}'$	0.0	0.0	0.0	0.0	0.0
		$(\gamma')^2$	0.505	0.562	0.606	0.673	0.716
		Int.	7.6	9.6	11.6	15.3	18.2
$\nu_{10}(E_g)$	2504.2	$\bar{\alpha}'$	0.0	0.0	0.0	0.0	0.0
		$(\gamma')^2$	1.924	2.138	2.306	2.571	2.736
		Int.	29.6	37.6	45.2	60.0	71.3
$\nu_{11}(E_g)$	2444.6	$\bar{\alpha}'$	0.0	0.0	0.0	0.0	0.0
		$(\gamma')^2$	0.319	0.355	0.383	0.426	0.454
		Int.	5.1	6.5	7.8	10.3	12.3
$\nu_{12}(E_g)$	2414.9	$\bar{\alpha}'$	0.0	0.0	0.0	0.0	0.0
		$(\gamma')^2$	0.523	0.582	0.627	0.697	0.742
		Int.	8.5	10.8	13.0	17.2	20.5

Appendix I , continued

			D_2O ice II force field B				
Mode	ν/cm^{-1}		RP=5.6	RP=7.5	RP=10	RP=20	RP=50
$\nu_1(A_g)$	2527.4	$\bar{\alpha}'$	0.266	0.248	0.235	0.216	0.204
		$(\gamma')^2$	0.835	0.930	1.003	1.117	1.189
		Int.	9.7	11.6	13.4	16.9	19.5
$\nu_2(A_g)$	2482.9	$\bar{\alpha}'$	-0.125	-0.117	-0.111	-0.101	-0.096
		$(\gamma')^2$	1.596	1.776	1.916	2.134	2.271
		Int.	14.3	18.2	21.7	28.5	33.7
$\nu_3(A_g)$	2398.9	$\bar{\alpha}'$	-0.466	-0.434	-0.412	-0.377	-0.357
		$(\gamma')^2$	0.148	0.164	0.177	0.198	0.210
		Int.	10.2	10.6	10.9	11.5	12.1
$\nu_4(A_g)$	2349.7	$\bar{\alpha}'$	-1.537	-1.434	-1.359	-1.245	-1.177
		$(\gamma')^2$	0.045	0.050	0.054	0.060	0.064
		Int.	100	100	100	100	100
$\nu_9(E_g)$	2554.2	$\bar{\alpha}'$	0.0	0.0	0.0	0.0	0.0
		$(\gamma')^2$	0.446	0.496	0.535	0.596	0.635
		Int.	7.3	9.4	11.2	14.9	17.7
$\nu_{10}(E_g)$	2494.1	$\bar{\alpha}'$	0.0	0.0	0.0	0.0	0.0
		$(\gamma')^2$	1.826	2.032	2.193	2.442	2.599
		Int.	31.2	39.9	47.8	63.3	75.3
$\nu_{11}(E_g)$	2453.7	$\bar{\alpha}'$	0.0	0.0	0.0	0.0	0.0
		$(\gamma')^2$	0.551	0.613	0.661	0.737	0.784
		Int.	9.7	12.3	14.8	19.6	23.3
$\nu_{12}(E_g)$	2416.1	$\bar{\alpha}'$	0.0	0.0	0.0	0.0	0.0
		$(\gamma')^2$	0.444	0.494	0.535	0.594	0.632
		Int.	8.0	10.2	12.3	16.2	19.2

Appendix I, continued

Mode	ν/cm^{-1}		D_2O ice IX force field A				
			RP=5.6	RP=7.5	RP=10	RP=20	RP=50
$\nu_1(A_1)$	2522.5	$\bar{\alpha}'$	-0.003	-0.002	-0.002	-0.002	-0.002
		$(\gamma')^2$	0.813	0.904	0.975	1.086	1.156
		Int.	6.0	7.7	9.2	12.1	14.4
$\nu_2(A_1)$	2416.9	$\bar{\alpha}'$	-0.081	-0.076	-0.072	-0.066	-0.062
		$(\gamma')^2$	0.145	0.161	0.174	0.194	0.206
		Int.	1.4	1.7	2.0	2.5	3.0
$\nu_3(A_1)$	2341.3	$\bar{\alpha}'$	1.629	1.521	1.441	1.321	1.249
		$(\gamma')^2$	0.096	0.107	0.115	0.128	0.137
		Int.	100	100	100	100	100
$\nu_7(B_1)$	2526.8	$\bar{\alpha}'$	0.0	0.0	0.0	0.0	0.0
		$(\gamma')^2$	0.024	0.027	0.029	0.032	0.034
		Int.	0.2	0.2	0.3	0.4	0.4
$\nu_8(B_1)$	2467.8	$\bar{\alpha}'$	0.0	0.0	0.0	0.0	0.0
		$(\gamma')^2$	3.119	3.467	3.738	4.165	4.433
		Int.	23.9	30.4	36.5	48.1	57.1
$\nu_9(B_1)$	2412.1	$\bar{\alpha}'$	0.0	0.0	0.0	0.0	0.0
		$(\gamma')^2$	0.445	0.495	0.534	0.595	0.633
		Int.	3.5	4.5	5.4	7.1	8.5
$\nu_{10}(B_2)$	2513.4	$\bar{\alpha}'$	0.0	0.0	0.0	0.0	0.0
		$(\gamma')^2$	0.349	0.388	0.419	0.467	0.496
		Int.	2.6	3.3	4.0	5.2	6.2
$\nu_{11}(B_2)$	2457.3	$\bar{\alpha}'$	0.0	0.0	0.0	0.0	0.0
		$(\gamma')^2$	0.075	0.083	0.090	0.100	0.107
		Int.	0.6	0.7	0.9	1.2	1.4
$\nu_{12}(B_2)$	2401.4	$\bar{\alpha}'$	0.0	0.0	0.0	0.0	0.0
		$(\gamma')^2$	0.049	0.055	0.059	0.066	0.070
		Int.	0.4	0.5	0.6	0.8	0.9
$\nu_{13}(E)$	2516.0	$\bar{\alpha}'$	0.0	0.0	0.0	0.0	0.0
		$(\gamma')^2$	0.290	0.323	0.348	0.388	0.413
		Int.	4.3	5.5	6.6	8.7	10.3
$\nu_{14}(E)$	2492.2	$\bar{\alpha}'$	0.0	0.0	0.0	0.0	0.0
		$(\gamma')^2$	0.360	0.400	0.431	0.481	0.511
		Int.	5.4	6.9	8.3	11.0	13.0
$\nu_{15}(E)$	2464.0	$\bar{\alpha}'$	0.0	0.0	0.0	0.0	0.0
		$(\gamma')^2$	0.680	0.756	0.815	0.908	0.966
		Int.	10.4	13.3	15.9	21.0	25.0
$\nu_{16}(E)$	2461.7	$\bar{\alpha}'$	0.0	0.0	0.0	0.0	0.0
		$(\gamma')^2$	0.575	0.640	0.690	0.768	0.818
		Int.	8.8	11.3	13.5	17.8	21.2
$\nu_{17}(E)$	2395.2	$\bar{\alpha}'$	0.0	0.0	0.0	0.0	0.0
		$(\gamma')^2$	0.121	0.134	0.145	0.161	0.172
		Int.	1.9	2.5	3.0	3.9	4.6
$\nu_{18}(E)$	2360.1	$\bar{\alpha}'$	0.0	0.0	0.0	0.0	0.0
		$(\gamma')^2$	0.002	0.002	0.002	0.002	0.002
		Int.	0.03	0.04	0.04	0.05	0.06

Appendix I, continued

			D_2O ice IX force field B				
Mode	ν/cm^{-1}		RP=5.6	RP=7.5	RP=10	RP=20	RP=50
$\nu_1(A_1)$	2520.8	$\bar{\alpha}'$	0.029	0.027	0.026		0.022
		$(\gamma')^2$	0.909	1.012	1.091		1.294
		Int.	6.7	8.5	10.2		16.0
$\nu_2(A_1)$	2416.3	$\bar{\alpha}'$	0.012	0.011	0.011		0.009
		$(\gamma')^2$	0.071	0.079	0.085		0.100
		Int.	0.6	0.7	0.9		1.3
$\nu_3(A_1)$	2325.5	$\bar{\alpha}'$	1.632	1.523	1.443		1.250
		$(\gamma')^2$	0.073	0.081	0.088		0.104
		Int.	100	100	100		100
$\nu_7(B_1)$	2532.9	$\bar{\alpha}'$	0.0	0.0	0.0		0.0
		$(\gamma')^2$	0.001	0.001	0.001		0.001
		Int.	0.01	0.01	0.01		0.01
$\nu_8(B_1)$	2467.8	$\bar{\alpha}'$	0.0	0.0	0.0		0.0
		$(\gamma')^2$	2.828	3.148	3.395		4.026
		Int.	21.4	27.3	32.8		51.5
$\nu_9(B_1)$	2422.1	$\bar{\alpha}'$	0.0	0.0	0.0		0.0
		$(\gamma')^2$	0.754	0.839	0.905		1.073
		Int.	5.9	7.5	9.0		14.1
$\nu_{10}(B_2)$	2510.9	$\bar{\alpha}'$	0.0	0.0	0.0		0.0
		$(\gamma')^2$	0.410	0.457	0.492		0.584
		Int.	3.0	3.9	4.6		7.3
$\nu_{11}(B_2)$	2463.1	$\bar{\alpha}'$	0.0	0.0	0.0		0.0
		$(\gamma')^2$	0.006	0.007	0.007		0.008
		Int.	0.04	0.06	0.1		0.1
$\nu_{12}(B_2)$	2396.4	$\bar{\alpha}'$	0.0	0.0	0.0		0.0
		$(\gamma')^2$	0.057	0.064	0.069		0.081
		Int.	0.5	0.6	0.7		1.1
$\nu_{13}(E)$	2519.8	$\bar{\alpha}'$	0.0	0.0	0.0		0.0
		$(\gamma')^2$	0.546	0.608	0.656		0.778
		Int.	8.0	10.2	12.3		19.3
$\nu_{14}(E)$	2486.4	$\bar{\alpha}'$	0.0	0.0	0.0		0.0
		$(\gamma')^2$	0.302	0.336	0.363		0.430
		Int.	4.5	5.6	6.9		10.9
$\nu_{15}(E)$	2466.0	$\bar{\alpha}'$	0.0	0.0	0.0		0.0
		$(\gamma')^2$	0.104	0.116	0.125		0.148
		Int.	1.6	2.0	2.4		3.8
$\nu_{16}(E)$	2460.7	$\bar{\alpha}'$	0.0	0.0	0.0		0.0
		$(\gamma')^2$	1.026	1.142	1.231		1.460
		Int.	17.6	20.0	23.9		37.5
$\nu_{17}(E)$	2401.6	$\bar{\alpha}'$	0.0	0.0	0.0		0.0
		$(\gamma')^2$	0.043	0.048	0.052		0.061
		Int.	0.7	0.8	1.0		1.6
$\nu_{18}(E)$	2353.3	$\bar{\alpha}'$	0.0	0.0	0.0		0.0
		$(\gamma')^2$	0.004	0.005	0.005		0.006
		Int.	0.06	0.08	0.1		0.2

Appendix II

Intensities of a Fermi diad derived from degenerate perturbation theory

	$\Delta E/\Delta E_0=15$		$\Delta E/\Delta E_0=5$		$\Delta E/\Delta E_0=2$		$\Delta E/\Delta E_0=1.25$	
M_u/M_ℓ ($-M_u/M_\ell$)	W_{+ve} (W_{-ve})	W_{-ve} (W_{+ve})	W_{+ve} (W_{-ve})	W_{-ve} (W_{+ve})	W_{+ve} (W_{-ve})	W_{-ve} (W_{+ve})	W_{+ve} (W_{-ve})	W_{-ve} (W_{+ve})
1000	1.15	1.14	1.51	1.49	3.0	3.0	9.1	8.9
500	1.15	1.13	1.51	1.49	3.0	3.0	9.1	8.9
200	1.17	1.12	1.53	1.47	3.1	2.9	9.3	8.7
100	1.19	1.10	1.56	1.44	3.1	2.9	9.6	8.4
50	1.24	1.05	1.63	1.38	3.3	2.7	10.3	7.9
20	1.40	0.94	1.84	1.23	3.8	2.4	12.9	6.6
10	1.71	0.77	2.3	1.00	4.9	1.94	19.6	5.0
7.5	1.95	0.67	2.6	0.88	5.9	1.69	27	4.2
5	2.6	0.51	3.6	0.68	8.7	1.29	64	3.1
4	3.2	0.42	4.5	0.56	12.2	1.07	169	2.5
3	4.8	0.29	6.9	0.40	24	0.79	∞	1.78
2	11.4	0.138	19.8	0.20	278	0.44	49	1.00
1.5	36	0.055	106	0.094	240	0.24	13.4	0.60
1.0	898	0.0011	98	0.010	13.9	0.072	4.0	0.25
0.75	32	0.0119	16.3	0.0017	5.5	0.015	2.1	0.111
0.50	7.3	0.088	5.0	0.050	2.3	0.0036	1.00	0.020
0.20	1.95	0.38	1.48	0.28	0.77	0.11	0.33	0.016
0.10	1.30	0.58	1.00	0.44	0.52	0.20	0.20	0.051
0.05	1.07	0.72	0.82	0.54	0.42	0.26	0.15	0.078
0.02	0.95	0.81	0.72	0.61	0.37	0.30	0.13	0.097
0.01	0.91	0.84	0.69	0.64	0.35	0.32	0.12	0.104
0.001	0.88	0.87	0.67	0.66	0.33	0.33	0.11	0.110

Appendix III

Details of the Lattice Frequency Calculations for Ices II and IX

Crystal-Fixed Cartesian Axes

The crystal-fixed Cartesian axes $\underline{Y}$ that have been defined for the normal coordinate calculations for ice II were oriented relative to the axes of the rhombohedral cell[34] as follows

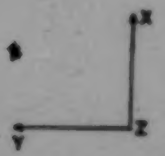

Cartesian

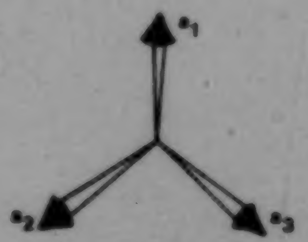

rhombohedral

The origins of the two sets of axes were coincident. From vector algebra, the relation for each atom between the distance coordinates $(X,Y,Z)_C$ with respect to these crystal-fixed Cartesian axes and the fractional coordinates[34] $(x,y,z)_R$ with respect to the rhombohedral cell is

$$\begin{pmatrix} X \\ Y \\ Z \end{pmatrix}_C = \begin{pmatrix} 7.495595 & -3.747798 & -3.747798 \\ 0.0 & 6.491376 & -6.491376 \\ 2.084335 & 2.084335 & 2.084335 \end{pmatrix} \begin{pmatrix} x \\ y \\ z \end{pmatrix}_R$$

The crystal-fixed Cartesian axes for ice IX were coincident with the axes of the tetragonal cell[38] of ice IX.

continued . . .

Appendix III, continued

The Cartesian coordinates of all atoms that were used in the true structure models of ices II and IX can be generated by symmetry from the fractional coordinates for the structures and the above axis conventions.

The Cartesian coordinates of the oxygen atoms of the linear structure models of ices II and IX were the same as those of the true structure models, and those of the hydrogen atoms can be generated by symmetry from the following coordinates:

			Crystal-fixed Cartesian coordinates (Å)		
			X	Y	Z
ice II	type I	H_7	1.733206	1.667339	0.099507
		H_{19}	2.351060	1.361437	1.248473
	type II	H_2	-1.217329	2.108089	3.178011
		H_{14}	-0.874493	3.492509	2.744866
ice IX	type 1	H_1	0.003839	2.241273	1.349196
		H_9	0.730678	1.068892	1.866688
	type 2	H_{17}	1.975326	2.427834	0.682503
		H_{21}	2.427834	1.975326	-0.682503

The Cartesian coordinates of all point masses that were used in the point mass models can be generated from the following eight points:

continued . . .

Appendix III, continued

			Crystal-fixed Cartesian coordinates (Å)		
			X	Y	Z
ice II	M_1 (type I)	H_2O	2.447659	1.162703	0.347231
		D_2O	2.413848	1.194375	0.374160
	M_7 (type II)	H_2O	-0.563800	2.726449	3.248871
		D_2O	-0.605747	2.735848	3.220465
ice IX	M_1 (type 1)	H_2O	0.690839	1.986488	1.928648
		D_2O	0.655696	1.952462	1.910023
	M_9 (type 2)	H_2O	2.594899	2.594899	0.0
		D_2O	2.557173	2.557173	0.0

Molecule-Fixed Cartesian Axes

The molecule-fixed Cartesian axes $\underline{X}$ coincide with the principal inertial axes of each molecule. The axis that roughly bisects the H-O-H angle was the molecular z-axis, and the axis perpendicular to the molecular plane was the molecular y-axis.

The molecule-fixed Cartesian axes of the molecules on a crystallographic site are symmetric with respect to the interchange group[155] of crystal symmetry operations. For both types of molecules of ice II the interchange group must be S_6, and for type 1 molecules of ice IX it must be D_4. For the type 2 molecules of ice IX the interchange group can be either C_4 or D_2. C_2 was used in this work.

continued . . .

Appendix III, continued

The $\underset{\sim}{T}$ Matrices

Under the above axis conventions, the crystal-fixed Cartesian coordinates $\underset{\sim}{Y}$ of molecule 1 (a type I molecule) of the true structure model of H_2O ice II were

	X	Y	Z
O_1	2.490037	1.123008	0.313484
H_7	1.721363	1.580650	-0.025012
H_{19}	2.501280	1.374873	1.255187

and the molecule-fixed Cartesian coordinates $\underset{\sim}{X}$ of all type I molecules of the true structure model of ice II were

	a	b	c
O(1)	0.002972	0.0	0.067105
H(2)	0.732745	0.0	-0.551203
H(4)	-0.779909	0.0	-0.513812

The moments of inertia about the a, b and c molecular axes were 0.644298, 1.798574, and 1.154275 amu $\mathring{A}^2$ respectively.

The transformation matrix $\underset{\sim}{T}$ for this molecule, defined by $\underset{\sim}{Y} = \underset{\sim}{T}\,\underset{\sim}{X}$, was found from the above coordinates to be

$$\underset{\sim}{T} = \begin{matrix} -0.499434 & 0.568523 & 0.653718 \\ 0.121279 & 0.793014 & -0.597009 \\ -0.857821 & -0.218885 & -0.465009 \end{matrix}$$

continued . . .

Appendix III, continued

The $\underset{\sim}{L}_x^{TR}$ Matrices

The $\underset{\sim}{L}_x^{TR}$ matrix, defined by $\underset{\sim}{X} = \underset{\sim}{L}_x^{TR} \underset{\sim}{Q}_{TR}$, is given by[135]

$$\begin{matrix} M^{-\frac{1}{2}} & 0 & 0 & 0 & c_i/(I_b)^{\frac{1}{2}} & -b_i/(I_c)^{\frac{1}{2}} \\ 0 & M^{-\frac{1}{2}} & 0 & -c_i/(I_a)^{\frac{1}{2}} & 0 & a_i/(I_c)^{\frac{1}{2}} \\ 0 & 0 & M^{-\frac{1}{2}} & b_i/(I_a)^{\frac{1}{2}} & -a_i/(I_b)^{\frac{1}{2}} & 0 \end{matrix}$$

where M is the mass of the molecule, a_i, b_i and c_i are the coordinates of atom i with respect to the molecule-fixed Cartesian axes, and I_a, I_b and I_c are the moments about the inertial axes. For the above molecule (and for all type I molecules) of H_2O ice II, $\underset{\sim}{L}_x^{TR}$ was

$$\begin{matrix} 0.235633 & 0 & 0 & 0 & 0.050037 & 0 \\ 0 & 0.235633 & 0 & -0.083601 & 0 & 0.002766 \\ 0 & 0 & 0.235633 & 0 & -0.002216 & 0 \\ 0.235633 & 0 & 0 & 0 & -0.411006 & 0 \\ 0 & 0.235633 & 0 & 0.686702 & 0 & 0.682021 \\ 0 & 0 & 0.235633 & 0 & -0.546373 & 0 \\ 0.235633 & 0 & 0 & 0 & -0.383125 & 0 \\ 0 & 0.235633 & 0 & 0.640119 & 0 & -0.725921 \\ 0 & 0 & 0.235633 & 0 & 0.581541 & 0 \end{matrix}$$

continued . . .

Appendix III, continued

The Symmetry Coordinates

The symmetry coordinates constructed for the calculations of the lattice vibrations of ices II and IX are given on the following pages. The normal coordinate of translation or rotation of the rigid molecules (Q_{TR}) that is involved in each symmetry coordinate is given in the second column of each table. T or R refers to the translational or rotational normal coordinate of the rigid molecule, the subscript (a, b or c) specifies the molecule-fixed axis along which the molecule is translating or about which it is rotating, and the superscript (I or II for ice II, 1 or 2 for ice IX) gives the type (Section 1.3) of the molecules involved in the symmetry coordinate. The coefficient of a term in the symmetry coordinates is given in parentheses when it is not equal to unity. The numbering of the molecules in the symmetry coordinates is the same as in Figures 1.3 and 1.4.

For example, the short-hand notation in the following table for the symmetry coordinates of ice II for coordinate number 4 of E_g symmetry is more explicitly written as

$$S_4 = 12^{-\frac{1}{2}} [2\,T_7(a) - T_8(a) - T_9(a) + 2\,T_{10}(a) - T_{11}(a) - T_{12}(a)]$$

where $T_7(a)$ is the unit displacement of molecule 7 along the a direction with respect to its molecule-fixed axes.

continued . . .

Appendix III, continued

Symmetry coordinates for ice II

		Symmetry coordinates	
no.	$\underline{Q}_{TR}$	A_g	A_u
1	T_a^I	$6^{-\frac{1}{2}}[1+2+3+4+5+6]$	$6^{-\frac{1}{2}}[1+2+3-4-5-6]$
2	T_b^I	$6^{-\frac{1}{2}}[1+2+3+4+5+6]$	$6^{-\frac{1}{2}}[1+2+3-4-5-6]$
3	T_c^I	$6^{-\frac{1}{2}}[1+2+3+4+5+6]$	$6^{-\frac{1}{2}}[1+2+3-4-5-6]$
4	T_a^{II}	$6^{-\frac{1}{2}}[7+8+9+10+11+12]$	$6^{-\frac{1}{2}}[7+8+9-10-11-12]$
5	T_b^{II}	$6^{-\frac{1}{2}}[7+8+9+10+11+12]$	$6^{-\frac{1}{2}}[7+8+9-10-11-12]$
6	T_c^{II}	$6^{-\frac{1}{2}}[7+8+9+10+11+12]$	$6^{-\frac{1}{2}}[7+8+9-10-11-12]$
7	R_a^I	$6^{-\frac{1}{2}}[1+2+3+4+5+6]$	$6^{-\frac{1}{2}}[1+2+3-4-5-6]$
8	R_b^I	$6^{-\frac{1}{2}}[1+2+3+4+5+6]$	$6^{-\frac{1}{2}}[1+2+3-4-5-6]$
9	R_c^I	$6^{-\frac{1}{2}}[1+2+3+4+5+6]$	$6^{-\frac{1}{2}}[1+2+3-4-5-6]$
10	R_a^{II}	$6^{-\frac{1}{2}}[7+8+9+10+11+12]$	$6^{-\frac{1}{2}}[7+8+9-10-11-12]$
11	R_b^{II}	$6^{-\frac{1}{2}}[7+8+9+10+11+12]$	$6^{-\frac{1}{2}}[7+8+9-10-11-12]$
12	R_c^{II}	$6^{-\frac{1}{2}}[7+8+9+10+11+12]$	$6^{-\frac{1}{2}}[7+8+9-10-11-12]$

continued . . .

Appendix III, continued

		Symmetry coordinates for ice II, continued	
no.	Q_{TR}	E_g	E_u
1	T_a^{I}	$12^{-\frac{1}{2}}$[(2)1-2-3+(2)4-5-6]	$12^{-\frac{1}{2}}$[(2)1-2-3-(2)4+5+6]
2	T_b^{I}	$12^{-\frac{1}{2}}$[(2)1-2-3+(2)4-5-6]	$12^{-\frac{1}{2}}$[(2)1-2-3-(2)4+5+6]
3	T_c^{I}	$12^{-\frac{1}{2}}$[(2)1-2-3+(2)4-5-6]	$12^{-\frac{1}{2}}$[(2)1-2-3-(2)4+5+6]
4	T_a^{II}	$12^{-\frac{1}{2}}$[(2)7-8-9+(2)10-11-12]	$12^{-\frac{1}{2}}$[(2)7-8-9-(2)10+11+12]
5	T_b^{II}	$12^{-\frac{1}{2}}$[(2)7-8-9+(2)10-11-12]	$12^{-\frac{1}{2}}$[(2)7-8-9-(2)10+11+12]
6	T_c^{II}	$12^{-\frac{1}{2}}$[(2)7-8-9+(2)10-11-12]	$12^{-\frac{1}{2}}$[(2)7-8-9-(2)10+11+12]
7	R_a^{I}	$12^{-\frac{1}{2}}$[(2)1-2-3+(2)4-5-6]	$12^{-\frac{1}{2}}$[(2)1-2-3-(2)4+5+6]
8	R_b^{I}	$12^{-\frac{1}{2}}$[(2)1-2-3+(2)4-5-6]	$12^{-\frac{1}{2}}$[(2)1-2-3-(2)4+5+6]
9	R_c^{I}	$12^{-\frac{1}{2}}$[(2)1-2-3+(2)4-5-6]	$12^{-\frac{1}{2}}$[(2)1-2-3-(2)4+5+6]
10	R_a^{II}	$12^{-\frac{1}{2}}$[(2)7-8-9+(2)10-11-12]	$12^{-\frac{1}{2}}$[(2)7-8-9-(2)10+11+12]
11	R_b^{II}	$12^{-\frac{1}{2}}$[(2)7-8-9+(2)10-11-12]	$12^{-\frac{1}{2}}$[(2)7-8-9-(2)10+11+12]
12	R_c^{II}	$12^{-\frac{1}{2}}$[(2)7-8-9+(2)10-11-12]	$12^{-\frac{1}{2}}$[(2)7-8-9-(2)10+11+12]
13	T_a^{I}	½ [2-3+5-6]	½ [2-3-5+6]
14	T_b^{I}	½ [2-3+5-6]	½ [2-3-5+6]
15	T_c^{I}	½ [2-3+5-6]	½ [2-3-5+6]
16	T_a^{II}	½ [8-9+11-12]	½ [8-9-11+12]
17	T_b^{II}	½ [8-9+11-12]	½ [8-9-11+12]
18	T_c^{II}	½ [8-9+11-12]	½ [8-9-11+12]
19	R_a^{I}	½ [2-3+5-6]	½ [2-3-5+6]
20	R_b^{I}	½ [2-3+5-6]	½ [2-3-5+6]
21	R_c^{I}	½ [2-3+5-6]	½ [2-3-5+6]
22	R_a^{II}	½ [8-9+11-12]	½ [8-9-11+12]
23	R_b^{II}	½ [8-9+11-12]	½ [8-9-11+12]
24	R_c^{II}	½ [8-9+11-12]	½ [8-9-11+12]

continued . . .

Appendix III, continued

Symmetry coordinates for ice IX

no.	Q_{TR}	Symmetry coordinates	
		A_1	B_2
1	T_a^1	$8^{-\frac{1}{2}}$[1+2+3+4+5+6+7+8]	$8^{-\frac{1}{2}}$[1+2-3-4+5+6-7-8]
2	T_b^1	$8^{-\frac{1}{2}}$[1+2+3+4+5+6+7+8]	$8^{-\frac{1}{2}}$[1+2-3-4+5+6-7-8]
3	T_c^1	$8^{-\frac{1}{2}}$[1+2+3+4+5+6+7+8]	$8^{-\frac{1}{2}}$[1+2-3-4+5+6-7-8]
4	T_c^2	$\frac{1}{2}$ [9+10+11+12]	$\frac{1}{2}$ [9+10-11-12]
5	R_a^1	$8^{-\frac{1}{2}}$[1+2+3+4+5+6+7+8]	$8^{-\frac{1}{2}}$[1+2-3-4+5+6-7-8]
6	R_b^1	$8^{-\frac{1}{2}}$[1+2+3+4+5+6+7+8]	$8^{-\frac{1}{2}}$[1+2-3-4+5+6-7-8]
7	R_c^1	$8^{-\frac{1}{2}}$[1+2+3+4+5+6+7+8]	$8^{-\frac{1}{2}}$[1+2-3-4+5+6-7-8]
8	R_c^2	$\frac{1}{2}$ [9+10+11+12]	$\frac{1}{2}$ [9+10-11-12]

		A_2	B_1
1	T_a^1	$8^{-\frac{1}{2}}$[1+2+3+4-5-6-7-8]	$8^{-\frac{1}{2}}$[1+2-3-4-5-6+7+8]
2	T_b^1	$8^{-\frac{1}{2}}$[1+2+3+4-5-6-7-8]	$8^{-\frac{1}{2}}$[1+2-3-4-5-6+7+8]
3	T_c^1	$8^{-\frac{1}{2}}$[1+2+3+4-5-6-7-8]	$8^{-\frac{1}{2}}$[1+2-3-4-5-6+7+8]
4	T_a^2	$\frac{1}{2}$ [9+10+11+12]	$\frac{1}{2}$ [9+10-11-12]
5	T_b^2	$\frac{1}{2}$ [9+10+11+12]	$\frac{1}{2}$ [9+10-11-12]
6	R_a^1	$8^{-\frac{1}{2}}$[1+2+3+4-5-6-7-8]	$8^{-\frac{1}{2}}$[1+2-3-4-5-6+7+8]
7	R_b^1	$8^{-\frac{1}{2}}$[1+2+3+4-5-6-7-8]	$8^{-\frac{1}{2}}$[1+2-3-4-5-6+7+8]
8	R_c^1	$8^{-\frac{1}{2}}$[1+2+3+4-5-6-7-8]	$8^{-\frac{1}{2}}$[1+2-3-4-5-6+7+8]
9	R_a^2	$\frac{1}{2}$ [9+10+11+12]	$\frac{1}{2}$ [9+10-11-12]
10	R_b^2	$\frac{1}{2}$ [9+10+11+12]	$\frac{1}{2}$ [9+10-11-12]

continued . . .

Appendix III, continued

Symmetry coordinates for ice IX, continued

no.	Q_{TR}	Symmetry coordinates	
		E_a	E_b
1	T_c^1	½ [1-2+5-6]	½ [1-2-5+6]
2	T_c^1	½ [3-4+8-7]	½ [3-4-8+7]
3	T_c^2	$2^{-\frac{1}{2}}$[9-10]	$2^{-\frac{1}{2}}$[11-12]
4	T_b^1	½ [1-2+5-6]	½ [1-2-5+6]
5	T_b^1	½ [3-4+8-7]	½ [3-4-8+7]
6	T_b^2	$2^{-\frac{1}{2}}$[11-12]	$2^{-\frac{1}{2}}$[9-10]
7	T_a^1	½ [1-2+5-6]	½ [1-2-5+6]
8	T_a^1	½ [3-4+8-7]	½ [3-4-8+7]
9	T_a^2	$2^{-\frac{1}{2}}$[11-12]	$2^{-\frac{1}{2}}$[9-10]
10	R_c^1	½ [1-2+5-6]	½ [1-2-5+6]
11	R_c^1	½ [3-4+8-7]	½ [3-4-8+7]
12	R_c^2	$2^{-\frac{1}{2}}$[9-10]	$2^{-\frac{1}{2}}$[11-12]
13	R_b^1	½ [1-2+5-6]	½ [1-2-5+6]
14	R_b^1	½ [3-4+8-7]	½ [3-4-8+7]
15	R_b^2	$2^{-\frac{1}{2}}$[11-12]	$2^{-\frac{1}{2}}$[9-10]
16	R_a^1	½ [1-2+5-6]	½ [1-2-5+6]
17	R_a^1	½ [3-4+8-7]	½ [3-4-8+7]
18	R_a^2	$2^{-\frac{1}{2}}$[11-12]	$2^{-\frac{1}{2}}$[9-10]

Appendix IV

Relative Raman intensities of the translational vibrations of ice II and ice IX, calculated with various values of RP(r).

	no.	ν_{calc}	RP(r)[a]			
			2	5	10	20
D_2O ice II	7	264.2	53.3	42.9	42.0	41.7
T_1^{II}	8	197.8	62.9	46.7	45.0	44.6
	9	156.0	4.1	1.5	1.2	1.11
	10	97.5	5.6	1.2	0.74	0.59
	11	82.8	22.5	4.3	2.5	1.90
	12	74.6	24.8	7.5	5.8	5.2
	31	271.3	44.4	44.4	44.4	44.4
	32	225.5	100.0	100.0	100.0	100.0
	33	186.3	20.2	20.2	20.2	20.2
	34	168.2	43.1	43.1	43.1	43.1
	35	89.5	2.2	2.2	2.2	2.2
	36	63.2	0.29	0.29	0.29	0.29
D_2O ice IX	5	247.4	40.5	33.5	32.8	32.6
T_1^{IX}	6	171.9	34.2	6.8	4.1	3.1
	7	95.3	245.	46.9	27.3	20.6
	8	81.0	239.	45.8	26.6	20.1
	24	240.2	0.014	0.014	0.014	0.014
	25	196.7	22.2	22.2	22.2	22.2
	26	191.0	60.2	60.2	60.2	60.2
	27	100.3	0.38	0.38	0.38	0.38
	28	60.8	0.36	0.36	0.36	0.36
	33	241.8	2.1	2.1	2.1	2.1
	34	212.0	10.7	10.7	10.7	10.7
	35	161.0	1.41	1.41	1.41	1.41
	36	79.1	0.057	0.057	0.057	0.057
	46	241.0	3.4	3.4	3.4	3.4
	47	233.8	3.3	3.3	3.3	3.3
	48	213.6	100.0	100.0	100.0	100.0
	49	202.1	21.5	21.5	21.5	21.5
	50	159.3	6.0	6.0	6.0	6.0
	51	142.6	0.43	0.43	0.43	0.43
	52	88.0	0.41	0.41	0.41	0.41
	53	71.8	2.0	2.0	2.0	2.0
	54	0	0	0	0	0

[a] $\alpha'_{\parallel}(\theta) = \alpha'_{\perp}(\theta) = 0.0$

Appendix V

Symmetrized eigenvectors for D_2O ice II, calculated under force field T_1^{II}. The order of the symmetry coordinates is the order of the translational symmetry coordinates given in Appendix III.

A_g	FREQ. = 264.2 CM-1	0.3692	0.2200	0.5672	-0.4050	0.2555	-0.5141
	FREQ. = 197.8 CM-1	0.6178	-0.3903	-0.1417	0.4189	0.5179	0.0477
	FREQ. = 156.0 CM-1	-0.3258	0.6007	0.1301	0.5799	0.4157	-0.0838
	FREQ. = 97.5 CM-1	-0.5280	-0.3429	-0.2417	-0.3563	0.6126	-0.2075
	FREQ. = 82.8 CM-1	-0.1365	-0.1706	0.6288	-0.0957	0.2188	0.7070
	FREQ. = 74.6 CM-1	-0.2801	-0.5402	0.4329	0.4337	-0.2658	-0.4285
A_u	FREQ. = 282.5 CM-1	0.0269	-0.0305	0.7511	0.1421	0.0072	0.6434
	FREQ. = 240.9 CM-1	0.1592	0.2575	-0.4764	-0.4212	0.2819	0.6515
	FREQ. = 210.5 CM-1	0.4893	0.5799	-0.1321	0.5250	-0.3590	0.0494
	FREQ. = 146.4 CM-1	-0.5025	0.3919	-0.0321	0.4546	0.6208	-0.0303
	FREQ. = 116.6 CM-1	-0.3408	0.6472	0.2834	-0.5156	-0.3005	-0.1686
	FREQ. = 0.0 CM-1	0.6049	0.1548	0.3318	-0.2330	0.5621	-0.3602
E_g	FREQ. = 271.3 CM-1	-0.1574 0.0132	0.2308 -0.0758	0.1692 0.6424	-0.2625 0.2356	-0.0641 0.1033	0.2870 0.5032
	FREQ. = 271.3 CM-1	0.0132 0.1574	-0.0758 -0.2308	0.6424 -0.1692	0.2356 0.2625	0.1033 0.0641	0.5032 -0.2870
	FREQ. = 225.5 CM-1	0.1938 0.2412	-0.1737 0.2384	0.1362 -0.4826	-0.1909 -0.2436	-0.1660 0.3018	0.1975 0.5589
	FREQ. = 225.5 CM-1	0.2412 -0.1938	0.2384 0.1737	-0.4826 -0.1362	-0.2436 0.1909	0.3018 0.1660	0.5589 -0.1975
	FREQ. = 186.3 CM-1	0.4662 0.2715	0.2959 0.2831	-0.0874 0.2127	0.4457 -0.0171	-0.4887 -0.1601	0.1431 -0.0670
	FREQ. = 186.3 CM-1	0.2715 -0.4662	0.2831 -0.2959	0.2127 0.0874	-0.0171 -0.4457	-0.1602 0.4887	-0.0670 -0.1431

continued . . .

Appendix V, continued

```
     FREQ. =  168.2 CM-1       -0.1080   0.5298   0.0103   0.4337   0.1605  -0.1636
                               -0.2479  -0.0792  -0.3801   0.2886  -0.0385   0.4123

     FREQ. =  168.2 CM-1        0.2479   0.0791   0.3801  -0.2886   0.0385  -0.4123
                               -0.1080   0.5298   0.0103   0.4337   0.1605  -0.1636

     FREQ. =   89.5 CM-1        0.1779   0.0171  -0.2225   0.1363   0.2759  -0.2786
                                0.5653  -0.2899   0.1157   0.1769   0.5457  -0.0132

     FREQ. =   89.5 CM-1        0.5653  -0.2899   0.1157   0.1769   0.5457  -0.0132
                               -0.1779  -0.0171   0.2225  -0.1363  -0.2759   0.2786

     FREQ. =   63.2 CM-1        0.2999  -0.3824  -0.1888  -0.0676  -0.4481  -0.0389
                               -0.2721  -0.4109  -0.1061   0.5050  -0.0142   0.1096

     FREQ. =   63.2 CM-1        0.2721   0.4109   0.1061  -0.5050   0.0142  -0.1097
                                0.2999  -0.3824  -0.1888  -0.0676  -0.4481  -0.0389

Eu   FREQ. =  236.4 CM-1        0.1347   0.3133   0.5871  -0.5117   0.0639  -0.3365
                                0.0158  -0.0384  -0.2539  -0.1467  -0.2375  -0.1255

     FREQ. =  236.4 CM-1       -0.0158   0.0384   0.2539   0.1467   0.2375   0.1255
                                0.1348   0.3133   0.5871  -0.5117   0.0639  -0.3365

     FREQ. =  229.1 CM-1        0.5181  -0.2024   0.0869   0.1006   0.3224  -0.4653
                                0.1354  -0.1685   0.3680   0.2258   0.0993   0.3309

     FREQ. =  229.1 CM-1       -0.1354   0.1685  -0.3680  -0.2258  -0.0993  -0.3309
                                0.5181  -0.2024   0.0869   0.1006   0.3224  -0.4653

     FREQ. =  180.9 CM-1        0.0507   0.3708  -0.2067   0.1186   0.4239   0.2236
                                0.4312  -0.1960  -0.2775  -0.3649  -0.0626   0.3673

     FREQ. =  180.9 CM-1       -0.4312   0.1960   0.2775   0.3650   0.0626  -0.3673
                                0.0507   0.3708  -0.2067   0.1186   0.4239   0.2236

     FREQ. =  127.9 CM-1       -0.0063   0.1048  -0.0716  -0.0799   0.0954   0.1170
                                0.3924   0.5540   0.0908   0.4985  -0.4866   0.0151

     FREQ. =  127.9 CM-1       -0.3924  -0.5540  -0.0908  -0.4985   0.4866  -0.0151
                               -0.0063   0.1048  -0.0716  -0.0799   0.0954   0.1170

     FREQ. =  104.8 CM-1        0.0796   0.3045  -0.3324   0.1166   0.5470  -0.1708
                               -0.5281   0.0802  -0.0966   0.1301  -0.0701  -0.3632

     FREQ. =  104.8 CM-1        0.5281  -0,0802   0.0966  -0.1301   0.0701   0.3632
                                0.0796   0.3045  -0.3324   0.1166   0.5470  -0.1708

     FREQ. =    0.0 CM-1        0.2445  -0.0216  -0.4356  -0.1435  -0.2992  -0.3740
                               -0.0852   0.4874  -0.0720  -0.4497  -0.0502   0.2127

     FREQ. =    0.0 CM-1       -0.0852   0.4874  -0.0720  -0.4497  -0.0501   0.2127
                               -0.2445   0.0216   0.4356   0.1435   0.2992   0.3740
```

continued . . .

Appendix V, continued

Symmetrized eigenvectors for D_2O ice II, calculated under force field T_2^{II}. The order of the symmetry coordinates is the order of the translational symmetry coordinates given in Appendix III.

A_g	FREQ. = 285.8 CM-1	-0.3438	-0.2353	-0.5778	0.4042	-0.2494	0.5167
	FREQ. = 213.4 CM-1	0.6115	-0.3799	-0.1211	0.4273	0.5330	0.0215
	FREQ. = 143.6 CM-1	-0.3110	0.6285	0.1173	0.6017	0.3526	-0.0900
	FREQ. = 96.6 CM-1	-0.5525	-0.3086	-0.2459	-0.3139	0.6193	-0.2387
	FREQ. = 81.8 CM-1	-0.1439	-0.1244	0.5929	-0.1095	0.2696	0.7263
	FREQ. = 74.7 CM-1	0.2919	0.5428	-0.4750	-0.4260	0.2705	0.3740
A_u	FREQ. = 308.4 CM-1	0.0358	-0.0324	0.7504	0.1388	-0.0021	0.6445
	FREQ. = 262.4 CM-1	-0.1547	-0.2613	0.4800	0.4074	-0.2938	-0.6520
	FREQ. = 227.8 CM-1	0.4854	0.5819	-0.1341	0.5279	-0.3567	0.0435
	FREQ. = 137.2 CM-1	-0.4918	0.3541	-0.0261	0.4835	0.6306	-0.0265
	FREQ. = 116.5 CM-1	0.3625	-0.6654	-0.2790	0.4980	0.2698	0.1648
	FREQ. = 0.0 CM-1	0.6049	0.1548	0.3318	-0.2330	0.5621	-0.3602
E_g	FREQ. = 294.0 CM-1	-0.0709 0.1437	0.0654 -0.2255	0.6259 0.2124	0.0412 0.3258	0.0370 0.1224	0.5925 0.0836
	FREQ. = 294.0 CM-1	-0.1437 -0.0709	0.2255 0.0654	-0.2124 0.6259	-0.3258 0.0412	-0.1224 0.0370	-0.0836 0.5925
	FREQ. = 238.5 CM-1	0.3251 -0.2024	0.2287 0.2655	-0.3630 -0.2080	-0.3502 0.1465	0.2583 0.3057	0.4963 -0.0706
	FREQ. = 238.5 CM-1	0.2024 0.3251	-0.2655 0.2287	0.2080 -0.3630	-0.1465 -0.3502	-0.3057 0.2583	0.0706 0.4963
	FREQ. = 184.8 CM-1	0.3752 0.3269	0.2829 0.4199	-0.1189 0.1372	0.4322 0.2479	-0.3474 -0.2913	0.0906 -0.0319
	FREQ. = 184.8 CM-1	0.3269 -0.3752	0.4199 -0.2829	0.1372 0.1189	0.2479 -0.4322	-0.2913 0.3475	-0.0319 -0.0906

continued . . .

Appendix V, continued

```
       FREQ. =  157.2 CM-1     -0.1052   0.3988   0.2041   0.2170   0.1973  -0.3341
                               -0.2307   0.0771  -0.4532   0.3799   0.0673   0.4209

       FREQ. =  157.2 CM-1     -0.2307   0.0771  -0.4532   0.3799   0.0673   0.4209
                                0.1052  -0.3988  -0.2041  -0.2170  -0.1973   0.3341

       FREQ. =   89.4 CM-1      0.1886   0.0094  -0.2113   0.1361   0.2805  -0.2814
                                0.5618  -0.2918   0.1316   0.1753   0.5420  -0.0261

       FREQ. =   89.4 CM-1      0.5618  -0.2918   0.1316   0.1753   0.5420  -0.0261
                               -0.1886  -0.0094   0.2113  -0.1360  -0.2805   0.2814

       FREQ. =   63.3 CM-1     -0.3196   0.3556   0.1790   0.1024   0.4475   0.0413
                                0.2497   0.4348   0.1185  -0.4987   0.0417  -0.1052

       FREQ. =   63.3 CM-1      0.2497   0.4348   0.1185  -0.4987   0.0417  -0.1052
                                0.3196  -0.3556  -0.1790  -0.1024  -0.4475  -0.0413

  Eu   FREQ. =  252.9 CM-1     -0.0495   0.3822   0.3144  -0.5812  -0.1317  -0.2079
                                0.0687  -0.1426  -0.4601  -0.0941  -0.2107  -0.2535

       FREQ. =  252.9 CM-1     -0.0686   0.1426   0.4601   0.0941   0.2107   0.2535
                               -0.0495   0.3822   0.3144  -0.5812  -0.1317  -0.2079

       FREQ. =  241.4 CM-1     -0.3948   0.1963  -0.3534   0.0361  -0.0900  -0.0968
                                0.4486   0.0473   0.1474  -0.0952   0.4159  -0.5046

       FREQ. =  241.4 CM-1      0.4486   0.0473   0.1474  -0.0952   0.4159  -0.5046
                                0.3948  -0.1963   0.3534  -0.0361   0.0900   0.0968

       FREQ. =  170.1 CM-1      0.1882   0.1397  -0.4526  -0.0854   0.2115   0.5183
                                0.2964  -0.3369  -0.1071  -0.3331  -0.2917   0.1038

       FREQ. =  170.1 CM-1     -0.2964   0.3369   0.1071   0.3330   0.2917  -0.1038
                                0.1882   0.1397  -0.4526  -0.0854   0.2115   0.5183

       FREQ. =  112.3 CM-1      0.1498   0.2650  -0.0474   0.0516  -0.0075   0.1174
                                0.3633   0.5397   0.0543   0.5339  -0.4176  -0.0538

       FREQ. =  112.3 CM-1     -0.3633  -0.5397  -0.0543  -0.5339   0.4176   0.0538
                                0.1497   0.2650  -0.0474   0.0516  -0.0075   0.1174

       FREQ. =  104.8 CM-1     -0.1819  -0.2060   0.2961  -0.0219  -0.5914   0.0713
                                0.5079  -0.1335   0.1970  -0.1172  -0.1051   0.3770

       FREQ. =  104.8 CM-1      0.5078  -0.1336   0.1970  -0.1172  -0.1051   0.3770
                                0.1819   0.2059  -0.2961   0.0218   0.5914  -0.0713

       FREQ. =    0.0 CM-1     -0.2377   0.3457   0.2720  -0.1987   0.1863   0.4193
                               -0.1027  -0.3442   0.3478   0.4282   0.2394   0.0966

       FREQ. =    0.0 CM-1      0.1027   0.3442  -0.3478  -0.4282  -0.2394  -0.0966
                               -0.2377   0.3457   0.2720  -0.1987   0.1863   0.4193
```

continued . . .

Appendix V, continued

Symmetrized eigenvectors for D_2O ice IX, calculated under force field T_1^{IX}. The order of the symmetry coordinates is the order of the translational symmetry coordinates given in Appendix III.

```
A1  FREQ. =  247.4 CM-1    0.5310  -0.0973   0.4659  -0.7011
    FREQ. =  171.9 CM-1    0.6059   0.7168  -0.0228   0.3443
    FREQ. =   95.3 CM-1   -0.5238   0.4571   0.7186   0.0175
    FREQ. =   81.0 CM-1    0.2769  -0.5174   0.5158   0.6242
A2  FREQ. =  226.3 CM-1    0.4621  -0.2751   0.4544   0.5497  -0.4495
    FREQ. =  209.3 CM-1   -0.5199  -0.5911  -0.2375   0.5223   0.2259
    FREQ. =  138.2 CM-1    0.6467   0.0069  -0.2756   0.2362   0.6708
    FREQ. =   74.3 CM-1   -0.0911  -0.2832   0.7607  -0.2829   0.5028
    FREQ. =    0.0 CM-1   -0.2993   0.7033   0.2872   0.5378   0.2099
B1  FREQ. =  240.2 CM-1   -0.0557   0.4470   0.8158  -0.1661   0.3225
    FREQ. =  196.7 CM-1    0.1498  -0.5696   0.4040   0.6845   0.1460
    FREQ. =  191.0 CM-1    0.7308  -0.1262  -0.1695  -0.2888   0.5812
    FREQ. =  100.3 CM-1    0.0179   0.6136  -0.3356   0.6347   0.3282
    FREQ. =   60.8 CM-1   -0.6634  -0.2886  -0.1731  -0.1325   0.6551
B2  FREQ. =  241.8 CM-1   -0.0470   0.5308   0.7411   0.4083
    FREQ. =  212.0 CM-1    0.4705   0.1734  -0.4880   0.7145
    FREQ. =  161.1 CM-1   -0.6326   0.6219  -0.4591  -0.0480
    FREQ. =   79.1 CM-1    0.6134   0.5490  -0.0424  -0.5662
Ea  FREQ. =  241.0 CM-1   -0.1516   0.5124   0.5792   0.1942   0.1998   0.2070
                          -0.4070   0.2668  -0.1472

    FREQ. =  233.8 CM-1    0.6462  -0.0469   0.2281   0.2874   0.0009  -0.3522
                           0.2636   0.4894   0.1120

    FREQ. =  213.6 CM-1   -0.2295   0.1855   0.2315  -0.0216  -0.6210  -0.0498
                           0.0617   0.0013   0.6833

    FREQ. =  202.1 CM-1    0.4098   0.5514  -0.4417  -0.4080   0.0313  -0.0920
                          -0.3517   0.0395   0.1781

    FREQ. =  159.3 CM-1    0.1163  -0.3451  -0.1935  -0.0423  -0.2706   0.6514
                          -0.2395   0.5224   0.0192

    FREQ. =  142.6 CM-1   -0.1555   0.0386   0.2485  -0.7466   0.1850   0.0511
                           0.4535   0.3332  -0.0403
```

continued . . .

Appendix V, continued

```
    FREQ. =   88.0 CM-1      0.0798  -0.0495  -0.0123   0.1413   0.6284   0.3683
                             0.1323  -0.1399   0.6351
    FREQ. =   71.8 CM-1     -0.0514   0.5232  -0.3127   0.3148  -0.1399   0.3390
                             0.5917   0.0501  -0.1993
    FREQ. =    0.0 CM-1     -0.5404  -0.0028  -0.4082   0.1857   0.2270  -0.3803
                            -0.0823   0.5308   0.1484
E_b FREQ. =  241.0 CM-1     -0.5124  -0.1517   0.5791  -0.1998   0.1942  -0.2071
                            -0.2667  -0.4071   0.1472
    FREQ. =  233.8 CM-1      0.0468   0.6462   0.2282  -0.0009   0.2875   0.3522
                            -0.4894   0.2635  -0.1119
    FREQ. =  213.6 CM-1      0.1855   0.2295  -0.2315  -0.6210   0.0216  -0.0498
                             0.0013  -0.0617   0.6833
    FREQ. =  202.1 CM-1      0.5514  -0.4098   0.4417   0.0313   0.4080  -0.0920
                             0.0395   0.3517   0.1781
    FREQ. =  159.3 CM-1     -0.3451  -0.1163   0.1936  -0.2706   0.0423   0.6513
                             0.5224   0.2395   0.0192
    FREQ. =  142.6 CM-1     -0.0386  -0.1555   0.2484  -0.1850  -0.7466  -0.0512
                            -0.3332   0.4535   0.0403
    FREQ. =   88.0 CM-1     -0.0495  -0.0798   0.0123   0.6284  -0.1413   0.3683
                            -0.1400  -0.1323   0.6352
    FREQ. =   71.8 CM-1      0.5232   0.0514   0.3127  -0.1398  -0.3147   0.3391
                             0.0501  -0.5917  -0.1992
    FREQ. =    0.0 CM-1      0.0028  -0.5404  -0.4082  -0.2271   0.1857   0.3803
                            -0.5308  -0.0823  -0.1485
```

continued . . .

Appendix V, continued

Symmetrized eigenvectors for D_2O ice IX, calculated under force field T_2^{IX}. The order of the symmetry coordinates is the order of the translational symmetry coordinates given in Appendix III.

```
A1   FREQ. =  246.8 CM-1      0.5535  -0.0701   0.4660  -0.6867
     FREQ. =  171.3 CM-1      0.5965   0.7065  -0.0451   0.3781
     FREQ. =   95.3 CM-1     -0.5171   0.4716   0.7140   0.0197
     FREQ. =   81.3 CM-1      0.2654  -0.5230   0.5206   0.6205
A2   FREQ. =  225.2 CM-1      0.5487  -0.1695   0.4843   0.4550  -0.4781
     FREQ. =  208.0 CM-1     -0.4458  -0.6279  -0.1550   0.6051   0.1299
     FREQ. =  139.1 CM-1      0.6342  -0.0043  -0.2825   0.2452   0.6766
     FREQ. =   74.1 CM-1     -0.0917  -0.2870   0.7610  -0.2783   0.5026
     FREQ. =    0.0 CM-1     -0.2993   0.7033   0.2872   0.5378   0.2099
B1   FREQ. =  243.9 CM-1     -0.0838   0.4357   0.8338  -0.1374   0.2983
     FREQ. =  192.8 CM-1      0.5686  -0.5215   0.2181   0.3596   0.4774
     FREQ. =  191.5 CM-1     -0.4782  -0.2763   0.3416   0.6569  -0.3830
     FREQ. =  100.4 CM-1      0.0155   0.6155  -0.3329   0.6345   0.3280
     FREQ. =   60.8 CM-1     -0.6639  -0.2882  -0.1723  -0.1331   0.6549
B2   FREQ. =  245.0 CM-1     -0.0915   0.5061   0.7890   0.3362
     FREQ. =  211.4 CM-1      0.4866   0.2043  -0.3950   0.7520
     FREQ. =  159.6 CM-1     -0.6163   0.6324  -0.4689  -0.0194
     FREQ. =   79.2 CM-1      0.6125   0.5497  -0.0401  -0.5667
Ea   FREQ. =  241.5 CM-1      0.1560  -0.5543  -0.5250  -0.1439  -0.2101  -0.2202
                              0.4496  -0.2365   0.1458

     FREQ. =  236.3 CM-1      0.6555  -0.0236   0.2393   0.2948   0.0348  -0.3230
                              0.2215   0.5150   0.0758

     FREQ. =  209.9 CM-1     -0.2582   0.1260   0.3176   0.0318  -0.6105  -0.0540
                              0.1182   0.0293   0.6521

     FREQ. =  201.8 CM-1     -0.3843  -0.5367   0.4521   0.4034   0.0588   0.1295
                              0.3140   0.0070  -0.2798

     FREQ. =  160.3 CM-1     -0.1134   0.3295   0.2145   0.0390   0.2822  -0.6540
                              0.2662  -0.5018  -0.0306

     FREQ. =  142.3 CM-1     -0.1350   0.0408   0.2257  -0.7566   0.1885   0.0668
                              0.4386   0.3495  -0.0476

     FREQ. =   88.0 CM-1      0.0770  -0.0554  -0.0081   0.1412   0.6266   0.3668
                              0.1324  -0.1406   0.6376
```

continued . . .

Appendix V, continued

```
        FREQ. =   71.8 CM-1      -0.0498   0.5244  -0.3133   0.3166  -0.1383   0.3407
                                  0.5905   0.0495  -0.1943

        FREQ. =    0.0 CM-1       0.5404   0.0028   0.4082  -0.1857  -0.2270   0.3803
                                  0.0823  -0.5308  -0.1484

E_b     FREQ. =  241.5 CM-1      -0.5543  -0.1562   0.5250  -0.2101   0.1438  -0.2203
                                 -0.2363  -0.4497   0.1458

        FREQ. =  236.3 CM-1       0.0235   0.6555   0.2394  -0.0348   0.2948   0.3230
                                 -0.5151   0.2214  -0.0758

        FREQ. =  209.9 CM-1       0.1260   0.2582  -0.3176  -0.6105  -0.0317  -0.0540
                                  0.0293  -0.1182   0.6521

        FREQ. =  201.8 CM-1       0.5367  -0.3843   0.4521  -0.0588   0.4034  -0.1295
                                 -0.0070   0.3140   0.2798

        FREQ. =  160.3 CM-1      -0.3295  -0.1134   0.2146  -0.2822   0.0389   0.6540
                                  0.5018   0.2662   0.0306

        FREQ. =  142.3 CM-1      -0.0407  -0.1350   0.2257  -0.1885  -0.7566  -0.0668
                                 -0.3495   0.4385   0.0475

        FREQ. =   88.0 CM-1      -0.0555  -0.0770   0.0081   0.6266  -0.1412   0.3668
                                 -0.1406  -0.1324   0.6376

        FREQ. =   71.8 CM-1       0.5244   0.0498   0.3133  -0.1382  -0.3166   0.3408
                                  0.0494  -0.5905  -0.1943

        FREQ. =    0.0 CM-1       0.0028  -0.5404  -0.4082  -0.2271   0.1857   0.3803
                                 -0.5308  -0.0823  -0.1485
```

Appendix VI

Calculated frequencies of the translational and rotational vibrations of the true and linear structure models of ice IX under three coordinate sets.

Coordinate set A^{OX}(H··O-H), true structure model

	no.	H_2O^a	D_2O^a	ν_H/ν_D
A_1	1	1156.8	838.9	1.379
	2	875.7	650.0	1.347
	3	810.1	584.8	1.385
	4	718.8	525.4	1.368
	5	277.5	261.6	1.061
	6	183.3	170.5	1.075
	7	134.8	126.9	1.062
	8	93.2	86.4	1.079
A_2	9	1170.2	853.3	1.371
	10	1119.9	822.5	1.362
	11	792.2	591.2	1.340
	12	693.5	544.7	1.273
	13	463.0	381.6	1.213
	14	236.6	221.6	1.068
	15	211.9	175.9	1.205
	16	131.0	114.4	1.145
	17	98.1	92.1	1.065
	18	0	0	-
B_1	19	1133.6	814.4	1.392
	20	929.2	702.0	1.324
	21	879.6	659.9	1.333
	22	685.3	521.0	1.315
	23	519.6	425.8	1.220
	24	247.0	229.2	1.078
	25	201.8	188.1	1.073
	26	172.3	145.8	1.182
	27	132.6	121.3	1.093
	28	66.6	61.4	1.085
B_2	29	1236.3	876.6	1.410
	30	924.2	685.2	1.349
	31	651.3	506.8	1.285
	32	440.0	331.6	1.327
	33	257.6	242.9	1.061
	34	243.1	226.9	1.071
	35	158.4	139.9	1.132
	36	91.0	82.5	1.103
E	37	1228.5	878.3	1.399
	38	1153.8	836.5	1.379
	39	1049.0	778.1	1.348
	40	893.8	667.1	1.340
	41	843.9	623.6	1.353
	42	727.4	542.8	1.340
	43	616.9	489.2	1.261
	44	593.9	462.2	1.285
	45	474.1	367.2	1.291
	46	260.4	243.3	1.070
	47	253.2	233.5	1.084
	48	231.7	214.9	1.078
	49	211.2	188.4	1.121
	50	160.7	142.1	1.131
	51	148.0	131.7	1.124
	52	115.9	108.2	1.071
	53	78.0	70.6	1.105
	54	0	0	-

[a] $k_r = 0.20$ mdyne Å^{-1}, $H_\theta = 0.0075$ mdyne Å^{-1}, $H_\phi = 0.160$ mdyne Å^{-1}.

continued . . .

Appendix VI, continued

Coordinate set A^{ox}(H··O-H), linear structure model

	no.	H_2O^b	D_2O^b	ν_H/ν_D
A_1	1	1178.3	854.8	1.378
	2	840.4	615.4	1.366
	3	801.4	576.1	1.391
	4	650.8	483.2	1.347
	5	276.0	260.5	1.060
	6	184.2	171.2	1.076
	7	130.7	123.8	1.056
	8	95.5	88.3	1.082
A_2	9	1198.1	873.0	1.372
	10	1109.4	811.0	1.368
	11	762.2	584.3	1.304
	12	664.0	507.5	1.308
	13	448.0	377.3	1.187
	14	232.7	217.4	1.070
	15	196.9	159.3	1.236
	16	134.1	118.7	1.130
	17	94.4	88.9	1.062
	18	0	0	-
B_1	19	1130.1	813.9	1.388
	20	912.8	684.8	1.333
	21	866.2	649.4	1.334
	22	711.8	543.2	1.310
	23	529.2	431.0	1.228
	24	247.7	230.5	1.075
	25	201.7	188.2	1.072
	26	172.5	145.9	1.182
	27	120.7	111.6	1.082
	28	65.8	60.5	1.088
B_2	29	1206.1	854.9	1.411
	30	920.2	676.8	1.360
	31	650.6	510.7	1.274
	32	455.7	341.3	1.335
	33	256.2	242.1	1.058
	34	240.5	225.6	1.066
	35	157.4	138.2	1.139
	36	91.1	83.2	1.095
E	37	1215.7	870.6	1.396
	38	1158.5	840.7	1.378
	39	1038.8	766.9	1.355
	40	867.1	639.8	1.355
	41	822.5	611.6	1.346
	42	736.9	554.8	1.328
	43	616.3	482.1	1.278
	44	584.8	456.5	1.281
	45	467.9	363.5	1.287
	46	259.7	243.5	1.067
	47	248.4	228.8	1.086
	48	224.4	209.3	1.072
	49	213.5	190.6	1.120
	50	159.8	142.2	1.124
	51	147.2	130.8	1.125
	52	107.0	99.6	1.074
	53	77.2	69.9	1.104
	54	0	0	-

---

[b] $k_r = 0.20$ mdyne Å^{-1}, $H_\theta = 0.0075$ mdyne Å^{-1}, $H_\phi = 0.160$ mdyne Å^{-1}.

continued . . .

Appendix VI, continued

Coordinate set A^{ox}(O··O-D), true structure model

	no.	H_2O^c	D_2O^c	ν_H/ν_D		no.	H_2O^c	D_2O^c	ν_H/ν_D
A_1	1	638.1	474.8	1.344	B_2	29	659.1	502.5	1.312
	2	597.6	433.0	1.380		30	593.0	424.7	1.396
	3	585.2	416.7	1.404		31	581.1	416.2	1.396
	4	477.0	359.8	1.326		32	483.6	364.6	1.326
	5	262.2	245.9	1.066		33	252.8	237.0	1.067
	6	176.1	161.2	1.092		34	228.9	216.9	1.055
	7	102.7	96.1	1.069		35	161.0	144.6	1.113
	8	89.7	84.0	1.068		36	81.7	75.7	1.079
A_2	9	649.3	498.9	1.301	E	37	654.6	500.4	1.308
	10	635.7	480.8	1.322		38	648.6	491.9	1.319
	11	595.2	434.6	1.370		39	642.1	488.1	1.316
	12	509.4	384.1	1.326		40	594.7	429.3	1.385
	13	477.7	358.3	1.333		41	587.8	427.7	1.374
	14	233.6	216.0	1.081		42	584.0	417.1	1.400
	15	206.7	181.9	1.136		43	509.9	386.6	1.319
	16	136.2	122.1	1.115		44	483.8	367.2	1.318
	17	83.0	78.6	1.056		45	480.8	362.9	1.325
	18	0	0	-		46	249.8	232.8	1.073
						47	241.1	220.6	1.093
B_1	19	659.6	502.4	1.313		48	217.0	199.4	1.088
	20	644.6	496.7	1.298		49	210.5	190.5	1.105
	21	583.4	422.5	1.381		50	160.2	145.4	1.102
	22	510.4	388.7	1.313		51	144.5	130.9	1.104
	23	487.4	369.5	1.319		52	93.3	86.4	1.080
	24	248.6	231.5	1.074		53	77.5	72.1	1.075
	25	201.1	184.5	1.090		54	0	0	-
	26	187.2	165.5	1.131					
	27	105.4	96.6	1.091					
	28	63.2	58.5	1.080					

---

[c] $k_r = 0.20$ mdyne Å^{-1}, $H_\theta = 0.0075$ mdyne Å^{-1}, $H_{\phi'} = 0.060$ mdyne Å^{-1}.

continued . . .

Appendix VI, continued

Coordinate set A^{ox}(H-H'), true structure model

	no.	H_2O^d	D_2O^d	ν_H/ν_D
A_1	1	823.0	578.9	1.422
	2	720.4	500.6	1.439
	3	587.0	464.6	1.263
	4	549.4	421.7	1.303
	5	399.9	338.2	1.182
	6	254.1	228.1	1.114
	7	151.4	147.3	1.031
	8	120.8	118.6	1.019
B_1	9	886.4	645.5	1.373
	10	808.8	578.0	1.399
	11	614.4	443.4	1.386
	12	562.7	406.3	1.385
	13	447.1	381.4	1.172
	14	264.3	215.8	1.225
	15	230.3	211.4	1.089
	16	172.1	169.4	1.016
	17	104.3	104.1	1.002
	18	0	0	-
B_1	19	854.4	618.4	1.382
	20	748.9	550.5	1.360
	21	686.5	510.5	1.345
	22	511.9	445.5	1.149
	23	432.4	386.3	1.116
	24	426.1	303.6	1.403
	25	246.7	234.8	1.051
	26	206.1	191.1	1.078
	27	138.3	137.9	1.003
	28	74.1	67.6	1.096
B_2	29	857.8	617.2	1.390
	30	792.3	596.1	1.329
	31	476.1	433.8	1.098
	32	435.0	376.6	1.155
	33	410.6	307.1	1.337
	34	364.6	294.1	1.240
	35	198.9	202.8	0.981
	36	103.1	93.8	1.099
E	37	877.6	635.7	1.381
	38	830.2	597.5	1.389
	39	812.4	587.0	1.384
	40	728.1	526.0	1.384
	41	656.7	505.9	1.298
	42	551.0	436.2	1.263
	43	520.4	406.9	1.279
	44	507.7	391.4	1.297
	45	437.6	364.6	1.200
	46	401.8	326.4	1.231
	47	340.2	293.0	1.161
	48	322.7	287.6	1.122
	49	233.3	218.7	1.067
	50	190.7	188.4	1.012
	51	183.7	176.4	1.041
	52	115.3	110.6	1.042
	53	89.4	82.4	1.085
	54	0	0	-

---

[d] $k_r = 0.20$ mdyne $\mathring{A}^{-1}$, $H_\theta = 0.0075$ mdyne $\mathring{A}^{-1}$, $k^H = 0.043$ to 0.28 mdyne $\mathring{A}^{-1}$

Appendix VII

Second derivatives of the Clementi pair potential evaluated at the equilibrium interatomic distances

Constants of ε_{INTER}:

$q^2 = 0.514783$ a.u.
$a_1 = 1734.196000$ a.u.
$b_1 = 2.726696$ a.u.
$a_2 = 1.061887$ a.u.
$b_2 = 1.460975$ a.u.
$a_3 = 2.319395$ a.u.
$b_3 = 1.567367$ a.u.
$a_4 = 0.436006$ a.u.
$b_4 = 1.181792$ a.u.

Interaction distances r_i and force constants k_i for the 56 types of interatomic interactions of ice II:

no.	r_i	k_i
1	2.328949	0.244915
2	2.498130	0.188012
3	2.337529	0.241521
4	2.427755	0.209296
5	2.467546	0.196889
6	2.475487	0.194531
7	2.439091	0.205658
8	2.441437	0.204916
9	3.163242	0.080723
10	3.767962	0.045468
11	3.375129	0.064941
12	3.801139	0.044222
13	3.853709	0.042344
14	3.751533	0.046104
15	3.932235	0.039743
16	3.695195	0.048381
17	2.023325	-0.573469
18	2.028362	-0.569207
19	3.185615	-0.146936
20	3.245418	-0.138962
21	2.065322	-0.539192
22	2.052900	-0.549039
23	3.406252	-0.120192
24	3.456775	-0.114999
25	2.938241	-0.185361
26	3.294350	-0.132861
27	3.030456	-0.170680
28	3.238218	-0.139891
29	3.293063	-0.133017
30	3.273811	-0.135377
31	3.250646	-0.138292
32	3.183930	-0.147169
33	1.811354	0.248923
34	3.038447	0.000240
35	3.024765	0.000361
36	1.864388	0.207149
37	3.178096	-0.000600
38	3.461850	-0.001036
39	3.227035	-0.000765
40	3.370602	-0.001007
41	3.443615	-0.001035
42	3.455686	-0.001036
43	3.337204	-0.000976
44	3.333647	-0.000972
45	1.844818	0.221723
46	3.222346	-0.000751
47	3.149833	-0.000478
48	1.843862	0.222460
49	2.768267	0.128141
50	2.802591	0.107368
51	2.844217	0.086641
52	2.780418	0.120364
53	2.782096	0.441185
54	2.798572	0.433439
55	2.893775	0.392051
56	2.858109	0.406912

Coordinate types 1 to 16 are H-H' interactions, 17 to 32 are H-M^- interactions, 33 to 48 are H-O interactions, 49 to 52 are O-O' interactions, and 53 to 56 are M^--M^- interactions.